Doctoral Dissertation
Doctoral Program in Energy Engineering (33th Cycle)

Hydrogen-based energy storage systems for off-grid locations

Paolo Marocco
* * * * * *

Supervisors
Prof. Massimo Santarelli, Supervisor
Prof. Andrea Lanzini, Co-Supervisor

Doctoral Examination Committee:
Prof. Dr. Robert Steinberger-Wilckens, Referee, University of Birmingham
Dr. Vibeke Stærkebye Nørstebø, Referee, SINTEF Ocean AS

Politecnico di Torino
June 09, 2021

I hereby declare that, the contents and organisation of this dissertation constitute my own original work and does not compromise in any way the rights of third parties, including those relating to the security of personal data.

Paolo Marocco

…….....

Paolo Marocco

Turin, June 09, 2021

Summary

Renewable energy sources (RESs) are key elements to promote the energy transition towards a decarbonized society. Their installed capacity is expected to increase considerably over the next few years to address the problems of fossil fuels depletion and mitigation of greenhouse gas emissions. However, the fluctuating behaviour of variable RESs (such as solar and wind) complicates their integration in electricity systems. Thus, electrical energy storage (EES) becomes crucial to address the RES-related issues and favor their widespread diffusion both in grid-connected and off-grid applications.

Focusing on off-grid areas, local RESs represent a promising way to decrease the use of diesel generators and avoid the need for unreliable and invasive connections to the grid. EES solutions should be integrated in stand-alone energy systems to improve the exploitation of local renewables and achieve higher RES penetration levels. At present, batteries are the most used EES option due to their high performance, flexibility, and increasingly lower costs. However, when the energy storage is required for longer periods, batteries alone become too expensive and their hybridization with other typologies of storage can result in a cost-effective solution.

The optimal design of off-grid hybrid renewable energy systems (HRESs) is a challenging task that often involves multiple and conflicting goals: cost of energy, reliability of the power supply service and environmental issues should be jointly addressed at the design stage of the HRES. Variability in RES production and load requires that the various components continuously adapt their operating point to reliably cover the load demand and store the surplus renewable energy. Thus, performance curves and modulation ranges should be implemented in the optimal design problem to simulate the part-load behavior of the HRES devices. The seasonal fluctuation of the RES supply and demand profiles also requires considering a year-long time horizon to adequately size the long-term storage, thus leading to a greater computational complexity of the sizing problem. Moreover, cost-effective system configurations usually involve the hybridization of power generators and storage systems, which increases the number of devices that have to be sized and operated.

The main objective of the present work is to address these challenges and better investigate the potential benefits arising from the inclusion of hydrogen-

based storage solutions. Different methods to deal with the optimal sizing of stand-alone HRESs were defined. The design optimization framework was then applied to different case studies and system configurations. However, this thesis seeks to provide a general modelling approach that can be applied to the design of any hybrid renewable energy system, going beyond the analysis of specific case studies. The work also takes advantage of valuable data and experience from the REMOTE project[1], whose aim is to develop and test hydrogen-battery storage systems to support communities characterized by unreliable, or even missing, connection to the grid.

Metaheuristic and mixed integer linear programming (MILP) methodologies were formulated to optimally size stand-alone HRESs based on batteries and/or hydrogen as storage medium. Both methods were found to be effective in modelling the longer-term storage capability of the hydrogen system. The MILP approach requires a higher computational time for the problem resolution because of the greater complexity and the much larger number of decision variables. However, the inclusion of representative days in the MILP problem allows the CPU time to be reduced significantly.

Hybrid renewable energy systems in different kinds of remote locations (from alpine to insular), with different typologies of local RESs (solar, wind, biomass and hydro) and user loads (residential and small industrial) were investigated. Techno-economic evaluations showed that the need for fossil fuels can be drastically reduced thanks to the exploitation of RESs integrated with a battery-hydrogen storage system. Moreover, the renewable solution was proved to be cheaper than the alternative options (diesel or grid-connection) either in the short term or longer term for all the sites. This is because of the high operating costs due to the diesel fuel consumption and of the capital-intensive initial cost to provide a connection to the main grid.

Results from the sizing simulations revealed that the hydrogen storage is crucial in off-grid areas to improve the independence from fossil fuels without causing a sharp increase in the cost of energy. In fact, because of its cost-effective long-term capability, hydrogen avoids the need for batteries with too large capacity and allows the local RESs to be better exploited.

[1] REMOTE project official website. 2018. https://www.remote-euproject.eu/

Acknowledgements

The research activity described in this thesis was performed at the Synergies of Thermochemical and Electrochemical Power Systems (STEPS) group, Department of Energy at Politecnico di Torino (Torino, Italy) and at the Norwegian Fuel Cell and Hydrogen Center, Sustainable Energy Technology Department at SINTEF Industry (Trondheim, Norway).

This work has received funding from the Fuel Cells and Hydrogen 2 Joint Undertaking under grant agreement No. 779541 (REMOTE, Remote area Energy supply with Multiple Options for integrated hydrogen-based Technologies). This Joint Undertaking receives support from the European Union's Horizon 2020 research and innovation programme, Hydrogen Europe and Hydrogen Europe research. The Research Council of Norway is also acknowledged for the support to the Norwegian Fuel Cell and Hydrogen Center, the Førny2020 project No. 296303 and the ENERSENSE program.

I would first like to thank my supervisor Massimo Santarelli for his continuous support, for the trust and responsibilities that he gave me and for granting me the possibility of pursuing my research interests in the hydrogen field. Special thanks also go to my co-supervisor Andrea Lanzini for his guidance and helpful advice throughout the entire PhD period.

I am really thankful to the Sustainable Energy Technology Department in SINTEF Industry: Kyrre Sundseth for allowing me to join his research group, Alejandro Oyarce Barnett for sharing with me his great expertise in PEM electrolysis, Thor Aarhaug for introducing me to the fluorine chemistry, Magnus Thomassen for his wise suggestions, and finally Stig Yngve Martinsen and Tom-Andre Enebakk Eide for the technical assistance during the experimental tests.

I am grateful to the doctoral examination committee for the detailed and constructive review: Robert Steinberger-Wilckens from University of Birmingham and Vibeke Stærkebye Nørstebø from SINTEF Ocean AS.

I would like to thank my office mates Marco and Valeria for the everyday-life support and confrontations. I would also like to gratefully acknowledge all the members of the STEPS group: Domenico, Marta, Mohsen and Salvatore for the continuous interactions, scientific discussions and inspiring collaborations we had together. Furthermore, I want to thank all my other colleagues, both inside and

outside POLITO, I have met and worked with during these years: Alexandru, Daniele, Davide, Emanuele G., Emanuele M., Fabio, Gabriel, Gabriele, Giovanna, Giulio, Marco, Miguel, Riccardo and Sonja.

I also acknowledge all the people involved in the REMOTE project, with whom it was a pleasure to collaborate over the whole PhD period.

And finally, the most important acknowledgment goes to my parents, my brother Amedeo and my sister Lucia for their daily support and for always helping me achieve my goals.

Contents

List of Acronyms

ABSO	Artificial bee swarm optimization
ACO	Ant colony optimization
ALK	Alkaline
AST	Accelerated stress tests
ASR	Area specific resistance
AT	Annual throughput
AWE	Alkaline water electrolyzer
BP	Bipolar plate
BG	Biomass generator
BOL	Beginning of life
BOP	Balance of plant
BPSE	Ballard Power System Europe
BSS	Battery storage system
BT	Battery
CAES	Compressed air energy storage
CCM	Catalyst coated membrane
CHP	Combined heat and power
CL	Catalyst layer
CPU	Central processing unit
CSA	Crow search algorithm
CTF	Cycles to failure
DD	Design day
DF	Diesel fraction
DFT	Density functional theory
DG	Diesel generator

DI	Deionized
DLC	Double layer capacitor
DOD	Depth of discharge
DRP	Demand response program
EC	Electrochemical characterization
ECSA	Electrochemical surface area
EDX	Energy-dispersive X-ray spectroscopy
EES	Electrical energy storage
EGP	Enel Green Power
EL	Electrolyzer
EMS	Energy management strategy
EOT	Equation of time
EPMA	Electron probe microanalysis
EPS	Electro Power System
EU	European Union
FC	Fuel cell
FCEV	Fuel cell electric vehicle
FES	Flywheel energy storage
FPA	Flower pollination algorithm
FRR	Fluoride release rate
GA	Genetic algorithm
GDP	Gross domestic product
GHG	Greenhouse gas
G2P	Gas to power
HER	Hydrogen evolution reaction
HICEV	Hydrogen internal combustion engine vehicle
HOR	Horizon SA
HRES	Hybrid renewable energy system
HS	Harmony search
HT	Hydrogen tank
HYG	Hydrogenics Europe
IC	Ion chromatography
ICR	Interfacial contact resistance
ISE	Ion selective electrode

KPI	Key performance indicator
LA	Lead acid
LCA	Life cycle analysis
LB	Lower bound
LCOE	Levelized cost of energy
LF	Load factor
LHV	Lower heating value
LI	Li ion
LOH	Level of hydrogen
LPM	Liters per minute
LPSP	Loss of power supply probability
LT	Lifetime throughput
MBA	Mine blast algorithm
MCM	Metrohm CO_2 suppressor
MEA	Membrane electrode assembly
MILP	Mixed integer linear programming
MINLP	Mixed-integer nonlinear program
MOP	Multi-objective optimization problem
MSM	Metrohm suppressor module
NOCT	nominal operating cell temperature
NPC	Net present cost
NSTF	Nano-structured thin film
OF	Objective function
OER	Oxygen evolution reaction
OM	Operation and maintenance
ORR	Oxygen reduction reaction
PEM	Proton exchange membrane
PEMFC	PEM fuel cell
PEMWE	PEM water electrolyzer
PFSA	Perfluorosulfonic acid
PHS	Pumped hydro storage
POW	Powidian
PR	Project
PSO	Particle swarm optimization

PTFE	Polytetrafluorethylene
PTL	Porous transport layer
PV	Photovoltaic
PWA	Piecewise affine
P2C	Power-to-chemicals
P2G	Power-to-gas
P2H	Power-to-hydrogen
P2L	Power-to-liquid
P2P	Power-to-power
P2X	Power-to-X
RB	Ruled based
RBS	Ruled based strategies
RES	Renewable energy source
SA	Simulated annealing
SEM	Scanning electron microscopy
SL	Single layer
SMES	Superconducting magnetic energy storage
SNG	Synthetic natural gas
SOC	State of charge
SPE	Solid polymer electrolyte
STC	Standard test condition
TEM	Transmission electron microscopy
TL	Two layer
TMY	Typical meteorological year
TOU	Time of use
TS	Tabu search
UB	Upper bound
WT	Wind turbine
XRD	X-Ray powder diffraction

List of Tables

List of Figures

Chapter 1

Introduction

1.1 Background

Energy transition towards a low-carbon economy is a key challenge for the next decades. Greenhouse gas (GHG) emissions due to human activities have been the dominant cause of the observed climate change since the mid-20th century. As reported in the IPCC Fifth Assessment Report, the global average surface temperature has increased by 0.85 °C in the period from 1880 to 2012 [1]. The estimated anthropogenic global warming is currently increasing by 0.2 °C per decade [2].

Prompt actions on a global scale through coordinated and cooperative responses are required to significantly reduce GHG emissions in the short term, thus limiting the risks related to climate change. The European Union (EU) is at the forefront of fighting climate change by means of ambitious policies, also in cooperation with international partners. The "2020 climate and energy package", adopted in 2009, set the following targets to be reached in EU by 2020: 20% reduction in greenhouse gas emissions from 1990 levels, increasing the share of renewable energy consumption to 20% and 20% improvement in the energy efficiency. The Paris Agreement is the first-ever universal, legally binding global climate change treaty. It was adopted by 196 Parties during the Paris climate conference (COP21) on 12 December 2015 and entered into force on 4 November 2016. The Paris Agreement long-term temperature goal is to keep the increase in global average temperature to well below 2 °C above pre-industrial levels, pursuing efforts to limit it to 1.5 °C to reduce as much as possible the risks and impacts of climate change. It also aims to achieve a "balance between anthropogenic emissions by sources and removal by sinks of greenhouse gases" by the second half of this century. According to the "2030 climate and energy framework", key targets for 2030 are the following: at least 40% cuts in GHG

emissions from 1990 levels, at least 32% share for renewable energy and 32.5% improvement in energy efficiency. As part of the EU Green Deal, the European Commission also proposed to raise the GHG emission target from 40% to 55% to better pursue the Paris Agreement objectives (and to be also in line with the intention of Europe to become carbon-neutral by 2050).

The development of non-fossil fuel sources and the attempt to reduce carbon dioxide emissions are leading to an increasing penetration of renewable energy sources (RESs). The EU share of renewable in the gross final energy consumption has progressively increased over the past fifteen years, reaching a value of approximately 19.5% in 2019, compared with 10.2% in 2005. The increased exploitation of RESs since 2005 allowed Europe to reduce its fossil fuel use by 155 Mtoe in 2019. The related CO_2 emission savings account for 513 Mt [3]. In absolute terms, the main RES market sector in EU is currently represented by heating and cooling, followed by electricity and transport. In 2019, renewable energy made up slightly more than one fifth (21.7%) of all the final energy consumed for heating and cooling with the largest contributions coming from solid biomass, heat pumps and biogas. Electricity is the second largest RES market sector in Europe: in 2019 renewable energy sources covered around 34% of the gross electricity consumption. More specifically, wind and hydro power accounted for roughly two-thirds of the overall electricity produced from RESs (35% each). The remaining one-third was from solar power (13%), solid biofuels (8%) and other renewable sources (9%). The recent growth in renewable electricity is mainly ascribed to wind power, solar power and solid biofuels, with solar representing the fasted growing source [3]. This has been possible thanks to the rapid technological progress and decreasing trends in costs of solar PV and wind technologies, which favoured their large-scale diffusion. The levelized cost of energy (LCOE) from most RESs is already competitive and, in some cases, even lower than generation costs from fossil fuels. In the period from 2010 to 2019, the costs of solar PV, onshore wind and offshore wind systems have shrunk by about 82%, 40% and 29%, respectively, and they are expected to drop even further in the coming years [4]. Renewables are required for long-term decarbonization scenarios and further considerable increase in their installed capacity is expected in the near future [3]. As an instance, approximately 323 to 397 GW of cumulative wind energy capacity are foreseen by 2030 according to [5]. In order to be in line with the 2030 GHG emission reduction objective, IRENA Remap hypotheses 327 GW of installed capacity for wind and 270 GW of solar PV, while other technologies (including biomass, hydropower, geothermal, concentrated solar power and marine) account for an additional 23 GW [6].

New renewables like solar PV and wind have thus shown considerable improvement in performance, cost reduction and dramatic growth trajectories, which makes them promising and ideal candidates to achieve the EU's sustainable energy goals. However, there are still important challenges that must be faced to further promote RES penetration and pursue the main decarbonization targets.

1.2 The key role of energy storage

The widespread diffusion of renewable energy sources, together with a general trend of increased electrification, require the development of more demanding and efficient solutions related to the power grid management and energy storage. Electrical energy storage (EES) systems are expected to increase their capacity to cope with the fluctuating and unpredictable nature related to new renewable generation (i.e., wind and solar), thus becoming key energy infrastructures both in grid-connected and off-grid applications. Main roles to be addressed by the EES are summarized below:

- Reducing the total generating costs by storing electricity during off-peak times and providing electricity during peak hours.
- Maintaining power quality, voltage and frequency by supplying/absorbing power from/into the EES when required.
- Mitigating network congestion.
- Providing stable power for off-grid systems.
- Providing emergency power supply.

According to the energy form, as displayed in Figure 1.1, EES systems can be classified into mechanical, electrochemical, chemical, electrical and thermal storage systems [7], [8].

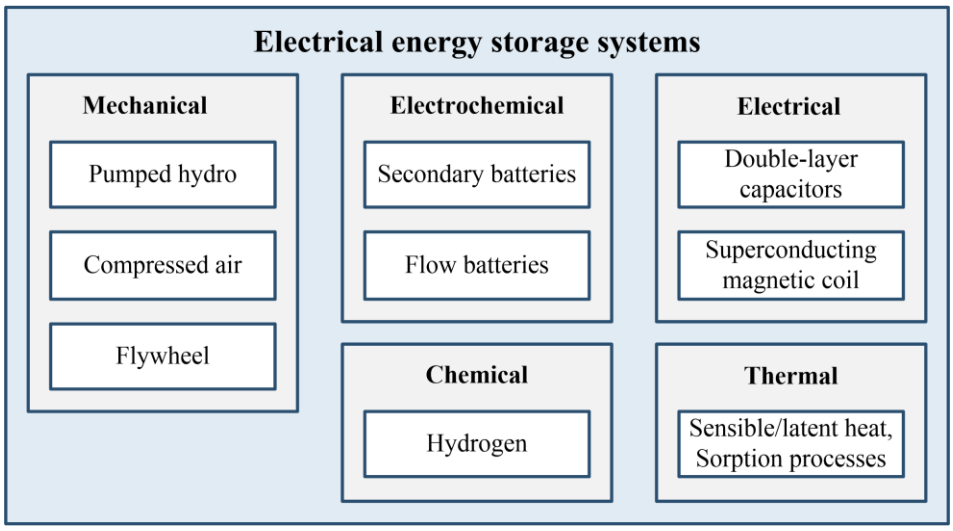

Figure 1.1 Classification of electrical energy storage systems according to the energy form. Modified from [7].

The most common mechanical storage systems include pumped hydro storage (PHS), compressed air energy storage (CAES) and flywheel energy storage (FES). Electrochemical storage systems comprise of secondary (lead-acid, NiCd/NiMH, Li-ion, metal air, sodium sulphur and sodium nickel chloride) and flow (redox

flow and hybrid flow) batteries. Chemical energy storage is based on hydrogen as starting point. Once hydrogen is generated, it can act as a multi-purpose energy carrier and additional conversion steps make it possible to store power in the form of various gaseous and liquid synthetic fuels and chemicals according to specific power-to-X (P2X) routes. Double-layer capacitors (DLCs) and superconducting magnetic energy storage (SMES) belong to the electrical-type storage. Finally, thermal storage technologies can be subdivided into storage of sensible heat, storage of latent heat and thermo-chemical adsorption/desorption processes. The above summarized EES systems have their own peculiar features in terms of storage capacity, energy density, power density, discharge time, self-discharge rate and cyclability, which makes each of these technologies suitable for a certain application [9], [10]. The different typologies of EES, rather than being competitive, are therefore complementary options to provide storage services in different areas of application.

Batteries are ideal candidates when small size and short-term energy storage is needed. Chemical storage is instead foreseen to be adopted mostly for large size and longer-term energy storage solutions, which will most probably be required in the next few years where a massive RES introduction is expected. More specifically, the main features that elect the chemical storage option as a promising strategy are as follows: high storage capability, great volumetric storage density, provision of system stabilization services, negligible self-discharge losses, flexibility to site topography and possibility for decentralized applications. The last two properties represent the main advantage with respect to the traditional long-term, high capacity PHS option [11].

Hydrogen is the simplest energy carrier that can be generated by power conversion through the power-to-hydrogen (P2H) route, first segment of the whole power-to-X scheme [12]. The electrolysis process represents the main way to convert electricity in the chemical form of hydrogen: by means of the water electrolysis reaction, electricity allows water to be divided into its elementary components, i.e., hydrogen and oxygen. At present, the main water electrolysis technologies are alkaline, polymer electrolyte membrane and solid oxide electrolysis [13], [14]. They are classified according to the type of electrolyte, which separates the two half reactions taking place at the anode and cathode side of the electrolyzer. Alkaline water electrolyzers (AWEs) represent the most mature technology, widely used for large scale industrial applications. AWEs are also characterized by higher durability (i.e., longer stack lifespan) and lower capital costs compared to the alternatives [14]. PEM water electrolyzers (PEMWEs) are less mature and more expensive than AWEs. Recently, increasing effort has been addressed to the PEM-based technology in order to reduce capital costs and enable the system scale-up [15]. PEMWEs are considered to be better suited for P2H applications in the future decarbonized power sector dominated by renewable sources [16]. In fact, PEMWEs offer higher flexibility than the alkaline alternative, in terms of load range and response time [17]. PEM electrolyzers are

also able to operate at much higher current densities with respect to AWEs, with consequent major stack compactness and potential for cost reduction [18], [19]. Solid oxide electrolyzers are less developed than AWEs and PEMWEs. However, they have already been demonstrated on laboratory scale and individual companies are currently trying to bring this technology to market [14], [20]. Because of the higher operating temperature, solid oxide electrolyzers are characterized by lower overpotential losses, i.e., higher efficiency compared to the PEM and alkaline systems [21]. Additional advantages include the possibility to operate in co-electrolysis mode, producing syngas ($CO + H_2$) from water and carbon dioxide [22]. Intermediate-temperature solid oxide electrolyzers (with both proton- and oxygen-ion conductive electrolytes) are currently under investigation with the purpose of maintaining the main benefits derived from operating at higher temperatures (i.e., greater performance) and, at the same time, mitigating the main drawbacks that affect more traditional solid oxide systems (i.e., durability, material and manufacturing issues because of the high working temperature) [23], [24]. In recent years, growing interest has also been addressed towards the development of anion exchange membrane water electrolyzers, which combine the positive effects arising from employing a solid polymer electrolyte membrane (i.e., improved safety and efficiency) and the presence of an alkaline medium (which allows the use of non-platinum group metals as catalysts, with consequent saving of cost) [25].

Once hydrogen is generated through electrolysis, it can be stored and later re-converted into electricity when required following the so-called power-to-power (P2P) route. It could be used for mobility applications feeding fuel cell electric vehicles (FCEVs) or even hydrogen internal combustion engine vehicles (HICEVs). H_2 can also be injected into the natural gas grid to some extent or used as a commodity in industrial sectors. Continuing along the P2X path, hydrogen can be subject to further conversion reactions in order to produce synthetic natural gas (SNG) by reacting with CO_2 according to the so-called power-to-gas (P2G) process [26], [27]. Additional P2X schemes can lead to the production of liquid fuels (such as alcohols, dimethyl ether, etc.) and green chemicals through specific power-to-liquid (P2L) and power-to-chemicals (P2C) routes, respectively [12]. The reuse of CO_2 to produce fuels and chemicals not only can cope with the problem of GHG emission mitigations, but also favors the transition towards a more sustainable economy since carbon dioxide becomes a valuable C-source to progressively replace conventional fossil fuels and manufacture green chemical and materials.

1.3 Off-grid areas

Focusing on off-grid areas, diesel engines still dominate the scene of local electricity generation, despite the related pollution concerns [28]–[30]. Besides environmental problems, operating costs are generally high due to fuel

transportation and logistic issues, in particular in case of isolated remote areas [31]. Grid connections, when feasible, are also considered as a possible choice. However, the required infrastructure to make the connection is highly expensive and invasive and the area would often face connection problems (e.g., instability and outages) due to its remoteness [32]. Alternative solutions must be considered to limit fossil fuels-related problems (i.e., environmental pollution and transportation/logistic issues) and avoid the need for unreliable and costly connections to the grid.

Worldwide, it is estimated that there are more than 10,000 islands inhabited by a total of about 750 million people. Islands throughout the world, especially those in the range of 1,000 to 100,000 inhabitants, still rely on the usage of diesel generators for the production of electricity, spending a considerable share of their gross domestic product (GDP) on the import of fuels [28]. Besides the insular context, there are thousands of mountain communities and other remote areas where the access to electricity can be difficult or simply not possible, expensive, and unreliable. At present, approximately 850 million people live without access to electricity [33].

Hence, there is a huge global development potential for incorporating RESs into mini-grids. Off-grid renewable energy systems can represent the most suitable and cheapest solution for population groups in developing countries [28]. However, electrical energy storage systems should be adopted to better optimize the exploitation of local RESs and achieve high renewable penetration levels, thus improving the energy self-sufficiency of the site.

In the short- to medium-term, the market for off-grid renewable energy systems is expected to increase through the hybridization of the already existing diesel-based systems with solar PV, wind, biomass gasification and small hydropower. Due to their increasing performance and declining costs, batteries (mainly lithium-ion and lead-acid types [31]) are at present the first choice as EES options to be integrated with local RESs in order to make the energy supply more reliable and effective. However, when the energy storage is required for longer periods (e.g., when trying to make the off-grid village energy autonomous by relying on RESs), batteries become expensive and their hybridization with other typologies of storage can result in a cheaper and more feasible solution [19].

1.3.1 Hydrogen energy storage

Hydrogen can represent an interesting energy storage option given its high energy density, long-term storage capability and cleanness in terms of local pollutants and CO_2 emitted. A typical H_2-based P2P energy system comprises of an electrolyzer (mainly of alkaline or PEM type) for the conversion of the surplus RES energy into hydrogen, a pressurized vessel to store the amount of hydrogen coming from the electrolyzer and a fuel cell (mainly of PEM type) to reconvert

hydrogen into electricity during power shortages, i.e., when renewable energy is not sufficient to cover the electrical demand.

Recently, increasing attention is therefore focusing on the investigation of H_2 usage in isolated remote environments. Among the European projects addressing this topic there are:

- ELY4OFF (2015 to 2019) [34]. The main goal of ELY4OFF is to develop and demonstrate the effectiveness of an autonomous off-grid electrolysis system linked to renewable energy sources. A 50 kW PEM electrolyzer was designed and operated in an off-grid context with direct coupling to photovoltaic generation. The demonstration period lasted 8 month and took place in Huesca, Spain.
- HAEOLUS (2018 to 2021) [35]. It proposes the integration of a 2.5 MW PEM electrolyzer in the remote region of Varanger (Norway) in a 45 MW wind farm, whose growth is limited due to bottle necks. The electrolyzer is intended to improve the grid integration and facilitate the management of power congestions. The electrolyzer will be also integrated with a pressurized hydrogen storage and an PEM fuel cell for re-electrification.
- REMOTE (2018 to 2023) [36]. The aim of the REMOTE project is to demonstrate the technical and economic feasibility of hydrogen-based energy storage solutions based on local RESs and located in different micro-grid and off-grid isolated areas. Depending on the location, different renewable sources will be exploited, such as sun, wind and waterfall. The architecture of the REMOTE storage system, which is graphically schematized in Figure 1.2, is of hybrid type, i.e., composed of both hydrogen and batteries. The various REMOTE case studies will be described in detail in Chapter 3.
- GREEN HYSLAND (2021 to 2025) [37]. The project will develop a fully integrated and functioning H_2-based ecosystem in the island of Mallorca (Spain). The ecosystem will include 7.5 MW of electrolysis capacity fed by PV plants. Hydrogen will be employed to power fuel cell buses, vehicles and ferries. It will be also exploited to generate heat and power for commercial and public buildings and injected in the gas pipeline network of the island.

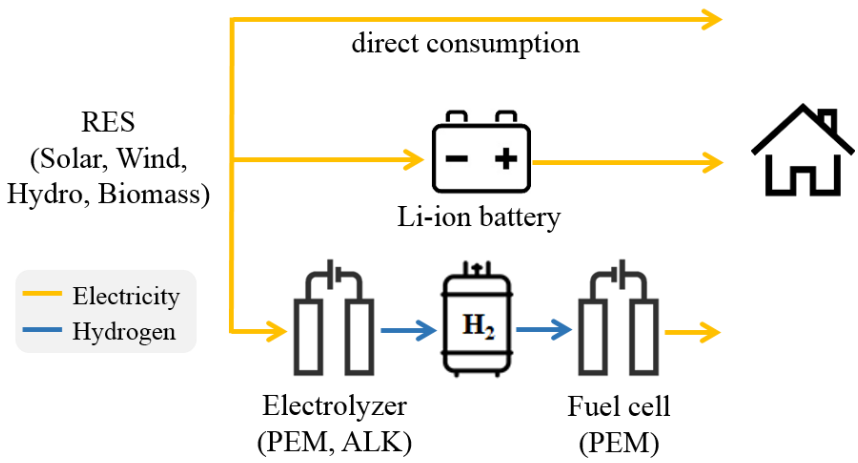

Figure 1.2 Schematic of the RES-based P2P system with H_2 and batteries as a storage medium.

The rising interest on this topic is also confirmed by the growing number of literature studies in the recent years. Zhang *et al.* [38] and Nordin *et al.* [39] reported that a stand-alone power system with only batteries is economically preferable to a configuration that relies only on hydrogen, mainly due to the high investment costs and low durability of H_2-based components. The energy storage hybridization (i.e., both battery and hydrogen) still remains more expensive than the case with only batteries according to the study by Hosseinalizadeh *et al.* [40]. However, renewable hydrogen can become a competitive solution in stand-alone power systems since its seasonal storage capability can help to avoid the installation of batteries with too large capacity [41]. Off-grid systems with both batteries and hydrogen were reported to be the most cost-effective solution by Dong *et al.* [42] and Dawood *et al.* [43], who analysed and compared the performance of different combinations of hybrid renewable energy systems (HRESs) for remote communities. Similarly, Li *et al.* [44] revealed that an off-grid hybrid battery-hydrogen system led to the cheapest configuration thanks to the high efficiency of batteries and the low cost of high-capacity hydrogen tanks. Richards *et al.* [45] showed that hydrogen-based technologies can become economically viable in HRESs located at more extreme latitudes, where the seasonal variation of the solar radiation is relevant. Nordin *et al.* [46] demonstrated that a stand-alone battery-hydrogen system can be economically advantageous if the excess renewable energy is converted into hydrogen and then sold to local consumers for the transportation sector. Hydrogen was also found to be profitable by Gracia *et al.* [47] when the seasonality of PV production is relevant, the available surface for PV installation is limited and the electrical load during night is high. A similar consideration was derived by Perrigot *et al.* [48], who observed hydrogen to become more interesting than batteries when a high amount of electricity consumption occurs at night.

The economic viability of stand-alone systems based on diesel generators (DGs) is highly dependent on the cost of fuel [49]. Due to geographic reasons and highly fluctuating fuel prices, the use of diesel generators in off-grid areas can result in really high costs [32], [50], [51]. The integration of diesel generators together with local RESs and electrical energy storage solutions can represent an effective way to decrease the cost of energy. Odou *et al.* [52] observed that batteries are crucial to lower DG operating costs, but at the same time diesel genset is required to reduce battery storage capacity by around 70%. Cai *et al.* [50] also showed that the inclusion of PV and batteries are necessary to significantly reduce system costs compared to an energy system with only diesel generators. This is because solar energy helps to lower the consumption of fuel, which accounts for a relevant share of the LCOE. According to the techno-economic study by Ozden *et al.* [53], energy systems based on solar energy and hydrogen most likely will become an economically competitive alternative to conventional diesel generators in the near future, thanks to the decreasing trend of PV panel costs and the rising diesel fuel prices. It is also noteworthy that, unlike diesel, RESs integrated with battery/hydrogen technologies for the development of a self-sustained power system can lead to advantages from an environmental point of view, since pollutants and GHG emissions are considerably reduced [54].

1.4 Research aim

In remote areas, local RESs are necessary to enhance the independence from imported fossil fuels. However, their exploitation causes fluctuations in power production that need to be tackled effectively. Off-grid HRESs must also address relevant and conflicting goals: high reliability of the power supply, low cost of energy and reduced carbon dioxide emissions. Cost-effective system solutions often require the hybridization of both power generators and storage devices, thus increasing the number of components that have to be sized and operated. Moreover, the HRES devices need to adapt continuously their operating point to match the fluctuating power supply from on-site renewable energy sources. All these issues make it complex the design of stand-alone RES-based energy systems.

The main objective of the present work is to address these challenges and to investigate the role and potential of hydrogen in providing a cost-effective and stable power supply service for off-grid communities. The analysis also takes advantage of valuable input data made available in the REMOTE project. Different methodologies for the optimal design of stand-alone HRESs were formulated. Sizing optimization is in fact a necessary step to achieve cost-competitive, reliable and sustainable energy systems.

The general layout of the proposed optimization framework is displayed in Figure 1.3, where the main input and output data are reported. Input parameters to the model include: the technical specifications of the HRES components

(efficiency curves, modulation ranges, etc.), time-dependent profiles of electrical demand and meteorological data (ambient temperature, solar irradiance, wind velocity), economic data (investment, operation, maintenance and replacement costs, fuel price, discount rate) and constraints (reliability of the energy system, CO_2 emissions, periodicity in the storage levels). The main outputs of the optimization problem are as follows: the sizes of all the HRES components, the HRES operation profiles (power distribution among the components, renewable energy usage and load coverage over the selected time horizon), economic indicators (levelized cost of energy, net present cost), technical indicators (the lifetime of components, etc.) and environmental indicators (the amount of CO_2 that has been released during the HRES operation).

The derived methodology was then tested and applied to different case studies and system configurations. However, the current research work aims to go beyond the analysis of specific case studies. In fact, as suggested by Figure 1.3, it provides a general approach that can be applied to the design of any stand-alone HRES, using the input parameters of that specific site (i.e., techno-economic assumptions, weather and load data).

It is also important to note that the proposed modelling framework, which has been developed for an off-grid context, could be further extended and easily adapted to other application areas. In fact, RESs and energy storage devices are fundamental building blocks to pursue decarbonization pathways not only of off-grid environments, but more broadly of the whole energy system.

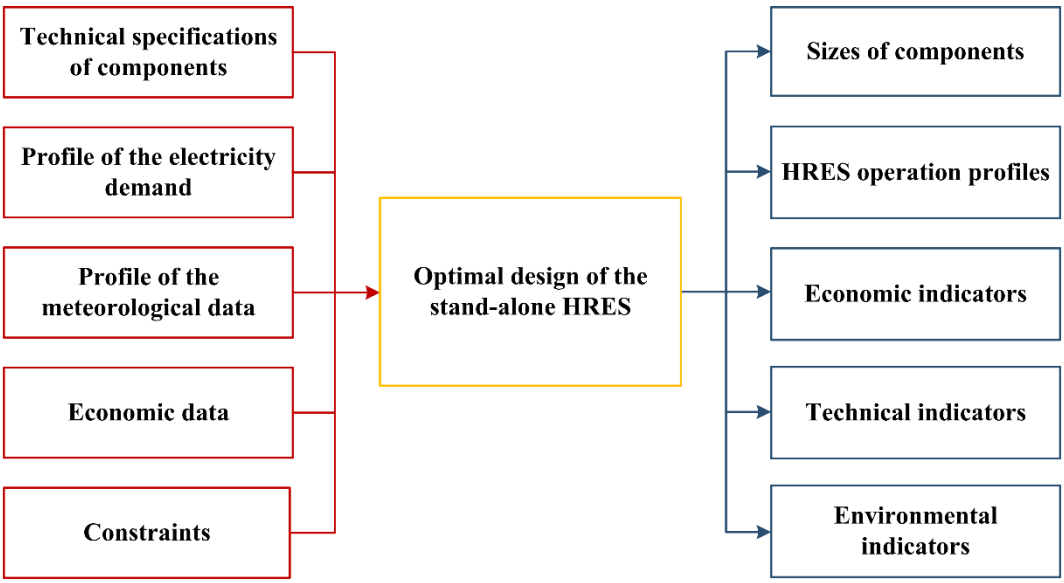

Figure 1.3 Optimization framework developed in this work to carry out the design of the stand-alone HRES.

1.5 Thesis layout

After presenting the general context of the thesis to highlight the importance of energy storage solutions with a focus on off-grid areas, the thesis layout is as follows.

The mathematical modelling of all the components involved in the HRES is described in Chapter 2. System efficiency curves are derived for the electrolyzer (both PEM and alkaline types) and PEM fuel cell systems starting from electrochemical models at single cell level. The costing methodology for the estimation of the net present cost (NPC) and the levelized cost of energy (LCOE) is reported. The modeling framework defined in Chapter 2 represents the backbone for the development of the techno-economic studies described in the subsequent chapters.

Chapter 3 deals with the techno-economic analysis of the four case studies that have been defined in the framework of REMOTE. By taking advantage of data supplied and/or verified directly by the project partners, the aim is to provide a more comprehensive overview about stand-alone battery-hydrogen storage systems in different kinds of remote locations.

A metaheuristic-based methodology for the optimal design of HRESs is then developed in Chapter 4. The design phase is addressed by means of the particle swarm optimization (PSO) algorithm and energy management strategies, previously defined in Chapter 3, are employed to manage the operation of the entire energy system. The main goal is to determine the optimal design of the HRES so as to make the power supply service reliable with the minimum system cost. Different P2P configurations are considered to better evaluate the role of hydrogen and batteries in achieving cost-effective stand-alone energy solutions.

In Chapter 5 the optimal sizing problem is further investigated by applying a different method based on mixed integer linear programming (MILP) techniques to simultaneously address the optimal design and scheduling of the off-grid system. Design days are also included in the MILP-based formulation. The aim is to lower the computational burden of the simulation, making the methodology suitable for even more complex problems.

Finally, Chapter 6 summarizes the main findings and outlines future developments connected to the thesis.

A “Supplementary Material” Chapter is also added focusing on the PEM electrolysis technology. Research on H_2-based components is strongly needed to further increase their performance, improve their lifetime and reduce their costs. This final Chapter is intended to highlight the main cost and durability issues that at present affect PEM electrolyzers. An experimental study about the membrane chemical degradation by means of Ion Chromatography is also presented. Performance data obtained by the characterization of the PEM electrolysis cell will be also helpful for the validation of the electrolyzer model described in Chapter 2.

1.6 Publications

Scientific publications

1. **P. Marocco**, D. Ferrero, E. Martelli, M. Santarelli and A. Lanzini, "An MILP approach for the optimal design of renewable battery-hydrogen energy systems for off-grid insular communities," *Energy Convers. Manag.*, vol. 245, p. 114564, 2021.
2. **P. Marocco,** D. Ferrero, A. Lanzini, and M. Santarelli, "Optimal design of stand-alone solutions based on RES + hydrogen storage feeding off-grid communities," *Energy Convers. Manag.*, vol. 238, p. 114147, 2021.
3. **P. Marocco**, K. Sundseth, T. Aarhaug, A. Lanzini, M. Santarelli, A.O. Barnett and M. Thomassen, "Online measurements of fluoride ions in proton exchange membrane water electrolysis through ion chromatography," *J. Power Sources*, vol. 483, p. 229179, 2021.
4. **P. Marocco**, D. Ferrero, M. Gandiglio, M.M. Ortiz, K. Sundseth, A. Lanzini and M. Santarelli, "A study of the techno-economic feasibility of H2-based energy storage systems in remote areas," *Energy Convers. Manag.*, vol. 211, p. 112768, 2020.
5. G. Buffo, **P. Marocco**, D. Ferrero, A. Lanzini, and M. Santarelli, "Power-to-X and power-to-power routes," *Sol. Hydrog. Prod.*, pp. 529–557, 2019.

Scientific articles that are currently under review:

6. **P. Marocco**, D. Ferrero, A. Lanzini and M. Santarelli "The role of hydrogen in the optimal design of off-grid hybrid renewable energy systems," under review.

Conferences

7. A. Calvo, **P. Marocco**, D. Ferrero, A. Lanzini and M. Santarelli, "Modelling of a stand-alone H2-based Energy Storage System for electricity production and H2 mobility," Energy Fuels Environment 2020, Kraków (Poland), https://www.agh.edu.pl/en/conferences/konferencja/article/energy-fuels-environment-conference/, 2020
8. **P. Marocco**, D. Ferrero, M. Gandiglio, A. Lanzini and M. Santarelli, "H2-based energy storage systems in remote areas: the REMOTE project," EFS2019, Turin (Italy), https://www.efs2019.uc.pt/projectos/efs2019/index.php?module=sec&id=739&f=1, 2019
9. **P. Marocco** *et al*., "REMOTE project: techno-economic analysis of H2-based energy storage systems in remote areas," EFCF 2019, Lucerne (Switzerland), https://www.efcf.com, 2019

10. **P. Marocco**, D. Ferrero, M. Gandiglio, A. Lanzini and M. Santarelli, "Optimal sizing of H2-based hybrid EES in remote areas: the case study of the island of Ginostra (IT)," ICE2019, Loen (Norway), www.sintef.no/projectweb/ice2019/, 2019

Part of the content of Chapter 1 originates from Papers 1, 2 and 5. The modelling methodology derived in Chapter 2 has already been reported in Paper 2. Main techno-economic outcomes related to Chapter 3 are based on Papers 4, 8 and 9. The key findings reported in Papers 2 and 6 are shown in Chapter 4. Part of Chapter 5 is based on the results from Paper 1. Finally, main experimental outcomes presented in the Supplementary Material have already been published in Paper 3.

Awards

- The presentation of Paper 9 at the EFCF2019 conference, during the event "3rd Grid Service Markets Symposium", was awarded as the most innovative contribution.
- The research work described in this thesis contributed to the achievement of the 2020 Quality Award by the PhD program in Energetics (POLITO).

Chapter 2

Modelling of the hybrid renewable energy system

Chapter 2 deals with the development of a methodology for the techno-economic modelling of the off-grid hybrid renewable energy system (HRES). A possible layout of the energy system is shown in Figure 2.1 [55].

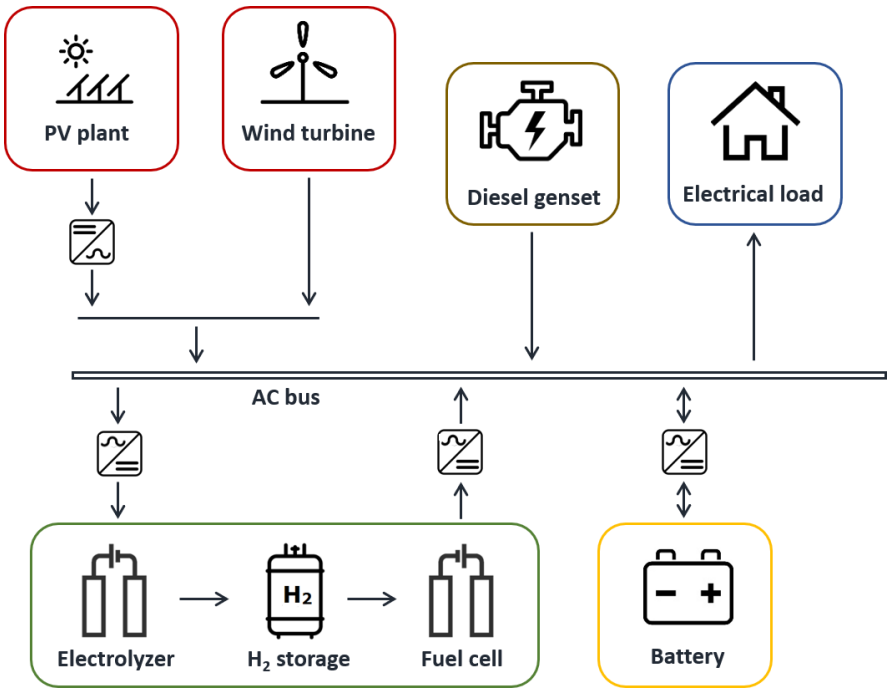

Figure 2.1 General layout of the hybrid renewable energy system

The HRES includes renewable energy sources (e.g., wind and solar plants) coupled with batteries (BTs) and hydrogen as storage medium. The hydrogen-based storage system consists of an electrolyzer (EL) for the conversion of

electricity into hydrogen, a pressurized hydrogen tank (HT) to store the gas and a fuel cell (FC) for the re-conversion of H_2 into electricity. The system configuration can also include a diesel generator to supply the final load. The energy system can be designed according to different architectures, including AC and/or DC bus bars [56], [57]. Both AC- and DC-based systems will be demonstrated in the framework of the REMOTE project [58].

In the following subsections, the mathematical models of each component of the microgrid system have been discussed. A methodology for the estimation of the levelized cost of energy (LCOE) was then defined. The LCOE parameter is needed to assess the economic feasibility of a certain system configuration and to perform the optimal design of HRESs in order to find the most cost-effective solution.

2.1 Hydrogen-based devices

Electrochemical models were formulated for the electrolyzer (alkaline and PEM) and PEM fuel cell devices to obtain an accurate description of their behaviour, which is typically nonlinear. The aim is to derive efficiency curves of the various H_2-based systems to be later used when modelling the entire renewable power system.

2.1.1 Alkaline electrolyzer

An alkaline electrolysis cell is composed of two electrodes separated by a diaphragm and surrounded by liquid electrolyte. By circulating a direct current through the electrode of the cell, the water molecule is divided into hydrogen and oxygen. The overall reaction of water electrolysis is represented by Eq. (2.1), whereas the cathodic and anodic half-reactions are described by Eqs. (2.2) and (2.3), respectively. Hydrogen is generated at the cathode by water reduction with subsequent release of hydroxide ions. The latter move through the diaphragm to the anode side where they are oxidized releasing oxygen and water.

$$H_2O \rightarrow H_2 + \frac{1}{2}O_2 \tag{2.1}$$

$$2H_2O + 2e^- \rightarrow H_2 + 2OH^- \tag{2.2}$$

$$2OH^- \rightarrow \frac{1}{2}O_2 + H_2O + 2e^- \tag{2.3}$$

Nickel is commonly employed as electrode material since it represents the best compromise between stability, performance, and cost. However, since Ni deactivation over time still represents a serious problem, alternative materials and stabilizing coatings for the electrodes are being investigated [11]. Diaphragms

must have good chemical and mechanical stability, high wettability, high OH^- conductivity and high Bubble Point pressure (the latter parameter is required to avoid the mixing of hydrogen and oxygen) [59]. Due to its great performance, Zirfon, which is composed of 60 to 80 wt% ZrO_2 in a polysulfone matrix, is a common choice for alkaline electrolysis diaphragms. The type and concentration of the electrolyte play a key role in achieving good ionic transfer in the solution and hence lower ohmic resistance. An aqueous solution of potassium hydroxide (KOH) is widely used in commercial alkaline electrolyzers. Despite the higher costs, KOH is in fact preferred over sodium hydroxide (NaOH) because of its better conductivity. The KOH electrolyte concentration (w_{KOH}) is usually in the range from 25 to 30 wt% since this allows the electrolyte ionic conductivity to be maximized (see Eq. (2.14)) [60].

Electrochemical model

The operating cell voltage is represented by the reversible voltage increased by irreversible losses including activation, ohmic and diffusion contributions.

$$V_{cell} = V_{rev} + V_{act} + V_{ohm} + V_{diff} \tag{2.4}$$

where V_{rev} (in V) is the reversible thermodynamic potential and V_{act}, V_{ohm} and V_{diff} (in V) represent the activation, ohmic and diffusion overpotentials, respectively.

The reversible voltage can be computed as follows [60]:

$$V_{rev} = V_{rev,ref} + \frac{R_U\, T}{z\, F}\, ln\left(\frac{\left(p_{cat} - p_{V,KOH}\right)\left(p_{an} - p_{V,KOH}\right)^{0.5}}{a_{H_2O,KOH}}\right) \tag{2.5}$$

where $V_{rev,ref}$ (in V) is the reversible voltage at the reference standard pressure of 1 bar, R_U (equal to 8.314 J/mol/K) is the universal gas constant, T (in K) is the operating temperature, z (equal to 2) represents the moles of electrons required to generate a mole of hydrogen, F (equal to 96,485 C/mol) corresponds to the Faraday constant, p_{cat} (in bar) is the operating pressure at the cathode side, p_{an} (in bar) is the operating pressure at the anode side, $p_{V,KOH}$ (in bar) is the vapor pressure of the KOH solution and $a_{H_2O,KOH}$ is the water activity of the KOH solution.

The $V_{rev,ref}$ term was calculated according to the following relationship [60], which is function of the working temperature of the alkaline electrolyzer:

$$V_{rev,ref} = 1.5184 - 1.5421 \cdot 10^{-3}\, T + 9.526 \cdot 10^{-5}\, T\, ln(T) + 9.84 \cdot 10^{-8}\, T^2 \tag{2.6}$$

The second term of Eq. (2.5) accounts for the influence of pressure on the cell reversible voltage. The vapor pressure of the KOH solution was computed as follows [61]:

$$p_{V,KOH} = exp\left(2.302\ a + b\ ln\left(p_{V,H_2O}\right)\right) \tag{2.7}$$

where p_{V,H_2O} (in bar) is the vapor pressure of pure water depending on the operating temperature and a and b are two parameters that depend on the molal concentration of the KOH solution [61]. The water activity was evaluated as a function of temperature and molality according to the following relationship [61]:

$$a_{H_2O,KOH} = exp\left(-0.05192\ m + 0.003302\ m^2 + \frac{3.177\ m - 2.131\ m^2}{T}\right) \tag{2.8}$$

where m (in mol/kg) is the molal concentration of the KOH solution, i.e., the number of KOH moles per kg of H_2O.

The activation overvoltage is associated to the electric charge transfer between chemical species and the electrode. An activation energy needs to be overcome to allow the transfer of charge at the electrode-electrolyte interface. The V_{act} contribution was computed by applying the well-known Butler-Volmer equation (with j = an, cat):

$$V_{act,j} = \frac{R_U\ T}{\alpha_j\ F}\ arcsinh\left(\frac{i}{2\ i_{0,j}\ (1-\theta)}\right) \tag{2.9}$$

where α is the charge transfer coefficient (fitted parameter in our model), i (in A/cm^2) is the operating current density, i_0 (in A/cm^2) is the exchange current density and θ corresponds to the fractional bubble coverage of the electrode surface.

The bubble coverage term was introduced to consider the effect of bubbles that are generated at the electrode surface and cover a fraction of the surface making it inactive. The evaluation of the θ term is a complex task since it is influenced by several parameters such as surface properties of the electrode, electrolyte surface tension and electrolyte circulation. In the present work, the bubble rate coverage was determined as a function of current density and temperature according to the following empirical expression [62]:

$$\theta = \left(-97.25 + 182\left(\frac{T}{298}\right) - 84\left(\frac{T}{298}\right)^2\right)\left(\frac{i}{i_{lim}}\right)^{0.3} \tag{2.10}$$

where i_{lim} (in A/cm^2) corresponds to the limiting current density. Vogt *et al.* [63] suggested a value of around 300 kA/m^2 for the limiting current density at 100% bubble coverage.

A temperature-dependent Arrhenius expression was adopted to estimate the exchange current density (with j = an, cat) [64], [65]:

$$i_{0,j} = \gamma_{R,j}\, exp\left[\frac{-E_{a,act,j}\, 10^3}{R_U}\left(\frac{1}{T} - \frac{1}{T_{ref}}\right)\right] i_{0,ref,j} \tag{2.11}$$

where γ_R is the roughness factor, $E_{a,act}$ (in kJ/mol) corresponds to the activation energy of the electrochemical reaction, T_{ref} (equal to 298.15 K) is the reference temperature and $i_{0,ref}$ (in A/cm^2) is the reference exchange current density at T_{ref}. The terms $i_{0,ref}$ and $E_{a,act}$ were treated as fitted parameters in this model.

The ohmic overpotential, due to electrodes, electrolyte and diaphragm losses, was modelled as:

$$V_{ohm} = ASR_{ohm}\, i = (ASR_{electric} + ASR_{KOH\ sol} + ASR_{mem})\, i \tag{2.12}$$

where ASR_{ohm} (in Ω cm^2) is the total ohmic area specific resistance (ASR), $ASR_{electric}$ (in Ω cm^2) is the electrical ASR (considered as a fitted parameter during the model calibration), $ASR_{KOH\ sol}$ (in Ω cm^2) is the ionic ASR due to the electrolyte and ASR_{mem} (in Ω cm^2) corresponds to the ionic ASR of the membrane.

The effect of the gas bubbles was considered when computing the electrolyte resistance. More specifically, $ASR_{KOH\ sol}$ was evaluated as follows [66]:

$$ASR_{KOH\ sol} = \frac{t_{an,mem} + t_{cat,mem}}{\sigma_{KOH\ sol,eff}} \tag{2.13}$$

where $\sigma_{KOH\ sol,eff}$ (in S/cm) is the effective conductivity of the KOH solution and $t_{an/cat,mem}$ (in cm) is the distance between the anodic/cathodic electrode and the diaphragm. As shown by Eq. (2.13), the smaller the electrode-membrane gap, the lower the ohmic cell resistance due to the aqueous solution. This distance can approach zero in the so called zero-gap configuration, whose aim is to minimize the $ASR_{KOH\ sol}$ term. The value of $\sigma_{KOH\ sol,eff}$ was determined starting from the electrolyte conductivity, which is function of temperature and molarity [66]–[68]:

$$\begin{aligned}\sigma_{KOH\ sol} = &-2.041\, M - 0.0028\, M^2 + 0.005332\, M\, T \\ &+ 207.2\, \frac{M}{T} + 0.001043\, M^3 - 0.0000003\, M^2\, T^2\end{aligned} \tag{2.14}$$

where $\sigma_{KOH\,sol}$ (in S/cm) is the conductivity and M (in mol/L) is the molar concentration, i.e., the number of KOH moles per liter of solution. The molar concentration depends on the KOH weight percentage (w_{KOH}) and on the KOH solution density. This last term was assessed by employing an empirical correlation reported by Bhanu *et al.* [67]. The conductivity of the KOH solution is negatively affected by the presence of bubbles in the bulk electrolyte since they have negligible electrical conductivity. $\sigma_{KOH\,sol}$ was hence corrected to take into account the gas void fraction by applying the Bruggeman's equation [66], [67], [69]:

$$\sigma_{KOH\,sol,eff} = \sigma_{KOH\,sol}\,(1-\varepsilon)^{3/2} \tag{2.15}$$

where the gas void fraction ε is a function of the fractional bubble coverage as follows [69], [70]:

$$\varepsilon = \frac{2}{3}\,\theta \tag{2.16}$$

The area specific resistance of the membrane was expressed by applying the following relationship [59], [71]:

$$ASR_{mem} = \frac{t_{mem}\,\tau_{mem}^{2}}{\sigma_{KOH\,sol}\,\varepsilon_{mem}\,\omega_{mem}} \tag{2.17}$$

where t_{mem} (in cm) is the membrane thickness, τ_{mem} is the membrane tortuosity, ε_{mem} is the membrane porosity and ω_{mem} is the membrane wettability factor, i.e., the ratio between the volume of absorbed electrolyte and the total pore volume. Similarly to what performed in Ref. [64], the value of wettability was derived by the model fitting process. As an alternative to Eq. (2.17), a temperature-dependent expression for the membrane resistance was reported by Henao *et al.* [66] referring to a membrane based on Zirfon.

Finally, the diffusion overvoltage was not considered since mass transfer effects are generally assumed to be negligible for alkaline electrolyzers [60].

Current efficiency needs to be assessed to properly compute the amount of hydrogen produced by the electrolysis reaction according to the Faraday's Law:

$$\dot{N}_{H_2} = \eta_I\,\frac{i}{2F} \tag{2.18}$$

where $\dot{N}_{H_2}$ (in mol/cm^2/s) is the specific H_2 molar flow rate and η_I is the current efficiency, representing the fraction of electric current that accomplishes the desired chemical reaction. Ideally, assuming a fully impermeable membrane, the current efficiency would be equal to 100%. However, in a real water electrolysis

cell, the current efficiency is less than 100% because of gas crossover and permeation effects. The η_I term was estimated through the following expression by Ulleberg *at al.* [72]:

$$\eta_I = \frac{i^2}{f_1 + i^2} f_2 \tag{2.19}$$

where the parameters f_1 and f_2 depend on temperature (we considered a temperature of 70°C, which is the value we used during the simulations). As an alternative, an empirical expression as a function of temperature and current was reported by Hug *et al.* [73].

Performance curve derivation

Model calibration was carried out minimizing the sum of the squared difference between experimental and model values of the cell operating voltage. The objective function to be minimized, i.e., the sum of squared residual, is defined in the following way:

$$\sigma^2 = \sum_{k=1}^{N} \left[V_{exp,k}(i_k, T_k, p_k) - V_{model,k}(i_k, T_k, p_k, \alpha, \beta)\right]^2 \tag{2.20}$$

where $V_{exp,k}$ is the voltage of the k-th experimental point, $V_{model,k}$ is the simulated voltage derived from the model at the same operating conditions of $V_{exp,k}$, α is the vector of the fitted parameters (Table 2.1) and β is the vector of the fixed parameters (Table 2.2).

The goal is to find the optimal values of the fitted parameters that allow to best fit the chosen experimental data set. Experimental polarization curves by Henao *et al.* [66] were considered for the validation of the alkaline electrolyzer model. They refer to tests performed in the temperature range of 40 to 80 °C, with current densities up to 0.3 A/cm^2 at 7 bar pressure. The resulting fitted parameters allow obtaining a maximum relative error on voltage of around 1.28%. Values for the charge transfer coefficient are reported to be in the range of 0 to 2 and 0 to 1 for the anode and cathode, respectively [74]. The anodic and cathodic reference exchange current densities are expected to lie in the range of 10^{-11} to 10^{-7} and 10^{-4} to 10^{-1} A/cm^2, respectively [64]. Reported values for the activation energy can be up to around 80 kJ/mol at the anode and 50 kJ/mol at the cathode [64]. A membrane wettability factor of around 0.8 to 0.9 was found by Abdin *et al.* [64]. As shown in Table 2.1, the values of the parameters obtained by the model calibration lie in the above cited ranges.

Table 2.1 Fitted parameters for the model of the alkaline electrolyzer cell

Fitted parameters	Value
$ASR_{electric}$	0.17 Ω·cm^2
$E_{a,act,an}$	82.27 kJ/mol
$E_{a,act,cat}$	32.76 kJ/mol
$i_{0,ref,an}$	9.83·10^{-8} A/cm^2
$i_{0,ref,cat}$	7.32·10^{-3} A/cm^2
α_{an}	0.99
α_{cat}	0.92
ω_{mem}	0.81

Table 2.2 Fixed parameters for the model of the alkaline electrolyzer cell

Fixed parameters	Value	Reference
f_1	225	[72]
f_2	0.9825	[72]
$t_{an,mem}$	0 cm	[64]
$t_{cat,mem}$	0 cm	[64]
t_{mem}	0.05 cm	[64]
w_{KOH}	30%	[66]
$\gamma_{R,an}$	2.5	[64]
$\gamma_{R,cat}$	1.5	[64]
ε_{mem}	0.42	[71]
τ_{mem}	2.18	[71]

Main operating parameters used to evaluate the performance curve of the alkaline water electrolyzer (AWE) are reported in Table 2.3. The operating temperature and pressure were taken from [32]. These values are in line with working values adopted for alkaline electrolyzers [14]. It was supposed the electrolyzer to work under pressurized conditions since this allows the energy system configuration to be simplified (the produced H_2 is stored in pressurized tanks). The maximum achievable current density was set to 0.35 A/cm^2, in line with what assumed by Parra *et al.* [18] and Buttler *et al.* [13]. In order to move

from the cell to the system efficiency curve, it is required to know the power consumption due to auxiliary components. It was assumed that the auxiliary consumption varies linearly from stand-by to nominal conditions [58]. More specifically, the auxiliary demand in nominal conditions was supposed to account for 10% of the electrolyzer rated power [75], [76]. Stand-by auxiliary consumption was taken from [58]. A system minimum power equal to 15% of the rated power was also imposed for a safe and efficient operation. Too low partial loads would in fact cause an enhancement of the H_2 in O_2 concentration at the anode side.

Table 2.3 Operating input parameters for the evaluation of the performance curve of the alkaline electrolyzer system.

Parameter	**Value**	**Reference**
Operating temperature	70 °C	[32]
Operating pressure	30 bar	[32]
System minimum power	15%	[17]
Max. current density	0.35 A/cm^2	[13], [18]
Aux. consumption in nominal condition[a]	10%	[75]
Aux. consumption in stand-by[b]	29%	[58]

[a] % of rated power
[b] % of aux. consumption in nom. condition

The resulting polarization of the alkaline cell is reported in Figure 2.2, where the various contributions to the overall cell voltage are shown. It can be noticed that the activation term accounts for the highest share of the overpotential losses, with the majority coming from the anode. Indeed, the kinetics of the OER taking place at the anode is slower compared to cathodic HER. This finds confirmation in the exchange current density values, which are lower for the anode side. Referring to the ohmic overvoltage, the most important contribution is caused by the membrane separator. No losses are associated to the electrolyte since, as shown in Table 2.2, a zero-gap configuration was considered. This solution is often adopted by the AWE manufactures to minimize the energy consumption [77]. It can be observed that the cell voltage is slightly lower than 2 V at a current density of 0.35 A/cm^2, which is in line with typical values for alkaline electrolyzer cells [18].

Figure 2.3 shows both the cell and system efficiency (on LHV basis) as a function of the normalized input electrical power. The performance curve presents a maximum when working at around 40% of the rated power. Below this value, the system efficiency decreases sharply since faradaic and auxiliary losses become

predominant. The obtained nominal specific energy consumption is approximately 5.26 kWh/Nm^3, which corresponds to an LHV efficiency of 0.56. This value lies in the range of 5.0 to 5.9 kWh/Nm^3 reported by Buttler *et al.* [13].

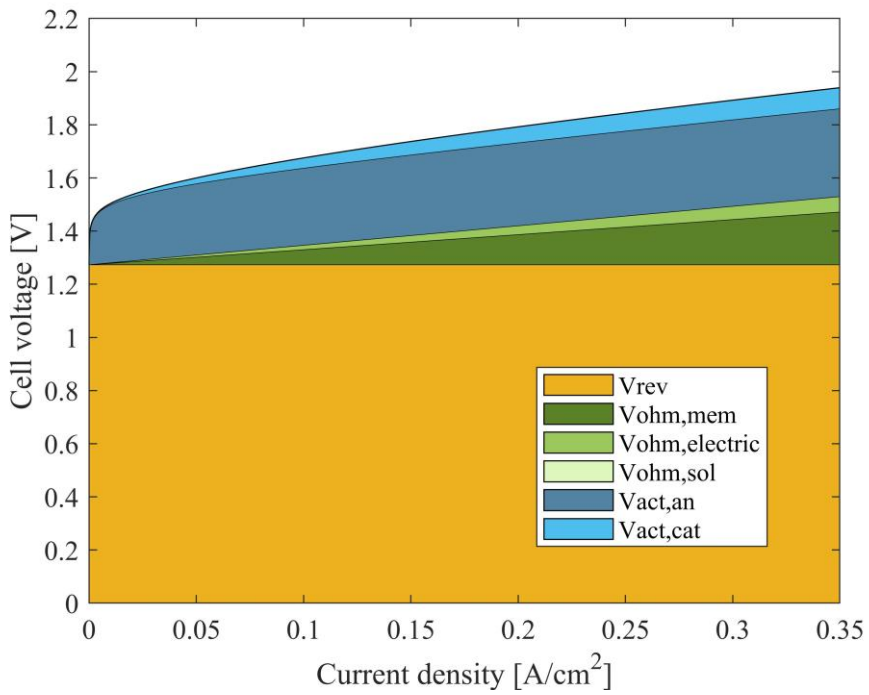

Figure 2.2 Contributions of the various overpotential terms to the polarization curve of the alkaline electrolyzer (70 °C and 30 bar)

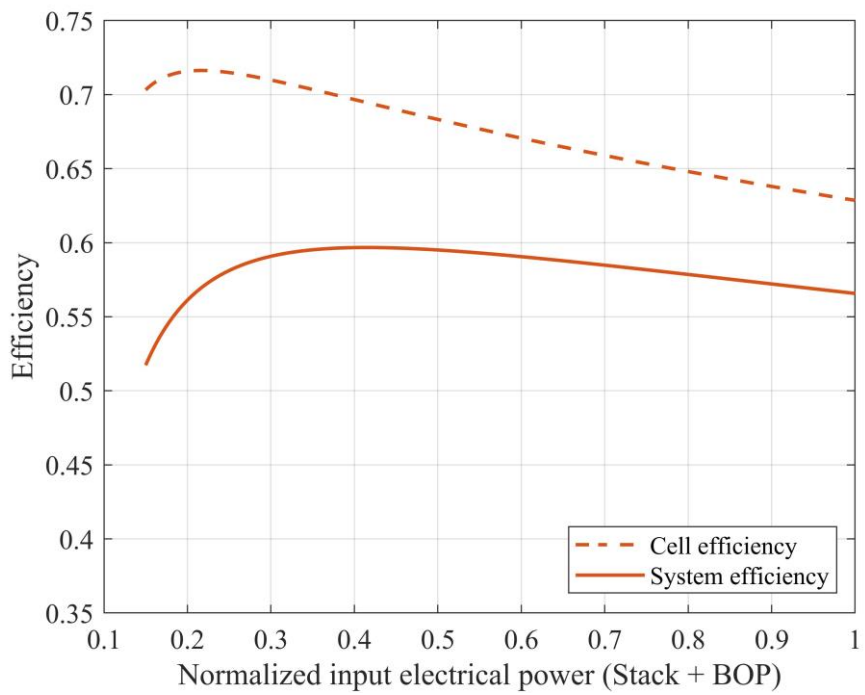

Figure 2.3 Cell and system efficiency curves of the alkaline electrolyzer at 70 °C and 30 bar

2.1.2 PEM electrolyzer

Analogously to the alkaline technology, PEM water electrolyzers (PEMWEs) allow water to be decomposed into hydrogen and oxygen when direct current is supplied to the cell. The overall water electrolysis reaction, described by Eq. (2.1), is the result of Eq. (2.21) and Eq. (2.22), which represent the anodic and cathodic half reactions, respectively. Water is decomposed into oxygen, protons and electrons at the anode side. Protons then move through the acidic electrolyte from the anode to the cathode where they are reduced generating hydrogen gas.

$$H_2O \rightarrow \frac{1}{2}O_2 + 2H^+ + 2e^- \tag{2.21}$$

$$2H^+ + 2e^- \rightarrow H_2 \tag{2.22}$$

The PEM cell has a compact structure with a typical thickness of 4 to 7 mm. The membrane consists of a solid polymer electrolyte (SPE) made of perfluorosulfonic acid (PFSA) with polytetrafluorethylene (PTFE) as a reinforcement. Its thickness lies in the range of 100 to 250 μm [78]. Thick membranes are especially required when working under pressure to mitigate gas cross-permeation phenomena. A catalyst coated membrane (CCM) is composed of the membrane together with the anodic and cathodic catalyst layers (CLs). CLs are characterized by a mixture of catalyst particles and PFSA ionomer chains. The cathodic catalyst layer consists of a porous micrometer-thick structure made of carbon-supported platinum nanoparticles embedded in PFSA ionomer. The anodic CL is instead few micrometers thick and composed of iridium or iridium dioxide nanoparticles with PFSA. The CCM is then closed between two porous transport layers (PTLs) to form the membrane electrode assembly (MEA). PTLs are generally made of carbon at the cathode and titanium and anode side. The cell is finally delimited by two titanium-based bipolar plates (BPs) [78]. Further information about PEMWE materials, manufacturing and durability are detailed in the Supplementary material.

Electrochemical model

The overall cell voltage was computed as the sum of the reversible voltage and all the various overpotential contributions, i.e., activation, ohmic and diffusion losses, according to Eq. (2.4).

The reversible voltage was expressed as follows [79]:

$$V_{rev} = V_{rev,ref} + \frac{R_U\,T}{2\,F} ln\left(\frac{\left(p_{cat} - p_{H_2O}\right)\left(p_{an} - p_{H_2O}\right)^{0.5}}{p_{H_2O}}\right) \tag{2.23}$$

where p_{H_2O} (in bar) is the partial pressure of water, which is supposed to be equal to the water saturation pressure since gases produced by electrolysis are generally saturated with water vapour. This assumption may not be valid when dealing with very high current densities [80]. In that case, in fact, there is an elevated bubble growth rate and gas bubbles quickly leave the catalyst layer before water vapor can saturate within them. The water saturation pressure was computed according to the formula reported by Balej [61]. Eq. (2.6) was employed to evaluate the reversible voltage at the reference standard pressure.

Activation losses are caused by the energy barrier to be overtaken in order to allow the occurrence of the electrochemical reaction [81]. Similarly to the alkaline electrolyzer, the Butler-Volmer equation was employed to compute the activation overvoltage [82], [83] (with j = an, cat):

$$\eta_{act,j} = \frac{R_U\, T}{\alpha_j\, F}\, arcsinh \frac{i}{2\, i_{0,j}} \tag{2.24}$$

The exchange current density i_0 was modelled through a temperature-dependent Arrhenius expression in the form of Eq. (2.11). The roughness factor, which is included in the i_0 expression, is defined as the ratio between the active electrocatalyst area and the geometric area of the electrode MEA. It was evaluated according to the following expression [78] (with j = an, cat):

$$\gamma_{R,j} = \varphi_{C,j}\, m_{C,j}\, \frac{6}{\rho_{C,j}\, d_{C,j}} \tag{2.25}$$

where φ_C is the fraction of the metal catalyst surface in contact with the ionomer (and generating the three-phase interface), m_C (in g/cm^2) is the catalyst loading, ρ_C (in g/cm^3) is the catalyst density and d_C (in cm) is the catalyst crystallite diameter.

The ohmic phenomena are caused by the resistance of the electrodes, bipolar plates, current collectors and interconnections to the electron flux, as well as by the resistance of the membrane to the ion flux. The ionic resistance, which is caused by protons flowing through the membrane, is usually the major contributor among the various ohmic terms [84], [85]. The overall ohmic overpotential was modelled as follows:

$$V_{ohm} = ASR_{ohm}\, i = (ASR_{electric} + ASR_{mem})\, i \tag{2.26}$$

where $ASR_{electric}$ (in Ω cm^2) is the electrical ASR related to the passage of electrons through electrically conductive components and ASR_{mem} (in Ω cm^2) is the ASR associated to the proton flow across the PEM membrane.

The electrical ASR was treated as a fitted parameter while the membrane ASR was computed in the following way:

$$ASR_{mem} = \frac{t_{mem}}{\sigma_{mem}} \tag{2.27}$$

where t_{mem} (in cm) is the membrane thickness and σ_{mem} (in 1/Ω/cm) is the membrane ionic conductivity, which is strongly correlated to the water content inside the membrane and the operating temperature. The ionic conductivity of the membrane is reported to increase linearly with increasing water content and exponentially with increasing temperature [86]. In the present model it was defined according to an Arrhenius-type equation in the following form [85], [87]:

$$\sigma_{mem} = \sigma_{mem,ref}\ exp\left[\frac{-E_{a,mem}\ 10^3}{R_U}\left(\frac{1}{T} - \frac{1}{T_{ref}}\right)\right] \tag{2.28}$$

where $\sigma_{mem,ref}$ (in 1/Ω/cm) is the reference membrane ionic conductivity at the reference temperature T_{ref} (298.15 K) and $E_{a,mem}$ (in kJ/mol) is the energy required for the proton transport in the membrane. Both $\sigma_{mem,ref}$ and $E_{a,mem}$ were considered as fitted parameters during the model calibration. As an alternative to Eq. (2.28), other formula exist in the literature for the estimation of σ_{mem}, e.g., relationships as a function of temperature and water content [82], [88] or including hydrogen ion concentration and diffusivity parameters [79], [89].

Diffusion losses are caused by mass transport limitations occurring in the electrodes. Their contribution to the total overvoltage is usually neglected in PEM electrolyzers since it is much lower compared to the activation and ohmic terms. However, diffusion overvoltage effects can become relevant, especially at the anode side, when operating at high current densities: in fact, bubbles of produced gases tend to accumulate disturbing the supply of water to the reaction sites [80], [85]. Since the anodic contribution is dominant with respect to the cathodic one [87], it was assumed the concentration overvoltage to occur only at the anode. It was simulated by introducing the limiting current density parameter $i_{l,an}$ (in A/cm^2) as follows:

$$V_{diff,an} = \frac{R_U\ T}{4\ F}\ ln\left(1 - \frac{i}{i_{l,an}}\right) \tag{2.29}$$

Analogously to the alkaline model, current efficiency η_I should be defined for an accurate evaluation of the amount of hydrogen coming out of the cathode channel. Empirical expressions found in the literature to estimate the current efficiency refer to alkaline-type electrolyzers [72], [73]. In the present model, the η_I term was thus derived based on the hydrogen and oxygen fluxes crossing the membrane according to the following expression [90], [91]:

$$\eta_I = 1 - \frac{2\,F}{i}\left(\dot{N}_{H_2,cross,tot} + 2\,\dot{N}_{O_2,cross,tot}\right) \tag{2.30}$$

where $\dot{N}_{H_2,cross}$ and $\dot{N}_{O_2,cross}$ (in mol/cm^2/s) are the total H_2 and O_2 fluxes moving through the PEM membrane. In the above formula it is supposed that all the oxygen reaching the cathode is electrochemically reduced or catalytically reacts with hydrogen generating water.

The overall hydrogen amount crossing the membrane from cathode to anode is given by different diffusive and convective mass transfer mechanisms:

$$\dot{N}_{H_2,cross,tot} = \dot{N}_{H_2,diff} + \dot{N}_{H_2,dp} - \dot{N}_{H_2,eod} \tag{2.31}$$

where $\dot{N}_{H_2,diff}$, $\dot{N}_{H_2,dp}$ and $\dot{N}_{H_2,eod}$ (in mol/cm^2/s) correspond to the H_2 molar flux caused by diffusion, differential pressure and electro-osmotic drag phenomena, respectively.

The diffusive contribution was computed by applying the Fick's law as follows [92]:

$$\dot{N}_{H_2,diff} = D^{eff}_{H_2,mem}\,\frac{\Delta c_{H_2}}{t_{mem}} \tag{2.32}$$

where $D^{eff}_{H_2,mem}$ (in cm^2/s) is the H_2 effective diffusion coefficient in the membrane and Δc_{H_2} (in mol/cm^3) is the H_2 concentration gradient across the membrane. Considering that diffusion through the solid phase of a fully hydrated Nafion membrane is one order of magnitude lower than diffusion through the liquid phase [93], it was assumed that only species dissolved in water can diffuse across the membrane. The concentration of dissolved hydrogen was expressed as a function of its partial pressure and solubility according to the Henry's law. Considering also that H_2 concentration at the anode side is negligible, the $\dot{N}_{H_2,diff}$ term was rearranged as [92]:

$$\dot{N}_{H_2,diff} = D^{eff}_{H_2,mem}\,S_{H_2}\,\frac{p_{H_2,cat}}{t_{mem}} \tag{2.33}$$

where S_{H_2} (in mol/cm^3/bar) is the hydrogen solubility in water and $p_{H_2,cat}$ (in bar) is the hydrogen partial pressure at the cathode side. A relationship from Refs. [94]–[96] was employed to express the S_{H_2} term as a function of temperature and pressure. $D^{eff}_{H_2,mem}$ was derived by correcting the H_2 diffusion coefficient in water (reported by Wise and Houghton [97] in the form of an Arrhenius-type correlation) with the porosity and tortuosity of the membrane according to the following equation [92]:

$$D_{H_2,mem}^{eff} = \frac{\varepsilon_{mem}}{\tau_{mem}} D_{H_2} \tag{2.34}$$

As reported by Eq. (2.31), in addition to diffusion, gas crossover is also caused by convection processes such as differential pressure and electro-osmotic drag. The general expression for convective permeation is given by:

$$\dot{N}_{H_2,conv} = v_{H_2O}\, c_{H_2} \tag{2.35}$$

where v_{H_2O} (in cm/s) is the velocity of the solvent, i.e., liquid water moving through the membrane and c_{H_2} (in mol/cm^3) is the concentration of dissolved hydrogen estimated by the Henry's law.

Concerning the differential pressure mechanism, the velocity of water was described by applying the Darcy's law [79], [83], [92]:

$$v_{H_2O,dp} = \frac{K_{mem}}{\mu_{H_2O}} \frac{\Delta p}{t_{mem}} \tag{2.36}$$

where K_{mem} (in cm^2) is the hydraulic permeability of the membrane, μ_{solv} (in Pa s) is the dynamic viscosity of water and Δp (in Pa) is the pressure difference between the cathodic and anodic side, which is null in case of equi-pressure configuration. An expression as a function of temperature from Refs. [98], [99] was adopted to evaluate the water dynamic viscosity.

The velocity of water related to electro-osmotic drag was defined as [92]:

$$v_{H_2O,eod} = \frac{1}{c_{H_2O}} \frac{n_{eod}\, i}{F} \tag{2.37}$$

where c_{H_2O} (in mol/cm^3) is the concentration of solvent in the membrane and n_{eod} is the electro-osmotic drag coefficient, i.e., the number of water moles transported from anode to cathode for each mole of protons traversing the membrane. The relationship as a function of temperature reported by Onda *et al.* [100] was used for the estimation of the n_{eod} term.

Regarding the oxygen species, O_2 crossover through the membrane in the anode to cathode direction was derived according to the following expression:

$$\dot{N}_{O_2,cross,tot} = \dot{N}_{O_2,diff} - \dot{N}_{O_2,dp} + \dot{N}_{O_2,eod} \tag{2.38}$$

where the diffusive ($\dot{N}_{O_2,diff}$), pressure difference ($\dot{N}_{O_2,dp}$) and electro-osmotic drag ($\dot{N}_{O_2,eod}$) oxygen fluxes were assessed similarly to what performed for the hydrogen species by using Eqs. (2.32) to (2.37). Solubility values of oxygen in

water were taken from [95], [96]. A temperature dependent correlation for the diffusion coefficient of dissolved oxygen in water is instead reported in Ref. [97].

Performance curve derivation

The fitted parameters were determined by performing a non-linear fitting process according to Eq. (2.20). Experimental data by Marocco *et al.* [101], referred to an N117-based membrane at different current densities (up to 2 A/cm^2) and temperatures (60, 70 and 80 °C), were used for the model calibration. Fitted and fixed parameters are reported in Table 2.4 and Table 2.5, respectively. By performing the calibration process, the maximum relative error (modelled voltage with respect to experimental voltage) was found to be approximately 1.55%.

Charge transfer coefficient values are often set to 2 for the anode and 0.5 for the cathode [82], [102], [103]. It is also common to assume both coefficients equal to 0.5 [87]. In general, ranges from the literature are around 0 to 2 for the anode and 0 to 1 for the cathode [104]. The cell performance is heavily influenced by the value adopted for the exchange current density. This term depends on several catalyst-related physical and morphological properties that are difficult to quantify. A summary of exchange current density values was reported by Carmo *et al.* [65]. Exchange current densities are often stated to be in the range of 10^{-12} to 10^{-7} and 10^{-4} to 10^{-3} A/cm^2 for the anode and cathode side, respectively [104], [105]. The activation energy of the electrode was assumed to be around 76 kJ/mol for the anode and 4.3 kJ/mol for the cathode in the work by Liso *et al.* [79]. As shown in Table 2.4, fitted parameters obtained from the present model validation are in agreement with values from the literature. The pre-exponential ($\sigma_{mem,ref}$) and exponential ($E_{a,mem}$) terms of the membrane ionic conductivity are also well in accordance with conductivity values estimated by an alternative relationship reported in Refs. [82], [88] when considering a membrane water content (λ) of approximately 22. This value is typical for PEM-based cells operating in electrolysis mode. As an example, λ values of 20, 22 and 25 were considered in Refs. [83], [102] and [106], respectively when modelling the performance of PEM electrolyzers. Indeed, referring to standard membranes, the water content is around 0.5 in dry conditions, around 12 to 14 in the presence of water saturated gas and 22 when exposed to liquid water (as in the case of electrolysis operation) [104].

Concerning the fixed parameters of the model (Table 2.5), the mean of 37 and 43 mol/L was assumed for the concentration of water inside the membrane, as reported by Schalenbach *et al.* [91]. This value is in between the 37 mol/L and 55 mol/L values adopted by Trinke *et al.* [92] and Rahim *et al.* [107], respectively. Parameters for the estimation of the roughness factor (Eq. (2.25)) were taken from Bessarabov *et al.* [78]. It can be noticed that the catalyst loading at the cathode side is lower than the amount that is required for the anode catalyst layer. This is because of the slower kinetics of the OER taking place at the anode. Moreover, as

further described in the Supplementary material, durable catalyst supports for the anode (which would reduce the catalyst loading) still remain to be developed.

Table 2.4 Fitted parameters for the model of the PEM electrolyzer cell

Fitted parameter	Value
$ASR_{electric}$	$7.48 \cdot 10^{-2}$ Ω·cm^2
$E_{a,act,an}$	59.95 kJ/mol
$E_{a,act,cat}$	8.57 kJ/mol
$E_{a,mem}$	10.32 kJ/mol
$i_{0,ref,an}$	$4.38 \cdot 10^{-9}$ A/cm^2
$i_{0,ref,cat}$	$4.94 \cdot 10^{-3}$ A/cm^2
α_{an}	0.69
α_{cat}	0.56
$\sigma_{mem,ref}$	0.106 1/Ω/cm

Table 2.5 Fitted and fixed parameters for the model of the PEM electrolyzer cell

Fixed parameters	Value	Reference
c_{H_2O}	40 mol/cm^3	[91]
$i_{l,an}$	6 A/cm^2	[108]
$d_{C,an}$	$2.9 \cdot 10^{-7}$ cm	[78]
$d_{C,cat}$	$2.7 \cdot 10^{-7}$ cm	[78]
K_{mem}	$5 \cdot 10^{-16}$ cm	[92]
$m_{C,an}$	0.001 g/cm^2	[78]
$m_{C,cat}$	0.0003 g/cm^2	[78]
t_{mem}	0.0183 cm	[101]
ε_{mem}	0.42	[109]
$\rho_{C,an}$	22.56 g/cm^3	[78]
$\rho_{C,cat}$	21.45 g/cm^3	[78]
τ_{mem}	1.5	[110]
$\varphi_{C,an}$	0.75	[78]
$\varphi_{C,cat}$	0.75	[78]

Table 2.6 reports the operating parameters that are required for the construction of the polarization and efficiency curves. The operating pressure and temperature were set to 60 °C and 30 bar, respectively in accordance to [32]. Increasing the operating temperature would lead to an improvement of the electrolyzer efficiency, but at the expense of the membrane chemical stability as discussed in the Supplementary material. A value of around 60 °C can be considered as a good trade-off between performance and stability [111]. The maximum current density for the PEM device was set to 1.8 A/cm^2, which is between the 1.7 and 2 A/cm^2 values reported by Mayyas *et al.* [76] and Parra *et al.* [18], respectively. It can be noticed that the PEM electrolyzer is able to operate at a much higher current density with respect to the alkaline alternative. This results in higher hydrogen production per unit of cell area, which means greater compactness of the PEM stack compared to the alkaline one. A minimum operating power of 10% (defined as a percentage of the rated power) was imposed to avoid the operation at too low efficiencies and as a safety precautions (to prevent excessive increase in the hydrogen concentration in the anode compartment). Consumption due to auxiliary components was also considered to evaluate the performance of the electrolyzer at system level. A linear behaviour was assumed for the auxiliary consumption curve [58].

Table 2.6 Operating input parameters for the evaluation of the performance curve of the PEM electrolyzer system.

Parameter	**Value**	**Reference**
Operating temperature	60 °C	[32]
Operating pressure	30 bar	[32]
System minimum power[a]	10%	[112]
Max. current density	1.8 A/cm^2	[113]
Aux. consumption in nominal condition[a]	10%	[75], [76]
Aux. consumption in stand-by[b]	29%	[58]

[a] % of rated power
[b] % of aux. consumption in nom. condition

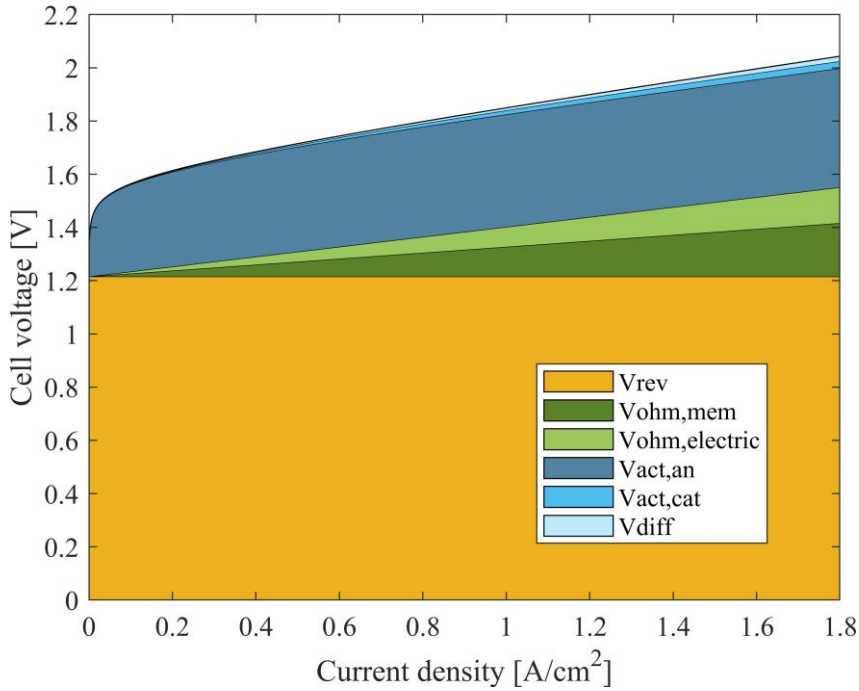

Figure 2.4 Contributions of the various overpotential terms to the polarization curve of the PEM electrolyzer (60 °C and 30 bar)

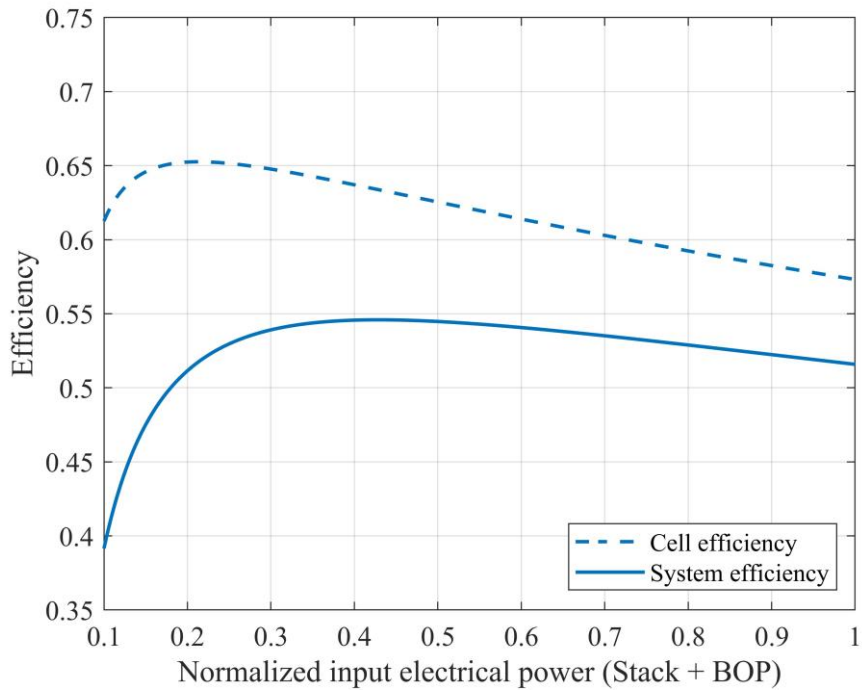

Figure 2.5 Cell and system efficiency curves of the PEM electrolyzer at 60 °C and 30 bar

Figure 2.4 shows the contribution of each source of overpotential to the polarization curve of the PEM electrolyzer at the selected operating conditions

(i.e., 60°C and 30 bar). The influence of the diffusion term is much smaller than the activation and ohmic losses. Indeed, the high value that was assumed for the limiting current density (i.e., 6 A/cm^2) makes the diffusion contribution almost null in the operating range of 0 to 1.8 A/cm^2. The most important contribution is represented by the activation overpotential at the anode side. The kinetics of the anodic OER is in fact slower than the cathodic HER, resulting in higher overpotential at the anode. The activation losses at the cathode were found to be almost negligible in line with what reported by Liso *et al.* [79]. Concerning the ohmic term, more than half of this overvoltage is of ionic-type, due to the polymeric membrane.

Cell and system efficiency curves of the PEM electrolyzer are displayed in Figure 2.5 as a function of the normalized input electrical power, which includes both the stack and balance-of-plant (BOP) consumption. Similarly to the alkaline system, the peak of efficiency occurs at around 40% of the rated power. The system efficiency (on LHV basis) in nominal conditions is around 0.52, corresponding to a specific energy consumption of 5.76 kWh/Nm^3. This value is in line with the range 5.0 to 6.5 reported by Buttler *et al.* [13]. By looking at Figure 2.5, it can be noticed that the modulation range of the PEM system is from 0.1 to 1, as imposed by the minimum operating power of Table 2.6.

2.1.3 PEM fuel cell

Polymer electrolyte membrane fuel cells allow the chemical energy stored in H_2 fuel to be directly converted into electrical energy, with water as the only by-product. The humidified hydrogen stream is supplied to the anode inlet, whereas humidified air is fed to the cathode side. At the anode, H_2 diffuses through the porous transport layer (PTL) and is oxidized at the catalyst layer, where it decomposes into protons and electrons according to Eq. (2.39). Protons then move through the electrolyte membrane from the anode to the cathode. Electrons are instead carried to the cathode through an external circuit. After diffusing through the PTL, oxygen is reduced at the cathode catalyst layer, generating water according to Eq. (2.40).

$$H_2 \rightarrow 2H^+ + 2e^- \tag{2.39}$$

$$\frac{1}{2}O_2 + 2H^+ + 2e^- \rightarrow H_2O \tag{2.40}$$

The electrolyte consists of a polymeric membrane, usually made of Nafion, which works as proton conductor, electronic insulator and separator of reactant gases [114]. Membrane hydration, which is performed by proper reactant humidification, is required to achieve good PEM fuel cell performance. Too little water can cause membrane dehydration, thus increasing the membrane resistance

due to the worsening of the membrane proton conductivity. On the other hand, excessive water can lead to electrode flooding and hamper the transport of gases to the CLs. The anode and cathode catalyst layers are based on carbon-supported catalyst and ionomer porous composite. Platinum (or Pt alloys) and carbon black are common materials for the catalyst and support, respectively [114]. Porous transport layers, which are placed between the CL and BP, are composed of highly porous material, usually carbon fibre-based papers. They enable the diffusion of gases towards the reaction sites, serve as electronic connection between the CL and BP and favour the management of heat and water. The MEA is then located between two bipolar plates made of carbon-based composites or metals [115].

Electrochemical model

The operating cell voltage was derived from the reversible voltage decreased by the activation, ohmic and diffusion overvoltage terms:

$$V_{cell} = V_{rev} - V_{act} - V_{ohm} - V_{diff} \tag{2.41}$$

The reversible voltage was evaluated according to the following expression [116]–[118]:

$$V_{rev} = 1.228 - 0.85 \cdot 10^{-3}\,(T - 298.15) + 4.3086 \cdot 10^{-5}\,T\,ln\left(p_{H_2,an,ch}\right) + 0.5\,ln\left(p_{O_2,cat,ch}\right) \tag{2.42}$$

where $p_{H_2,an,ch}$ and $p_{O_2,cat,ch}$ (in bar) correspond to the hydrogen and oxygen effective partial pressures at the anode and cathode channel, respectively.

Main relationships to evaluate the amount of species required at the fuel cell inlet are reported below. The molar flow rate of H_2 at the anode inlet (in mol/s) was expressed according to the Faraday's law as follows:

$$\dot{n}_{H_2,an,in} = \lambda_{H_2}\,\frac{i}{2\,F}\,A_{cell} \tag{2.43}$$

where λ_{H_2} is the hydrogen excess and A_{cell} (in cm^2) is the cell area. The humidification of reactant gases is usually performed to keep the membrane hydrated. The molar flow rate of water supplied to the anode was derived as [84]:

$$\dot{n}_{H_2O,an,in} = \lambda_{H_2}\,\frac{i}{2\,F}\,A_{cell}\,\frac{\varphi_{an}\,p_{sat}}{p_{an} - \varphi_{an}\,p_{sat}} \tag{2.44}$$

where φ_{an} corresponds to the relative humidity in the anode flow channel and p_{sat} (in bar) is the water saturation pressure, which was estimated at the operating temperature of the fuel cell.

Referring to the cathode side, the O_2 molar flow rate entering the cathode was determined according to the Faraday's law and including an air excess term (λ_{air}) as follows:

$$\dot{n}_{O_2,cat,in} = \lambda_{air} \frac{i}{4\,F} A_{cell} \tag{2.45}$$

Analogously to the hydrogen stream, oxygen entering the cell should be humidified. The amount of water at the cathode inlet was then defined in the following way [84]:

$$\dot{n}_{H_2O,cat,in} = \frac{\lambda_{air}}{y_{O_2,dry,cat,in}} \frac{i}{4\,F} A_{cell} \frac{\varphi_{cat}\, p_{sat}}{p_{cat} - \varphi_{cat}\, p_{sat}} \tag{2.46}$$

where $y_{O_2,dry,cat,in}$ is the dry molar fraction of oxygen at the cathode channel inlet and φ_{cat} is the relative humidity.

By applying mass balance equations in stationary conditions both at the anode and cathode channel, flow rates of various species were computed also at the fuel cell outlet. The effective oxygen partial pressure ($p_{O_2,cat,ch}$) was then derived using a log-mean average of the inlet and outlet oxygen partial pressures. The arithmetic mean was instead used to compute the effective hydrogen partial pressure ($p_{H_2,an,ch}$) [118].

Similarly to the modelling approach of the PEM electrolyzer, the activation overvoltage term was evaluated according to Eq. (2.24). Eq. (2.11) was employed to model the exchange current density in the form of an Arrhenius-type expression depending on temperature. The total ohmic overvoltage was computed by applying Eq. (2.26), where both the electrical and the ionic contributions are taken into account. Referring to the ionic term, a temperature-dependent relationship in the form of Eq. (2.28) was used to estimate the membrane ionic conductivity and hence the membrane ASR.

Mass transport phenomena effects were also considered by adding the following concentration overvoltage term (with j = an, cat):

$$V_{diff,j} = \frac{R_U\, T}{z_j\, F}\, ln\left(1 - \frac{i}{i_{l,j}}\right) \tag{2.47}$$

where i_l (in A/cm^2) is the limiting current density, whose value is up to 2 A/cm^2 when referring to commercial PEM fuel cell systems [86], [119]. The z parameter is equal to 2 and 4 at the anode and cathode side, respectively. Alternatively, the contribution due to diffusion losses could be determined by directly computing the species concentration at the reaction sites, according to Eq. (2.48) and (2.49).

$$V_{diff,an} = \frac{R_U\,T}{2\,F}\,ln\left(\frac{p_{H_2,an,ch}}{p_{H_2,an,cl}}\right) \tag{2.48}$$

$$V_{diff,cat} = \frac{R_U\,T}{4\,F}\,ln\left(\frac{p_{O_2,cat,ch}}{p_{O_2,cat,cl}}\right) \tag{2.49}$$

The terms $p_{H_2,an,cl}$ and $p_{O_2,cat,cl}$ (in bar) correspond to the partial pressures of hydrogen and oxygen at the anode and cathode catalyst layer, respectively. They can be derived by applying the Stefan-Maxwell equation to model the diffusion of multicomponent gas streams through the electrode [88]:

$$\frac{dy_i}{dz} = \frac{R_U\,T\,10}{p_{an/cat}}\sum_j \frac{y_i\,\dot{N}_j - y_j\,\dot{N}_i}{D_{i,j,eff}} \tag{2.50}$$

where $y_{i/j}$ is the molar fraction of the i/j-th species, $\dot{N}_{i/j}$ (in mol/cm^2/s) is the molar flux of the i/j-th species and $D_{i,j,eff}$ (in cm^2/s) is the effective binary diffusivity of the i-j pair in the porous medium. R_U is equal to 8.413 J/mol/K, the temperature T is in K and the anode/cathode pressure $p_{an/cat}$ is in bar. The binary diffusion coefficient can be estimated by applying the Slattery and Bird correlation [120], [121], corrected to consider that the diffusion process occurs in a porous medium [122], [123]. By supposing the gas mixture at the anode to be composed of hydrogen and water vapour, $p_{H_2,an,cl}$ becomes [118]:

$$p_{H_2,an,cl} = \varphi_{an}\,p_{sat}\left(\frac{1}{y_{H_2O,an,ch}\,exp\left(\frac{R_U\,T\,i\,l_{PTL,an}\,10}{2\,F\,p_{an}\,D_{H_2O,H_2,eff}}\right)} - 1\right) \tag{2.51}$$

where $y_{H_2O,an,ch}$ is the molar fraction of water vapor in the anode channel, $l_{PTL,an}$ (in cm) is the length of the anode porous transport layer and $D_{H_2O,H_2,eff}$ (cm^2/s) is the H_2O-H_2 effective diffusion coefficient. Concerning the cathode side, in case the gas stream is a mixture of air (i.e., mainly oxygen and nitrogen) and water vapor, the O_2 partial pressure at the reaction site can be defined as [118]:

$$p_{O_2,cat,cl} = p_{cat} - p_{N_2,cat,cl} - \varphi_{cat}\,p_{sat} \tag{2.52}$$

The nitrogen partial pressure can be rearranged as follow:

$$p_{N_2,cat,cl} = p_{N_2,cat,ch}\,exp\left(\frac{R_U\,T\,i\,l_{PTL,cat}\,10}{4\,F\,p_{cat}\,D_{N_2,O_2,eff}}\right) \tag{2.53}$$

where $p_{N_2,cat,ch}$ (in bar) is the nitrogen partial pressure in the cathode channel, $l_{PTL,cat}$ (in cm) is the length of the cathode porous transport layer and $D_{N_2,O_2,eff}$ (in cm^2/s) is the N_2-O_2 effective diffusion coefficient.

Performance curve derivation

Similarly to the alkaline and PEM electrolyzer, a nonlinear regression approach was applied to calibrate the PEM fuel cell model. Fitted parameters were adjusted so as to minimize the sum of the squares of the differences between experimental and related model voltage values, as described in Eq. (2.20). The present model was fitted to the experimental data by Corrêa *et al.* [119] with a maximum relative error on voltage of around 2.41%. The resulting values of the fitted parameters are reported in Table 2.7, whereas fixed model parameters are listed in Table 2.8.

The reference exchange current densities are in the range of 10^{-9} to 10^{-12} A/cm^2 for the cathodic O_2 reduction reaction and 10^{-4} to 10^{-3} A/cm^2 for the anodic H_2 oxidation reaction [84]. The charge transfer coefficients for anode and cathode are stated to range from 0 to 1 and 0 to 2, respectively [84]. Our fitted values for $i_{0,ref}$ and α parameters lie in these ranges. The activation free energy values ($E_{a,act}$) we found are in accordance with what suggested by Abdin *et al.* [84]. Finally, the fitted terms referred to the membrane ionic conductivity formula ($E_{a,mem}$ and $\sigma_{mem,ref}$) provide conductivity values in line with common values for PEM fuel cells [86].

Table 2.7 Fitted parameters for the model of the PEM fuel cell

Fitted parameters	Value
$ASR_{electric}$	$2.96 \cdot 10^{-2}$ Ω·cm^2
$E_{a,act,an}$	19.92 kJ/mol
$E_{a,act,cat}$	70.09 kJ/mol
$E_{a,mem}$	9.82 kJ/mol
$i_{0,ref,an}$	$4.6 \cdot 10^{-3}$ A/cm^2
$i_{0,ref,cat}$	$1.39 \cdot 10^{-8}$ A/cm^2
α_{an}	0.44
α_{cat}	0.74
$\sigma_{mem,ref}$	0.070 1/Ω/cm

Table 2.8 Fixed parameters for the model of the PEM electrolyzer

Fixed parameters	Value	Reference
$d_{C,an}$	$2.7 \cdot 10^{-7}$ cm	[78]
$d_{C,cat}$	$2.9 \cdot 10^{-7}$ cm	[78]
$i_{l,an}$	2 A/cm^2	[86]
$i_{l,cat}$	2 A/cm^2	[86]
$m_{C,an}$	0.0003 g/cm^2	[78]
$m_{C,cat}$	0.001 g/cm^2	[78]
t_{mem}	0.0183 cm	[119]
$\rho_{C,an}$	21.45 g/cm^3	[78]
$\rho_{C,cat}$	22.56 g/cm^3	[78]
$\varphi_{C,an}$	0.75	[78]
$\varphi_{C,cat}$	0.75	[78]

Operating parameters for the derivation of the PEM fuel cell performance curve are listed in Table 2.9. The operating temperature is 60 °C, which is the same value that was adopted for the PEM electrolyzer since it is a good compromise between performance and stability when dealing with PFSA-based membranes. Unlike the electrolyzer system (where pressurized conditions are chosen so as to avoid the need for a compression step between the electrolyzer and the hydrogen storage), the fuel cell was assumed to work at ambient pressure [32]. Referring to the maximum achievable current density, the adopted value of 1.2 A/cm^2 lies in the range of 1 to 1.5 A/cm^2 reported in Refs. [119], [124]. Similarly to the approach taken for the alkaline and PEM electrolyzer, auxiliary consumption was supposed to vary linearly from stand-by to nominal condition [58]. Relative humidity values for the anode and cathode compartments were taken from Refs. [118], [125]. Relative humidity must be controlled to maintain a proper level of wet conditions and ensure high membrane proton conductivity [126]. Stoichiometric flow ratio values are also important to prevent reactant gas starvation and guarantee quite uniform distribution of H_2 and O_2 gases along the channel [126]. Hydrogen and air excess were set to 1.2 and 2, respectively [84].

Table 2.9 Operating input parameters for the evaluation of the performance curve of the PEM fuel cell system.

Parameter	Value	Reference
Operating temperature	60 °C	[32]
Operating pressure	1 bar	[32]
System minimum power[a]	6%	[32]
Max. current density	1.2 A/cm^2	Assumption
Aux. consumption in nominal condition[a]	8%	[32]
Aux. consumption in stand-by[b]	50%	[58]
Air excess (λ_{air})	2	[84]
Hydrogen excess (λ_{H_2})	1.2	[84]
Anode relative humidity (φ_{an})	0.5	[118], [125]
Cathode relative humidity (φ_{cat})	1	[118], [125]

[a] % of rated power
[b] % of aux. consumption in nom. condition

The contribution of each source of overpotential to the PEM fuel cell polarization curve is displayed in Figure 2.6. The activation term was found to be the major contribution due to the sluggish electrode kinetics, mainly related to the oxygen reduction reaction at the cathode side. The cathodic OER is in fact very slow, whereas hydrogen oxidation at the anode is considerably faster [127], making the anodic activation overvoltage almost negligible [128]. Another important contribution to the voltage loss is represented by the ohmic overpotential (green areas in Figure 2.6). This term is mainly due to the ionic resistance, which is associated to the proton flow through the polymeric membrane. This is in accordance with what reported by Abdin *et al.* [84], who showed that the ionic resistance accounted for the major share of the ohmic overpotential. The minor electrical ohmic contribution, which is related to the resistance of the electrically conductive components to the passage of electrons, is mostly caused by the lack of proper contact between PTLs, BPs and other interconnects [84]. Finally, the diffusion overpotential is very low in the operating range under analysis, being the limiting current density of around 2 A/cm^2 [86].

The PEM fuel cell efficiency curves, both at cell and system level, are shown in Figure 2.7 as a function of the normalized output electrical power. The resulting system efficiency in nominal conditions is approximately 0.43 (on LHV basis), which is close to the value in [32]. The operating point at maximum efficiency occurs at around 30% of the rated power of the fuel cell. This value is

in accordance with what suggested by fuel cell suppliers involved in the REMOTE project [36].

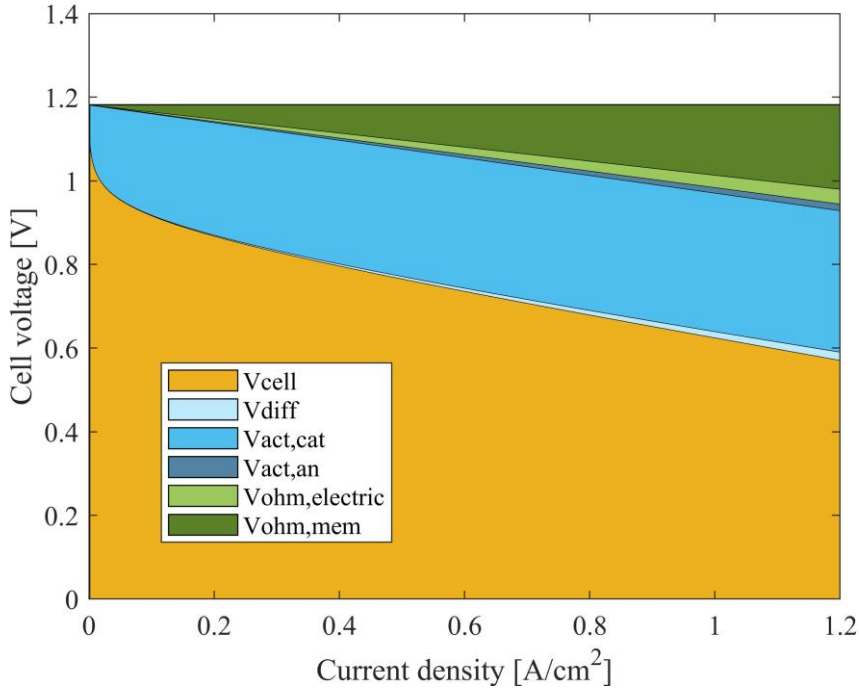

Figure 2.6 Contributions of the various overpotential terms to the polarization curve of the PEM fuel cell (60 °C and 1 bar)

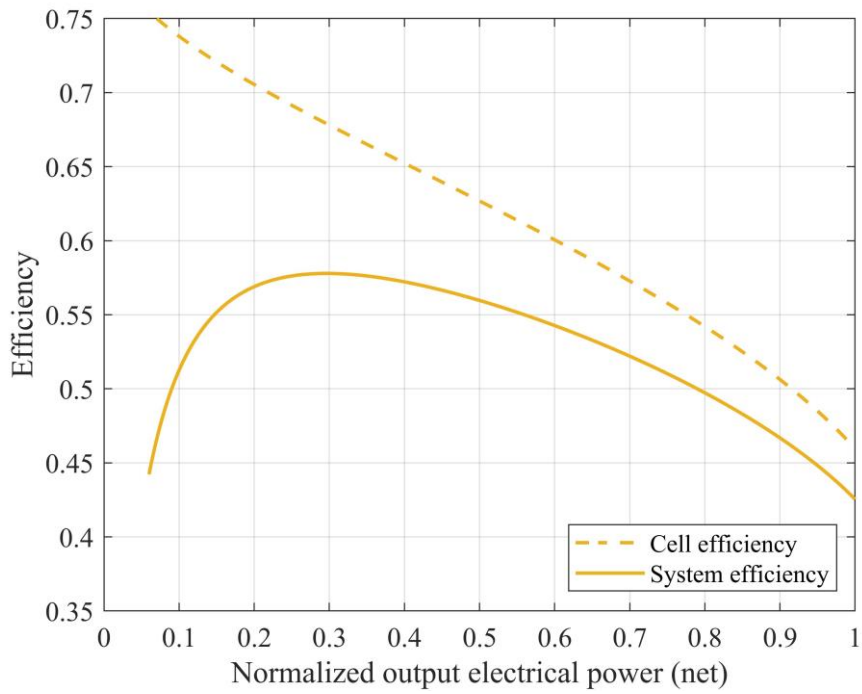

Figure 2.7 Cell and system efficiency curves of the PEM fuel cell at 60 °C and 1 bar

2.2 Other components

2.2.1 PV power plant

The power produced by the PV generator was computed as [129]–[131]:

$$P_{PV}(t) = f_{PV}\, P_{PV,rated}\, \frac{G(t)}{G_{STC}} \left(1 + \gamma_T \left(T_{cell}(t) - T_{cell,STC}\right)\right) \tag{2.54}$$

where G (in kW/m^2) is the total irradiance incident on the PV array, G_{STC} (equal to 1 kW/m^2) is the incident irradiance at standard test conditions (STC), $P_{PV,rated}$ (in kW) is the rated PV power, T_{cell} (in °C) is the PV cell temperature, $T_{cell,STC}$ (equal to 25 °C) corresponds to the PV cell temperature at standard test conditions, f_{PV} is the derating factor and γ_T (in 1/K) is the temperature coefficient. The cell temperature T_{cell} was expressed as [132]:

$$T_{cell}(t) = T_a(t) + \frac{G(t)}{0.8}\,(NOCT - 20) \tag{2.55}$$

where T_a (in °C) is the ambient temperature and $NOCT$ (in °C) represents the nominal operating cell temperature. The total irradiance G over the tilted PV surface was determined as follows [133], [134]:

$$G(t) = G_{b,n}(t)\, cos(\theta) + G_{d,h}(t)\, F_{c,s} + G_{t,h}(t)\, \rho_g\, F_{c,g} \tag{2.56}$$

where $G_{b,n}$ (in kW/m^2) is the direct normal irradiance, $G_{d,h}$ (in kW/m^2) is the diffusive irradiance over the horizontal surface, $G_{t,h}$ (in kW/m^2) is the total irradiance over the horizontal surface, ρ_g is the ground albedo, $F_{c,s}$ is the collector-sky view factor, $F_{c,g}$ is the collector-ground view factor and θ is the angle of incidence to the tilted surface. The hourly values of diffusive and total irradiance on the horizontal plane, direct normal irradiance and ambient temperature were taken from the Photovoltaic geographical information system (PVGIS) software [135], referring to a typical meteorological year (TMY) for the location under analysis. The terms $F_{c,s}$ and $F_{c,g}$ were determined in the following way:

$$F_{c,s} = \frac{1 + \cos(\beta)}{2} \tag{2.57}$$

$$F_{c,g} = \frac{1 - \cos(\beta)}{2} \tag{2.58}$$

where β represents the slope of the PV panel tilted surface, whose value was taken from PVGIS tool [135]. The angle of incidence (θ) was evaluated by applying the following relationship:

$$cos(\theta) = \cos(\beta)\, cos(\theta_z) + \sin(\beta)\, sin(\theta_z) \cos\,(\phi_s - \phi) \qquad (2.59)$$

where θ_z is the zenith angle, ϕ_s is the solar azimuth and ϕ is the PV panel surface azimuth. The zenith angle (θ_z) parameter was defined as:

$$cos(\theta_z) = cos(\Phi)\, cos(\delta)\, cos(\omega) + sin(\Phi)\, sin(\delta) \qquad (2.60)$$

where Φ is the latitude, δ is the declination and ω is the hour angle. The declination can be derived by applying the approximated Cooper formula, which is function of the day of the year n as follows:

$$\delta = 23.45\, sin\left(360\, \frac{284 + n}{365}\right) \qquad (2.61)$$

The hour angle was instead assessed as:

$$\omega = (h - h_{culm})\frac{360}{24} \qquad (2.62)$$

where h corresponds to the standard time, i.e., the time given by local clock and h_{culm} is the noon time, i.e., the time given by local clock when the sun is at its highest point above the horizon (crosses the local meridian). The term h_{culm} is given by:

$$h_{culm} = 12 + \frac{L_{loc} - L_{ref}}{15} - \frac{EOT}{60} + DST \qquad (2.63)$$

where L_{loc} is the longitude of the observer's meridian, L_{ref} is the longitude of the meridian for the local time zone, EOT (in minutes) is the equation of time and DST is the daylight saving time parameter (equal to 1 when in force and 0 otherwise). Finally, the following expression was employed to determine the solar azimuth angle (ϕ_s):

$$cos(\phi_s\,) = \frac{cos(\theta_z)\sin(\Phi) - \sin\,(\delta)}{sin(\theta_z)\cos(\Phi)} \qquad (2.64)$$

Technical parameters of the photovoltaic system are listed in Table 2.10. Main features of the PV modules were taken from [136]. Optimal values, derived from PVGIS, were considered for PV surface slope and azimuth. The albedo of

the ground was assumed equal to 0.2. This average value was suggested by Laoun *et al.* [133] when no specific information about the location are available.

Table 2.10 Technical parameters for the PV power plant

PV power plant		
Derating factor, f_{PV}	0.86	[135]
Nominal operating cell temperature, $NOCT$	44°C	[136]
Temperature coefficient, γ_T	-0.003 1/K	[136]
PV surface slope, β	Optimized	[135]
PV surface azimuth, ϕ	Optimized	[135]
Albedo of the ground, ρ_g	0.2	[133]
Incident irradiance at STC, G_{STC}	1 kW/m^2	
PV cell temperature at STC, $T_{cell,STC}$	25 °C	

2.2.2 Wind power plant

The output power of the wind turbine was computed by employing a characteristic power versus wind speed curve, as the one described below [137], [138]:

$$P_{WT}(t) = \begin{cases} 0, & if\ v_w(t) \leq v_{w,ci} \\ P_{WT,rated}\ \dfrac{v_w^3(t) - v_{w,ci}^3}{v_{w,r}^3 - v_{w,ci}^3}, & if\ v_{w,ci} \leq v_w(t) \leq v_{w,r} \\ P_{WT,rated}, & if\ v_{w,r} \leq v_w(t) \leq v_{w,co} \\ 0, & if\ v_w(t) \geq v_{w,co} \end{cases} \quad (2.65)$$

where $v_{w,ci}$, $v_{w,co}$ and $v_{w,r}$ (in m/s) correspond to the cut-in, cut-out and rated wind speed, respectively. $P_{WT}(t)$ (in kW) is the produced wind power, whereas $P_{WT,rated}$ (in kW) represents the rated power of the machine. When the wind speed is lower than $v_{w,ci}$ or higher than $v_{w,co}$, no power is produced. Instead, if the wind speed is in between $v_{w,r}$ and $v_{w,co}$, the output power has to be limited in order to avoid damages to the turbine. TMY hourly wind speed data were taken from [135], referring to a reference height (h_{ref}) of 10 meters. They need thus to be corrected to the turbine height (h_{WT}):

$$v_w(t) = v_{w,ref}(t)\left(\frac{h_{WT}}{h_{ref}}\right)^{\alpha} \tag{2.66}$$

where $v_{w,ref}$ (in m/s) is the wind speed measured at the reference height and α is the exponent law coefficient, which depends on the surface topology.

Technical parameters for the wind power curve are listed in Table 2.11. Main features of the wind power curve were taken from Ref. [139].

Table 2.11 Technical parameters for the wind power plant

Wind power plant		
Turbine height, h_t	30 m	[139]
Wind speed reference height, h_{ref}	10 m	[135]
Exponent law coefficient, α	0.14	[140]
Cut-in wind speed, $v_{w,ci}$	3 m/s	[139]
Cut-out wind speed, $v_{w,co}$	25 m/s	[139]
Rated wind speed, $v_{w,r}$	13 m/s	[139]

2.2.3 Battery storage system

The battery component was treated as an energy tank, modifying its charge level based on the power exchanged with the bus bar. The state-of-charge (SOC) parameter was used to model the state of the battery storage system. It represents the ratio of the stored energy to the battery capacity [32]:

$$SOC(t) = SOC(t-1)(1-\sigma_{BT}) + \frac{P_{BT,ch}(t-1)\,\Delta t\,\eta_{BT,ch}\,\eta_{conv}}{Cap_{BT}} - \frac{P_{BT,dc}\,(t-1)\,\Delta t}{\eta_{conv}\,\eta_{BT,dc}\,Cap_{BT}} \tag{2.67}$$

where σ_{BT} is the self-discharge rate of the battery, $P_{BT,ch/dc}$ (in kW) is the battery charging/discharging power, $\eta_{BT,ch/dc}$ is the battery charging/discharging efficiency, η_{conv} is the efficiency of the battery converter and Cap_{BT} (in kWh) is the capacity of the battery.

During the operation of the battery, its SOC must be bounded between a minimum and maximum value:

$$SOC_{min} \leq SOC(t) \leq SOC_{max} \tag{2.68}$$

The lower SOC threshold was imposed to avoid damaging the storage bank by excessive discharge.

Table 2.12 and Table 2.13 report the main technical parameters for the Li-ion and lead-acid technology, respectively. It can be noticed that Li-ion batteries are generally preferable from a technical point of view since they are characterized by higher roundtrip efficiency, lower self-discharge rate and also wider cycling modulation range. On the other hand, as shown in Section 2.3.2, currently lead-acid devices have lower costs than the Li-ion alternative.

Table 2.12 Technical parameters for the Li-ion battery

Li-ion battery		
Charging efficiency, $\eta_{BT,ch}$	0.95	[31], [141]
Discharging efficiency, $\eta_{BT,dc}$	0.95	[31], [141]
Self-discharge, σ_{BT}	5%/month	[47]
Maximum SOC, SOC_{max}	1	
Minimum SOC, SOC_{min}	0.2	[31], [47]

Table 2.13 Technical parameters for the lead acid battery

Lead-acid battery		
Charging efficiency ($\eta_{BT,ch}$)	0.9	[31]
Discharging efficiency ($\eta_{BT,dc}$)	0.9	[31]
Self-discharge (σ_{BT})	0.25%/day	[47]
Maximum SOC (SOC_{max})	1	[47]
Minimum SOC (SOC_{min})	0.4	[142]

2.2.4 Pressurized hydrogen tank

Similarly to the battery system, the hydrogen tank was described by introducing the level-of-hydrogen (LOH) parameter, which is defined as the ratio of the amount of energy contained in the hydrogen tank to its maximum capacity [32]:

$$LOH(t) = LOH(t-1) + \frac{P_{EL}(t-1)\,\Delta t\,\eta_{EL}}{Cap_{H2}} - \frac{P_{FC}(t-1)\,\Delta t}{\eta_{FC}\,Cap_{H2}} \quad (2.69)$$

where $P_{EL/FC}$ (in kW) is the electrolyzer/fuel cell operating power, $\eta_{EL/FC}$ is the efficiency of the electrolyzer/fuel cell system (including also converter losses) and Cap_{H2} (in kWh) is the capacity of the hydrogen tank.

At any time interval, the constraints on LOH lower and upper boundaries must be respected:

$$LOH_{min} \leq LOH(t) \leq LOH_{max} \quad (2.70)$$

The minimum LOH was computed as the ratio between the minimum and maximum operating pressure of the H_2 tank. This value was chosen so as to effectively overcome downstream pressure drops, thus allowing hydrogen to be supplied to the fuel cell.

Minimum and maximum tank pressures and lower and upper LOH bounds are shown in Table 2.14. Since the maximum operating pressure of the electrolyzer is assumed to be slightly higher than the H_2 tank maximum pressure, the compression step between the electrolyzer and the pressurized hydrogen tank is not necessary [32].

Table 2.14 Technical parameters for the hydrogen tank

Hydrogen tank		
Minimum pressure, p_{min}	3 bar	[32]
Maximum pressure, p_{max}	28 bar	[32]
Minimum LOH, LOH_{min}	p_{min}/p_{max}	
Maximum LOH, LOH_{max}	1	

2.2.5 Diesel generator

Fuel consumption (in L/h) was computed according to a relationship from Refs. [143]–[146]:

$$cons_{DG}(t) = cons_{DG,op}(t) + cons_{DG,start}(t) \quad (2.71)$$

where $cons_{DG,op}$ (in L/h) is the fuel consumption occurring during DG operation and computed from the fuel consumption curve, whereas $cons_{DG,start}$ (in L/start-up) represents the DG start-up penalty. The first term was derived as:

$$cons_{DG,op}\,(t) \;= a_{DG}\,P_{DG,rated} + b_{DG}\,P_{DG}(t) \tag{2.72}$$

where $P_{DG,rated}$ (in kW) is the DG rated power and P_{DG} (in kW) is the DG operating power. The terms a (in L/kWh) and b (in L/kWh) correspond to the coefficients of the fuel consumption curve. The term $cons_{DG,start}$ was expressed as follows:

$$cons_{DG,start} \;= F_{start}\left(a_{DG}\,P_{DG,rated} + b_{DG}P_{DG,rated}\right) \tag{2.73}$$

where F_{start} represents a factor accounting for the extra fuel due to the DG start-up. Its value is usually lower than 0.083, equal to around 5 min at rated power [145], [146]. In the present work, we considered a value of 0.067, representing approximately 4 min of continuous high load operation [147].

A minimum service level was imposed to the diesel generator to avoid its operation with too low efficiency:

$$P_{DG}(t) \geq y_{DG,min}\,P_{DG,rated} \tag{2.74}$$

where $y_{DG,min}$ is the minimum output power, set to 30% of the rated power [146], [148].

Pollutant and GHG emissions are also associated to diesel fuel consumption. Carbon dioxide accounts for the highest percentage when fuel is burnt and it also represents the main cause of the greenhouse effect [149]. The amount of CO_2 (in kg/h) that is released because of DG operation was estimated according to the following expression:

$$m_{CO_2,op}(t) = cons_{DG}(t)\,c_{CO_2,DG} \tag{2.75}$$

where $c_{CO_2,DG}$ (in kg/L) is the CO_2 emission coefficient for the fuel consumption. Dufo-López *et al.* [150] and Fleck *et al.* [151] assumed a value of 3.5 kg/L and 2.86 kg/L, respectively. Jakhrani *et al.* [152] reported the emission factor to be in the range of 2.4 to 3.5 kg/L. The values adopted in the present work for the DG parameters are summarized in Table 2.15.

Table 2.15 Technical parameters for the diesel generator

Diesel generator		
Fuel consumption curve parameter, a_{DG}	0.08415 L/kWh	[144]–[146]
Fuel consumption curve parameter, b_{DG}	0.246 L/kWh	[144]–[146]
Start-up extra fuel parameter, F_{start}	0.067	[147]
Minimum power, $y_{DG,min}$ (% of rated power)	30%	[146], [148]
CO_2 emissions, $c_{CO_2,DG}$	3 kg/L	[152]

2.3 Economic analysis

Main relationships to evaluate the levelized cost of energy are presented below. Economic assumptions for all the components of the HRES are also shown and discussed.

2.3.1 LCOE estimation

The levelized cost of energy (in €/kWh) was computed as follows:

$$LCOE = \frac{C_{NPC,tot}}{\sum_{j=1}^{L_{PR}} \frac{E_{tot,j}}{(1+d)^j}} \tag{2.76}$$

where $C_{NPC,tot}$ (in €) is the total net present cost (NPC), $E_{tot,j}$ (in kWh) corresponds to the total amount of energy provided by the off-grid energy system to the final user along the j-th year, L_{PR} is the lifetime of the project and d corresponds to the real discount rate, which was derived as [32]:

$$d = \frac{d' - ir}{1 + ir} \tag{2.77}$$

where d' and ir stand for the nominal discount rate and inflation rate, respectively, whose values are reported in Table 2.23. The resulting value of d (i.e., 4.9% [32]) lies in the average range of 3% to 6% reported in Ref. [153], where a review about discount rates in cost-optimality calculations was performed.

The total net present cost is given by the sum of the present value of all the costs incurred by the system (capital, OM and replacement contributions) minus the present value of all the revenues (i.e., salvage contributions) over the system lifetime:

$$C_{NPC,tot} = C_{inv,tot} + C_{NPC,OM,tot} + C_{NPC,rep,tot} - C_{NPC,sal,tot} \quad (2.78)$$

The various terms that are included in the above NPC formula were derived according to Eqs. (2.79) to (2.82).

$$C_{inv,tot} = \sum_{i=1}^{N_{c,tot}} C_{inv,i,0} \quad (2.79)$$

$$C_{NPC,OM,tot} = \sum_{j=1}^{L_{PR}} \frac{\sum_{i=1}^{N_{c,tot}} C_{OM,i,j}}{(1+d)^j} \quad (2.80)$$

$$C_{NPC,rep,tot} = \sum_{j=1}^{L_{PR}} \frac{\sum_{i=1}^{N_{c,rep,tot}} C_{rep,i,j}}{(1+d)^j} \quad (2.81)$$

$$C_{NPC,rep,tot} = \sum_{j=1}^{N_{c,rep,tot}} \frac{C_{sal,i,L_{PR}}}{(1+d)^{L_{PR}}} \quad (2.82)$$

where $C_{inv,i,j}$, $C_{OM,i,j}$, $C_{rep,i,j}$ and $C_{sal,i,j}$ (in €) correspond to the investment, operation and maintenance (OM), replacement and salvage costs referred to the i-th component for the j-th year. Investment costs are performed at the beginning of the analysis period (i.e., j=0). The replacement cost of a certain i-th component is accounted for at the end of its lifetime (and no replacement is allowed at L_{PR} year). As described by Eq. (2.82), it was assumed the salvage cost to occur at the end of the project lifetime (i.e., j=L_{PR}). $N_{c,tot}$ is total number of components that belong to the energy system, whereas $N_{c,rep,tot}$ refers to the components that could need replacement over the lifetime of the project (i.e., battery, electrolyzer, fuel cell and diesel generator devices).

The annual cost related to operation and maintenance of the i-th component comprises of a variable and/or fixed term as described by Eq. (2.83). The variable contributor ($C_{OM,var,i}$) was considered for the fuel cell, electrolyzer and diesel generator.

$$C_{OM,i} = C_{OM,fix,i} + C_{OM,var,i} \quad (2.83)$$

The salvage value represents the economic value of a component at the end of the analysis period and it was supposed to be directly proportional to its remaining life. This term was considered for components that are potentially subject to replacement and was computed as follows:

$$C_{sal,i} = C_{rep,i} \frac{L_{rem,i}}{L_i} \tag{2.84}$$

where L_i (in years) is the component lifetime and $L_{rem,i}$ (in years) is the remaining component lifetime at the end of the project period. This last term was defined as (for $L_i \neq L_{PR}$):

$$L_{rem,i} = L_i - \left[L_{PR} - L_i \cdot INT\left(\frac{L_{PR}}{L_i}\right)\right] \tag{2.85}$$

where INT is a function that returns the integer amount of a real number. $L_{rem,i}$ is zero if L_i is equal to L_{PR}.

2.3.2 Economic input data

Main economic parameters required as input for the economic analysis of the hybrid renewable energy system are listed in Table 2.19 to Table 2.23, distinguished between RES generators, battery, H_2-based storage system, diesel generator and other general assumptions. Overall, the costs that have been adopted are also in line with the REMOTE partners' knowledge.

Since the cost of H_2-based devices is highly size-dependent, scale dependencies of costs have been considered for both the electrolyzer and fuel cell systems. In order to evaluate the effect of capacity on purchased equipment cost, a power function in the following form was employed (with i = EL, FC):

$$c_{inv,i} = \left(\frac{S_i}{S_{ref,i}}\right)^{n_i} \frac{c_{inv,ref,i}\, S_{ref,i}}{S_i} \tag{2.86}$$

where $c_{inv,i}$ (in €/kW) represents the specific investment cost of the component, whose size is S_i (in kW). The term $c_{inv,ref,i}$ (in €/kW) corresponds instead to the specific investment cost of the same equipment with reference size $S_{ref,i}$ (in kW). The term n_i stands for the cost exponent of the power function. The values adopted for these parameters are reported in Table 2.20. Concerning the alkaline electrolyzer, the reference specific investment cost of 2,000 €/kW was taken from [154], considering a reference size of 312 kW. The cost exponent n was set equal to 0.65 to be in agreement with the cost trend reported by Proost [15]. A reference specific cost of 4,600 €/kW for a size of 50 kW with a cost exponent of 0.65 was instead considered for the PEM electrolyzer [15]. The fuel cell specific cost of 3,947 €/kW was taken from [155] considering a reference size of 10 kW. The FC cost exponent n was set equal to 0.7, in agreement with previous studies [18]. The FC cost curve thus obtained is in accordance with data from [47] and [156].

Figure 2.8 reports the specific investment cost as a function of the rated power for alkaline and PEM electrolyzers. The cost functions, derived from Eq. (2.86), agree well with both data from the literature and the REMOTE project. It can be noticed that alkaline systems are currently a little cheaper than the PEM alternative. This is because AWEs still remain the most established and mature technology to perform water electrolysis.

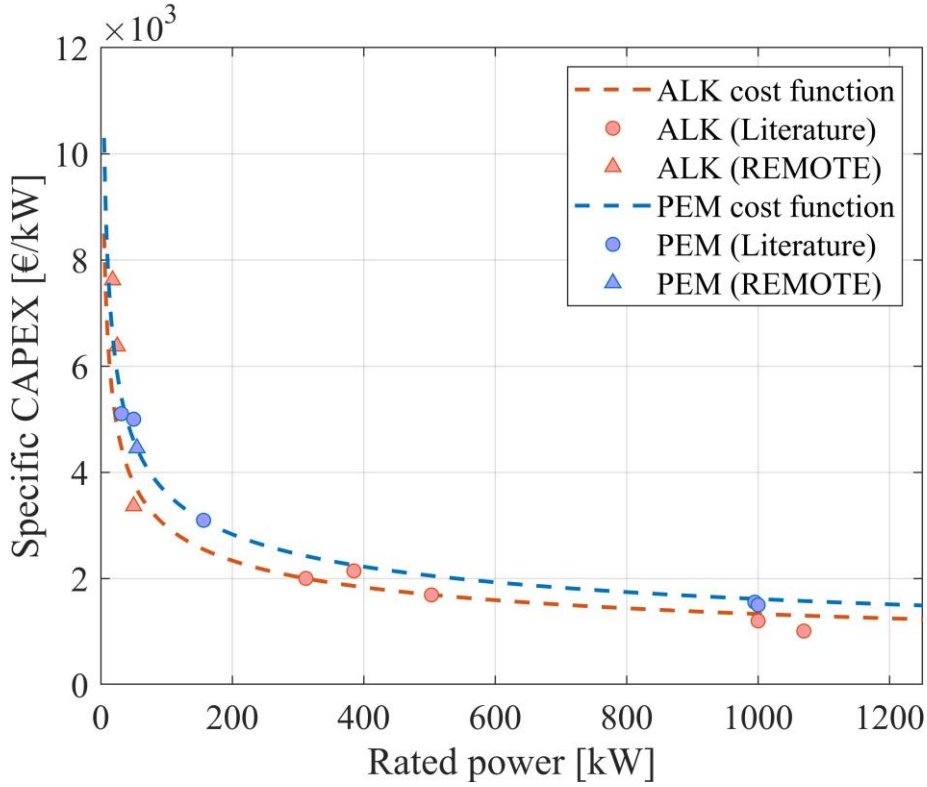

Figure 2.8 Power cost function for the alkaline and PEM electrolyzer: specific CAPEX as a function of the rated power

The OM cost referred to electrolyzer and fuel cell systems is assumed to be 4% of the total system investment cost. It is composed of 1/3 fixed and 2/3 variable contributions, similarly to what reported in Ref. [17]. The variable costs are supposed to be proportional to the EL/FC operating time, as described by the following relationship (with i = EL, FC):

$$c_{OM,var,i} = \frac{2}{3}\,\frac{4}{100}\,\frac{c_{inv,j}}{8760}\,N_{h,yr,i} \tag{2.87}$$

where $c_{OM,var,i}$ (in €/kW/y) corresponds to the annual OM cost per unit of size of the EL/FC component and $N_{h,yr,i}$ is the yearly number of operating hours of the EL/FC (which depend on the simulation).

A variable OM term was also assumed for the diesel generator based on the amount of fuel that is consumed and the number of diesel generator operating hours:

$$C_{OM,var,DG} = \sum_{t=1}^{T} cons_{DG}(t)\, cost_{fuel} + C_{OM,op,h,DG}\, N_{h,yr,DG} \qquad (2.88)$$

where $C_{OM,var,DG}$ (in €/y) is the variable yearly OM cost of DG, $cost_{fuel}$ (in €/L) is the fuel price, $C_{OM,op,h,DG}$ (in €/h) is the hourly OM cost associated to DG operation and $N_{h,yr,DG}$ (in h) is the number of DG operating hours over the reference year. The fuel price is generally high in off-grid remote locations. A value of around 2 €/L was suggested in Refs. [147], [157]. This value was also assumed as a reference in the framework of the REMOTE project [32]. Alberizzi *et al.* [157] reported the fuel price to vary from approximately 1.4 €/L up to 3 €/L in remote areas. A 2 €/L price was hence considered in the present work.

Lifetimes of all components of the stand-alone energy system must be known for a proper evaluation of the replacement and salvage costs. RES generators (except the biomass generator) and the H_2 storage tank were assumed to have a lifetime equal to the project duration, which means that they do not need to be replaced. In the literature, lifetimes of components that are potentially subject to replacement (i.e., battery, electrolyzer, fuel cell and diesel generator) are often treated as values known a-priori and imposed as input data of the techno-economic analysis. In the present work they were instead derived according to how they operate along the reference year.

The battery life was evaluated by computing the total amount of energy that can flow throughout it, i.e., the lifetime throughput (LT). This parameter was estimated starting from the lifetime curve, which is provided by the battery manufacturer. The curve shows different depth-of-discharge (DOD) values and the related cycles-to-failure (CTF). The lifetime throughput was obtained as [158]:

$$LT = \sum_{i=1}^{n} \frac{2\, Cap_{BT}\, DOD_i\, CTF_i}{n} \qquad (2.89)$$

where DOD_i and CTF_i correspond to the DOD and CTF values of the i-th point of the lifetime curve, respectively and the term n stands for the number of points in the lifetime curve. The battery lifetime was then assessed as:

$$L_{BT} = min\left(\frac{LT}{AT}, L_{PR}\right) \qquad (2.90)$$

where AT (in kWh) is the annual throughput and represents the energy flowing throughout the battery over the reference year. It was evaluated at the end of the yearly time horizon in the following way:

$$AT = \sum_{t=1}^{8760} \left(P_{BT,ch}(t)\, \eta_{BT,ch}\, \eta_{conv} + \frac{P_{BT,dc}(t)}{\eta_{BT,dc}\ \eta_{conv}} \right) \tag{2.91}$$

Concerning Li-ion batteries, data for the lifetime throughput evaluation were taken from Zia *et al*. [159] and are shown in Table 2.16. They are in accordance with what reported by Few *et al.* [160], who stated around 2,500 cycles at 80% DOD, and May *et al.* [161]. Lifetime curve values for the lead acid battery, from Bordin *et al.* [158], are instead displayed in Table 2.17.

Table 2.16 Li-ion battery: Cycles to failure versus depth-of-discharge

Depth of discharge (%)	Cycles to failure
50	5,000
70	3,000
80	2,500

Table 2.17 Lead-acid battery: Cycles to failure versus depth-of-discharge

Depth of discharge (%)	Cycles to failure
10	5,700
25	2,100
35	1,470
50	1,000
60	830
70	700
80	600

The electrolyzer stack replacement is usually planned when the energy efficiency drops to 90% of its initial nominal value [17]. The same considerations are also valid for the fuel cell stack [162]. Referring to the electrolyzer, the total amount of working hours was computed by considering the efficiency degradation over time with continuous operation. By supposing an efficiency degradation of 0.13%/1,000h for the PEMWE and 0.25%/1,000h for the AWE [17] and imposing the stack replacement when efficiency goes below 90% of its initial value, the

total amount of operating hours is around 80,000 and 40,000 hours for the alkaline and PEM stacks, respectively. A value of 30,000 hours was instead supposed for the PEM fuel cell stack lifetime [130], [140]. As well as by the number of working hours of continuous operation, the EL/FC lifetime is also affected by the number of start-ups. A value of 5,000 on/off switching cycles was reported by Santos *et al.* [163] for the PEM electrolyzer. The alkaline device is instead reported to tolerate around 5,000 to 10,000 start/stop cycles [77]. A value of 7,500 cycles was then taken as an average in the present study. Finally, referring to the PEM fuel cell, Torreglosa *et al.* [164] stated that an FC start-up corresponds to approximately 3 working hours in continuous operation.

The lifetime of the electrolyzer and the fuel cell was computed based on the effective number of operating hours and start-ups occurring during the year according to the simulation. The following formula was adopted (with i = EL, FC):

$$L_i = min\left(\left(\frac{N_{h,yr,i}}{N_{h,tot,i}} + \frac{N_{st,yr,i}}{N_{st,tot,i}}\right)^{-1}, L_{PR}\right) \tag{2.92}$$

where $N_{h,tot,i}$ and $N_{st,tot,i}$ represent the total amount of working hours and start-ups of the EL/FC component during its lifetime, respectively. The terms $N_{h,yr,i}$ and $N_{st,yr,i}$ correspond to the number of working hours and start-ups of the EL/FC occurring during the yearly simulation, respectively. Parameters that are required for the lifetime estimation are summed up in Table 2.18.

Table 2.18 Parameters for the estimation of the electrolyzer and fuel cell lifetime

Parameter	Alkaline electrolyzer	PEM electrolyzer	PEM fuel cell
$N_{h,tot}$	76,923 h [17]	40,000 h [17]	30,000 [130], [140]
$N_{st,tot}$	7,500 [77]	5,000 [163]	10,000 [164]

Concerning the diesel generator, its lifetime was determined based the total amount of DG working hours ($N_{h,tot,DG}$) and the number of DG yearly working hours ($N_{h,yr,DG}$) as follows:

$$L_{DG} = min\left(\frac{N_{h,tot,DG}}{N_{h,yr,DG}}, L_{PR}\right) \tag{2.93}$$

As shown in Eqs. (2.90), (2.92) and (2.93), the lifetime of the battery, H_2-based components and diesel generator is set equal to L_{PR} if the computed lifespan value is higher than the duration of the project.

Table 2.19 Economic input parameters for the RES generators

PV power plant		
Investment cost	1,547 €/kW	[32]
Replacement cost[a]	-	
OM fixed costs (% of Inv. cost)	24 €/kW/y	[32]
Wind power plant		
Investment cost	1,175 €/kW	[165]
Replacement cost[a]	-	
OM fixed costs (% of Inv. cost)	3%/y	[32]
Hydro power plant		
Investment cost[b]	-	
Replacement cost[a]	-	
OM fixed costs	20,000 €/y	[32]
Biomass generator		
Investment cost	6316 €/kW	[32]
Replacement cost	245 €/kW (3 y)[c]	[32]
OM variable costs	5.28 €/h[d] + 0.0333 €/kWh	[32]

[a] Replacement cost is null since its lifetime is set equal to the project lifetime
[b] Hydro power is already existing in the demo site (Agkistro demo)
[c] Replacement cost (every 3 years) referred to the reformer and motor component
[d] OM cost referred to the biomass consumption

Table 2.20 Economic input parameters for the hydrogen-based storage system

Alkaline electrolyzer		
Ref. specific investment cost, $c_{inv,ref}$	2000 €/kW	[154]
Ref. rated size, $P_{rated,ref}$	312 kW	[154]
Cost exponent, n_{inv}	0.65	
Replacement cost (% of Inv. Cost)	26.7%	[163], [166]
OM fixed costs (% of Inv. Cost)	1/3·4%/y	[17]
OM variable costs (% of Inv. Cost)	2/3·4%/y	[17]
PEM electrolyzer		
Ref. specific investment cost, $c_{inv,ref}$	4,600 €/kW	[15]
Ref. rated size, $P_{rated,ref}$	50 kW	[15]
Cost exponent, n_{inv}	0.65	[15]
Replacement cost (% of Inv. Cost)	26.7%	[163], [166]
OM fixed costs (% of Inv. Cost)	1/3·4%/y	[17]
OM variable costs (% of Inv. Cost)	2/3·4%/y	[17]
PEM fuel cell		
Ref. specific investment cost, $c_{inv,ref}$	3,947 €/kW	[155]
Ref. rated size, $P_{rated,ref}$	10 kW	[155]
Cost exponent, n_{inv}	0.7	[18]
Replacement cost (% of Inv. Cost)	26.7%	[163], [166]
OM fixed costs (% of Inv. Cost)	1/3·4%/y	[17]
OM variable costs (% of Inv. Cost)	2/3·4%/y	[17]
Hydrogen tank		
Investment cost	470 €/kg	[17]
Replacement cost[a]	-	
OM fixed costs	2%/y (of Inv. cost)	[17]

[a] Replacement cost is null since its lifetime is set equal to the project lifetime

Table 2.21 Economic input parameters for the battery system

Li-ion battery		
Investment cost (system)	550 €/kWh	[32][47]
Replacement cost (% of Inv. cost)	50%	[167]
OM fixed costs	10 €/kWh/y	[31]
Lead-acid battery		
Investment cost (system)	250 €/kWh	[167]
Replacement cost (% of Inv. cost)	50%	[168]
OM fixed costs	7€/kWh/y	[31]

Table 2.22 Economic input parameters for the diesel generator

Diesel generator		
Investment cost	420 €/kW	[47]
Replacement cost	420 €/kW	[47]
OM variable costs, $C_{OM,op,h,DG}$	0.4 €/h	[47]
Fuel cost, $cost_{fuel}$	2 €/L (Ref. case)	[32]

Table 2.23 Other general assumptions

Other general assumptions		
Nominal discount rate (d')	7%	[32]
Inflation rate (ir)	2%	[32]
Project lifetime (L_{PR})	20 years	

Chapter 3

Techno-economic analysis of H_2-based energy systems in remote areas

The aim of Chapter 3 is to show the effectiveness of H_2-battery power-to-power (P2P) solutions in reducing the use of fossil fuels or the need for grid connections in a cost-effective way under different load and environment conditions. Four different case studies, defined in the framework of the REMOTE project [36], have been analysed. For each site, the innovative renewable configuration was compared with an alternative option. The economic viability of the considered scenarios was outlined by computing the net present cost (NPC) and the related levelized cost of energy (LCOE). The mathematical modelling of each component and the main techno-economic input data and assumptions are reported in Chapter 2. Energy management strategies were also developed to address the operation of the entire system and perform energy simulations on a yearly basis.

3.1 Introduction

Electrical energy storage solutions are necessary for off-grid energy systems to optimize the exploitation of local renewable energy sources (RESs) and achieve higher RES penetration levels. Stationary batteries are generally used to store energy on daily basis. However, when the energy storage is required for a longer period, batteries become expensive and their integration with H_2-P2P systems with medium/long-term capabilities can be a viable and reliable option [44]. The combination of hydrogen and batteries for storage purposes has been widely analysed in the literature, showing great potential in providing power source to customers in a reliable and sustainable manner [169]. The research on such kind

of hybrid storage systems is mainly addressed to their optimal design with the aim of achieving the minimum system cost [170]–[172]. Environmental objectives (e.g., reducing CO_2 emissions) can be also considered in the sizing problem [149], [173], [174]. The adoption of a proper energy management strategy (EMS) is essential for a correct interaction of the various sub-systems to achieve good energy and economic performances [175]. However, the task is challenging because of the high number of technologies to be integrated (i.e., RES power systems, battery and hydrogen-based devices). Vivas *et al.* [56] and Olatomiwa *et al.* [176] presented a comprehensive review about EMSs for renewable hybrid energy systems with the latter focusing in particular on hydrogen technologies. The main objectives of a control strategy can be summarized as follows [177]:

- Reliable coverage of the electricity loads.
- Ensuring that the system components work under optimal conditions, avoiding their operation outside safe and inefficient working ranges.
- Optimising the average roundtrip efficiency over the year.

The fluctuating behaviour of most RESs (e.g., wind and solar) causes variability in the power production that must be properly faced. Recurrent changes in the operation of the fuel cell and electrolyzer components should be avoided to limit their performance degradation and preserve their lifetime. A battery bank becomes thus useful as an instantaneous and daily energy buffer, smoothing down the RES high-frequency variability [178]. However, the battery device should be protected from heavy utilization, avoiding excessive charging/discharging in order not to negatively affect its life span. EMSs are therefore necessary to operate the various P2P subsystems properly and safely, while satisfying the load requirements. Rule-based strategies (RBSs) are often employed when simulating the microgrid operation [56]. In fact, they are practical, effective and easy to implement and operate [141], [179]. RBSs control the operation of the system based on its actual status. Alternative strategies may rely on predictive methodologies, e.g., by means of model predictive control (MPC) approaches, in which a forecast of supply and load profiles is applied to evaluate the optimal schedule of the system [180], [181].

Concerning RBSs, priority of intervention is usually given to the route with higher transmission efficiency for the energy flow in order to keep the efficiency of the system operation as high as possible [177]. To this aim, a typical hierarchy consists of using the battery and then the hydrogen pathway, i.e., electrolyzer and fuel cell [178], [182]–[184]. The net power, the battery state-of-charge (SOC) and the hydrogen level are the main key decision factor of the EMS [185]. Following a ruled-based approach, a set of predetermined rules is here defined and used for the techno-economic analysis of the REMOTE HRESs. These strategies will be then employed in Chapter 3 to deal with the optimal design of off-grid energy systems by means of a metaheuristic-based approach. In fact, as will be explained,

priority rules are very suitable to be implemented in two-layers (TL) frameworks to optimally size HRESs with the use of metaheuristic algorithms.

To our knowledge, no literature exists that comprehensively assess H_2-battery energy storage systems in different kinds of remote locations in Europe, from alpine to insular, with different typologies of local renewable energy sources and loads. The assessment also takes advantage of unique data and information provided or verified directly by international technology developers and end-user actors. The present analysis can hence be helpful to give a wider and more complete insight into the feasibility of these kinds of systems in micro grid environments.

3.2 Specifications of the REMOTE case studies

The case studies under analysis are characterized by different typologies of RESs (i.e., solar, wind, biomass, and hydro) and user loads (i.e., residential and small industrial), which will affect differently the design and management of the P2P system. A summary of the main components involved in the REMOTE solution is reported in Table 3.1 for all the four sites.

REMOTE will install and demonstrate a total power output (from fuel cell) of at least 250 kW. The storage system that is proposed in the project consists of a hybrid configuration based on electrolysers (both alkaline and PEM technology) for the conversion of RES electricity into hydrogen and PEM fuel cells for electricity generation, including also Li-ion batteries to ensure both short- and long-term storage. A detailed description of the various case studies (including data about RESs, load and technical features of the different components) is provided in the next sections.

Table 3.1 Components of the renewable battery/hydrogen system for the REMOTE case studies.

		1. Ginostra (Italy)	**2. Agkistro** (Greece)	**3. Ambornetti** (Italy)	**4. Froan** (Norway)
RES	Typology	PV	Hydro	PV + Bio	PV + Wind
	Size	170 kW	0.9 MW	75 kW PV 49 kW Bio	250 kW PV 675 kW Wind
P2P	Typology	Integrated	Integrated	Non-integrated	Non-integrated
	Supplier	ENGIE-EPS	ENGIE-EPS	BPSE, ENGIE-EPS	HYG, BPSE, POW
	P2G				
	Technology	Alkaline	Alkaline	Alkaline	PEM
	Rated Power	50 kW	25 kW	18 kW	55 kW
	G2P				
	Technology	PEM	PEM	PEM	PEM
	Rated Power	50 kW	50 kW	85 kW	100 kW
	H_2 storage				
	Gross energy (LHV)	1793 kWh	996 kWh	498 kWh	3333 kWh
	Battery				
	Technology	Li-ion	Li-ion	Li-ion	Li-ion
	Rated energy	600 kWh	92 kWh	92 kWh	550 kWh

3.2.1 Ginostra

Ginostra is a village on the island of Stromboli in southern Italy. The site is classified as off-grid since not connected to neither the Italian distribution and transmission grid nor the main Stromboli island micro-grid. All loads are residential and currently satisfied by employing diesel-based power generators. Because of the remoteness of the area, the fuel has to be transported in by helicopter leading to high costs for electricity generation. Enel Green Power (EGP) [186] is the final user of Ginostra site. The current diesel-based and REMOTE solutions are depicted in Figure 3.1. Main drivers to move to the renewable hydrogen-battery system can be summed up as follows:

1. Reducing current diesel consumption to lower the cost of electricity production and decrease the local pollution.
2. Enhancing the reliability of the electricity service.

3. Avoiding prohibitively high costs due to grid connection.
4. Gaining experience from the P2P operation to replicate in other European islands.

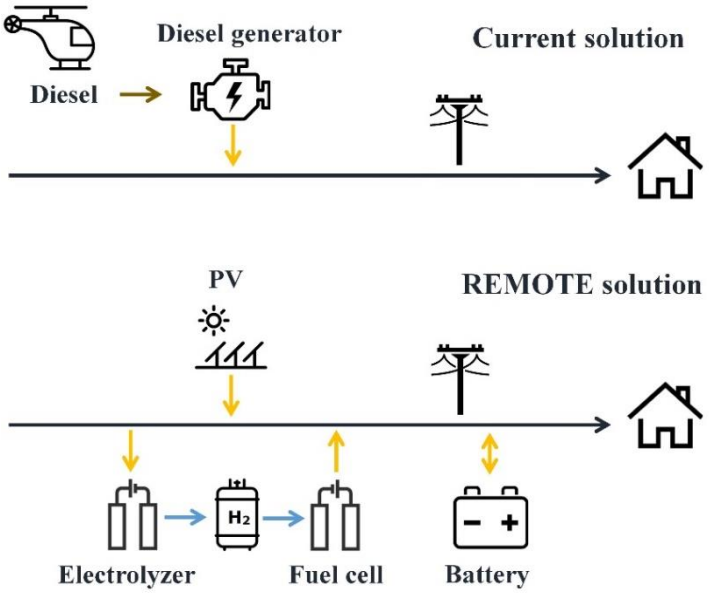

Figure 3.1 The current (diesel only) and suggested (renewable P2P) solutions for Ginostra.

Meteorological and load data for the Ginostra site, namely the hourly profiles over the year of the ambient temperature (in °C), solar irradiance on the PV plane (in kW/m^2), wind velocity (in m/s) and electrical demand (in kW), are displayed in Figure 3.2. PVGIS tool was used to evaluate the meteorological data, referring to a typical meteorological year (TMY) [135]. The island is characterized by a large availability of the solar source, whereas wind potential is scarce, as evidenced by the low wind velocity values. Hourly electrical load data were taken from [32]. The load profile exhibits relevant seasonal variation with a summer peak slightly higher than 60 kW in August. This is mainly due to summer tourism, which causes the number of inhabitants to increase up to about 200 people during summertime (the village counts only 40 people living there throughout all the year). Thus, an effective EES solution needs to be integrated to cope with the variability of RESs and the seasonal behaviour of the electrical load.

Main technical specifications of the proposed renewable battery-H_2 system are set out below. Regarding the RES power plant, a 170 kW PV system from EGP was chosen. The hybrid energy storage system includes a 600 kWh Li-ion battery bank from EGP and an integrated hydrogen-based solution from Engie-Electro Power System (EPS) [187]. More specifically, the H_2 system is composed of a 50 kW alkaline electrolyzer, a 50 kW PEM fuel cell (i.e., two 25 kW P2P modules) and a hydrogen storage with total capacity of 21.6 m^3. Two 48 kW diesel generators will be maintained as a final back-up unit.

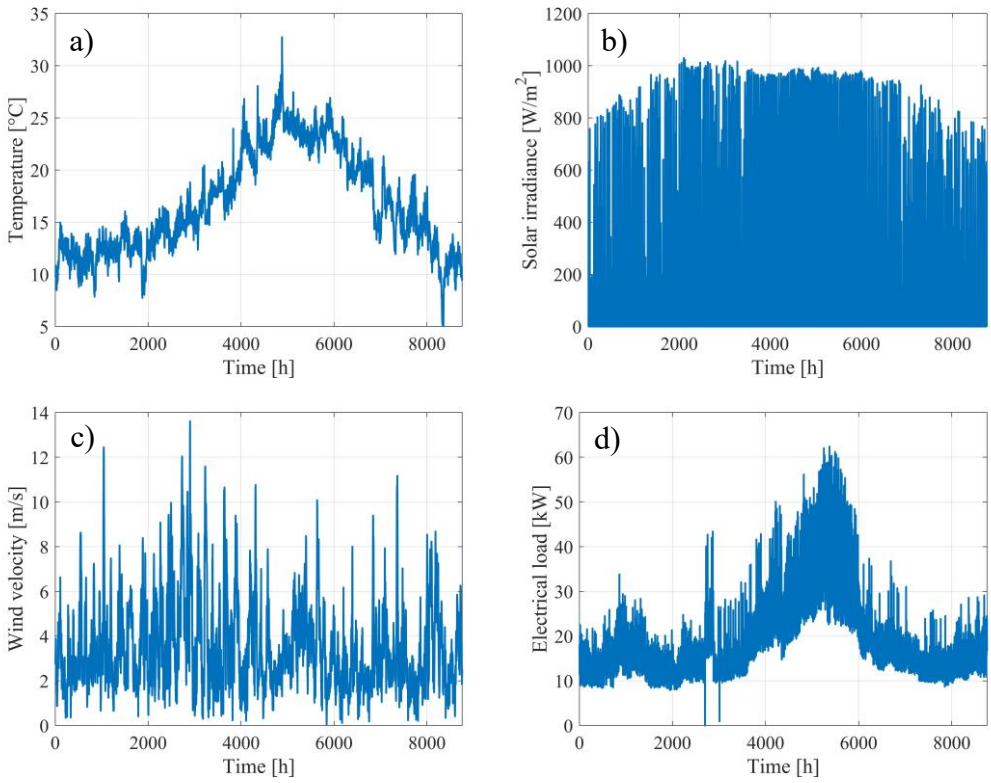

Figure 3.2 Meteorological and load data for the Ginostra site: ambient temperature (a), total solar irradiance (b), wind velocity at 10 m ref. height (c), and electrical load (d) in hourly resolution.

Main results on yearly basis from the analysis of RES supply and load data are summarized in Table 3.2. Monthly distribution of RES, load, deficit and surplus energy quantities are displayed in Figure 3.3.

Table 3.2 Load and RES (PV) supply data on yearly basis in Ginostra.

Energy parameter	**Value**
Total load	171.54 MWh
RES production	262.58 MWh
Direct RES consumption	76.43 MWh
RES surplus	186.15 MWh
Deficit	95.11 MWh

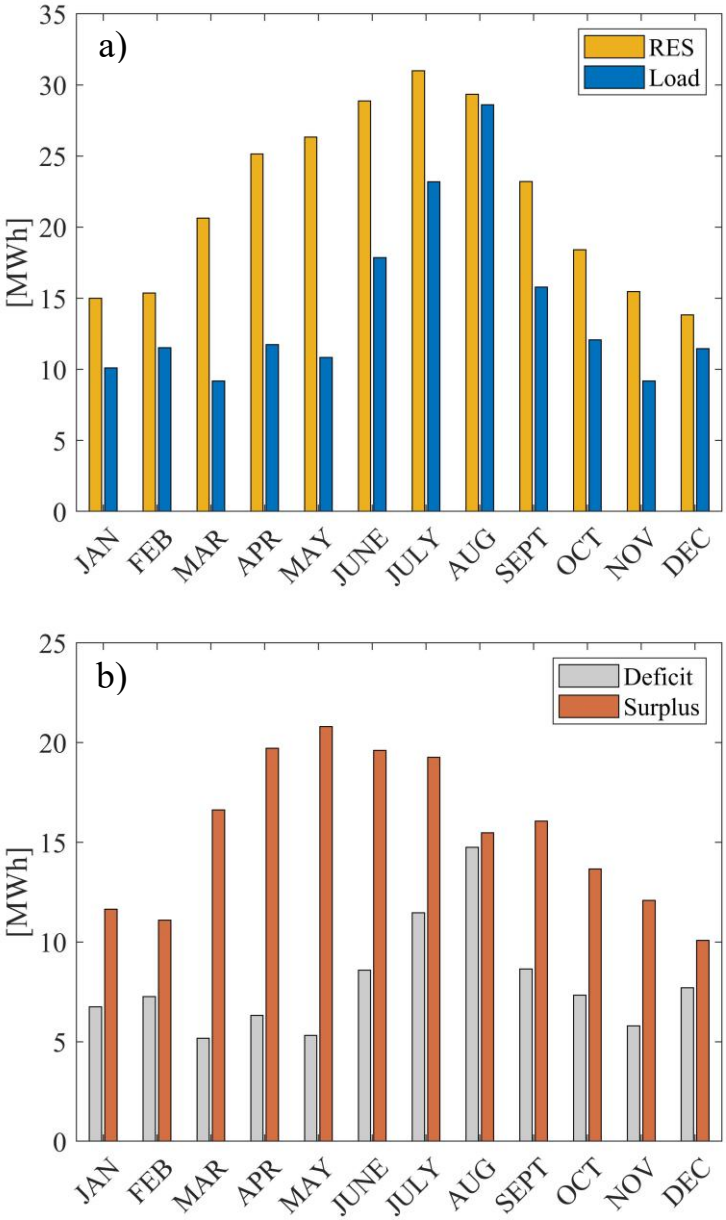

Figure 3.3 Ginostra: a) monthly distribution of RES production (170 kW PV) and load; b) monthly distribution of surplus and deficit.

The total annual electrical load, which is currently covered by diesel generators, is around 172 MWh. The proposed PV power plant is estimated to produce about 263 MWh/year. It can be noticed that less than one third of the overall annual energy from PV (about 76 MWh) can be directly consumed by the load. An energy storage system is therefore required to maximize the exploitation of local RES and consequently minimize the intervention of diesel generators. Surplus renewable energy should be stored in the hybrid battery-hydrogen system to be used later when the PV system is not able alone to satisfy all the load. Figure

3.3b suggests that the high amount of excess solar energy during spring could be stored and employed later in the summer to face the load increase because of tourism. This could be performed by taking advantage of the long-term energy storage capability of hydrogen.

3.2.2 Agkistro

Agkistro is a remote village in the Serres region, in North Greece close to Bulgaria. A hydroelectric plant, owned by Horizon SA (HOR) [188], is located near the demo site and is connected to the grid to sell the produced electricity. HOR company, which is the end user, is going to build an agri-food processing unit very close to its power plant. In order to connect the new facility to the grid, the company should create a separate line directly to a transformer 20 km away since the local one is full. In this grid-based scenario, besides the expensive and invasive works due to the connection, the company would buy electricity from the grid at a price higher than the value of the sold hydropower energy. The aim is therefore to make the new processing unit energy autonomous, avoiding the grid connection and relying only on the hydro plant and on the H_2-based P2P storage as a back-up system, as displayed in Figure 3.4. Main drivers to move to this solution are summarized below:

1. Avoiding the high expenses due to grid connection works.
2. Improving the electrical supply reliability avoiding grid-related problems, i.e., instability and frequent outages due to the site remoteness.
3. Avoiding buying electricity from the grid at high prices.
4. Gaining experience in the P2P storage solution for the replication in other remote areas.

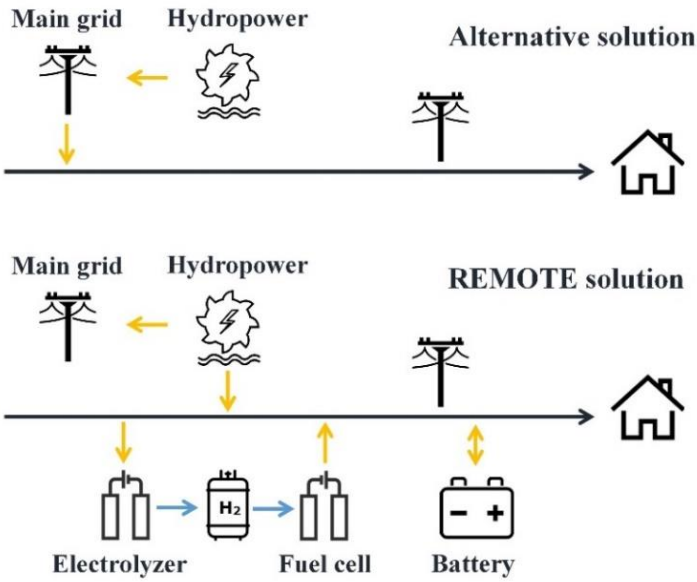

Figure 3.4 Alternative (grid connection) and suggested (renewable P2P) solutions for Agkistro.

The hydroelectric plant has a total capacity of 0.9 MW (with two turbines of 0.65 and 0.25 MW, respectively). Currently, it provides electricity to the main grid. From now on, the power plant will be also employed to directly feed the agri-food building with electricity. Similarly to the Ginostra site, an integrated P2P system delivered by Engie-EPS is adopted. The hybrid storage solution includes a 92 kWh Li-ion battery bank, an alkaline electrolyzer of 25 kW, an PEM fuel cell of 50 kW and a 12 m^3 H_2 storage tank. An oxygen vessel with total capacity of 6 m^3 will be also installed to power the O_2-fed fuel cell. The minimum available electrolyzer size from the manufacturer, i.e., 25 kW, was chosen since the site benefits from continuous availability of renewable source (hydro plant). Two fuel cell units (25 kW each) were instead considered for the G2P section in order to cover the highest load request occurring over the year, which is around 40 kW. Considering that the electrical load demand is approximately 193 kWh/day for a reference working day, the chosen H_2 storage capacity can guarantee backup energy for roughly two days and a half.

Since the hydro plant works all year-round providing electricity to the main grid, RES electricity production is much higher than the load of the agri-food unit, as graphically reported in Figure 3.6. Referring to a medium year, the total annual production from the hydroelectric plant is in fact around 3739 MWh, whereas the total yearly electrical energy required by the new facility is estimated to be only 51 MWh. Load profiles for a typical working and non-working day are shown in Figure 3.5. There are changes in electricity consumption over the year due to the seasonal use of some mechanical equipment (e.g., drying of herbs performed is specific periods of the year) and the summer cooling and winter heating needs. In a framework with high RES electricity generation and quite predictable and stable electrical demand, the P2P system is thus conceived as a backup unit in case of emergency or scheduled hydro plant downtime due to maintenance.

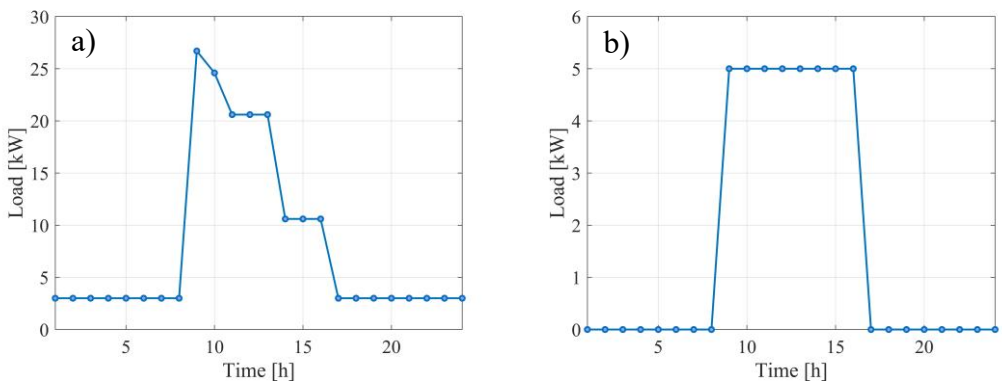

Figure 3.5 Load profiles for a typical working (a) and non-working (b) day in Agkistro site.

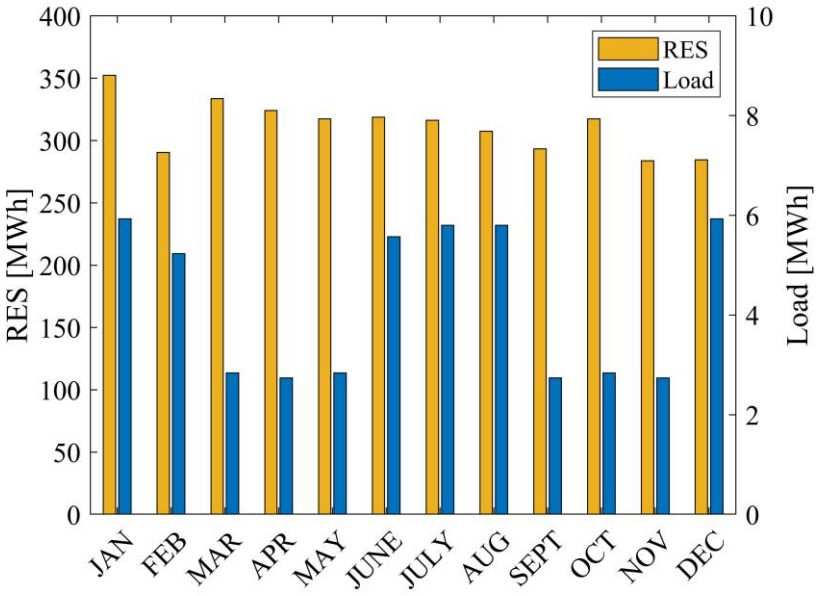

Figure 3.6 Agkistro: monthly distribution of RES production (0.9 MW hydro) and load.

3.2.3 Ambornetti

Ambornetti is a mountain hamlet located in North Italy, Piedmont. The goal is to turn this rural area into an energy autonomous community with neutral impact to the environment, in the framework of a renovation project funded by local private investors including IRIS company [189]. The new resort will host 23 rooms, an SPA, a restaurant and a coworking and conference room. The connection to the power grid would cause significant and unaffordable investments, being the nearest point of access 400 m below. Moreover, since the site is located in a protected natural area, the use of diesel generators is not recommended. The REMOTE and diesel-based options are outlined in Figure 3.7. Main drivers and advantages derived from adopting the PV/biomass + P2P solution are:

1. Minimizing the overall lifecycle impact based on the renovation project aim.
2. Avoiding expensive and invasive works and infrastructures for connection to the grid.
3. Avoiding the employment of traditional fossil fuel generators.
4. Gaining experience in the P2P storage solution for potential replication in other Alpine areas.

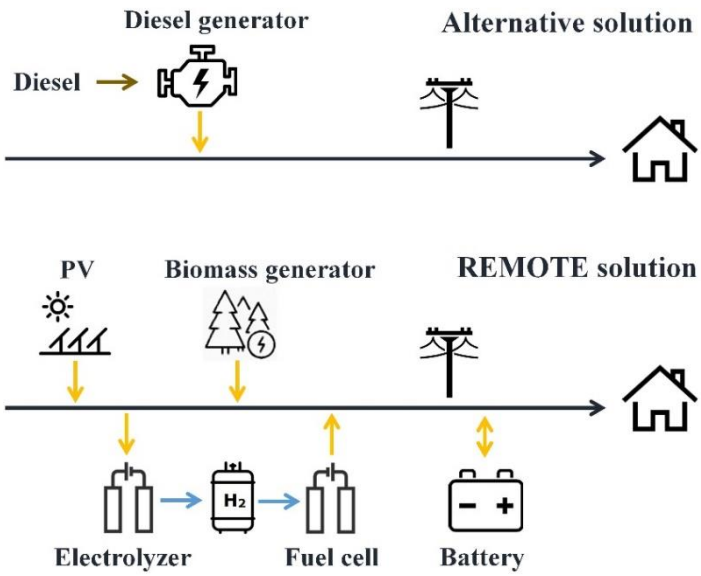

Figure 3.7 Alternative (diesel only) and suggested (renewable P2P) solutions for Ambornetti.

Meteorological and load data for the Ambornetti site are shown in Figure 3.8. Temperature, solar irradiance and wind velocity profiles are referred to a typical meteorological year [135]. Concerning the electricity consumption, reference daily load profiles for each month of the year were provided by IRIS. It can be observed that there are no relevant variations in the electrical load demand over the year (Figure 3.8d).

Referring to the electrical production from local RES, a 75 kW PV power plant and a 49 kW biomass generator (BG) [190] were selected to provide electricity to the off-grid community (wind turbines were not considered because of the scarce availability of wind source in the selected site, as displayed in Figure 3.8c). The biomass system is able to work up to around 8500 hours per year, providing a constant net electrical power of 41 kW (49 kW in total, of which 8 kW are self-consumed). It is reported that the biomass consumption is about 44 kg per hour. Maintenance of the BG plant is scheduled around every 300 hours. Biomass will be supplied from surrounding forests management and local agricultural waste. Regarding the storage system, a 18 kW alkaline electrolyzer from Engie-EPS and a 85 kW air-fed PEM fuel cell from BPSE were considered. The hydrogen tank has a volume of 6 m^3. Li-ion batteries with a total storage capacity of 92 kWh were also selected to store surplus renewable energy.

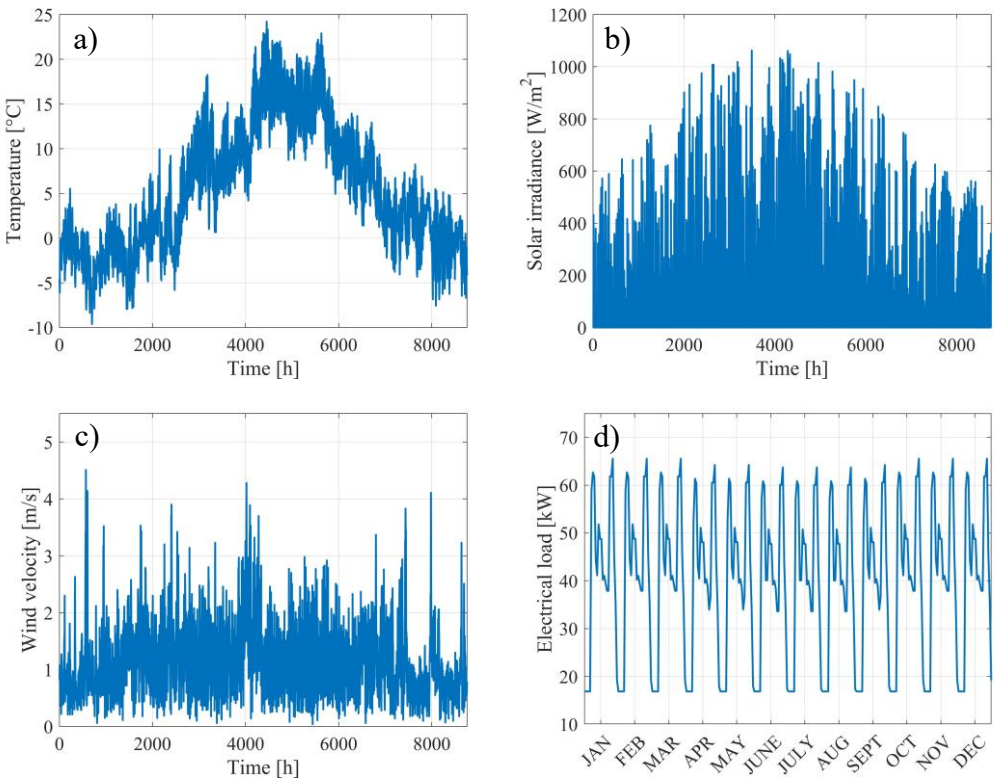

Figure 3.8 Meteorological and load data for the Ambornetti site: ambient temperature (a), total solar irradiance (b), wind velocity at 10 m ref. height (c), and electrical load (d) in hourly resolution.

Load and RES supply data for a reference year in Ambornetti are reported in Table 3.3. Monthly energy values are instead shown in Figure 3.9.

Table 3.3 Load and RES (PV+BG) supply data on yearly basis in Ambornetti.

Energy parameter	**Value**
Total load	348.23 MWh
RES production	420.42 MWh
Direct RES consumption	303.90 MWh
RES surplus	116.52 MWh
Deficit	44.33 MWh

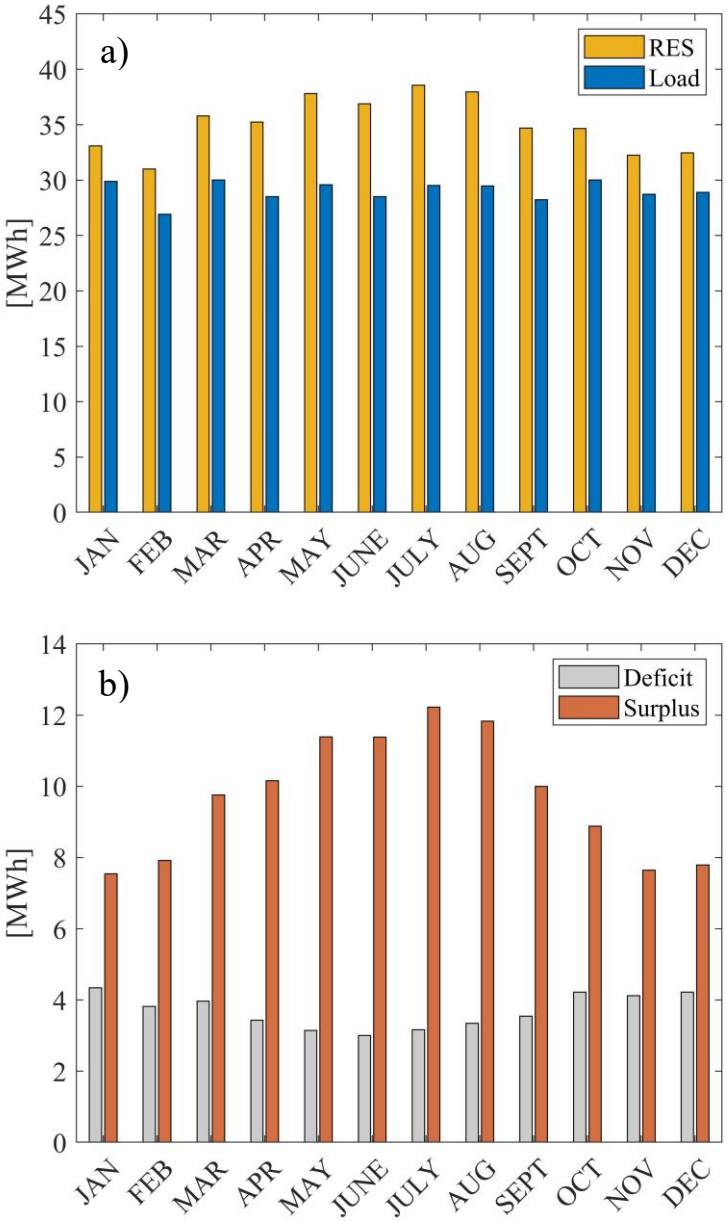

Figure 3.9 Ambornetti: a) monthly distribution of RES production (75 kW PV and 49 kW BG) and load; b) monthly distribution of surplus and deficit.

The annual electrical energy required by Ambornetti site is around 348 MWh. The yearly electrical energy produced by the PV system and by the biomass generator is approximately 76 MWh and 345 MWh, respectively. Most of the load is directly met by RES, mainly thanks to the biomass system, which is able to guarantee an output net power of 41 kW all day long. However, daily load peaks up to around 60 kW (see Figure 3.8d) cannot be met by the BG alone. Solar energy together with proper energy storage solutions are therefore necessary to allow the site to rely exclusively on local renewable sources, making it totally independent from fossil fuels. Moreover, the biomass plant periodically requires

maintenance and needs to be shut down for approximately 10 hours each time. The hybrid energy storage must be able to complement the PV source and make the power supply reliable even in these challenging conditions.

3.2.4 Froan

Norway has a peculiar geography characterized by a large number of islands, many of them located close to the mainland and interconnected to the national grid through sea cables. The outdatedness of subsea connections requires expensive replacements or to consider other alternatives for providing power to the islands. In the REMOTE project, the exploitation of local RESs, i.e., solar and wind, together with a H_2-battery storage system has been considered, as shown in Figure 3.10. Main drivers to prefer this alternative are:

1. Avoiding the high-priced and invasive replacement of the sea cable.
2. Avoiding diesel power generation because of cost and polluting issues.
3. Learning from the H_2-based system operation in a northern climate and evaluating whether to propose it to other remote areas.

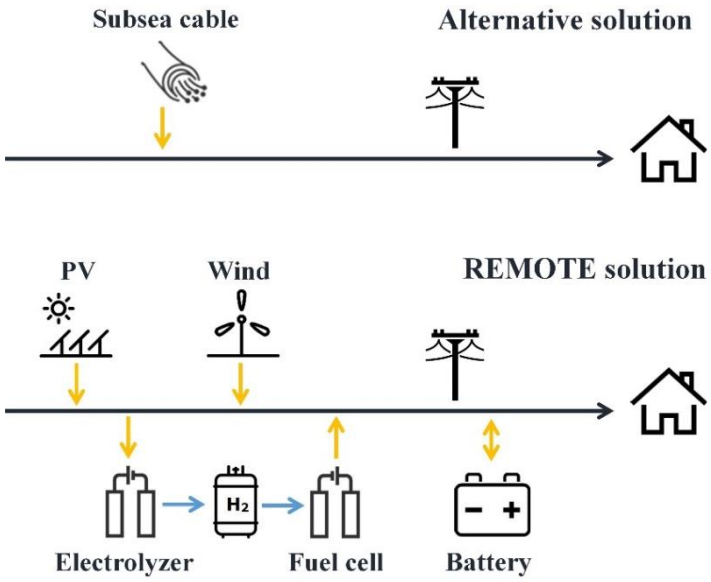

Figure 3.10 Alternative (grid connection by sea cable replacement) and suggested (renewable P2P) solutions for Froan..

As a case study to develop the analysis for Norway, the Froan islands have been selected. Froan is an archipelago of four islands located off the west coast of Norway, near the city of Trondheim. The islands are currently interconnected by electric grid with one connection to the mainland through an outdated sea cable (owned by the company TrønderEnergi [41]) whose expected remaining lifetime

is around 5 years. During the course of the project, the complete P2P system will be validated and tested at Rye, a site located near the city of Trondheim on the mainland, while a suitable island site is in the phase of identification for the future installation of the demo. The Rye site has characteristics similar to the Froan case study in terms of load and installed RESs. The data obtained from the operation in Rye will be thus relevant for a fair comparison with the simulated case study.

Main meteorological and load hourly profiles over a reference year for the Froan islands are reported in Figure 3.11. Temperature, solar irradiance and wind velocity data were taken from PVGIS [135] referring to a TMY, whereas electrical load profiles were provided by TrønderEnergi. Unlike the other sites under analysis, it can be noticed that the Froan islands are characterized by high availability of the wind source. On the other hand, solar energy is scarce in the selected site, which is typical for northern climates. Regarding the load, summer consumption is primarily due to tourism, whereas during winter (where a maximum peak of slightly less than 110 kW occurs) the power consumption is mainly related to heating and, to a lesser extent, to lightning.

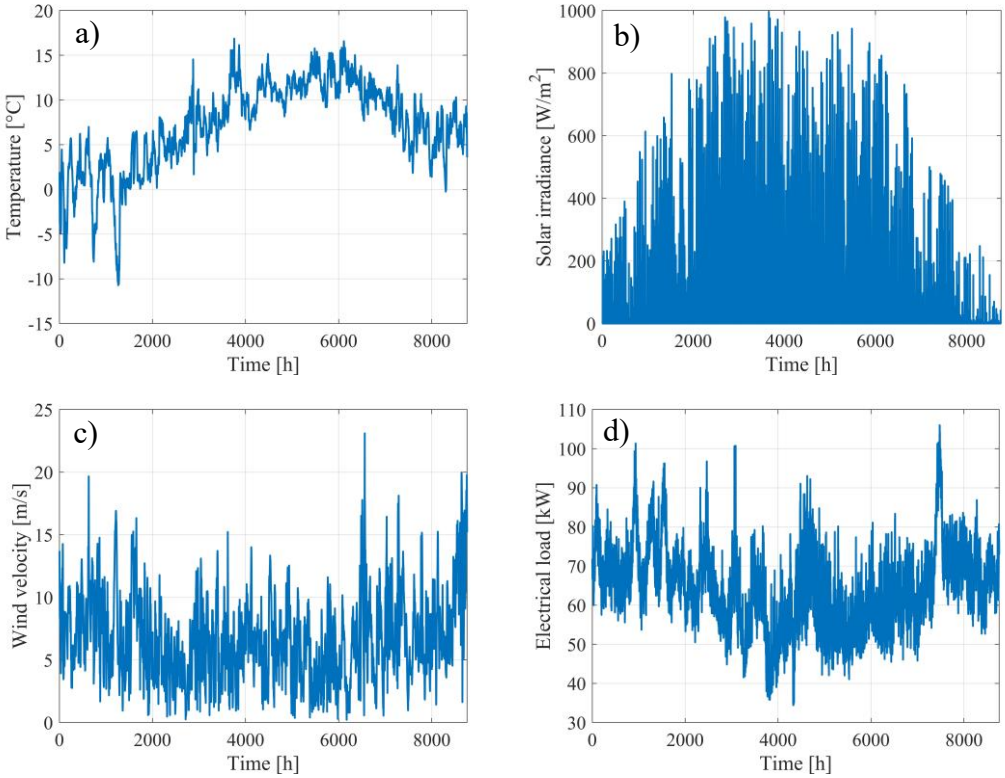

Figure 3.11 Meteorological and load data for the Froan site: ambient temperature (a), total solar irradiance (b), wind velocity at 10 m ref. height (c), and electrical load (d) in hourly resolution.

A combination of PV modules and wind turbines was considered for the Froan site. Three wind turbines of 225 kW each were supposed to be built, together with a 250 kW PV system. Concerning the storage system, a non-

integrated P2P solution, with a 50 kW PEM electrolyzer from Hydrogenics (HYG) and a 100 kW air-fed PEM fuel cell from Ballard Power System Europe (BPSE), was chosen. The hydrogen storage tank has about 100 kg of hydrogen capacity and is provided by Powidian (POW). A Li-ion battery bank, consisting of 5 racks of 110 kWh each, was also adopted as a short term and quick-response storage. The whole system is integrated and managed by POW. A diesel generator with rated power of 100 kW will be also installed as a backup system, but its operation will be limited since the renewable P2P system is expected to cover a high fraction of the electrical load.

Analogously to the other sites, Froan has been investigated in terms of RES supply and load data. Main results on yearly basis are summed up in Table 3.4. In Figure 3.12, the monthly trends of the total RES production, load, energy surplus and deficit are reported. The annual electrical load to be covered is approximately 561 MWh. Around 1315 MWh and 195 MWh were estimated for the wind and solar yearly production, respectively (corresponding to a total annual RES generation of 1510 MWh). The analysis of PV/wind production and load hourly profiles shows that about 445 MWh of the total RES generation are directly used to cover the load. The high amount of surplus renewable energy (accounting for approximately 1065 MWh/year) should be stored through batteries and hydrogen to be later used during the occurrence of energy shortages.

Table 3.4 Load and RES (PV+WT) supply data on yearly basis in Froan.

Energy parameter	**Value**
Total load	561.20 MWh
RES production	1510.14 MWh
Direct RES consumption	445.33 MWh
RES surplus	1064.82 MWh
Deficit	115.88 MWh

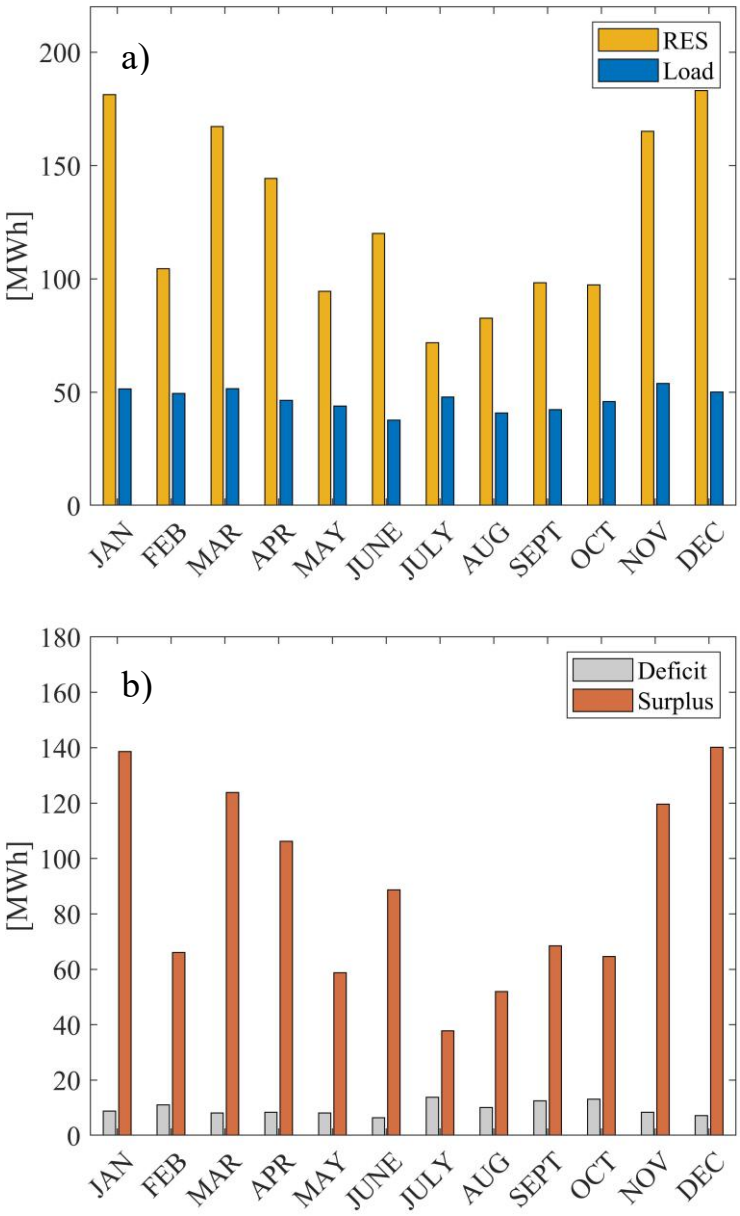

Figure 3.12 Froan: monthly distribution of RES production (250 kW PV and 675 kW WT) and load; b) monthly distribution of surplus and deficit.

3.3 Energy management strategy

An energy management strategy for the off-grid energy system has been defined in order to perform energy simulations and prove the usefulness of the proposed renewable P2P solution in covering the electrical demand. Results will be also helpful for the development of the subsequent economic study.

Local RESs (e.g. solar, wind, biomass and water) are required to meet the load demand of the site. Any surplus of energy can be stored by battery charging

or in the form of hydrogen through water electrolysis. By contrast, any shortage of power can be covered by the discharge of the battery or by the fuel cell operation. Fuel cell and electrolyser devices should be protected from recurrent start-ups and shut-downs, which could accelerate performance degradation and lifetime reduction. The battery component becomes therefore useful to smoothen the high variability of renewable energy sources. However, excessive charging and discharging of the battery should be avoided so as not to negatively affect the battery life span.

The considered control strategy integrates batteries as short-term storage system operating in first instance to absorb/provide electricity when necessary, and hydrogen as longer-term storage medium working when the operating limits of the battery are reached. In the hybrid energy storage system, priority of operation is thus given to the battery component. The state of charge of the battery represents the main control parameter of the EMS. The maximum and minimum battery SOC levels are considered as indicators to evaluate when switching on/off the fuel cell and the electrolyzer. When the SOC lies between its lower and upper boundary, priority is given to the battery component. During charging (RES power higher than the load demand), if the SOC has reached its maximum allowed level, the electrolyzer is activated to convert the surplus renewable energy into hydrogen. By contrast, during discharging (RES power lower than the load demand), the fuel cell is employed to prevent the battery SOC to go below SOC_{min}. Information about the level of hydrogen (LOH) of the storage tank is also required: the electrolyzer can operate until the H_2 container is full and the fuel cell can produce electricity only if enough hydrogen is present. Modulation ranges of electrolyzer and fuel cell need finally to be respected for a correct operation of the system. The following constraints have therefore to be checked by the control strategy:

- SOC limits of the battery
- LOH limits of the hydrogen storage
- modulation ranges of the electrochemical devices

For the sake of clarity, Table 3.5 below reports the main power variables involved in the selected energy management strategy:

Table 3.5 Main variables (in kW) of the selected EMS.

Variable	Description
$P_{BT,ch}(t)$	Charging power of the battery
$P_{BT,dc}(t)$	Discharging power of the battery
$P_{BT,SOC,ch}(t)$	Maximum battery power to not go above SOC_{max}
$P_{BT,SOC,dc}(t)$	Maximum battery power to not go below SOC_{min}
$P_{CT}(t)$	Curtailed power
$P_{DG}(t)$	Diesel generator power
$P_{DG,max}$	Maximum diesel generator power
$P_{DG,min}$	Minimum diesel generator power
$P_{FC}(t)$	Fuel cell power
$P_{FC,LOH}(t)$	Maximum fuel cell power to not go below LOH_{min}
$P_{FC,max}$	Maximum fuel cell power
$P_{FC,min}$	Minimum fuel cell power
$P_{EL}(t)$	Electrolyzer power
$P_{EL,LOH}(t)$	Maximum electrolyzer power to not go above LOH_{max}
$P_{EL,max}$	Maximum electrolyzer power
$P_{EL,min}$	Minimum electrolyzer power
$P_{NS}(t)$	Not satisfied power

Figure 3.13 describes the detailed logical block diagram for the charging case, referring to a fully renewable configuration with hybrid storage (i.e., RES together with both battery and hydrogen). In case the RES electrical power exceeds the demand of the end-user load, the surplus power is first employed to charge the battery. When the maximum battery SOC is reached, surplus electricity is supplied to the electrolyzer for hydrogen production. The electrolyzer, which is operated within its modulation range, works until the storage tank is completely filled with hydrogen (i.e., an LOH value equal to 1 is reached), and the remaining excess RES energy, if present, is curtailed.

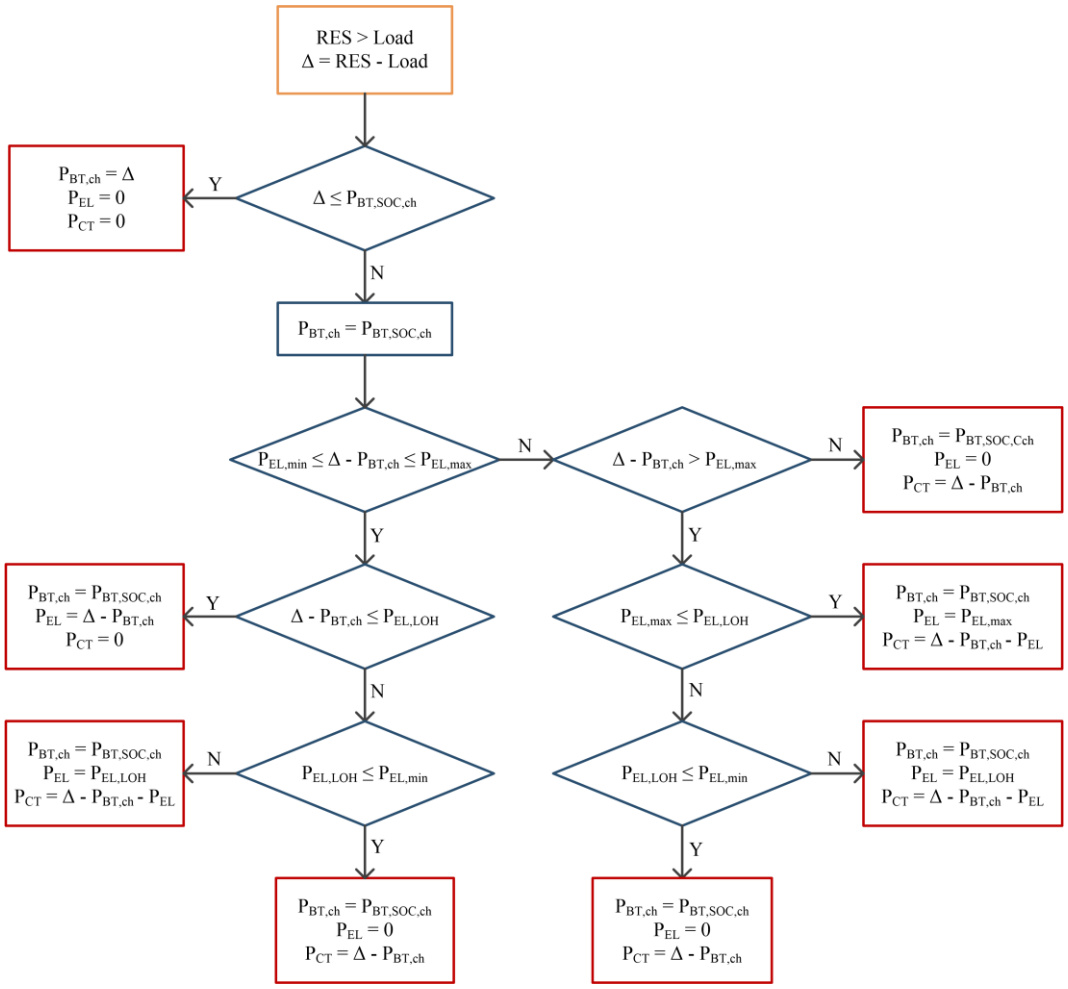

Figure 3.13 Logical block diagram for the charging case (RES supply higher than load demand).

The control strategy for the discharging case of the battery-hydrogen system is shown in Figure 3.14. When the load is higher than the power available from RES, the additional power that is required to cover the load is provided by the battery or the fuel cell depending on the battery SOC value. In case the minimum SOC of the battery is reached, the fuel cell device is activated to meet the power deficit in order to avoid discharging the battery too much. The EMS allows the fuel cell to work between its minimum and maximum operating points ($P_{FC,min}$ and $P_{FC,max}$) if enough hydrogen is present inside the pressurized container. If the electrical load to be covered is lower than the minimum fuel cell power, the fuel cell is imposed to operate at $P_{FC,min}$ (if possible) and the excess FC power (if any) is employed to charge the battery and/or curtailed. Finally, the fraction of the power deficit that cannot be satisfied by both the battery and the fuel cell remains unmet.

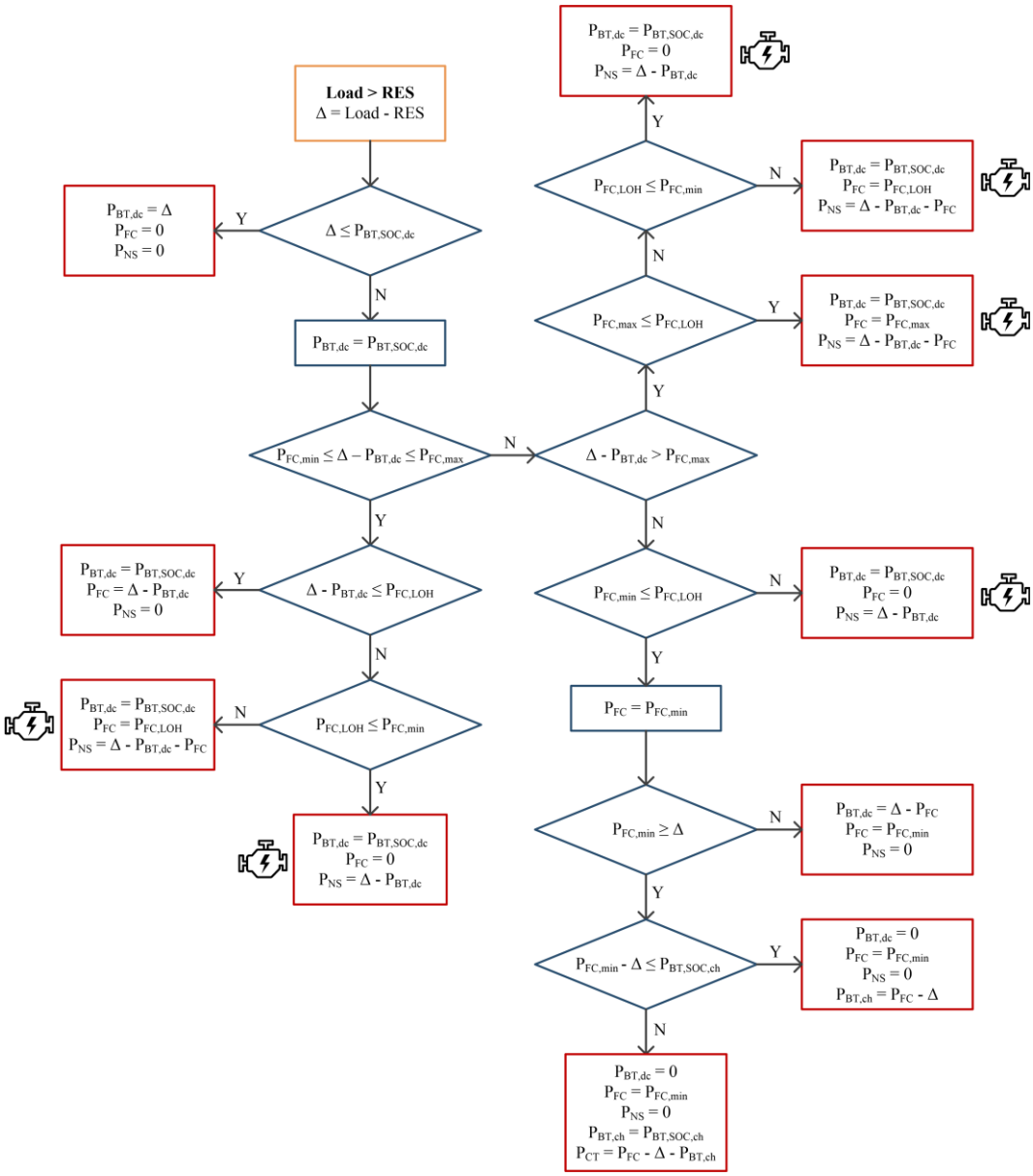

Figure 3.14 Logical block diagram for the discharging case (RES supply lower than load demand).

If a diesel generator is present in the energy system configuration, the remaining power deficit can be covered by its operation (compatibly with DG maximum operating power). DG acts thus as a backup system, which intervenes when no more energy is available from RES and the hybrid storage. In case the power still to be covered is lower than the DG minimum power, the diesel generator is forced to work at $P_{DG,min}$. The control logic for this specific situation is detailed in Figure 3.15 (where $P_{BT,dc,old}$ corresponds the $P_{BT,dc}$ variable computed by applying the EMS of Figure 3.14). The block diagram is written in a compact form to unify in a single scheme all cases of Figure 3.14 where DG must intervenes (i.e., P_{NS} is different from zero).

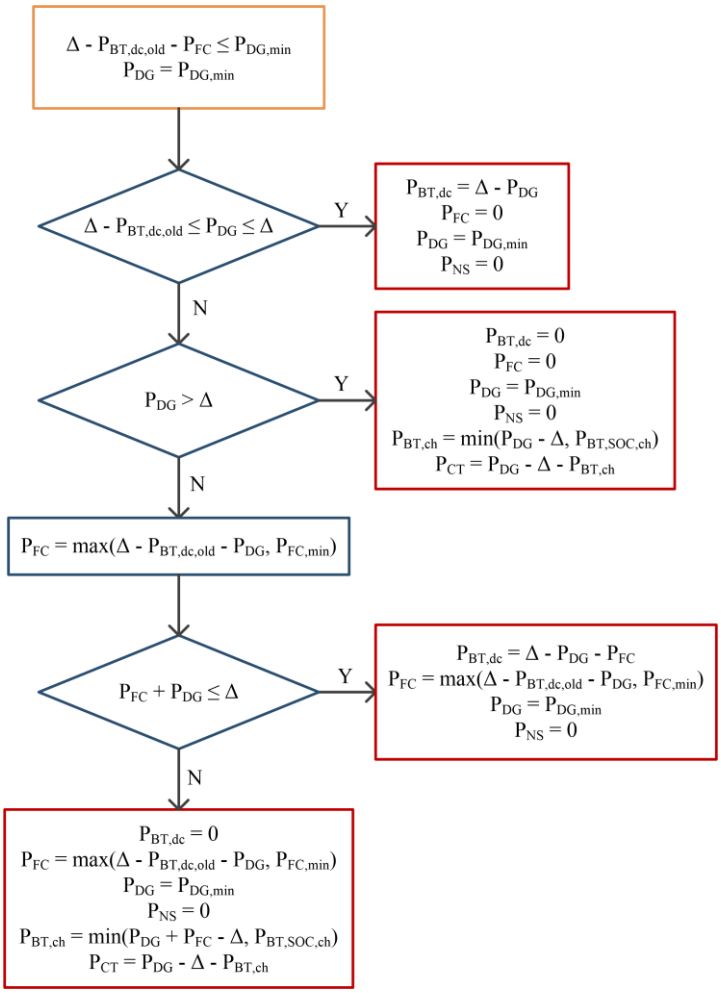

Figure 3.15 Logical block diagram for the discharging case with the presence of DG: power to be supplied by DG is lower than $P_{DG,min}$.

SOC and LOH values were computed at each time step according to Eq. (2.67) and Eq. (2.69) described in Chapter 2. The maximum charging/discharging power that does not cause the SOC to go above/below its upper/lower limit was derived as follows:

$$P_{BT,SOC,ch}(t) = Cap_{BT} \frac{(SOC_{max} - SOC(t))}{\Delta t} \frac{1}{\eta_{BT,ch}\, \eta_{conv}} \tag{3.1}$$

$$P_{BT,SOC,dc}(t) = Cap_{BT} \cdot \frac{(SOC(t) - SOC_{min})}{\Delta t}\, \eta_{BT,dc}\, \eta_{conv} \tag{3.2}$$

where Cap_{BT} (in kWh) is the battery capacity, $\eta_{BT,ch}$ is the battery charging efficiency, $\eta_{BT,dc}$ is the battery discharging efficiency, η_{conv} is the efficiency of the battery converter and Δt is the time interval (1 hour in this study).

Analogously, the maximum electrolyzer/fuel cell power that allows the H_2 storage not to go above/below its upper/lower LOH is:

$$P_{EL,LOH}(t) = Cap_{H2} \frac{\left(LOH_{max} - LOH(t)\right)}{\Delta t} \frac{1}{\eta_{EL}} \tag{3.3}$$

$$P_{FC,LOH}(t) = Cap_{H2} \cdot \frac{(LOH(t) - LOH_{min})}{\Delta t} \eta_{FC} \tag{3.4}$$

where Cap_{H2} (in kWh) is the capacity of the H_2 storage, η_{EL} is the electrolyzer efficiency and η_{FC} is the fuel cell efficiency. The EL and FC efficiency terms already include the converter losses. Performance curves derived in the previous chapter (Section 2.1) were used to model the efficiency of the H_2-based devices.

3.4 Results

3.4.1 Energy simulations

Energy balance simulations on a yearly basis have been performed for the four case studies by implementing the operation strategies defined in Section 3.3 (with 1-hour time step resolution). The hourly profiles of RES production and load described in Section 3.2 were considered. Techno-economic parameters from Chapter 2 were used as input for the feasibility analysis.

Main results about the yearly load coverage are summarized in Table 3.6. For Agkistro site, a RES supply failure was instead simulated assuming the storage system at full capacity. The aim is to demonstrate the effectiveness of the H_2-based P2P solution in reducing the usage of diesel-based generators by maximizing the exploitation of local RESs.

Technical outcomes referred to the hybrid P2P system are also shown in Table 3.7. Lifetime values of the P2P devices were derived based on how they operate along the year according to the energy system simulation. These values will then be used as input for the subsequent economic evaluations.

Table 3.6 Annual load coverage results

	Ginostra		Ambornetti		Froan	
	[MWh]	[%]	[MWh]	[%]	[MWh]	[%]
Load directly covered by RES	76.4	44.6	303.9	87.3	445.4	79.4
Load covered by hybrid P2P	93.2	54.3	44.3	12.7	95.9	17.1
Load covered by diesel generator	1.9	1.1	0.0	0.0	20.0	3.6
Total load	171.5	100	348.2	100	561.2	100

Table 3.7 Main technical KPIs for the hybrid storage solution derived from the energy simulations

Parameter		Ginostra	Ambornetti	Froan
EL operating hours per year	[h]	322	1319	2231
EL on-off per year	[-]	89	380	182
EL lifetime	[y]	NR*	15	11
FC operating hours per year	[h]	250	613	783
FC on-off per year	[-]	40	225	130
FC lifetime	[y]	NR*	NR*	NR*
BT lifetime	[y]	13	5	17

NR*: No replacement

Concerning the Ginostra demo, simulations show that the solar energy together with the hybrid P2P solution enable to drastically decrease the use of diesel generators to a value slightly higher than 1% of the total yearly demand. When the RES power is not enough to directly satisfy the load, the shortage is mainly met by the battery (approximately 52%), acting as shorter term storage. The fuel cell instead only accounts for approximately 2% of the load; but its presence is required due to the longer-term storage capability of hydrogen. The fuel cell is in fact mostly used in the summer period, which is characterized by a higher energy demand because of tourism. This is clearly displayed in Figure 3.16, where the behaviour of the hydrogen level and power deficit (i.e., the fraction of load that is not covered directly by the PV) over the year are shown. The LOH remains almost constant over the spring period (since the power deficit is mainly met by the battery storage) and then sharply decreases in July because of

the fuel cell operation, in concomitance to an increase in the energy deficit. It can be seen that the storage tank is quickly filled with hydrogen at the beginning of the year thanks to the conversion of the RES surplus through the electrolyzer. Around 24% of the yearly available PV energy was found to be curtailed. A better exploitation of the local solar source could be achieved by increasing the size of the storage system. In this way RES curtailment during the spring period would be reduced, with a consequent further reduction in the diesel generator intervention. The proposed RES-based solution is able to significantly reduce CO_2 emissions to less than 3 tonnes per year. A much higher value, approximately 284 t/y, is instead found for the current configuration (which relies only on diesel generation).

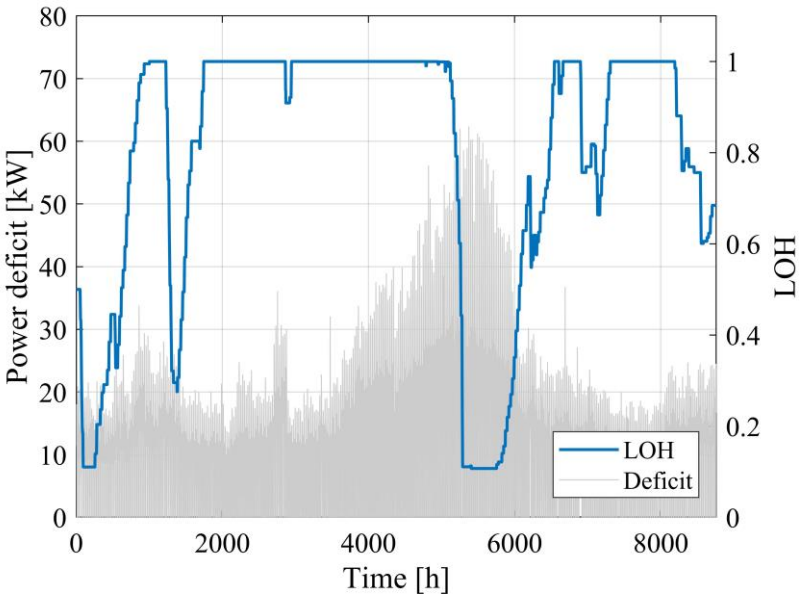

Figure 3.16 Power deficit and LOH along the year in Ginostra. (Power deficit is the fraction of load that is not covered directly by the PV system).

Regarding the Agkistro demo, since the hydroelectric production is always much higher than the load demand, it can be supposed that the hybrid storage system is at full capacity all year long, thus ready to intervene as a back-up in case of emergency (e.g., RES supply failure or maintenance). By applying the control strategy for the discharging case reported in Figure 3.14, in case of RES failure (i.e., RES power set equal to zero), the back-up hybrid storage system was found to be able to sustain the energy demand for almost three days. This period of energy autonomy is mainly due to the hydrogen-tank capacity of almost 1 MWh (it was considered an electrical load consumption of approximately 193 kWh, which is typical for a reference working day of the agri-food unit).

In Ambornetti, a June representative day with no maintenance of the biomass generator is reported in Figure 3.17a. The daily RES and load behaviours of any

other day with no BG maintenance have similar trends. The biomass system together with the PV plant are able to cover a great fraction of the electrical load. The battery bank needs also to intervene every day during the morning and evening load peaks when renewable power (i.e., solar plus biomass) is not enough alone to satisfy all the electrical demand. The battery SOC is daily regenerated by charging the battery during night (thanks to the power production from biomass) and, during the summer months, also in the middle of the day (thanks to the surplus RES power due to the increased PV production). In the presence of maintenance of the biomass generator (Figure 3.17b), the battery storage is not sufficient and the energy stored in the hydrogen tank is also required. The battery component in fact quickly reaches its minimum SOC and the fuel cell has to be switched on consuming hydrogen. Therefore, the LOH periodically drops because of the fuel cell intervention during downtime of the biomass generator. CO_2 emissions due to the biomass combustion account for about 419 tonnes per year (the CO_2 emission coefficient and the biomass LHV were taken from Refs. [191], [192]). Although CO_2 is released, biomass can be considered an almost carbon-free fuel because the CO_2 resulting from its combustion will be absorbed while growing the replacement biomass. However, biomass is not completely carbon neutral because CO_2 emissions will occur during the harvesting, processing and transport of the fuel. These contributions are very low compared to the amount of CO_2 associated to the combustion process (it should also be noted that, in Ambornetti, the contribution due to transport is even lower since only local biomass sources are used).

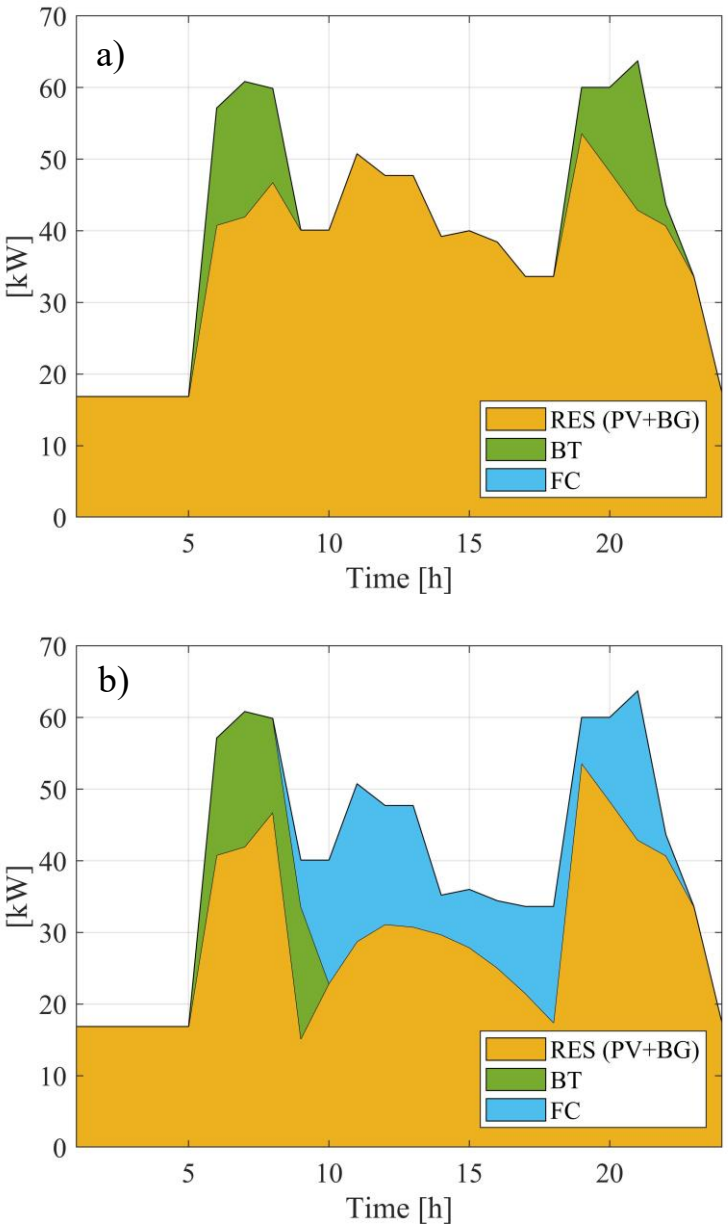

Figure 3.17 Daily load coverage with (a) and without (b) biomass generator in Ambornetti.

In Froan, local RESs coupled with the hydrogen-battery energy storage systems are effective in decreasing the amount of energy required by back-up diesel generators to a value lower than 4% of the annual load request (which corresponds to approximately 28.8 tonnes of CO_2 per year). Wind and PV plants directly cover approximately 79.4% of the total load. The hybrid storage system accounts instead for about 17.1%, of which approximately 11.5% covered by batteries and 5.6% by the fuel cell. The evolution throughout the year of the amount of hydrogen in the tank is represented in Figure 3.18. With respect to the Ginostra case, here the fuel cell intervenes more frequently and there is no evident seasonal behavior of the hydrogen level, mainly because of randomness of the

wind power. It can be noticed greater emptying of the hydrogen storage in February and in the July-October period when the RES availability is scarcer. Slightly more than half of the total renewable energy was found to be curtailed, which is unavoidable in stand-alone systems that wish to achieve high RES penetration levels (especially when dealing with highly variable renewable sources).

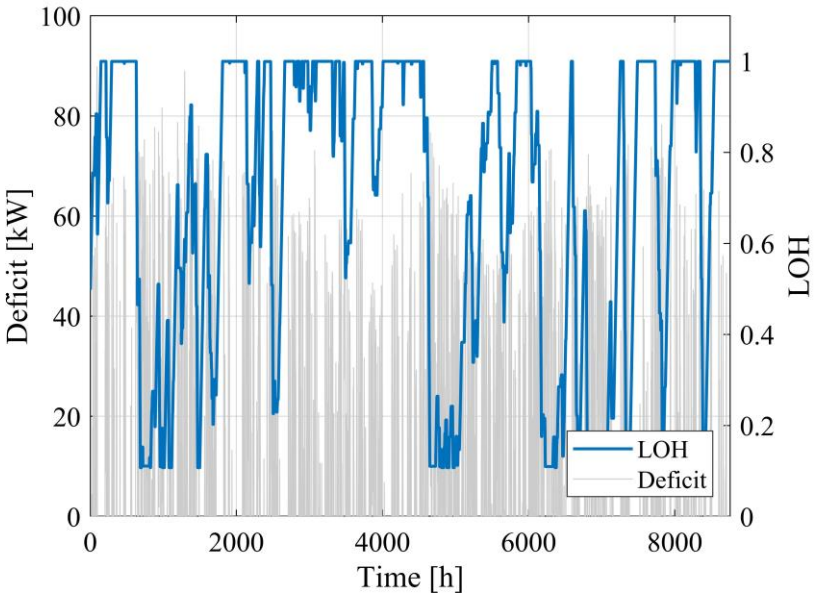

Figure 3.18 Power deficit and LOH along the year in Froan.

3.4.2 Cost comparison among the analyzed configurations

Building on the data of the four case studies, an economic analysis was then performed to compute the LCOE values for the various configurations. For each site, the following options are compared to the hydrogen-based one: usage of current diesel generators in Ginostra, connection to the grid in Agkistro, employment of a hypothetic diesel generator in Ambornetti and replacement of the current sea cable in Froan. Input data for the grid connection scenario in Agkistro (i.e., investment and maintenance cost for a new transmission line and operational expenditures associated to the purchase of electricity) were directly provided by the end-user Horizon SA. Analogously, costs related to the cable replacement in Froan (cable investment and maintenance and electricity purchase) were supplied by TrønderEnergi. Cost details referred to these two grid-based scenarios are not shown due to confidentiality issuses.

The net present cost as a function of the time horizon is reported in Figure 3.19 for the case study of Ginostra. The DG scenario presents no initial investment since diesel generators are already installed on the island. The NPC

then sharply increases with time because of the high costs related to the use of diesel generators (i.e., high diesel fuel prices). Referring to the RES-based solution, most of costs are instead associated to the initial investment incurred for the purchase of the PV system and the hybrid energy storage. This results in a fairly limited increase in the system NPC with time. It can be noticed that the RES + P2P solution becomes more attractive than the current diesel-based system after around 9 years. Moreover, the LCOE of the renewable solution is approximately 0.57 €/kWh at the end of the project lifetime (i.e., year 20), which is 33% lower than the LCOE value of the configuration that relies on diesel only.

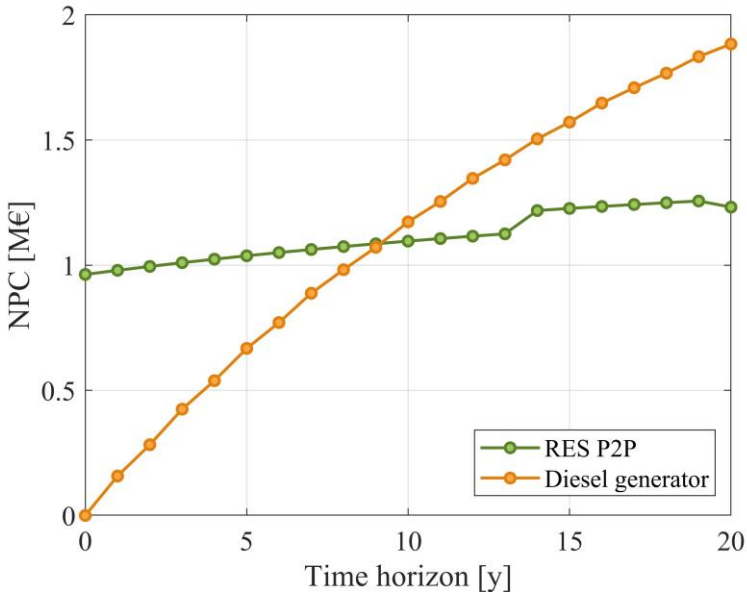

Figure 3.19 NPC over time for the diesel-based and suggested RES + P2P solutions in Ginostra

The LCOE breakdown in the 20th year is displayed in Figure 3.20. It can be observed that the highest share, approximately 37%, is given by the battery component. The hydrogen system (i.e., electrolyzer, gas storage tank and fuel cell) also accounts for an important contribution of the total electricity cost. However, the presence of an energy storage solution is necessary to better exploit local renewable sources and consequently minimize the consumption of fossil fuels. Moreover, even though batteries contribute most to the load coverage, hydrogen presence is required for its higher energy capacity and thus to avoid installing batteries with too large size. The role of hydrogen and the effect of storage hybridization will be further investigated in the following chapters when addressing the problem of the optimal design of hybrid renewable energy systems.

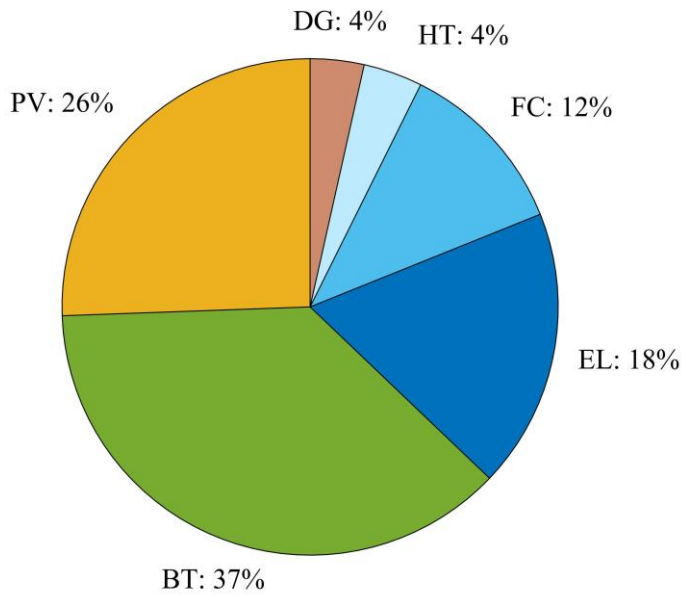

Figure 3.20 LCOE breakdown at 20-year time horizon in Ginostra.

Economic results referred to Agkistro site are shown in Figure 3.21. It can be observed that the renewable solution is more attractive than the alternative already at the beginning of the simulation. In fact, the investment cost incurred for the installation of a separate line would be very high, making this option not economically viable. The resulting LCOE at year 20 is approximately 1.12 €/kWh when considering hydro energy together with the hydrogen-battery system. The cost of energy would rise to 1.66 €/kWh for the alternative case based on the connection to the grid.

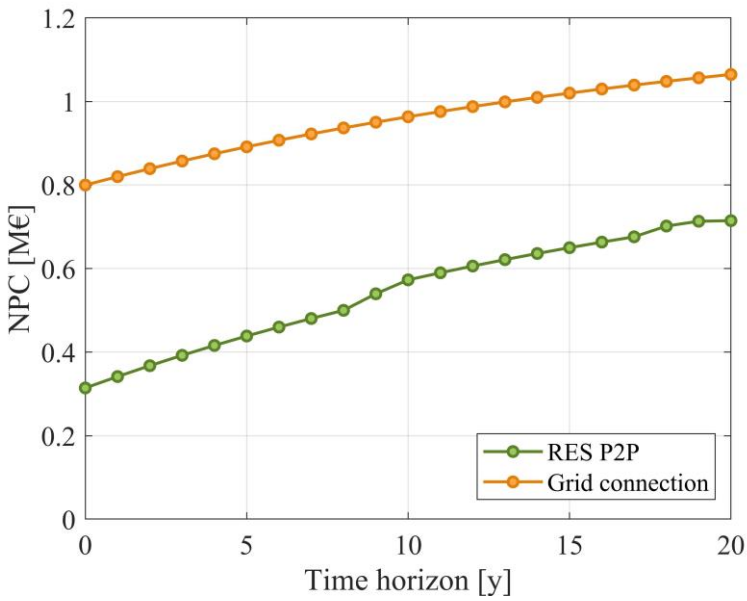

Figure 3.21 NPC over time for the suggested RES + P2P and alternative (grid connection) solutions in Agkistro.

As displayed in Figure 3.22, most of the expenses of the RES-based configuration in Agkistro are associated to the hybrid storage system and, in particular, to the hydrogen equipment. However, the H_2 system is essential in Agkistro to improve the reliability of the power supply service. Indeed, the agri-food operation in case of fault/maintenance of the hydro plant is mainly ensured by the energy stored in the form of hydrogen (around two days and a half). In the economic analysis, the cost term related to the hydro-power plant only accounts for operational expenses. In the initial investment there are no costs associated to the hydro generator since it is already installed in Agkistro site.

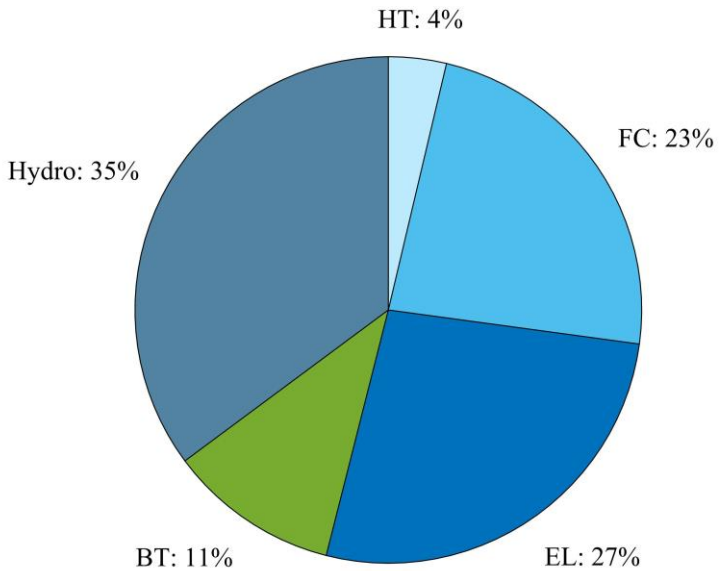

Figure 3.22 LCOE breakdown at 20-year time horizon in Agkistro.

Concerning the Ambornetti case study, the net present cost as a function of time is displayed in Figure 3.23. Relying on local biomass and solar energy coupled with storage devices is proved to be more convenient than using diesel generators. In fact, the high operating costs linked to the use of diesel generators (a reference diesel fuel price of 2 €/L was supposed) causes the NPC of the diesel-based scenario to exceed the NPC of the renewable scenario in the fifth year. The high initial investment for the hybrid renewable energy system is rewarded with quite low operational expenses over the lifetime of the project. At 20-year time horizon, the NPC (and hence the LCOE) of the renewable solution is around half the value of the fossil fuel-based scenario (LCOE of 0.38 compared to 0.74 €/kWh).

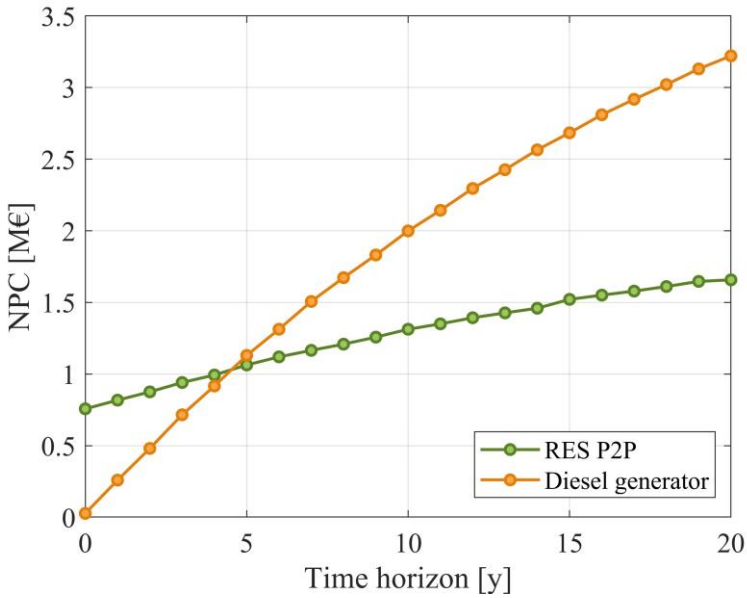

Figure 3.23 NPC over time for the suggested RES + P2P and alternative (diesel generator) solutions in Ambornetti.

Referring to the RES-based configuration in Ambornetti, the LCOE breakdown at the end of the project duration is shown in Figure 3.24. The biomass generator accounts for the highest share of the LCOE. An important contribution is also given by the hydrogen system, whose role is required to guarantee the site energy-independence during shutdown periods of the biomass generator.

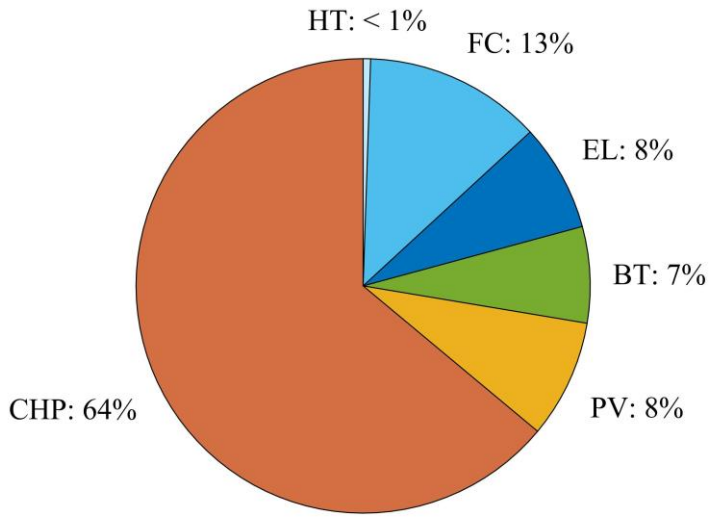

Figure 3.24 LCOE breakdown at 20-year time horizon in Ambornetti.

Finally, main results for Froan are reported in Figure 3.25 and Figure 3.26. As for the site of Agkistro, the solution relying on local RESs is cheaper than the

alternative option already at the beginning of the project period. At 20-year time horizon, the levelized cost of energy is around 0.40 €/kWh for the RES-based solution, compared to 0.63 €/kWh when considering the sea cable replacement. However, as displayed in Figure 3.25, high initial investment costs must be covered for both the scenarios under analysis.

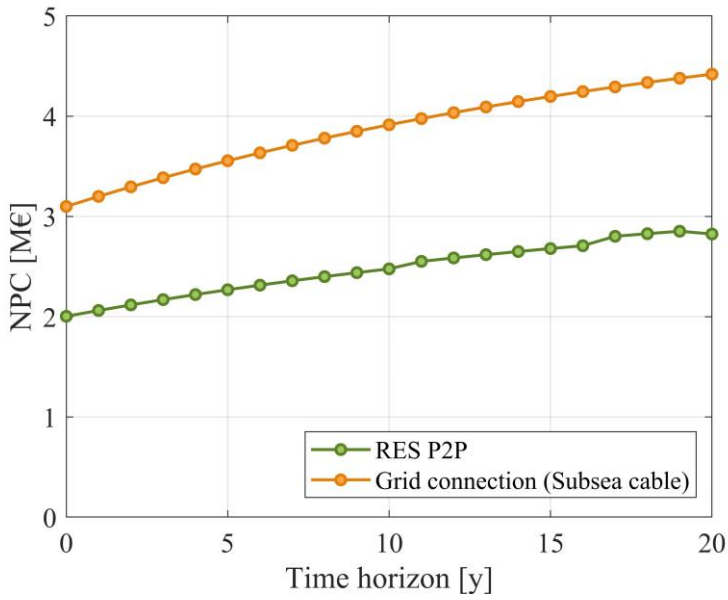

Figure 3.25 NPC over time for the suggested RES + P2P and alternative (grid connection) solutions in Froan

The highest share of the LCOE of the renewable solution is represented by wind turbines (accounting for almost 40% of the cost of energy). The energy system in fact relies heavily on the energy locally produced by the wind source, which is highly abundant in Froan. A lower LCOE fraction, around 17%, is attributed to the PV system, whose presence is required to make the power supply service more reliable thanks to the higher predictability of solar energy compared to wind. Another great contribution is given by the hybrid storage system, approximately 14% due to batteries and 23% due to the hydrogen equipment. However, the cost associated to storage devices is unavoidable to allow the DG load coverage to be reduced to less than 5%. Further considerations about the influence of different storage architectures on the system cost will be performed in Chapter 4.

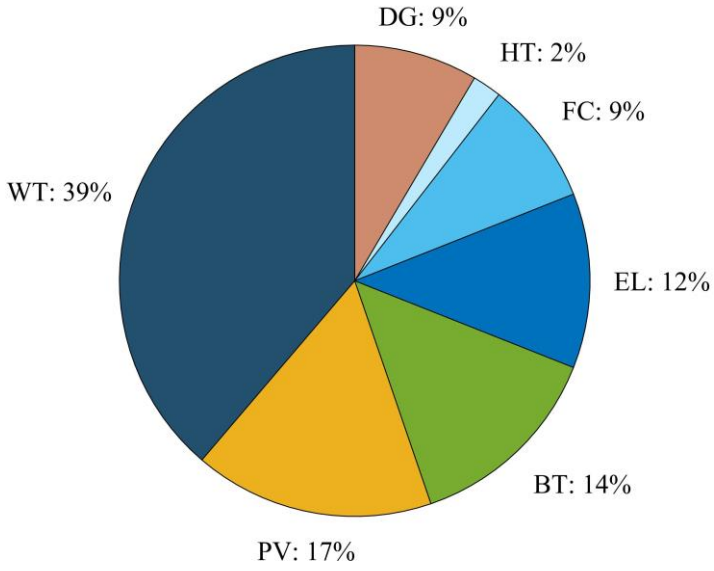

Figure 3.26 LCOE breakdown at 20 year time horizon in Froan.

Main results derived from the economic analysis are summed up in Table 3.8, where the LCOE values for the renewable and alternative solutions are reported for the four case studies.

Table 3.8 LCOE at 20-year time horizon for the four case studies under analysis

	RES + P2P	**Alternative**
Ginostra	0.571 €/kWh	0.863 €/kWh
Agkistro	1.115 €/kWh	1.661 €/kWh
Ambornetti	0.379 €/kWh	0.736 €/kWh
Froan	0.401 €/kWh	0.627 €/kWh

As displayed in Table 3.8, the REMOTE solution is cheaper than the diesel- or grid-based options for all the REMOTE sites. However, there is a fairly significant cost difference between the four case studies: from roughly 0.4 €/kWh in Ambornetti and Froan to more than 1 €/kWh in Agkistro. This LCOE discrepancy may be due to several factors, such as the use of different RES technologies, system size (because of scale dependencies of costs), RES supply and load demand profiles.

Figure 3.27 reports the LCOE versus the load factor (LF) for all the HRESs under analysis. The load factor is here defined as the ratio of the average load (over the year) to the peak load. It can be noted that the cost of energy is higher for the systems characterized by a lower value of the LF. The highest LCOE, of

around 1.12 €/kWh, is found in Agkistro where the LF is the lowest among the four cases (0.19). In Ambornetti and Froan, where the cost of energy is similar, the load factor parameter is almost the same, of approximately 0.60. The slightly lower LCOE in Ambornetti (0.38 €/kWh) compared to Froan (0.40 €/kWh) may be due to the usage of the biomass generator, which causes the power supply to be more stable and predictable with consequent lower need for storage autonomy.

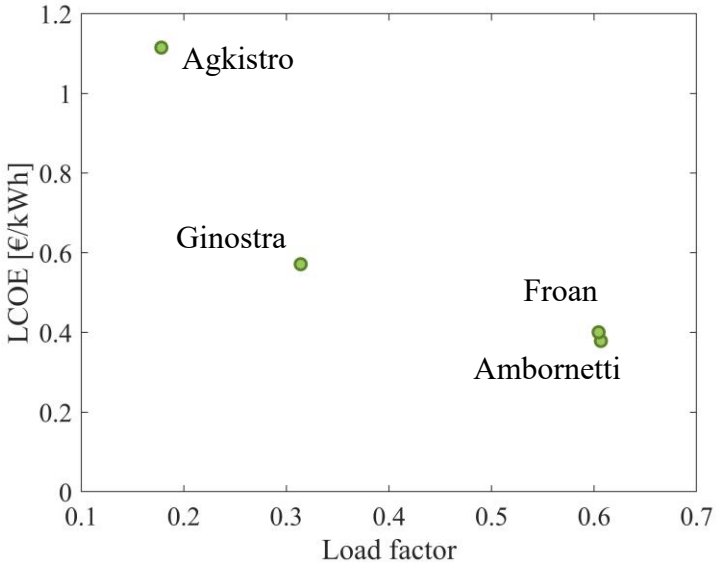

Figure 3.27 LCOE versus load factor for the four REMOTE case studies

It should also be noted that environmental advantages are linked to these types of hybrid energy storage systems since they represent an interesting low-carbon alternative to the use of traditional fossil fuels. An economic evaluation of the emissions reduction could further improve the results of the RES-based scenarios.

Conclusions

An analysis of techno-economic feasibility has been performed for the four case studies defined in the REMOTE project. A ruled-based control strategy was derived for the renewable P2P system to manage the energy exchanges among the various components and perform energy simulations on a yearly basis.

Local RESs coupled with a hybrid battery-H_2 storage system were shown to be able to significantly reduce or even eliminate the use of fossil-based power generators. In Ginostra, the renewable configuration allows the diesel share to be reduced to slightly more than 1% of the total electrical demand of the local community. In Froan, only around 3.6% of the annual load has to be supplied by diesel genset. A completely energy autonomy was found to be possible in Ambornetti thanks to the exploitation of local solar and biomass energy. Finally,

in Agkistro, the P2P configuration was proved to be effective as a backup solution, guaranteeing almost three days of energy independence in case of failure or maintenance of the hydro plant. Overall, it can be said that the hydrogen solution is useful for its longer-term storage capability, intervening mainly during maintenance, emergency or periods of the year with a higher electrical demand.

An economic analysis was then performed to demonstrate the economic viability of the RES-based solution by comparing it with alternative scenarios in terms of LCOE. For all the case studies, the exploitation of local renewables together with the adoption of a hybrid P2P system was proved to be more cost-effective than traditional options either in the short or longer term. Outcomes of these simulations have thus shown the usefulness and economic feasibility of P2P systems located in remote micro-grid areas. Moreover, environmental benefits, such as reduced CO_2 emissions due to the lower DG share and avoidance of invasive works because of grid connections, make these solutions even more attractive. It is important to note that the H_2-based P2P systems under analysis do not represent mass produced units. Their capital costs are therefore expected to decrease with further development of hydrogen technologies and their market diffusion.

Simulations carried out so far are based on component sizes and system configurations already known (defined in the framework of REMOTE). In the following chapter, techno-economic optimizations will be performed to evaluate the optimal design of the energy system, so as to guarantee the total load coverage with the minimum LCOE. Different architectures of the P2P system will be also taken into account to better investigate the role of batteries and hydrogen-based devices in achieving cost-effective and reliable off-grid solutions.

Chapter 4

A metaheuristic approach for the optimal design of off-grid H_2-based energy systems

Chapter 4 deals with the optimal design of stand-alone hybrid renewable energy systems (HRESs) by means of a metaheuristic-based approach. Different HRES configurations have been analysed, involving batteries and hydrogen as means to store energy, to find out which is the most cost-effective configuration in remote areas. Cost-emissions Pareto fronts were also developed to gain greater awareness about the potential of renewable-based energy systems in off-grid applications. The proposed methodology was applied to two different case studies: Ginostra (Italy) and Froan archipelago (Norway), which are representative of many other insular mini-grid environments in the Mediterranean area and northern Europe, respectively.

4.1 Introduction

System cost and reliability must be addressed when designing a hybrid renewable energy system. The optimal sizing of HRESs is a challenging task since multiple and conflicting goals need to be tackled [193]. Design optimization means to always satisfy the load demand while minimizing a certain objective function, often described in terms of system cost or cost of energy. The reliability of the system can be assessed by using several indices, among which the loss of power supply probability (LPSP) is often adopted [171].

The HOMER software is widely employed as a simulation program for the optimal sizing of RES-based energy systems since it is able to combine a high number of components and to perform optimization and sensitivity analyses,

which makes straightforward the evaluation of the cheapest system configuration [194], [195]. Concerning H_2-based stand-alone systems, HOMER has been applied to optimize the design of several system combinations: PV-wind-H_2-battery [43], [169], [196], PV-wind-H_2 [197], wind-H_2 [198], PV-H_2-battery [129], PV-H_2-supercapacitor [199], PV-wind-biomass-biogas-H_2-battery [200], [201] and PV-wind-diesel-H_2-battery [54], [202]. However, this software presents important limitations of editable parameters when H_2-based technologies are included in the system configuration [47].

Metaheuristic-based optimization algorithms are also often adopted, such as: particle swarm optimization (PSO) [48], [170], [203]–[205], genetic algorithm (GA) [149], [173], [174], [206], [207], ant colony optimization (ACO) [42], artificial bee swarm optimization (ABSO) [208], flower pollination algorithm (FPA) [209], [210], simulated annealing (SA) [170], tabu search (TS) [170], harmony search (HS) [170], crow search algorithm (CSA) [49] and mine blast algorithm (MBA) [211]. Combinations of different algorithms have also been considered as for example PSO-HS [212] and SA-HS-chaotic search (CS) [38]. All the above cited works deal with renewable energy systems based on hydrogen. A broader overview about intelligent techniques to optimally design energy systems can be found in the review by Lian *et al.* [172].

Among the various artificial intelligence techniques, PSO is one of the most used methods when dealing with the optimal design of renewable-based systems [194]. Compared to the other methodologies, PSO may be easier to implement since it requires fewer parameters [213]. It is also characterized by great robustness and high convergence speed, which makes it a suitable choice for the design of energy systems [214]. Maleki *et al.* [170] investigated different optimization methodologies (i.e., PSO, TS, SA and HS) to optimally size HRESs and showed that the PSO algorithm has better performance and higher robustness with respect to the other tested methods. Clarke *et al.* [204] reported that PSO is an effective technique to carry out the optimal design and operation of hydrogen systems. PSO was successfully employed by Kaviani *et al.* [203] and Baghaee *et al.* [205], who performed the optimal sizing of a microgrid with hydrogen storage, including outage probabilities of renewable generators. PSO was also shown to be useful when facing the design of more complex stand-alone energy systems to cover both electrical and cold needs [48].

The genetic algorithm has also been extensively applied, showing its effectiveness especially when dealing with multi-objective optimization problems (MOPs) [149]. In addition to objectives of an economic type, MOPs generally include environmental concerns such as operational CO_2 emissions [215]–[217], equivalent life cycle CO_2 emissions [218]–[220] and fossil-fuel consumption [221]. Three-objective optimization problems are also found in the literature about HRES works: as an example, unmet load and accumulated voltage deviations were added as third objective by Sharafi *et al.* [213] and Rodríguez-Gallegos *et al.* [218], respectively (together with cost of energy and CO_2 emissions). According

to the search approach, MOPs can be classified into: 1) Pareto-based techniques that employ ranking and selection in the population to generate the Pareto front and 2) non-Pareto-based techniques that involve the combination of objective functions and problem transformation [222].

Metaheuristic methods for the HRES optimal design mainly rely on rule-based dispatch strategies [56], such as those defined in Chapter 3. Concerning RBSs, decisions are taken depending on the properties of components and on the actual status of the microgrid. As an alternative, the dispatch problem might be addressed by means of predictive control strategies, which are able to identify the optimal solution by taking advantage of the future behaviour of exogenous factors (e.g., load and meteorological data). However, the implementation of predictive-based approaches causes greater computational complexity, making it necessary to increase the degree of approximation of the sizing problem, e.g., by considering a reduced time horizon [130]. Mazzola *et al.* [223] derived a methodology for the design and dispatch of stand-alone rural microgrids. The authors formulated a predictive control strategy based on the MILP technique to optimally operate the stand-alone system. They addressed the design phase by varying the sizes of the components involved in the energy system. A multidimensional grid was thus created by discretely changing the component sizes over a certain size range. Mazzola *et al.* [224] applied a similar methodology to deal with the design and operation of PV-battery-diesel microgrids and evaluated the effect of different operation strategies, including a predictive EMS. However, their design approach was based on running the program for each configuration of the multidimensional grid, which might become unfeasible when analysing energy systems with a higher number of components (e.g., when a hydrogen P2P system is also introduced).

In the present study, ruled-based strategies were thus employed. This enabled the usage of a metaheuristic approach for the design phase, while also considering a full-year time horizon with hourly resolution. A year-long period allows the seasonal variation of supply and load to be considered, which is required for a reliable design of stand-alone energy systems that are based on local RESs. Given its proven effectiveness, the optimization problem was tackled by means of the PSO technique. Studies dealing with the design optimization of hydrogen storage systems usually model the electrolyzer and fuel cell devices by assuming a constant efficiency. In this work, part-load performance curves (which were derived from bottom-up electrochemical models) have been implemented in the optimization routine. This is particularly suited when dealing with devices that need to adapt continuously their operating point to match the fluctuating power supply from on-site renewable sources. Unlike most works where pre-defined lifetime values are adopted, the electrolyzer and fuel cell lifespans were computed based on the yearly number of simulated working hours and start-ups, for a more accurate assessment of the P2P system costs. Several energy storage solutions were analysed, considering various types of batteries (Li-ion and lead acid) and

electrolyzers (alkaline and PEM), to better investigate the role of hydrogen in off-grid environments. Moreover, cost of energy and environmental issues were simultaneously addressed by means of the ε-constraint method with the aim of generating cost-emissions Pareto fronts for different HRES configurations. The sizing methodology was applied to two real insular communities to gain more insight into the feasibility of hydrogen-based energy systems in different geographical contexts, from the Mediterranean area up to the northern Europe.

4.2 Optimal sizing methodology

4.2.1 Particle swarm optimization

Particle swarm optimization represents a population-based stochastic search technique inspired by the movement of organisms in a bird flock or fish school. This computational method is originally attributed to Kennedy and Eberhart [225] and was first intended for simulating social behaviour. Compared to GA, PSO is easier to implement as it deals with fewer parameters (i.e., position and velocity) and no evolution operators such as crossover and mutation are used.

In the initialization phase, the algorithm creates the initial population composed of a pre-defined number of particles, each of which characterized by an initial velocity. Each i-th particle (p_i) in the swarm has a position, represented by a row vector with n_{var} elements:

$$p_i = \left[x_{i,1}, x_{i,2}, \dots, x_{i,n_{var}}\right] \tag{4.1}$$

The value of each j-th element ($j \in \{1, \dots, n_{var}\}$) of each i-th particle must lie within specific pre-defined bounds:

$$x_{i,j,min} \leq x_{i,j} \leq x_{i,j,max} \tag{4.2}$$

At each iteration, the particle's velocity is updated depending on its previous velocity, on the distance of its current position from its own best position, as well as from the best experienced global position:

$$v_i(t+1) = w\, v_i(t) + c_1\, \varepsilon_1 \left(p_{i,best} - p_i(t)\right) + c_2\, \varepsilon_2 \left(p_{g,best} - p_i(t)\right) \tag{4.3}$$

where w is the inertia coefficient (representing the tendency of the particle to remain in its current position), $p_{i,best}$ is the i-th particle best known position, $p_{g,best}$ is the best position in the swarm, c_1 is the weighting coefficient of the personal best position, c_2 is the weighting coefficient of the global best position and finally ε_1 and ε_2 are random numbers between 0 and 1, whose value is updated at each iteration.

Once the new velocity is known, the particle's position is modified as follows:

$$p_i(t+1) = p_i(t) + v_i(t+1) \tag{4.4}$$

The objective function can thus be computed for each particle with subsequent update of the $p_{i,best}$ and $p_{g,best}$ values. The PSO routine continues by iteratively updating the particle velocities and locations until the algorithm reaches a stopping criterion. During the iterative process, the algorithm forces all the particles and velocity components to be within their bounds.

4.2.2 Sizing approach

The working principle of the PSO-based design optimization process is summarized in Figure 4.1. The number of elements of each i-th particle is equal to the number of decision variables (i.e., sizes of all the components of the HRES):

$$p_i = [S_{i,1}, S_{i,2}, \dots, S_{i,n_{var}}] \tag{4.5}$$

As stated in Eq. (4.2), component sizes to be optimized were also imposed to vary between specific lower and upper bounds:

$$S_{i,j,min} \leq S_{i,j} \leq S_{i,j,max} \tag{4.6}$$

where $S_{i,j}$ is the size of the j-th component referred to the i-th particle. $S_{i,j,min}$ was set to 0 for all the variables. During the PSO main loop, the velocities and positions of the particles were iteratively changed until reaching one of the following stopping criteria:

1. Reaching a maximum number of iterations equal to It_{MAX};
2. No changes in 30 iterations for the global best position (relative change less than 10^{-6}).

It_{MAX} is the maximum number of iterations, which should be chosen high enough so as not to be reached. A value of 100 was considered for the size of population (i.e., number of particles in the swarm). The weighting coefficients of the personal best (c_1) and global best (c_2) positions were set to 2, as also suggested in the literature [170], [203], [211].

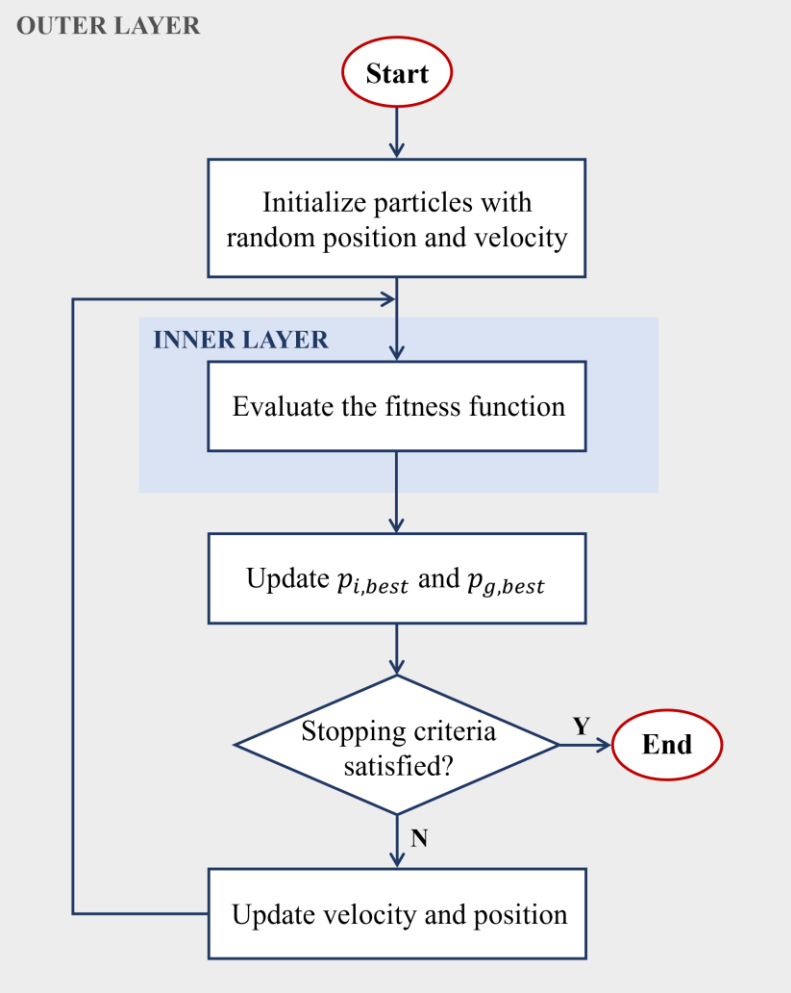

Figure 4.1 Working principle of the metaheuristic-based design optimization algorithm.

As displayed in Figure 4.1, an inner layer was implemented in the PSO algorithm to deal with the HRES operation and subsequent evaluation of the objective function, i.e., the levelized cost of energy. The inner layer structure is schematized in Figure 4.2. Based on the input meteorological and load data, it is first performed hour by hour the energy simulation of the HRES over a specific time horizon (a reference year in the present analysis) by means of pre-defined ruled-based control strategies. An economic analysis is subsequently carried out with the aim of evaluating the LCOE, which has to be minimized by the optimization problem. The cost of energy can be finally penalized to discourage and discard the solutions where some specific constraints are not satisfied (e.g., constraints (4.8), (4.9), (4.10) and (4.11)).

Technical specifications of all the HRES components are reported in Chapter 2 (Sections 2.1 and 2.2). The efficiency curves of the electrolyzer and fuel cell systems were approximated by means of polynomial fitted curves to be used in the optimal sizing problem. The LCOE was computed by adopting the methodology and the economic data detailed in Section 2.3.

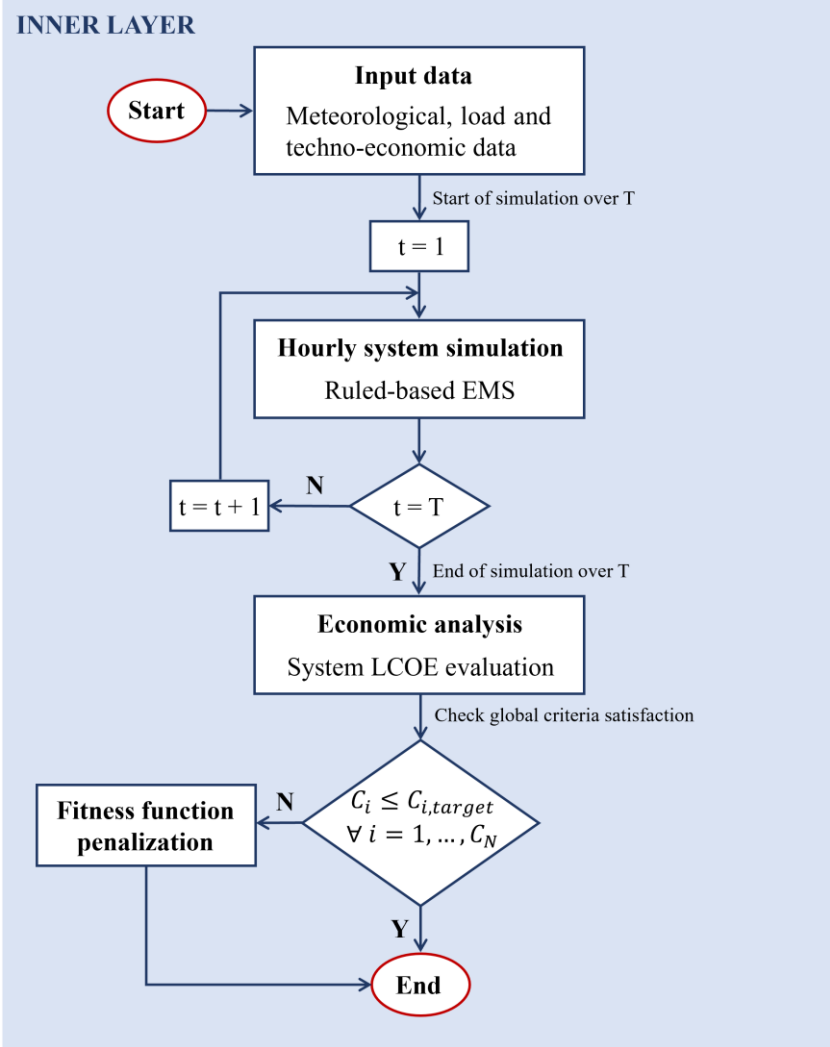

Figure 4.2 Schematic of the inner layer dealing with the system operation and LCOE evaluation.

The loss of power supply probability (LPSP) index over a given time period T (in this case, the whole year) was employed in order to evaluate the reliability of the off-grid system in covering the electrical load [172]. It is defined as the ratio of the total not served energy to the total energy demand over the selected time horizon T (in this case, the entire year):

$$LPSP = \frac{\sum_{t=1}^{T} P_{NS}(t)\, \Delta t}{\sum_{t=1}^{T} P_{LD}(t)\, \Delta t} \tag{4.7}$$

where P_{NS} (in kW) is the demand fraction that is not satisfied and P_{LD} (in kW) is the electrical power demand. The reliability constraint is expressed as follows:

$$LPSP \leq LPSP^{*} \tag{4.8}$$

where $LPSP^*$ is the LPSP target value that must be achieved by the stand-alone HRES. In the present work it was set to 0%, meaning that the electrical demand is covered at all times by the energy system [47], [221].

The following storage constraints were also introduced:

$$SOC(t_{end}) \geq SOC(t_{in}) \tag{4.9}$$

$$LOH(t_{end}) \geq LOH(t_{in}) \tag{4.10}$$

Constraints (4.9) and (4.10) verify that the SOC and LOH values at the end of the reference year are not lower than the values set at the beginning of the year [140]. A value of 0.5 was chosen for both the SOC and LOH in this study.

In case the HRES also includes a diesel generator as available technology, cost-emission Pareto fronts were derived by applying the ε-constraint method [213], [226], which allows both the LCOE and CO_2 emissions to be minimized. According to this technique, the multi-objective optimization problem is solved by optimizing one objective and considering the remaining ones as constraints. First, two different single-objective optimization problems were performed to find the upper and lower limits of the annual CO_2 emissions. In order to evaluate the $m_{CO_2,op,year,max}$ value, a single-objective minimum-cost optimization was carried out, independently of the CO_2 emissions. The $m_{CO_2,op,year,min}$ value was instead quantified by performing a single-objective minimum-emissions optimization, independently of the costs. The CO_2 emission interval thus obtained was divided into n steps. The Pareto front was then generated by performing n single-objective optimization problems that minimize the LCOE while being subject to the corresponding emission constraint, which is represented by the relationship below:

$$\sum_{t=1}^{T} m_{CO_2,op}(t) \leq m_{CO_2,op,year,\varepsilon} \tag{4.11}$$

where $m_{CO_2,op}$ is the CO_2 that is generated at time t. It can be derived multiplying the diesel fuel consumption by the related CO_2 emission coefficient as described by Eq. (2.75). The quantity $m_{CO_2,op,year,\varepsilon}$ was varied between the minimum and maximum yearly values of CO_2 so as to build up the optimal Pareto front.

4.2.3 Energy management strategy

As shown in Figure 4.2, the energy simulation of the hybrid renewable energy system was carried out by means of ruled-based (RB)-type energy management strategies (EMSs). The detailed logical block diagram of the adopted control strategy has been previously discussed in Chapter 3, Section 3.3.

Whenever the electrical demand is higher than the renewable power, priority of intervention is given to the battery discharging. The fuel cell device is then activated to cover the remaining energy deficit in order to avoid excessive discharging of the battery, keeping the SOC parameter higher than SOC_{min}. The diesel generator is finally operated as a back-up device and according to a load following dispatch strategy [141], i.e., whenever it is switched on, it produces only enough power to cover the unmet fraction of primary load.

Instead, in case the electrical demand is lower than the renewable power, the surplus RES energy is first used to charge the battery bank until reaching the maximum SOC, then converted into hydrogen through the electrolyzer and finally curtailed. In this EMS, batteries act thus as shorter-term storage operating first when required (and thus limiting the number of start-ups of the electrolyzer and fuel cell); whereas hydrogen works as longer-term storage medium intervening when the upper and lower operating limits of the battery are reached (so as to limit the degradation, and hence loss of performance, of the battery).

The EMS above described is referred to the complete HRES including batteries, hydrogen and diesel genset. It also remains valid (in terms of priority of intervention) when analysing systems with fewer components.

4.3 Results and discussion

4.3.1 Ginostra case study

The sizing optimization was performed on a renewable P2P system assumed to be installed in the off-grid site of Ginostra, previously introduced in Chapter 3, Section 3.2. Currently, the electrical load is covered exclusively by the use of diesel generators. The final cost of energy is thus heavily dependent on the cost of fossil fuel, its logistic and transportation (which is only possible by helicopter due to the remoteness of the area). Being diesel genset the only source of electricity generation, any failure to the power system would expose the inhabitants to the possibility of a prolonged period of absence of the electrical service. It is therefore of great interest for the site to maximize the exploitation of local RESs with the aim of increasing the reliability of the power supply service and decrease the current LCOE value. The investigation of different typologies of electrical energy storage solutions becomes essential to find out a cost-effective solution to ensure high levels of RES penetration and achieve the independence from fossil fuels.

Main results of the sizing optimization are reported in Table 4.1. Table 4.2 shows the main technical KPIs for the various renewable P2P configurations: lifetimes of P2P devices, number of yearly operating hours and number of yearly start-ups of the electrolyzer and fuel cell. A graphical comparison of the LCOE of all the investigated configurations is also shown in Figure 4.3, where it is displayed how the different components contribute to the overall LCOE. Configurations 1 and 2 rely only on batteries as energy storage medium. In the

third and fourth configuration, renewable energy is stored by means of hydrogen. The remaining ones (from C_5 to C_8) present a hybrid storage architecture, i.e., with both batteries and hydrogen.

Generally, it can be noticed that the cost of energy is lower when considering Li-ion batteries compared to the lead-acid technology. As previously described in Chapter 2, despite the higher specific investment costs, Li-ion devices are characterized by a higher roundtrip efficiency, lower self-discharge rate, higher lifetime throughput and wider cycling modulation range with respect to the lead-acid alternative. As an example, referring to the first two configurations, the LCOE moves from 0.60 to 0.54 €/kWh when changing from LA to LI batteries. In fact, the lithium-ion technology leads to lower PV panel nominal size (291 kW instead of 342 kW) and battery rated capacity (941 kWh instead of 1327 kWh). Moreover, as shown in Table 4.2, unlike the lead-acid technology (C_1), no replacement is required for the LI battery bank (C_2) over the lifetime of the project.

Comparing C_1 and C_2 to C_3 and C_4 configurations, it can be observed that a stand-alone renewable energy system with only batteries as energy storage (0.54 to 0.59 €/kWh) is currently cheaper than a configuration that relies only on hydrogen (0.74 to 0.84 €/kWh). This is due to the high investment costs associated to the electrolyzer and fuel cell systems.

Focusing on the H_2-based configurations, as clearly shown by the C_3 and C_4 sizing results, alkaline electrolyzers are a more cost-effective choice with respect to PEM devices. The levelized cost of energy is around 0.84 and 0.74 €/kWh for the P2P system with PEM (C_3) and alkaline (C_4) electrolyzers, respectively. This is mainly because of the lower cost and higher durability of the ALK-type technology. As reported in Table 4.2, the frequency of stack replacement was found to be every 11 years for the ALK EL and 7 years for the PEM EL. However, the PEM-based technology is characterized by faster dynamic response time and wider modulation range, which could be preferable when dealing with variable renewable energy sources [14].

The energy storage hybridization including both battery and hydrogen (C_5 to C_8) allows the cheapest system configuration to be obtained. Concerning a system with Li-ion batteries, the inclusion of hydrogen leads to an LCOE reduction from 0.54 €/kWh to around 0.51 and 0.50 €/kWh when PEM and alkaline electrolyzers are installed, respectively. Similarly, the LCOE value of 0.60 €/kWh of C_1 (with only lead-acid BT) drops to approximately 0.54 to 0.56 €/kWh if batteries are coupled with hydrogen to store the excess renewable energy. Indeed, the presence of hydrogen makes it possible to avoid the battery oversizing: as an example, the LI BT rated capacity moves from 941 kWh for configuration 2 to around 591 to 595 kWh for the hybrid storage cases. Moreover, when considering both BT and H_2, the required PV rated power also decreases, from 291 kW to slightly more than 200 kW, which means that the local renewable resource is better exploited.

The lower cost share of the PV component for configurations with storage hybridization (i.e., from C_5 to C_8) is graphically displayed in Figure 4.3.

It is noteworthy that the use of lifetime values depending on the cumulative operational duty of P2P devices leads to a more precise and system-specific estimation of the LCOE. As an example, when considering only hydrogen (i.e., C_3 and C_4), the fuel cell lifetime becomes around 5 years, which is in agreement with values that are often adopted in techno-economic evaluations [32]. If instead batteries are coupled with hydrogen, this results in lower usage of the H_2-based components, with consequent no necessity to replace the FC stack over the lifetime of the project. Similarly, the electrolyzer lifespan improves as well for the energy systems where the energy storage is hybridized. Unlike the H_2-based devices, the battery component shows a higher lifetime when considering an HRES that includes only batteries, which is due to the battery oversizing (i.e., higher lifetime throughput before replacement).

Table 4.1 Sizing results and LCOE values for the different renewable P2P configurations.

Configurations		**PV [kW]**	**EL [kW]**	**FC [kW]**	**HT [kWh]**	**BT [kWh]**	**LCOE [€/kWh]**
C1.	PV+LA BT	342	-	-	-	1327	0.596
C2.	PV+LI BT	291	-	-	-	941	0.544
C3.	PV+H_2 (PEM EL)	320	154	63	9798	-	0.836
C4.	PV+H_2 (ALK EL)	309	164	64	9373	-	0.736
C5.	PV+LA BT+H_2 (PEM EL)	215	9	33	4063	824	0.556
C6.	PV+LA BT+H_2 (ALK EL)	215	12	33	3572	809	0.543
C7.	PV+LI BT+H_2 (PEM EL)	211	7	34	3505	595	0.512
C8.	PV+LI BT+H_2 (ALK EL)	205	9	33	3414	591	0.500

Table 4.2 Main technical KPIs for the different renewable P2P configurations.

		$N_{h,yr,EL}$ [h]	$N_{st,yr,EL}$ [-]	L_{EL} [y]	$N_{h,yr,FC}$ [h]	$N_{st,yr,FC}$ [-]	L_{FC} [y]	L_{BT} [yr]
C1.	PV+LA BT	-	-	-	-	-	-	7
C2.	PV+LI BT	-	-	-	-	-	-	NR*
C3.	PV+H_2 (PEM EL)	2794	417	7	5199	394	5	-
C4.	PV+H_2 (ALK EL)	2646	420	11	5215	396	5	-
C5.	PV+LA BT+H_2 (PEM EL)	1549	295	10	248	51	NR*	4
C6.	PV+LA BT+H_2 (ALK EL)	1255	249	NR*	266	56	NR*	4
C7.	PV+LI BT+H_2 (PEM EL)	1655	312	10	214	46	NR*	13
C8.	PV+LA BT+H_2 (ALK EL)	1380	265	19	229	48	NR*	13

*No replacement

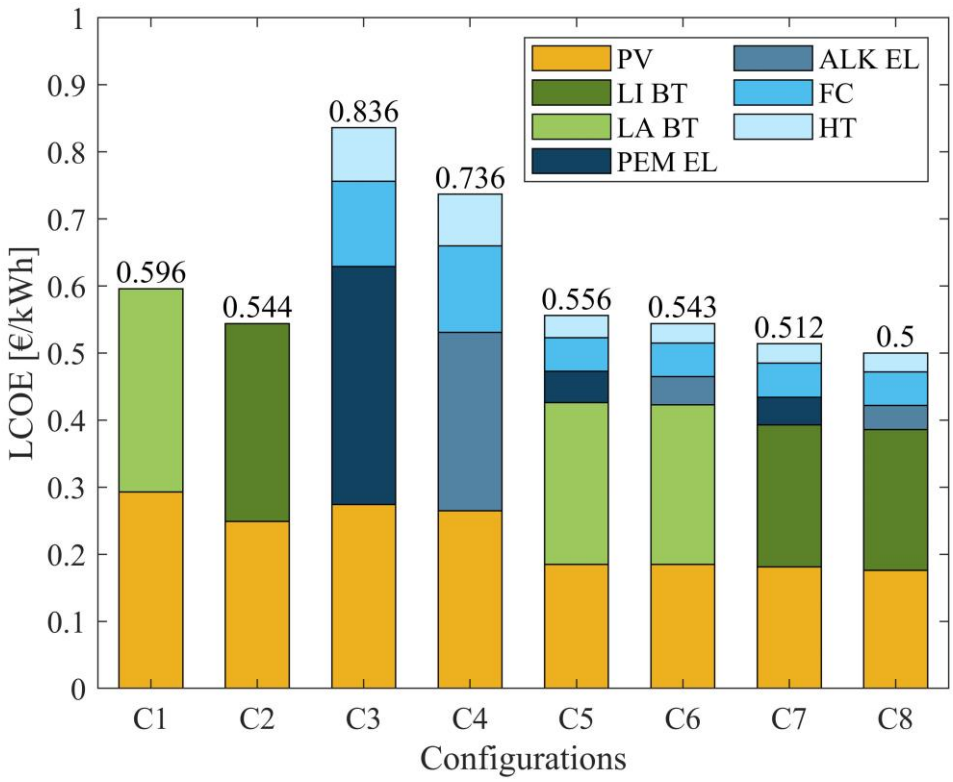

Figure 4.3 Contributions to the LCOE for the various renewable P2P configurations.

The resulting optimal HT capacities are in accordance with sizes considered in the framework of the REMOTE project [36]. As a general consideration, in

case of excessive storage capacity and consequent safety (e.g., Seveso-III directive) or space issues, an upper limit on the storage capacity could be set during the optimal sizing process. Problems of space unavailability could also be addressed by increasing the H_2 storage pressure (with consequent inclusion of a compressor after the electrolyzer).

The profile of the level of hydrogen over the year is reported in Figure 4.4 for configurations 4 and 8, both of which rely on alkaline electrolyzers to produce hydrogen. The LOH graphs referred to the PEM EL device are analogous. A value of 0.5 was imposed for the LOH at the beginning of the year. It can be noticed that the LOH at the end of the reference year reaches again the initial value as described by the constraint (4.10). When only hydrogen is employed to store the surplus renewable energy, a H_2 storage capacity of slightly less than 9400 kWh is required (C_4). The size of the hydrogen storage is roughly three times lower when both batteries and hydrogen are included in the stand-alone energy system (C_8). However, for both configurations it is clearly visible the long-term storage capability of hydrogen: the pressurized tank is filled with hydrogen earlier in the year; the LOH then sharply decreases during summer to cope with the increase in the electrical load due to tourism. Referring to the hybrid storage case (Figure 4.4b), the LOH rise in spring is more gradual. The main function of the electrolyzer is in fact to guarantee that the H_2 tank is full for the start of the summer season. It is thus not required to have an electrolyzer with high nominal size since the EL device can gradually fill the H_2 tank along the spring period. Instead, concerning configuration 4 (Figure 4.4a), the fuel cell has to be used more continuously since it is the only power source when local RES is not sufficient to cover the load. The H_2 storage capacity and the electrolyzer size are therefore higher (the EL size is around 164 kW and 9 kW for C_4 and C_8, respectively). Moreover, it can be observed that the LOH trend is more scattered for C_4 than for C_8 due to the fuel cell intervention which is more frequent for C_4 (the yearly number of fuel cell start-ups is 396 and 48 for C_4 and C_8, respectively).

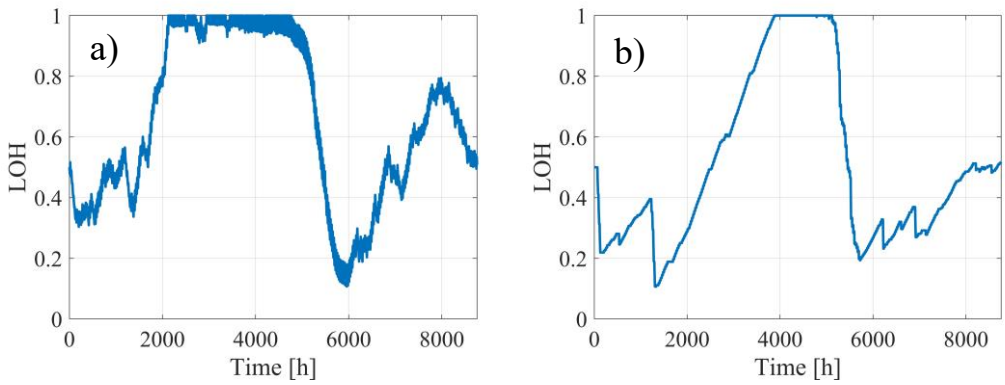

Figure 4.4 LOH profile over the year for a) Configuration 4 with PV+H_2 (HT of 9373 kWh and ALK EL of 164 kW) and b) Configuration 8 with PV+ LI BT +H_2 (HT of 3414 kWh and ALK EL of 9 kW).

Configuration 8 is characterized by the same P2P architecture of the REMOTE system, i.e., alkaline electrolyzer, PEM fuel cell and Li-ion batteries. However, the LCOE of C_8 (0.500 €/kWh) is lower than that found in Chapter 3 for the REMOTE project (0.571 €/kWh). This cost difference is mainly due to the electrolyzer and fuel cell, whose sizes are higher in the REMOTE configuration. In fact, as previously stated, the hydrogen equipment in REMOTE is constrained by a minimum installed power (and also by the specific sizes of the products that are available from the project suppliers). It should be noted that a higher capacity of the hydrogen tank is found in the optimized configuration (C_8). As highlighted in Section 3.4.1, this is necessary to make the village completely autonomous from the use of diesel.

Generally, it can be said that the analysed renewable P2P systems are more cost-competitive with respect to the exiting diesel-based option (whose LCOE is around 0.86 €/kWh as previously reported in Table 3.8), even considering the most expensive configurations that relay only on local RES and hydrogen (around 0.84 €/kWh referring to the case with PEM electrolyzers). Moreover, besides the proven economic profitability, environmental advantages are also associated to these types of stand-alone RES-based power systems since they can avert the release of pollutants and GHG emissions, which are mainly related to the combustion of diesel fuel. [152]. It was found that approximately 286 tonnes of CO_2 are at present emitted per year by using diesel generators in Ginostra. Their release could be avoided by employing a renewable P2P system, such as those presented in this analysis.

4.3.2 Froan case study

The Froan islands are at present connected to the mainland grid through an outdated submarine cable that has to be replaced in the near future (see Chapter 3, Section 3.2). The replacement of the sea cable would require expensive engineering and civil works (as also shown by the economic outcomes reported in Figure 3.25). Alternative solutions need therefore to be considered to provide electrical power to the site. An immediate choice could be the installation of an on-site diesel generator; however, its usage should be limited as much as possible, being the Froan archipelago a nature reserve and conservation area. Energy production based on local RESs thus represents an interesting and eco-friendly alternative. Electrical energy storage systems should be accounted for in the RES-based solution to make the island independent from imported fuels. EES devices would in fact improve the exploitation of local renewable energy and mitigate the variability in renewable energy production and load demand, thus securing the power supply throughout the entire year. In addition to being an environmentally sustainable alternative, relying on local RESs could potentially lead to cost saving from not having to ship diesel fuel regularly to the islands.

The optimal sizing was first performed focusing on a system that fully rely on wind and solar energy. The lithium-ion technology was considered for the battery storage, given its better performance compared to the lead-acid alternative. PEM electrolyzers were supposed for the hydrogen production since they are better suited to be coupled with the highly variable wind energy source. These choices are also in line with the REMOTE solution designed for the Norwegian demonstration site.

Main sizing outcomes are reported in Table 4.3. The optimal fossil-fuel free configuration is characterized by the hybridization of both power sources (PV and WT) and storage (BT and H_2). Even though solar energy is scarce in the selected site (which is typical for northern climates), it is economically convenient to install PV together with wind turbines due to the higher predictability of the solar energy, which helps to mitigate the higher variability of the wind source. The optimal capacity of the battery system is 277 kWh. The required hydrogen storage capacity is instead much bigger, about 24 MWh, corresponding to slightly more than 700 kg of hydrogen. The resulting system LCOE is about 0.41 €/kWh, which is lower than the cost of energy referred to the alternative scenario involving sea cable replacement (approximately 0.63 €/kWh as reported in Table 3.8).

Most of the electrical load (approximately 77%) is covered by direct consumption of energy coming from the PV and WT. However, in order to make the site energy independent, the hybrid P2P system must intervene covering around 23% of the total load, of which around two-thirds are met by the fuel cell and the remaining part by the battery component. Approximately 32% of the entire RES production must be curtailed. This is a high value, but it is unavoidable in off-grid systems that aim at achieving the energy self-sufficiency by relaying completely on local renewable energy sources.

Table 4.3 Main sizing results referred to the totally renewable power system.

WT [kW]	**PV [kW]**	**BT [kW]**	**EL [kW]**	**FC [kW]**	**HT [kWh]**	**LCOE [€/kWh]**
483	318	277	115	90	23,926	0.410

Main technical key performance indicators (KPI) are summarized in Table 4.4: according to the system simulation, battery modules and fuel cell stacks must be replaced once during the project lifespan (supposed to be 20 years) with lifetimes of 12 and 11 years, respectively; whereas the electrolyzer stack, whose lifetime is around 7 years, needs two replacements.

Table 4.4 Main technical KPIs referred to the totally renewable power system.

$N_{h,yr,EL}$ [h]	$N_{st,yr,EL}$ [-]	L_{EL} [y]	$N_{h,yr,FC}$ [h]	$N_{st,yr,FC}$ [-]	L_{FC} [y]	L_{BT} [y]
3,294	293	7	2,022	234	11	12

The resulting HT capacity of about 23,926 kWh (i.e., 718 kg) is high, but still reasonable and technically feasible. For the sake of completeness, an additional simulation was performed considering a maximum storage pressure of 200 bar, which might be required to reduce the HT volume in case of space unavailability in the site (the maximum storage pressure for the reference case is 30 bar). Given that the operating pressure of the electrolyzer is 30 bar, it is necessary the installation of a compressor to allow the produced hydrogen to be stored in the HT. Compression costs were taken from Yang *et al.* [227]. Storage costs were modified to take into account that the hydrogen vessel must withstand a higher pressure [228]. Increased power consumption due to compression operation was also considered. The LCOE of the new configuration was found to be approximately 0.428 €/kWh, which is slightly higher than the cost of energy of the reference case with 30 bar maximum pressure (0.410 €/kWh as reported in Table 4.3). Even though the hydrogen P2P pathway becomes more expensive because of the presence of the compressor and of the higher pressure to be managed, hydrogen still plays a key role in this alternative HRES layout with about 20,120 kWh of storage capacity. Overall, it can be noted that the required capacity of the hydrogen vessel is higher than that defined in the REMOTE project for the Froan site. However, this value is necessary to achieve the independence from fossil fuels in a cost-competitive way. More comparable sizes are found when allowing the diesel generator to operate along the year, as in the case of the REMOTE system (see Table 4.5).

The sizing optimization was then performed including the diesel generator component to better investigate the role of hydrogen in the optimal design of stand-alone HRESs. Cost-emissions Pareto fronts were derived considering different system scenarios: 1) RES+DG+BT+H_2 (BT+H_2), 2) RES+DG+BT (BT), 3) RES+DG+H_2 (H_2) and finally 4) RES+DG (No EES). Main techno-economic outcomes of the sizing simulations are summarized in Table 4.5.

From Figure 4.5 to Figure 4.8, the LCOE values are displayed as a function of the yearly CO_2 emissions (in tonnes per year) and fuel consumption (in litres per year). For the sake of comparison, a sensitivity analysis on the diesel fuel cost was performed in the range from 1 to 3 €/L. Diesel fraction (DF) values are also displayed for the cheapest configuration of each cost-emission curve. DF represents the fraction of the yearly electrical demand that is covered by the diesel

generator. For all the 4 scenarios, it can be seen that a reduction in the LCOE implies an increase in CO_2 emissions (or related fuel consumption).
Concerning the hybrid storage scenario (Figure 4.5) and 2 €/L as fuel price, it was found that the most cost-effective configuration has an LCOE of around 0.34 €/kWh with approximately 84 tonnes of CO_2 released yearly by the system operation (the related DF value is around 11.6 %). The LCOE of the cheapest configuration moves to 0.26 and 0.38 €/kWh when considering a fuel price of 1 and 3 €/L, respectively, which shows the high influence of this value on the final cost of energy.

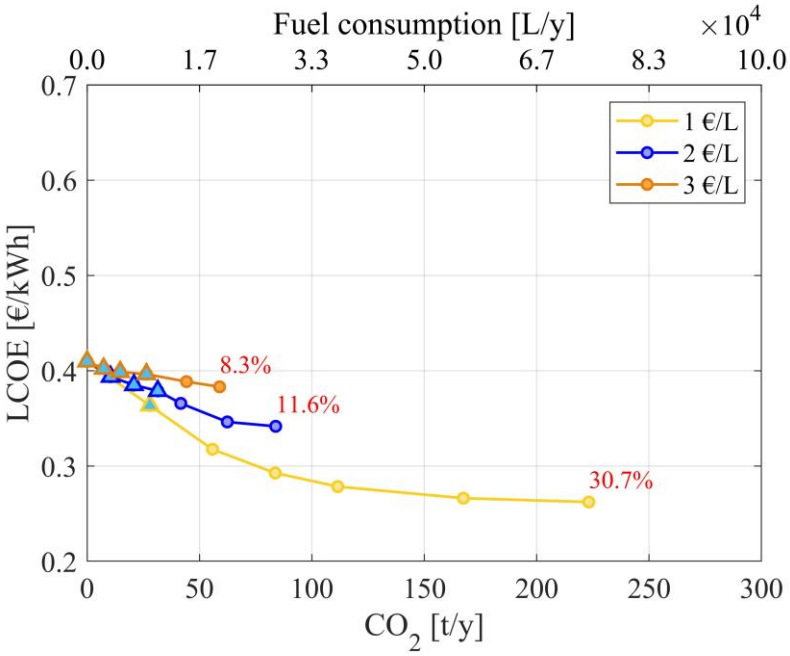

Figure 4.5 Cost-emission Pareto front for the BT + H_2 scenario (light blue triangles correspond to configurations with the presence of hydrogen. Red coloured percentages represent DF values).

By comparing Figure 4.5 and Figure 4.6, it can be noted that the least expensive configurations are the same for the BT+H_2 and BT scenarios. This means that there is no need to include hydrogen when no constraints on the use of diesel generators are imposed: the cost optimal system is in fact composed of RESs (both PV and WT) together with batteries and diesel generators. By decreasing the amount of allowed CO_2 in the BT+H_2 scenario, it can be observed that the hydrogen storage system appears in the optimal system configuration at around 30 to 40 tonnes of CO_2 per year (light blue triangles in Figure 4.5). The cost of energy then slightly increases up to 0.41 €/kWh when a totally renewable-based system is achieved. Regarding instead a system that relies only on batteries as energy storage (Figure 4.6), by progressively limiting the operation of the diesel generator, the LCOE rises sharply to a maximum of 0.64 €/kWh. Hydrogen

thus turns out to be necessary to limit system costs when energy independence from fossil fuels is pursued.

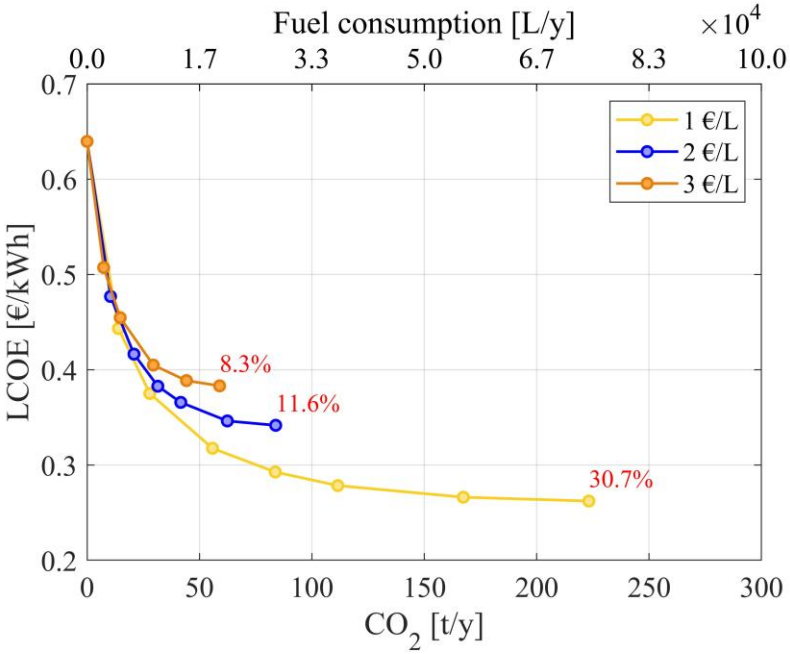

Figure 4.6 Cost-emission Pareto front for the BT scenario (red coloured percentages represent DF values).

Results for the H_2 scenario (where only hydrogen is assumed as energy storage medium) are shown in Figure 4.7. The related costs are a bit higher compared to the H_2+BT scenario of Figure 4.5. However, the LCOE trends are similar without an abrupt LCOE rise in the low CO_2 region. In fact, the cost of energy slowly increases until reaching a value of 0.44 €/kWh for the diesel-free configuration.

Figure 4.8 refers to a scenario with only RES and diesel genset, without the inclusion of electrical energy storage devices. It is shown that yearly CO_2 emissions cannot go below 81 tonnes per year, which corresponds to an DF of around 10.7%. The LCOE at this DF value is in the range from 0.77 to 0.9 €/kWh. For the sake of completeness, a system configuration with only DG was also simulated resulting in an LCOE of 0.81 €/kWh (considering 2 €/L as fuel price) and approximately 648 tonnes of CO_2 per year. Energy storage systems are therefore crucial to reduce the system cost and reach higher levels of RES penetration.

It is also noteworthy that the renewable configurations based on EES devices are cost-competitive compared to an alternative solution based on the sea cable replacement (whose LCOE is 0.630 €/kWh).

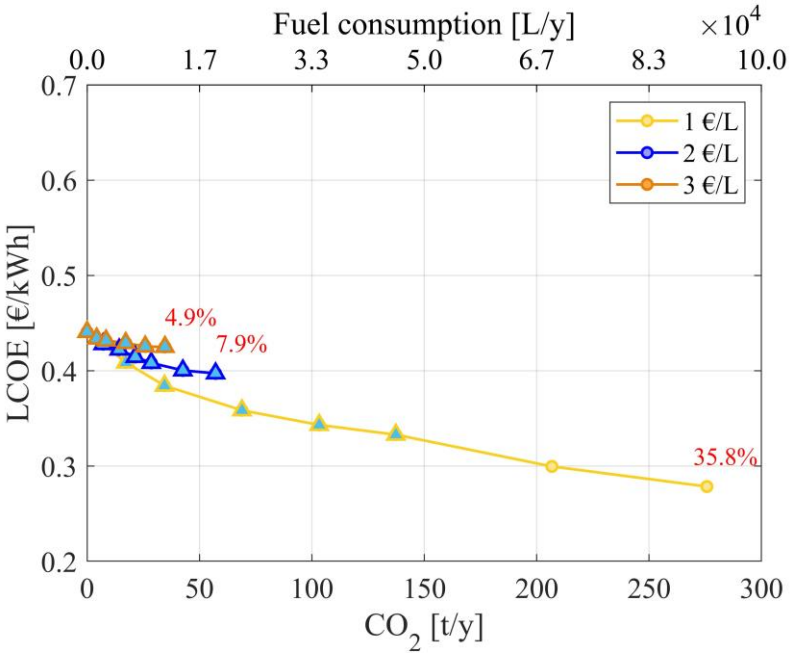

Figure 4.7 Cost-emission Pareto front for the H_2 scenario (light blue triangles correspond to configurations with the presence of hydrogen. Red coloured percentages represent DF values).

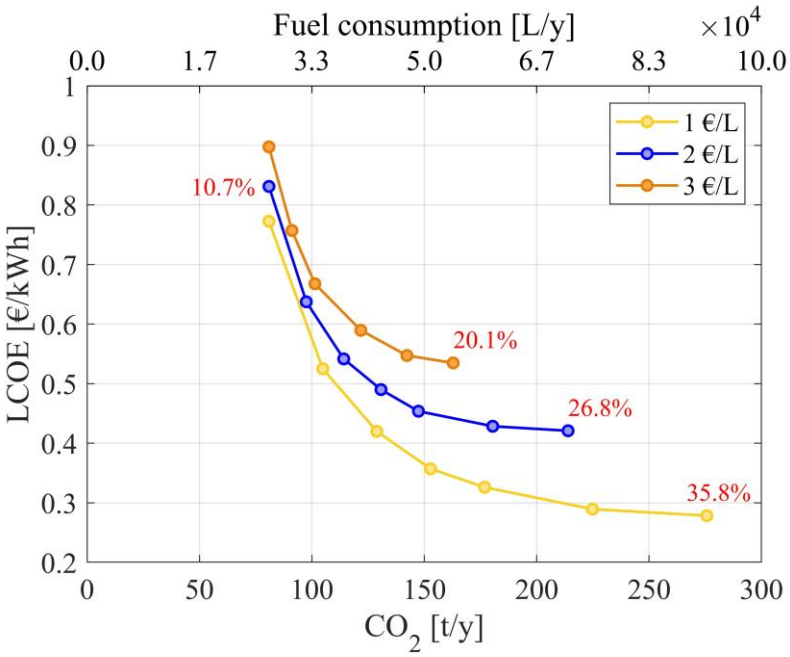

Figure 4.8 Cost-emission Pareto front for the No EES scenario (red coloured percentages represent DF values).

Figures Figure 4.9, Figure 4.10 and Figure 4.11 focus on the BT+H_2 and BT scenarios to better understand the LCOE trends previously reported. The cheapest configuration is characterized by the same system architecture for the two scenarios: around 254 kW of PV, 407 kW of WT, 774 kWh of BT and 90 kW of

DG. By limiting the operation of the DG, the resulting LCOE increment is due to an increase in size of the EES and RES technologies.

More specifically, concerning the BT scenario, Figure 4.9 shows that the rated capacity of the battery increases sharply, reaching a value of around 3,090 kWh for the configuration with no DG (which is approximately 4 times higher than the battery capacity with no CO_2 constraints). As displayed in Figure 4.10, PV and WT sizes increase as well, moving from 254 and 407 kW to around 512 and 912 kW, respectively.

The system configuration of the BT+H_2 scenario is the same as that of the BT scenario until around 40 tonnes of CO_2 per year (i.e., 120,000 L of diesel fuel per year). Below this CO_2 value, installing an H_2-based storage system becomes economically convenient. Figure 4.11 shows that the required FC and EL sizes lie in the range of 80 to 90 kW and 105 to 115 kW, respectively. The H_2 tank capacity instead increases considerably up to about 718 kg when no diesel fuel is consumed. The lower LCOE for configurations with storage hybridization (i.e., battery plus hydrogen) can be graphically explained through Figure 4.9 and Figure 4.10. The presence of hydrogen is useful to avoid the oversizing of the battery component thanks to the low-cost high-capacity H_2 tanks: when no CO_2 is released by the system, the battery capacity is around 277 kWh in the BT+H_2 scenario, which is approximately 11 times lower than the size that is required in the BT scenario. The hybrid storage case also needs smaller PV and WT sizes: 318 kW compared to 512 kW for PV and 483 kW compared to 912 kW for WT in the DG-free case. This is because the long-term capability of the hydrogen storage leads to a better exploitation of the local renewable energy sources.

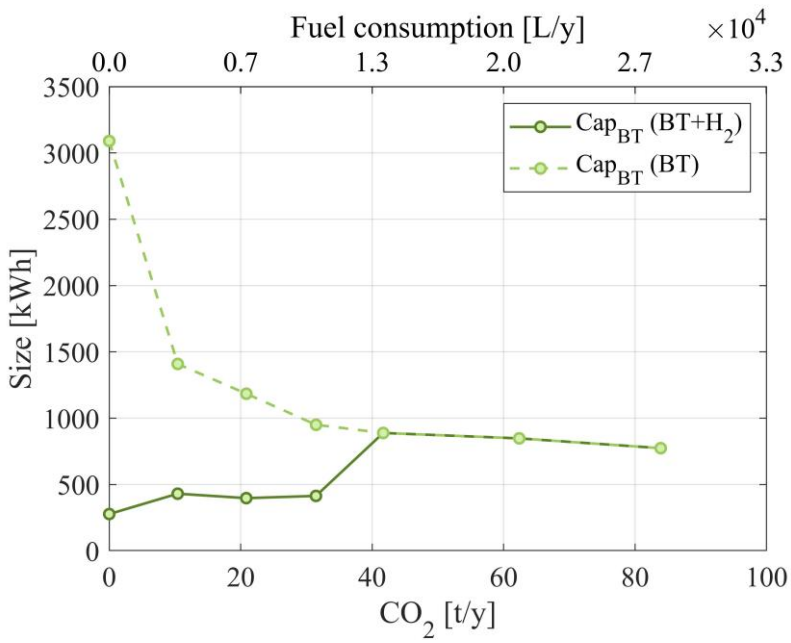

Figure 4.9 Battery capacity for the BT+H_2 and BT scenarios (case with diesel fuel cost of 2 €/L).

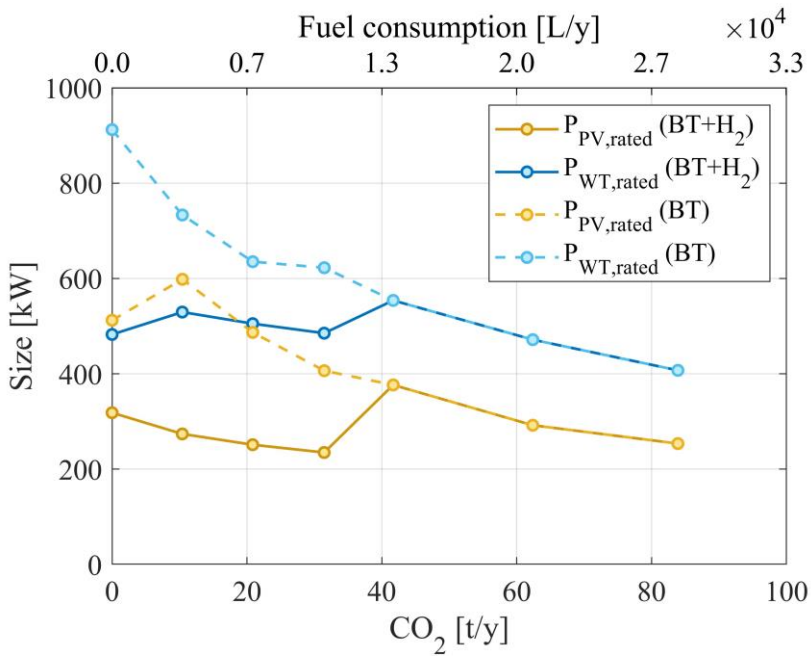

Figure 4.10 RES (PV and WT) rated power for BT+H_2 and BT scenarios (case with diesel fuel cost of 2 €/L).

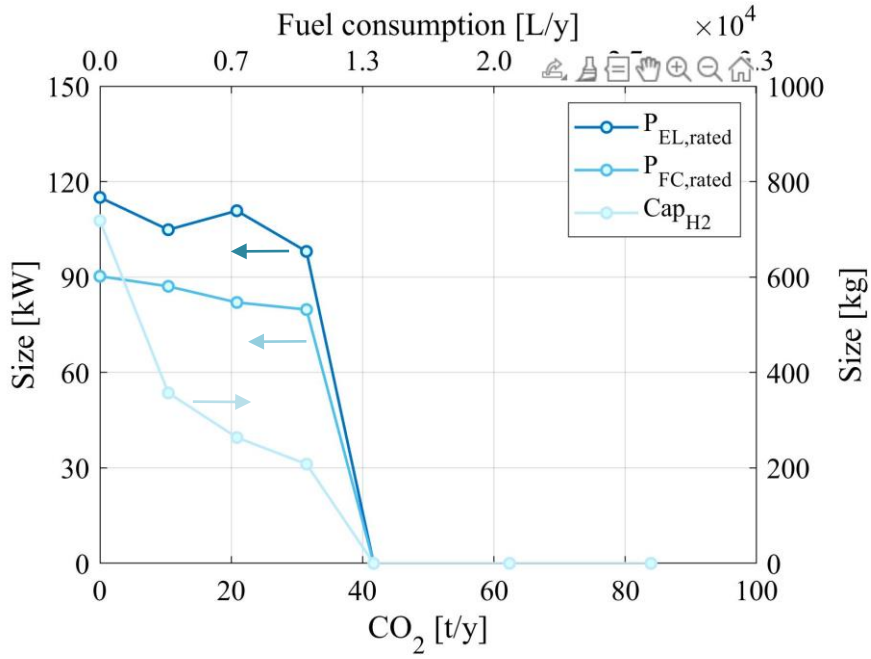

Figure 4.11 EL and FC rated power (left) and HT capacity (right) for BT+H_2 scenario (case with diesel fuel cost of 2 €/L).

Table 4.5 Sizing results and LCOE values for the different scenarios (case with diesel fuel cost of 2 €/L).

Config.	WT [kW]	PV [kW]	BT [kWh]	EL [kW]	FC [kW]	HT [kWh]	DG [kW]	CO_2 [t/y]	LCOE [€/kWh]
1. BT+H_2	483	318	277	115	90	23926	0	0	0.410
	530	274	431	105	87	11902	78	10	0.394
	505	251	397	111	82	8786	78	21	0.385
	485	235	414	98	80	6932	78	31	0.379
	554	377	889	-	-	-	81	42	0.366
	472	292	848	-	-	-	87	63	0.346
	407	254	774	-	-	-	90	84	0.342
2. BT	912	512	3090	-	-	-	0	0	0.640
	733	598	1409	-	-	-	74	10	0.477
	635	487	1185	-	-	-	77	21	0.416
	623	406	950	-	-	-	77	31	0.383
	554	377	889	-	-	-	81	42	0.366
	472	292	848	-	-	-	87	63	0.346
	407	254	774	-	-	-	90	84	0.342
3. H_2	526	361	-	148	93	25369	-	0	0.441
	570	305	-	153	90	17580	64	7	0.428
	557	303	-	131	90	16783	78	14	0.422
	561	307	-	139	87	9445	78	21	0.415
	551	294	-	125	84	8879	78	29	0.408
	525	256	-	115	81	7587	78	43	0.400
	519	235	-	95	76	7091	81	57	0.397
4. No EES	1977	1046	-	-	-	-	88	81	0.831
	1534	613	-	-	-	-	89	98	0.637
	1136	516	-	-	-	-	89	114	0.542
	1010	349	-	-	-	-	90	147	0.490
	808	307	-	-	-	-	90	181	0.454
	577	254	-	-	-	-	90	214	0.429

The ability of hydrogen to mitigate the LCOE rise is also clearly displayed in Figure 4.12 and Figure 4.13, where the LCOE breakdown is shown considering a diesel price of 2 €/L. By decreasing the diesel fuel consumption, the steep rise in LCOE of the BT scenario could be avoided through the inclusion of hydrogen: the cost contributions due to battery, photovoltaic and wind turbine systems (green, yellow and dark blue regions, respectively) remain almost constant, or even decrease, when hydrogen appears in the cost-optimal configuration (Figure 4.12). These contributions, instead, become increasingly relevant when trying to

enhance the independence from fossil fuels relying only on batteries as EES (Figure 4.13).

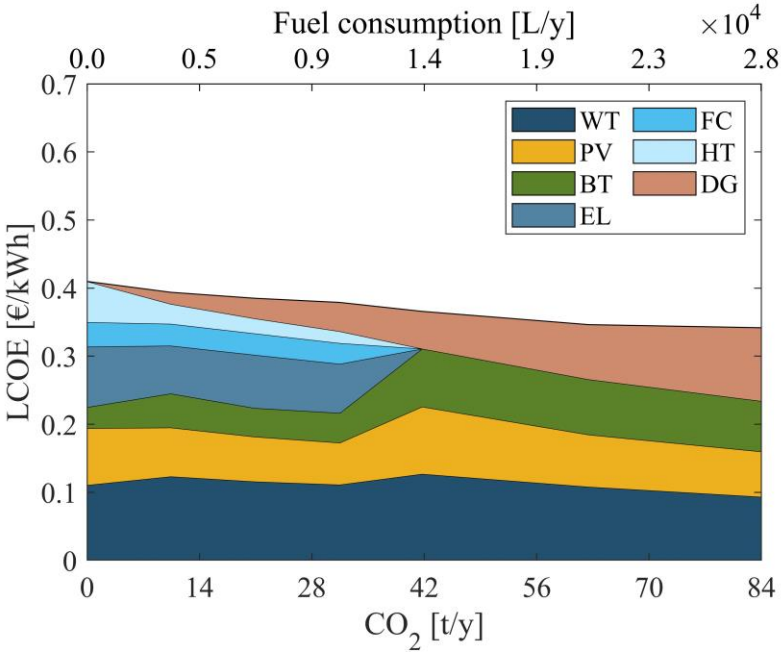

Figure 4.12 LCOE breakdown for the BT+H_2 scenario as a function of the yearly CO_2 emissions and fuel consumption (case with diesel fuel cost of 2 €/L).

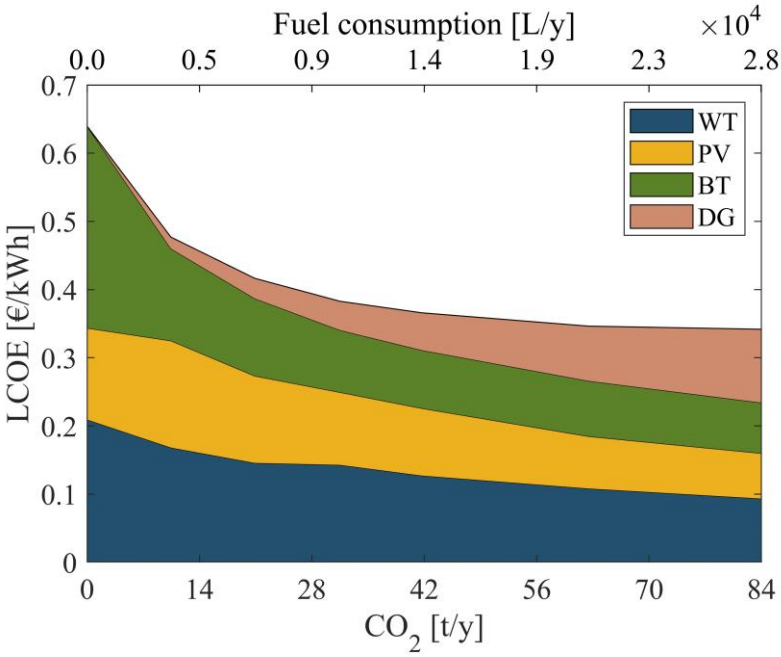

Figure 4.13 LCOE breakdown for the BT scenario as a function of the yearly CO_2 emissions and fuel consumption (case with diesel fuel cost of 2 €/L).

Conclusions

A methodology for the optimal sizing of stand-alone renewable P2P systems has been developed by means of the PSO technique. Different typologies of batteries (Li-ion and lead-acid) and electrolyzers (alkaline and PEM) were investigated to provide a wider overview on different technology options for P2P systems in off-grid remote areas. When including a diesel generator, cost-emission Pareto fronts were also developed for different energy system configurations. The ε-constraint method was employed to address the multi-objective optimization problem, minimizing both the LCOE and CO_2 emissions of the system. The sizing methodology was applied to two real insular communities: Ginostra in the south of Italy and the Froan islands in Norway.

Concerning Ginostra, it was found that local RESs coupled with battery and/or hydrogen are cost-competitive compared to the current power system based on diesel generators (whose cost of energy is around 0.86 €/kWh). The adoption of Li-ion batteries is a better choice with respect to the lead-acid alternative even though investment, operation and maintenance costs of Li-ion batteries are higher. Regarding the H_2-based energy system, alkaline electrolyzers are at present more cost-effective than PEM devices because of the lower cost and higher durability (i.e., lower number of stack replacements). However, the PEM electrolyzer is characterized by greater compactness and better dynamic performance, which is positive when coupled with highly fluctuating renewable energy sources. A P2P solution that relies only on batteries (0.54-0.60 €/kWh) is cheaper than a system with only hydrogen (0.74-0.84 €/kWh). However, the cheapest configuration consists of both batteries and hydrogen (0.50-0.51 €/kWh for the hybrid storage with Li-ion BTs). In fact, the storage hybridization is useful to avoid the over-dimensioning of the battery capacity and to enhance the exploitation of the local solar source.

Local renewable energy sources are also highly effective in the northern climate of Froan. When no constraints are imposed on the operation of the DG, the cheapest configuration includes renewable generators (PV and WT), batteries and diesel genset. The DG component is required to avoid the installation of batteries with too large capacities. At the same time, batteries are necessary to better exploit renewable energy and reduce fuel consumption, thus lowering the cost of energy. By progressively increasing the energy independence from fossil fuels, the inclusion of hydrogen was shown to be essential to limit the LCOE rise thanks to its cost-effective longer-term storage capability, which allows the battery and the PV/WT systems not to be oversized. Concerning the case with no diesel, the cost of energy of the HRES with storage hybridization is around 0.41 €/kWh, which is approximately two thirds of the LCOE of the BT scenario. The battery capacity that is required in the hybrid storage case is roughly 11 times smaller than that of a system with only batteries. Moreover, the RES rated power is almost halved when switching from battery-only storage to hybrid storage.

To sum up, storage systems are key components in remote areas to enhance the energy independence from fossil fuels, with hydrogen playing an essential role in reducing the cost of energy. In the following chapter, the HRES optimization problem will be further investigated by means of a different technique based on mixed integer linear programming (MILP) to address both the design and dispatch optimization.

Chapter 5

An MILP approach for the optimal design of off-grid H_2-based energy systems

Chapter 5 focuses on the development of an MILP-based optimization framework to perform the design and dispatch of off-grid hybrid renewable energy systems. A year-long time horizon was considered to model high-capacity energy storage solutions, which are necessary for off-grid areas that aim at achieving energy independence by relying on local renewable sources. Degradation costs of batteries and H_2-based devices were included in the objective function of the MILP problem. It is also performed the design optimization of the stand-alone microgrid in the presence of a general demand response program (DRP), in order to assess its impact on the sizing results. The optimization algorithm was also formulated with the inclusion of representative days to investigate benefits arising from their use. The modelling methodology was applied to the off-grid village of Ginostra and results were then compared to those obtained with the metaheuristic-based methodology defined in the previous chapter.

5.1 Introduction

The optimal design of hybrid renewable energy systems (HRESs) represents a critical stage that must be addressed to make the energy supply reliable, cost effective and less polluting. Different techniques can be found in the literature to deal with the design and scheduling sub-problems. The usage of representative periods could also be necessary to decrease the computational complexity of the problem.

Two-layer model

As reported in Chapter 4, two-layer (TL) models are largely used for the design optimization of HRESs. Design and dispatch problems are decoupled: the outer loop iteratively generates a potential design solution, whereas the inner one deals with the dispatch estimating the operational expenses referred to that system configuration. Design optimization is usually performed by employing metaheuristic algorithms, among which particle swarm optimization (PSO) and genetic algorithm (GA) are the most used. Referring to the dispatch problem, ruled-based strategies (RBSs) are widely employed since they represent a fast and realistic way of simulating the microgrid operation [141]. RBSs consist of a set of pre-defined priority rules to control the system based on the status and characteristics of the installed equipment. A detailed review about metaheuristic algorithms coupled with RBSs to cope with the optimal sizing of H_2-based systems can be found in Chapter 4 (Section 4.1). More advanced methods to deal with the second-layer scheduling problem can rely on mixed integer linear programming (MILP) techniques [130], [140], [229], [230], which have the advantage of handling the optimization of the units on/off status and operating power [231]. On the other hand, MILP-based approaches can cause increased complexity of implementation and computational burden compared to RBSs. This can result in further modelling approximations and reduced time horizons to allow the optimization problem to be solved through an MILP formulation. Li *et al.* [130] combined a GA-based sizing algorithm and an MILP-based scheduling algorithm to carry out the optimal sizing of a hydrogen-battery power-to-power (P2P) system. In order to limit the simulation time to a reasonable value, they used weekly average data as input for the bi-level optimization process. A similar bi-level procedure was then applied by Li *et al.* [229] to a more complex system dealing with cooling, heat and power loads. However, authors considered only 12 peak demand days to avoid long simulation times. A bi-level framework was also suggested by Rullo *et al.* [140], who employed an GA approach to search for the best system configuration and a rolling horizon MILP technique to find the best operation strategy of the system. They compared their sizing methodology with a more common procedure based on an RBS, showing investment saving as well as reduction of the operating costs in case the MILP approach was adopted. Comparisons among priority- and MILP-based operational strategies were also carried out by Fioriti *et al.* [230], who performed the outer optimization loop by means of PSO. They observed that the predictive approaches allowed a slightly lower system cost to be achieved, but at the expense of increased computational requirements.

Single-layer model

HRES design optimization can also be tackled by means of single-layer (SL) MILP formulations, which allow the system design and dispatch to be jointly

optimized. Unlike the two-layer methodology, the SL approach is able to impose constraints over specific time spans, e.g., yearly system reliability or CO_2 emissions over the year (in TL models, instead, this can only be done by penalizing a posteriori the fitness function of design solutions that do not satisfy the global constraints) [141]. The optimal sizing and scheduling of isolated mini-grids based on RESs coupled with batteries and diesel by means of a single-layer MILP was investigated in Refs. [141], [148], [157], [232]. By applying the MILP-based methodology, Malheiro *et al*. [148] observed that RES hybridization led to lower cost of energy and that the presence of diesel generators was necessary to limit the cost of the system, avoiding the battery oversizing. Moretti *et al.* [141] developed an MILP algorithm for the predictive design and dispatch optimization of microgrids, comparing it with a previously developed heuristic methodology. Authors formulated the SL MILP by considering only four weeks as representative of the entire year. They showed that the MILP-based approach led to lower electricity cost, improved reliability and greater RES penetration. A single-layer MILP formulation was also developed by Alberizzi *et al.* [157], [232], who performed the HRES sizing problem with limited time spans of 1 day and 1 month.

Representative periods

Representative periods are intended to reduce the computational burden of the sizing problem. Different techniques have been developed to select typical periods for the optimal system design. The averaging approach is an easy-applicable and straightforward technique and consists in taking the averaged value of different period [233]. Recently, increasing attention has been addressed towards clustering approaches such as k-means [226], k-medoids [234], [235] and hierarchical clustering [236]. There are also other time-series clustering methods such as dynamic time warping barycentre [237] and k-shape [237], but they have not been widely applied in the energy systems optimization field. In addition to clustering-based methodologies, typical periods can also be selected on the basis of pre-defined quality indexes [238], [239].

Schütz *et al.* [240] performed a comparison between aggregation methods for the selection of typical demand days for building energy systems. They investigated several clustering algorithms, which were found to significantly reduce the simulation time. In particular, they observed that the k-medoids provided the most reliable clustered load profile for the optimization of the system design. Different time series aggregation technique were also tested and compared by Kotzur *et al*. [233], who revealed that clustering algorithms (i.e., k-means, k-medoids and hierarchical) performed much better compared to the averaging method. Teichgraeber *et al.* [237] compared both conventional methods (k-means, k-medoids and hierarchical) and shape-based clustering methods (dynamic time warping barycentre and k-shape) with the electricity price as the clustered

attribute. They noticed that centroid-based clustering methods, such as k-means, represented the system operation more predictably than medoid-based approaches.

Particular attention should be given to the modelling of seasonal storage devices. Kotzur *et al*. [233] showed that traditional approaches including typical periods are not suitable for the design of systems based on seasonal storage. The use of typical weeks instead of typical days allowed them to improve the results, but still was not able to model the seasonality of the storage system. The design of long-term storage systems requires the time series to cover the whole year. Therefore, techniques based on representative periods should be applied to reduce the computational complexity of the problem and, at the same time, preserving the essential information that are required to size the long-term capacity of the storage device. Gabrielli *et al.* [226] proposed a novel MILP formulation based on the coupling of typical design days. This methodology allowed them to simulate a year time horizon with hourly resolution, while reducing the number of binary variables and thus the complexity of the optimization problem. The algorithm was then successfully applied for the design of a residential multi-energy system, which was optimized in terms of total annual costs and carbon dioxide emissions. Based on the work by [226], Kotzur *et al.* [241] derived a two-layer state methodology to link typical days over the year. They compared the novel approach with a more traditional one (characterized by independent aggregated typical periods), showing its advantages when applied to systems that heavily rely on long-term storage options. The methodology with interconnected representative days was also considered by Van der Heijde *et al.* [239] for the design of a solar district heating system with seasonal storage. They carried out the optimal scheduling in the form of a linear programming problem, whereas the design optimization was built through a genetic algorithm. The linked-days method was proved to replicate the behaviour of the full-year operation optimization with acceptable accuracy.

Demand response program

Demand response program (DRP) consists in modifying the load profile to best serve a specific objective. The aim of DRP is to reduce the mismatch between generation and consumption profiles by time shifting of dispatchable loads, with consequent economic benefits. An increasing number of studies is addressing the problem of demand response strategies for the optimum power management [242]. Nojavan *et al.* [243] investigated the operation of a grid connected PV-battery-fuel cell system in the presence of DRP. They found that DRP was effective both from an economic and environmental (i.e., lower CO_2 emissions) point of view. Majidi *et al.* [244] analyzed the optimal operation of an energy system including batteries and fuel cell and connected to the grid. They observed that the operating costs were reduced by around 5.5% when including a demand-side management mechanism. Economic benefits from DPR adoption

were also shown by Palma-Behnke *et al.* [245], [246], who investigated the operation of an off-grid HRES (composed of PV, wind turbine, diesel genset and battery bank) feeding residential loads. However, the literature about DRP applied to design optimization problem is very scarce [247], [248], and no studies were found about hydrogen-based systems. Tu *et al.* [247] developed a two-stage MILP model for the optimal sizing and scheduling of a PV-wind-battery-diesel system, including DRP. Results revealed that load deferring was effective at better aligning the electricity demand and RES generation profiles, thus reducing the required battery capacity (with consequent reduction in the system costs). Similar considerations were also reported by Amrollahi *et al.* [248], who performed the techno-economic optimization of a stand-alone energy system based on RESs coupled with batteries.

In the present study, a single-layer MILP method was formulated to deal with both the design and the scheduling of the system. A year-long time horizon, with hourly resolution, was considered to account for the seasonality of RES production and electrical demand, and thus to size seasonal energy storage devices (which are key components for off-grid communities that rely on local RESs) more accurately. The wear costs of batteries and H2-based devices were considered, in terms of operating costs included in the objective function of the optimization problem, in order to preserve as much as possible their state-of-health. Piecewise affine approximations of the efficiency curves of the electrolyzer and fuel cell were also implemented for a more detailed modelling of their performance. This is particularly suited when analyzing energy systems that involve variable renewable energy sources. To the best of our knowledge, no studies have been published that have dealt with single-layer MILP methods with 1-year time horizon and with the inclusion of degradation costs of the P2P components. Moreover, the effect of the demand response program (DRP) on the optimal size of the components was investigated. As previously stated, in the literature, demand-side management is mainly addressed by focusing on the system operation. Thus, it can be of great interest the analysis of how DRP can affect the optimal LCOE and system design.

5.2 MILP-based modelling of the HRES

An MILP problem is composed of an objective function, decision variables and constraints. The aim of the optimization process is to minimize the objective function by choosing the best set of decision variables that have to satisfy some specific constraints. The MILP problem can be expressed in the following general form:

$$\min_{x,y} OF = c^T x + d^T y \tag{5.1}$$

which is subjected to:

$$\begin{cases} A\,x + B\,y \leq b \\ x \geq 0, x \in \mathbb{R}^n \\ y \in \{0,1\}^m \end{cases} \tag{5.2}$$

where OF is the objective function to be minimized; x (whose dimension is n) and y (whose dimension is m) are the vectors of continuous and binary variables, respectively; c and d are the corresponding vectors containing the objective coefficients; A and B are the constraint matrixes and b is the constraint known-term vector. Both the objective function $OF = c^T\,x + d^T\,y$ and the various constraints $A\,x + B\,y \leq b$ are defined as linear combinations of the continuous and binary variables x and y.

A single-layer MILP problem was developed considering a time horizon T of one year with a time step discretization of one hour. The model is able to evaluate the optimal design of the off-grid energy system together with its optimal hourly dispatch strategy over the entire year.

Input data for the optimization problem are:

1. Meteorological data (i.e., site-specific temperature, irradiance and wind velocity data) ∀ t ∈ T.
2. The electricity demand ∀ t ∈ T.
3. Performance and cost data of the various components, i.e., photovoltaic panels (PV), wind turbines (WT), electrolyzer (EL), fuel cell (FC), hydrogen tank (HT), battery (BT) and diesel generator (DG).

The following decision variables are computed by the MILP methodology:

1. The sizes of the various components (i.e., PV, WT, EL, FC, HT, BT and DG), which are treated as continuous variables allowed to vary over a certain size range.
2. The on/off status of EL, FC, BT and DG ∀ t ∈ T.
3. The input and output power of EL and FC, the charging/discharging power of BT and the operating power of DG ∀ t ∈ T.
4. The energy stored in the HT and BT ∀ t ∈ T.
5. The curtailed power and not satisfied load ∀ t ∈ T.
6. The amount of load increase/decrease in case of DRP ∀ t ∈ T.

The power balance that must be satisfied at any time step on the AC bus is represented by the following equation:

$$\begin{aligned} P_{PV}(t) + P_{WT}(t) + P_{BT,dc}(t) + P_{FC}(t) + P_{DG}(t) + P_{NS}(t) \\ = P_{LD}(t) + P_{BT,ch}(t) + P_{EL}(t) + P_{CT}(t) \end{aligned} \tag{5.3}$$

where P_{PV} and P_{WT} represent the renewable power produced by PV and WT; $P_{BT,dc}$ and $P_{BT,ch}$ correspond to the discharging and charging power of the battery; P_{FC}, P_{EL} and P_{DG} are the operating powers of fuel cell, electrolyzer and diesel generator; P_{LD} is the total required power by the load; P_{NS} is the not satisfied load (i.e., the fraction of load not covered by the hybrid energy system) and finally P_{CT} is the curtailed power.

The sizing methodology by means of the MILP approach is outlined in Figure 5.1. Performance curves of the hydrogen-based devices were described by means of piecewise-affine approximations to be implemented in the MILP framework. Both design and operating variables are returned by the optimization problem, whose aim is to minimize the total annual cost of the HRES. A reliability constraint (in terms of loss of power supply probability, LPSP) was imposed to ensure the self-sufficiency of the stand-alone system. After the first MILP run, another MILP was performed to better evaluate the HRES yearly operation and hence the LCOE. Unlike the first MILP, in this second run, decision variables are only of an operational type (since component sizes have already been determined). The various steps of the optimal sizing procedure are discussed in detail in the following subsections.

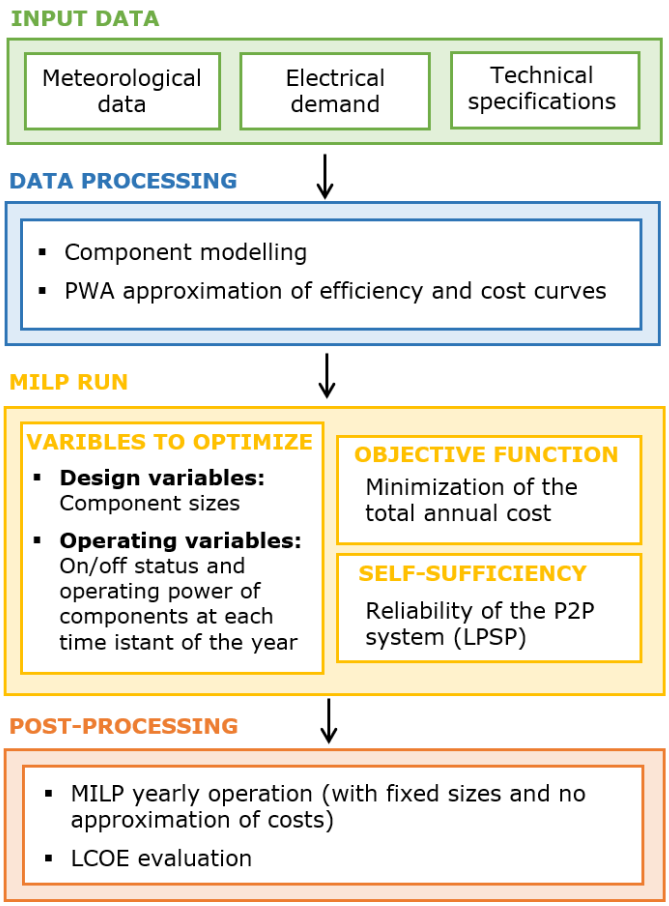

Figure 5.1 Sizing methodology of the HRES by means of the MILP technique.

5.2.1 Modelling of components

The modelling methodology described in Chapter 2 is here taken up and modified to be implemented in an MILP optimization framework. Below, updated and new mathematical formulations are presented and discussed.

The size of each component of the energy system was imposed to lie between a minimum and maximum value according to the following constraints (with j = PV, WT, FC, EL, DG and i = BT, HT):

$$P_{j,rated,min} \leq P_{j,rated} \leq P_{j,rated,max} \tag{5.4}$$

$$Cap_{i,min} \leq Cap_i \leq Cap_{i,max} \tag{5.5}$$

where $P_{j,rated}$ (in kW) corresponds to the rated power of the j-th component and Cap_i (in kWh) represents the rated storage capacity of the i-th component. In particular, $P_{EL,rated}$ is the gross inlet rated power of the electrolyzer (gross of BOP losses) and $P_{FC,rated}$ is the net outlet rated power of the fuel cell (net of BOP losses). The lower size limit of each technology was set to zero. A certain component is thus selected in the system configuration whenever the MILP simulation returns a value of its size greater than zero.

Electrolyzer and fuel cell

In order to define the minimum and maximum operating power of the electrolyzer and fuel cell, the following auxiliary variable must be defined (with j = EL, FC):

$$P_{j,rated,aux}(t) = P_{j,rated}\, \delta_j(t) \tag{5.6}$$

where $P_{j,rated}$ (in kW) is the EL/FC rated power and δ_j is a binary variable that is equal to 1 in case the EL/FC device is operating and 0 otherwise. The auxiliary variable of Eq. (5.6) allows the product of the two decision variables to be transformed in the following set of linear inequalities (5.7) to (5.10):

$$P_{j,rated,aux}(t) \leq P_{j,rated} - \left(1 - \delta_j(t)\right) P_{j,rated,min} \tag{5.7}$$

$$P_{j,rated,aux}(t) \geq P_{j,rated} - \left(1 - \delta_j(t)\right) P_{j,rated,max} \tag{5.8}$$

$$P_{j,rated,aux}(t) \leq P_{j,rated,max}\, \delta_j(t) \tag{5.9}$$

$$P_{j,rated,aux}(t) \geq P_{j,rated,min}\, \delta_j(t) \tag{5.10}$$

It is thus possible to impose the constraint on the minimum and maximum operating power of the electrolyzer and fuel cell as follows (with j = EL, FC):

$$y_{j,min}\, P_{j,rated,aux}(t) \leq P_j(t) \leq y_{j,max}\, P_{j,rated,aux}(t) \tag{5.11}$$

where the terms $y_{j,min}$ and $y_{j,max}$ represent the lower and upper bounds of the EL/FC modulation range.

A piecewise-affine (PWA) approximation was implemented to describe the detailed nonlinear performance curves of the electrolyzer and fuel cell devices, i.e., the relationship between the input and output operating power. The curves were described by means of n line segments and the positions of the related n+1 breakpoints (i.e., $\{(x_1,\ y_1),\ \ldots,\ (x_{n+1},\ y_{n+1})\}$) were found by performing an optimization problem [249]. First, a discretized performance curve composed of M points $\{(p_{in,model,1},\ p_{out,model,1}),\ \ldots,\ (p_{in,model,M},\ p_{out,model,M})\}$ was generated starting from the electrolyzer/fuel cell models described in Chapter 2. Then the optimal positions of the n+1 breakpoints were computed by minimizing the sum of the squares of the difference between the approximated and model value of the electrolyzer/fuel cell outlet power:

$$min\left(\sum_{m=1}^{M}\left(p_{out,approx,m} - p_{out,model,m}\right)^2\right) \tag{5.12}$$

where $p_{out,approx,m}$ and $p_{out,model,m}$ (in kW/cm^2) represent the approximated and model specific outlet powers, respectively. The term $p_{out,approx,m}$ was derived according to the following relationship:

$$p_{out,approx,m} = \alpha_i\left(p_{in,model,m} - x_i\right) + y_i \tag{5.13}$$

where the slope of the i-th line segment is:

$$\alpha_i = \frac{y_{i+1} - y_i}{x_{i+1} - x_i} \tag{5.14}$$

and $p_{in,model,m}$ lies in the following operating range:

$$x_i \leq p_{in,model,m} \leq x_{i+1} \tag{5.15}$$

The following constraint was also added to the fitting problem:

$$x_{i+1} \geq x_i \tag{5.16}$$

Moreover, unlike [249], the first and last breakpoints were imposed to coincide with the first and last point of the original curve, similarly to what performed by Gabrielli *et al.* [161], as follows:

$$(x_1, y_1) = \left(p_{in,model,1}, p_{out,model,1}\right) \tag{5.17}$$

$$(x_{n+1}, y_{n+1}) = \left(p_{in,model,M}, p_{out,model,M}\right) \tag{5.18}$$

The PWA approximation of the performance curve was then implemented in the MILP formulation. This was performed by applying the following relationship for each i-th line segment of the curve (with j = EL, FC):

$$P_{j,out}(t) \leq \alpha_{j,i}\, P_{j,in}(t) + \beta_{j,i}\, \delta_j(t) \tag{5.19}$$

where $P_{j,in}$ and $P_{j,out}$ correspond to the inlet and outlet power of the EL/FC device, respectively. For the fuel cell, the inlet and outlet power correspond to the inlet hydrogen power (LHV basis) and generated electrical power (net value), respectively. For the electrolyzer, the inlet and outlet power represent instead the absorbed electrical power (gross value) and the produced hydrogen power (LHV basis). The term $\alpha_{j,i}$ is the slope of the i-th segment; whereas $\beta_{j,i}$ represents its intercept. The term $\alpha_{j,i}$ was computed in the following way:

$$\alpha_{j,i} = \frac{\eta_{j,i+1}\, z_{j,i+1} - \eta_{j,i}\, z_{j,i}}{z_{j,i+1} - z_{j,i}} \tag{5.20}$$

The intercept $\beta_{j,i}$ was instead derived as:

$$\beta_{EL,i} = \left[z_{EL,i}\, \eta_{EL,i} + \frac{\left(z_{EL,i+1}\, \eta_{EL,i+1} - z_{EL,i}\, \eta_{EL,i}\right) z_{EL,i}}{z_{EL,i} - z_{EL,i+1}}\right] P_{EL,rated} \tag{5.21}$$

$$\beta_{FC,i} = \left[z_{FC,i}\, \eta_{FC,i} + \frac{\left(z_{FC,i+1}\, \eta_{FC,i+1} - z_{FC,i}\, \eta_{FC,i}\right) z_{FC,i}}{z_{FC,i} - z_{FC,i+1}}\right] \frac{P_{FC,rated}}{\eta_{FC,n+1}} \tag{5.22}$$

where $\eta_{j,k}$ and $z_{j,k}$ represent the efficiency and the fraction of the rated inlet power (H_2 power for the FC and electrical power for the EL) referred to the k-th breakpoint of the performance curve, respectively. The term n stands for the number of line-segments of the curve. By grouping the various terms of Eq. (5.21) and (5.22) into the coefficient $c_{\beta_{j,i}}$ (except for the $P_{j,rated}$ term), Eq. (5.19) can be rearranged by including the auxiliary variable $P_{j,rated,aux}$, previously defined by Eq. (5.6), as follows:

$$P_{j,out}(t) \leq \alpha_{j,i}\, P_{j,in}(t) + c_{\beta_{j,i}}\, P_{j,rated,aux}(t) \tag{5.23}$$

Constraints were also added to impose the lower and upper bounds of the operating map:

$$z_1\, P_{EL,rated,aux}(t) \leq P_{EL,in}(t) \leq z_{n+1}\, P_{EL,rated,aux}(t) \tag{5.24}$$

$$\frac{z_1}{\eta_{n+1}}\, P_{FC,rated,aux}(t) \leq P_{FC,in}(t) \leq \frac{z_{n+1}}{\eta_{n+1}}\, P_{FC,rated,aux}(t) \tag{5.25}$$

Battery storage system

The battery component was modelled by introducing an energy balance in the form of the following linear equation:

$$E_{BT}(t) = E_{BT}(t-1)(1-\sigma_{BT}) + P_{BT,ch}(t-1)\,\Delta t\,\eta_{conv}\,\eta_{BT,ch} - \frac{P_{BT,dc}(t-1)\,\Delta t}{\eta_{BT,dc}\,\eta_{conv}} \tag{5.26}$$

where E_{BT} (in kWh) is the amount of energy stored in the battery, σ_{BT} is the battery self-discharge coefficient, η_{conv} is the efficiency of the battery converter, $\eta_{BT,ch}$ is the battery charging efficiency and $\eta_{BT,dc}$ is the battery discharging efficiency.

A certain energy content was imposed in the battery at the beginning of the simulation:

$$E_{BT}(t_{in}) = Cap_{BT}\, SOC_{in} \tag{5.27}$$

where SOC_{in} corresponds to the initial state of charge and Cap_{BT} (in kWh) is the battery rated capacity. The battery SOC is here defined as the ratio of the energy stored in the battery to the battery rated capacity. The following constraint was also introduced to enforce that the state of charge of the battery at the end of the year is equal to the initial one:

$$E_{BT}(t_{end})(1-\sigma_{BT}) + P_{BT,ch}(t_{end})\,\Delta t\,\eta_{rect}\,\eta_{BT,ch} - \frac{P_{BT,dc}(t_{end})\,\Delta t}{\eta_{BT,dc}\,\eta_{inv}} = Cap_{BT}\, SOC_{in} \tag{5.28}$$

At each time step, the energy stored in the battery should lie between a minimum and maximum value:

$$Cap_{BT}\, SOC_{min} \leq E_{BT}(t) \leq Cap_{BT}\, SOC_{max} \tag{5.29}$$

where SOC_{min} corresponds to the minimum SOC below which the battery should not operate in order to avoid a significant decrease in the number of cycles before replacement. SOC_{max} is instead the state of charge value that is reached by the battery when it is fully charged.

Unlike what performed in Refs. [130], [140], [229], it is not required the definition of binary variables specifying whether the battery is charging or discharging, with consequent saving of computational time. This is because the charging/discharging efficiency of the battery is lower than 1, and the energy lost by charging and discharging the battery at the same time instant has a greater influence than the chosen MIP gap Therefore, the optimization process is able to automatically select the operating mode of the battery at each time step [161].

Pressurized hydrogen tank

Analogously to the battery storage, the energy that is stored in the tank in the form of hydrogen was determined at each time step according to the following energy balance equation:

$$E_{H2}(t) = E_{H_2}(t-1) + P_{EL,out}(t-1)\,\Delta t - P_{FC,in}(t-1)\,\Delta t \qquad (5.30)$$

where $P_{EL,out}$ (in kW) is the electrolyzer outlet power (corresponding to the generated H_2 power on LHV basis) and $P_{FC,in}$ (in kW) is the fuel cell inlet power (corresponding to the consumed H_2 power on LHV basis).

The equality constraints (5.31) and (5.32) were also considered to impose the same storage level at the beginning and at the end of the year so as to guarantee the self-sufficiency of the hydrogen storage:

$$E_{H2}(t_{in}) = Cap_{H2}\,LOH_{in} \qquad (5.31)$$

$$E_{H2}(t_{end}) + P_{EL,out}(t_{end})\,\Delta t - P_{FC,in}(t_{end})\,\Delta t = Cap_{H2}\,LOH_{in} \qquad (5.32)$$

where LOH_{in} corresponds to the level of hydrogen at the beginning of the simulation and Cap_{H2} (in kWh) is the hydrogen storage rated capacity. The LOH parameter can be defined as the ratio of the hydrogen pressure to the maximum storage pressure.

The energy content of the hydrogen tank should be between a minimum and maximum value, which are related to the hydrogen tank rated capacity and the LOH boundaries:

$$Cap_{H2}\,LOH_{min} \leq E_{H2}(t) \leq Cap_{H2}\,LOH_{max} \qquad (5.33)$$

In order to allow hydrogen to be supplied to the fuel cell, the H_2 pressure in the tank should not fall below a certain value (corresponding to a certain

LOH_{min}), which depends on the constraint on the FC supply pressure imposed by the manufacturer.

Diesel generator

Similarly to the electrolyzer and fuel cell, an auxiliary variable was introduced to deal with the product of a continuous ($P_{DG,rated}$) and binary (δ_{DG}) variable:

$$P_{DG,rated,aux}(t) = P_{DG,rated}\ \delta_{DG}(t) \tag{5.34}$$

where δ_{DG} is equal to 1 when DG is in operation and 0 when off. This new auxiliary variable allows transforming the product of $P_{DG,rated}$ and δ_{DG} in terms of linear constraints, in the same way as described for the H_2-based devices, i.e., Eqs. (5.7) to (5.10). The constraints below were then added to ensure that the diesel generator operates between a lower and upper bound:

$$y_{DG,min}\ P_{DG,rated,aux}(t) \leq P_{DG}(t) \leq y_{DG,max}\ P_{DG,rated,aux}(t) \tag{5.35}$$

where $y_{DG,min}$ and $y_{DG,max}$ define the modulation range of the diesel generator.

5.2.2 Objective function

The objective function of the optimization problem is given by the total annual cost of the system $C_{AC,tot}$ (in €/y) that is not discounted. It is composed of the following three contributions:

$$C_{AC,tot} = C_{AC,inv} + C_{AC,OM,fix} + C_{AC,op,var} \tag{5.36}$$

where $C_{AC,inv}$ is the annual investment cost, $C_{AC,OM,fix}$ corresponds to the yearly fixed costs related to maintenance and operation, which do not depend on the energy management strategy, and $C_{AC,op,var}$ represents the yearly operating costs that depend on the EMS.

The annual investment cost was defined as (with i = PV, WT, HT and j = EL, FC, BT, DG):

$$C_{AC,inv} = \frac{1}{L_{PR}} \left(\sum_i C_{inv,i} + \sum_j y_{BOP,j}\ C_{inv,j} \right) \tag{5.37}$$

where L_{PR} corresponds to the lifetime of the project, $C_{inv,i/j}$ is the investment cost of the i/j-th component and $y_{BOP,j}$ represents the fraction of the investment cost that is due to the balance of plant (BOP). The costs related to the battery

module, to the stack of the EL/FC devices and to the diesel engine are not included in the above equation since they are already accounted for in the $C_{AC,op,var}$ term. These costs in fact depend on the number of times the BT module, the EL/FC stacks and the DG genset are bought during the lifetime of the project (i.e., at the beginning of the project period and potentially one or more times due to replacements). And this number of purchases depends on their lifetime (which is a consequence of their size and degradation pattern related to the yearly dispatch profile). This also implies a linear depreciation of the components, meaning that their salvage value is directly proportional to their remaining life.
Concerning the investment cost of the electrolyzer and fuel cell, the power cost function described by Eq. (2.86) was used for C_{inv}. The PWA approach was chosen to approximate this cost function. The positions of the various breakpoints, related to the line segments of the PWA approximation, were computed by carrying out an optimization problem analogous to the one developed for the performance curves, i.e., Eqs. (5.12) to (5.18). However, when implementing the PWA approximation in the MILP problem, since the investment cost has to be minimized and the cost function is concave, the introduction of a binary variable is necessary for each of the n line segments in order to identify the active one. A continuous variable should also be added for each line segment. The detailed methodology used to implement the size dependency of the investment cost is described by Eqs. (5.38) to (5.43) below.

The rated power of the electrolyzer and fuel cell is given by (with j = EL, FC):

$$P_{j,rated} = \sum_{i=1}^{n} P_{j,rated,i} \tag{5.38}$$

where $P_{j,rated,i}$ represents the continuous variable associated to the i-th line segment, which must fulfil the following constraint:

$$z_{j,i}\, P_{j,rated,max}\, B_{j,i} \leq P_{j,rated,i} \leq z_{j,i+1}\, P_{j,rated,max}\, B_{j,i} \tag{5.39}$$

The constraint (5.40) must be introduced as well to ensure that no more than one binary variable $B_{j,i}$ is equal to 1:

$$\sum_{i=1}^{n} B_{j,i} \leq 1 \tag{5.40}$$

which means that the electrolyzer/fuel cell is installed when the sum of all $B_{j,i}$ variables is equal to 1. The electrolyzer/fuel cell investment cost for a certain rated power was then computed as follows:

$$C_{inv,j} = \sum_{i=1}^{n} \left(\alpha_{j,i} \, P_{j,rated,i} + \beta_{j,i} \, B_{j,i} \right) \tag{5.41}$$

where $\alpha_{j,i}$ and $\beta_{j,i}$ are the slope and the intercept of the i-th segment, respectively, and are defined as:

$$\alpha_{j,i} = \frac{c_{inv,j,i+1} \, z_{j,i+1} - c_{inv,j,i} \, z_{j,i}}{z_{j,i+1} - z_{j,i}} \tag{5.42}$$

$$\beta_{j,i} = \left[z_{j,i} \, c_{inv,j,i} + \frac{\left(z_{j,i+1} \, c_{inv,j,i+1} - z_{j,i} \, c_{inv,j,i} \right) z_{j,i}}{z_{j,i} - z_{j,i+1}} \right] P_{j,rated,max} \tag{5.43}$$

where $c_{inv,j,k}$ and $z_{j,k}$ represent the specific investment cost (in €/kW) and the fraction of the maximum rated power referred to the k-th breakpoint of the investment cost curve, respectively.

The fixed operating and maintenance cost term ($C_{AC,OM,fix}$) of Eq. (5.37) is given by the sum of the fixed OM costs of all the components in the system, which are expressed as a fraction of their investment cost (EL, FC, HT) or function of their rated size (PV, BT). The variable operating term ($C_{AC,op,var}$) was instead formulated according to the following expression (with i = BT_{ch}, BT_{dc}, EL, FC, DG):

$$C_{AC,op,var} = \sum_{t=1}^{8760} \sum_{i} C_{op,var,i}(t) \tag{5.44}$$

Below, all the various terms included in $C_{AC,op,var}$ are derived.

Battery operating cost

The battery operating cost was treated as a degradation cost, defined as the cost of the energy flowing through the battery bank. It is supposed that the battery component will be replaced once its overall throughput becomes equal to its lifetime throughput (LT). The lifetime throughput was computed starting from the lifetime curve in which different depth-of-discharge (DOD) values are reported together with the related cycles-to-failure (CTF) values [158], as described in Chapter 2 by Eq. (2.89). The battery operating cost during charging (in €/h) can then be estimated as [229]:

$$C_{op,var,BTch}(t) = \frac{C_{BT,mod}}{LT} \, P_{BT,ch}(t) \, \eta_{BT,ch} \, \eta_{rect} \tag{5.45}$$

By considering the definition of LT, the above equation can be rearranged as follows:

$$C_{op,var,BTch}(t) = \frac{c_{BT,mod}\ \eta_{BT,ch}\ \eta_{rect}}{2\ (DOD\ CTF)_{avg}}\ P_{BT,ch}(t) \tag{5.46}$$

Similarly, the operating cost during the battery discharging is:

$$C_{op,var,BTdc}(t) = \frac{c_{BT,mod}}{2\ (DOD\ CTF)_{avg}\ \eta_{BT,dc}\ \eta_{inv}}\ P_{BT,dc}(t) \tag{5.47}$$

where $C_{BT,mod}$ (in €) is the battery module cost, whereas $c_{BT,mod}$ (in €/kWh) is the specific battery module cost. As shown in Eq. (5.46) and (5.47), the average of the product of DOD and CTF was used as reported by the definition of the lifetime throughput.

Electrolyzer and fuel cell operating cost

The cost incurred in operating the electrolyzer and the fuel cell (in €/h) can be defined as (with j = EL, FC) [229]:

$$C_{op,var,j}(t) = \left(\frac{C_{j,stack}}{N_{h,tot,j}} + C_{OM,var,h,j}\right)\delta_j(t) + C_{j,start}(t) \tag{5.48}$$

where $N_{h,tot,j}$ (in h) represents the total number of life hours of the device, $C_{j,stack}$ (in €) is the EL/FC stack cost and $C_{OM,var,h,j}$ (in €/h) is the variable hourly OM cost. The variable OM cost term was instead neglected for the battery as commonly assumed in the literature [130], [229]. By considering the auxiliary variable $P_{j,rated,aux}(t)$, previously defined by Eq. (5.6), the above expression can be rearranged in the following way:

$$C_{op,var,j}(t) = \left(\frac{c_{j,stack}}{N_{h,tot,j}} + c_{OM,var,h,j}\right)P_{j,rated,aux}(t) + C_{j,start}(t) \tag{5.49}$$

where $c_{j,stack}$ (in €/kW) is the specific stack cost of the electrolyzer and fuel cell and $c_{OM,var,h,j}$ (in €/kW/h) is the specific variable hourly OM cost. As described in Section 2.3.2, the latter term is set to 2/3 of the total OM cost (4% of the investment cost) and is proportional to the operating time of the device:

$$c_{OM,var,h,j} = \frac{2}{3}\ \frac{4}{100}\ \frac{c_{inv,j}}{8760} \tag{5.50}$$

The variable $C_{j,start}(t)$ (in €/start-up) corresponds to the start-up cost associated to the electrolyzer and fuel cell, which occurs only in case the device is

turned on at time t. In the MILP formulation, it was described by the following two linear constraints:

$$C_{j,start}(t) \geq 0 \tag{5.51}$$

$$C_{j,start}(t) \geq \frac{c_{j,stack}}{N_{start,tot,j}} \left(P_{j,rated,aux}(t) - P_{j,rated,aux}(t-1)\right) \tag{5.52}$$

where $N_{start,tot,j}$ is the total amount of start-ups that the device can withstand during its lifetime.

The stack cost, as reported in Table 2.20, was defined as a fraction of the system investment cost. In order to avoid the introduction of new auxiliary variables, which would make the problem more complex, the investment cost that appears in Eq. (5.49) (in the $c_{j,stack}$, $c_{OM,var,j}$ and $C_{j,start}$ terms) was linearly approximated.

Diesel generator operating cost

The total operating cost related to the diesel generator component is:

$$C_{op,var,DG}(t) = C_{DG,fuel}(t) + C_{OM,op,h,DG}\, \delta_{DG}(t) + \frac{C_{rep,DG}}{N_{h,tot,DG}}\, \delta_{DG}(t) \tag{5.53}$$

where $C_{DG,fuel}$ (in €/h) is the DG cost related to fuel consumption, $C_{OM,op,h,DG}$ (in €/h) is the hourly OM cost related to DG operation, $C_{rep,DG}$ (in €) is the DG replacement cost and $N_{h,tot,DG}$ (in h) is the DG lifetime operating hours. The first term of Eq. (5.53) also accounts for a start-up penalty:

$$C_{DG,fuel}(t) = cons_{DG,op}(t)\, cost_{fuel} + C_{DG,fuel,start}(t) \tag{5.54}$$

where $cost_{fuel}$ (in €/L) is the fuel price, $cons_{DG,op}$ (in L/h) is the fuel consumption depending on the diesel generator output power and $C_{DG,fuel,start}$ (in L/start-up) is the cost associated to the extra fuel consumed because of the DG start-up. The $cons_{DG,op}$ term was expressed according to the fuel consumption curve reported in Eq. (5.55) (additional details can be found in Section 2.2.5).

$$cons_{DG,op}(t) = a_{DG}\, P_{DG,rated}\, \delta_{DG}(t) + b_{DG}\, P_{DG}(t) \tag{5.55}$$

By introducing the auxiliary variable $P_{DG,rated,aux}$, previously described by Eq. (5.34), the overall DG operating cost can be rearranged as follows:

$$\begin{aligned} C_{op,var,DG}(t) = {} & d_1\, P_{DG,rated,aux}(t) + d_2\, P_{DG}(t) + d_3\, \delta_{DG}(t) \\ & + C_{DG,fuel,start}(t) \end{aligned} \tag{5.56}$$

The start-up cost was finally treated by introducing the following two linear constraints:

$$C_{DG,fuel,start}(t) \geq 0 \tag{5.57}$$

$$C_{DG,fuel,start}(t) \geq d_4 \left(P_{DG,rated,aux}(t) - P_{DG,rated,aux}(t-1)\right) \tag{5.58}$$

Parameters for the estimation of the operating cost of the DG are listed in Table 5.1. The $c_{rep,DG}$ term (in €/kW) represents the specific replacement cost of the diesel generator.

Table 5.1 Coefficients for the operating cost of the diesel generator.

Parameter	Expression
d_1	$a_{DG}\ cost_{fuel} + \frac{c_{rep,DG}}{N_{h,tot,DG}}$
d_2	$b_{DG}\ cost_{fuel}$
d_3	$C_{OM,op,h,DG}$
d_4	$F_{start}\ (a_{DG} + b_{DG})\ cost_{fuel}$

5.2.3 Reliability constraint

Analogously to the PSO-based sizing problem, the loss of power supply probability (LPSP) index was used to quantify the reliability of the off-grid energy system [171]. The following constraint was introduced to ensured that a predefined LPSP value is satisfied:

$$\sum_{t=1}^{T} \frac{P_{NS}(t)}{P_{LD}(t)} = LPSP^* \tag{5.59}$$

A value of 0 was considered for $LPSP^*$ in order to make the off-grid system completely energy autonomous.

5.2.4 Demand response program

The aim of a demand response program is to reduce the overall costs by varying the load consumption patterns. Various techniques can be employed to

include the DRP in an optimization problem. In the present study, the time-of-use (TOU) rates of DRP [243], [244], [250] was considered. The load profile over a certain time horizon was changed by shifting a predefined percentage of load from expensive periods to other cheaper periods with the purpose of achieving a reduction in the total cost.

According to the TOU formulation, the new electrical load becomes equal to the base load plus a variable power term, which can be either positive or negative:

$$P_{LD,DRP}(t) = P_{LD}(t) + P_{LD}^{TOU}(t) \tag{5.60}$$

The amount of load increase/decrease must be less than a certain percentage of the base load (DRP_{MAX}), as described by the following linear constraint:

$$-P_{LD}(t)\, DRP_{MAX} \leq P_{LD}^{TOU}(t) \leq P_{LD}(t)\, DRP_{MAX} \tag{5.61}$$

The overall load over a certain time (T_{DRP}) remains fixed, as the DRP mechanism is just a translation of a certain amount of load from some periods to others to achieve a cost reduction. This can be expressed by the following constraint:

$$\sum_{t=1}^{T_{DRP}} P_{LD}^{TOU}(t) = 0 \tag{5.62}$$

A daily time horizon (i.e., T_{DRP}=24) was considered in this study. The DRP mechanism above described could be performed by sending online signals to consumers in order to modify their consumption pattern, leaving the daily energy demand constant, as defined by Eq. (5.62) [245], [246]. This can be done, for example, by means of a Supervisory Control and Data Acquisition (SCADA) approach, as described by Palma-Behnke *et al.* [251]. The DRP_{MAX} is often chosen in the range of 0 to 30% [243]–[246]. In our study, a sensitivity of DPR_{MAX} up to 30% was thus carried out to better evaluate the influence of a demand-side management mechanism on the optimal microgrid sizing.

5.2.5 LCOE estimation

After performing the full-year MILP simulation to optimally size the system, another full-year MILP simulation was carried out with fixed component sizes (i.e., no approximation of cost functions). This was done to obtain a more accurate estimate of the various techno-economic parameters to be used to compute the levelized cost of energy (LCOE). This is necessary to perform a fair comparison with the sizing results computed by the metaheuristic-based design optimization presented in Chapter 4.

The LCOE was estimated according to the general methodology described in Chapter 2 (Section 2.3.1). It is required to evaluate the lifespan of components that are potentially subject to replacement in order to know when and how many replacements occur over the project lifetime. The battery lifetime was derived by the ratio of the replacement cost to the yearly degradation cost as follows:

$$L_{BT} = min\left(\frac{C_{rep,BT}}{\sum_{t=1}^{8760} C_{op,var,BTch}(t) + C_{op,var,BTdc}(t)}, L_{PR}\right) \quad (5.63)$$

Similarly, the lifetime of the electrolyzer and fuel cell stack was defined as (with j = EL, FC):

$$L_j = min\left(\frac{C_{rep,j}}{\sum_{t=1}^{8760} C_{op,var,j}(t) - C_{OM,var,j} \sum_{t=1}^{8760} \delta_j(t)}, L_{PR}\right) \quad (5.64)$$

The variable OM term ($C_{OM,var,j}$) was removed from the denominator of the above equation since not accounting for the component degradation. Finally, the DG lifetime can be determined after computing the yearly number of operating hours of DG during the reference year, as follows:

$$L_{DG} = min\left(\frac{N_{h,tot,DG}}{\sum_{t=1}^{8760} \delta_{DG}(t)}, L_{PR}\right) \quad (5.65)$$

It is important to note that the above described lifetime relationships are equivalent to Eqs. (2.90), (2.92) and (2.93) reported in the techno-economic methodology of Chapter 2.

5.3 MILP-based modelling of the HRES with design days

The optimization framework described so far (summarized in Figure 5.1) was then updated to include design days (DDs). In the data processing step, the process of time series aggregation was carried out. All days of the year were merged into groups, i.e., design days, with the aim of reducing the computational time required for the sizing optimization of the energy system. Referring to the post-processing, a second MILP run was performed with fixed component sizes (i.e., only operating variables) and with 1-year time horizon without the presence of design days. The new modelling framework was developed so as to be equivalent to the one previously formulated when setting the number of DDs to 365.

In the following sections, after describing the clustering step, main equations of the MILP-based problem to deal with design days are presented.

5.3.1 Time series aggregation

Normalization

Prior to performing the clustering, data sets were normalized so that all the time series can be evaluated on the same scale [252]. Each time series v_a, which is referred to a certain attribute a ∈ {1, …, N_a}, is composed of N_t points $x_{a,t}$ where t ∈ {1, …, N_t}. There are various techniques that can be applied for the normalization process: Eq. (5.66) is based on the range of each time series, whereas Eq. (5.67) is based on the standard deviation [253]. The first one was chosen in the present analysis because of its proven effectiveness [233], [252].

$$v_{a,norm} = \frac{v_a - min(v_a)}{max(v_a) - min(v_a)} \tag{5.66}$$

$$v_{a,norm} = \frac{v_a}{std(v_a)} \tag{5.67}$$

The scaled time series were then arranged into a matrix in which the number of columns is equal to the product of the number of attributes (N_a) and the length of the reference period (N_h, equal to 24 if typical days with hourly resolution are considered). The number of rows corresponds instead to the number of periods over the whole simulation (N_d, equal to 365 if an yearly simulation with typical days is analyzed). The matrix thus derived was used to perform the clustering of the N_d periods into N_k reference periods.

Clustering techniques

Different time-series aggregation methods can be applied for the clustering process, e.g., averaging periods, k-means clustering, k-medoids clustering and hierarchical clustering [233]. The k-means and k-medoids techniques are widely used in the field of energy systems. Their basic principles are described below.

- **k-means clustering**

  k-means clustering is a partitioning method used to partition the N_d candidates into N_k clusters by minimizing the distance between the mean of a cluster and all candidates belonging to that cluster. The objective function to be minimized is reported below. The distance function is written in terms of squared error, i.e., Euclidean distance:

$$OF = \sum_{k=1}^{N_k} \sum_{d=1}^{N_d} \left[\sum_{h=1}^{N_h} \sum_{a=1}^{N_a} \left(x_{a,h,d} - \mu_{a,h,k} \right)^2 \right] \delta_{d,k} \tag{5.68}$$

where $\delta_{d,k}$ is a binary variable, which is equal to 1 if the period d is assigned to the cluster k. The term $x_{a,h,d}$ is the value of the attribute a in the period d at time step h and $\mu_{a,h,k}$ is the mean value. In order to allow each candidate period to be assigned to a cluster, the following constraint has to be introduced:

$$\sum_{k=1}^{N_k} \delta_{d,k} = 1 \; \forall \; d \in \{1, \dots, N_d\} \tag{5.69}$$

The k-means is hence formulated according to a mixed-integer nonlinear program (MINLP), which has to be implemented as a greedy algorithm converging to a local minimum [233], [252]. The major advantage related to this technique is that the total value of the original time series is preserved for each attribute since the representative period is computed as the mean profile of the cluster that it represents. On the other hand this smoothness effect could cause an underestimation of operational costs and of the installed capacity of components involved in the power system [252].

- **k-medoids clustering**

In the k-medoids, a real period of a cluster is chosen as representative of that cluster. This differs from the previous k-means method where the representative candidate is given by the mean of the cluster. The clustering based on k-medoids technique can be developed as a mixed-integer linear program by minimizing the following objective function:

$$OF = \sum_{i=1}^{N_d} \sum_{d=1}^{N_d} d_{i,d} \, \delta_{i,d} \tag{5.70}$$

where the distance between each pair of candidate periods $d_{i,d}$ is computed as:

$$d_{i,d} = \sum_{h=1}^{N_h} \sum_{a=1}^{N_a} \left(x_{a,h,i} - x_{a,h,d}\right)^2 \; \forall \; i, d \; \in \{1, \dots, N_d\} \tag{5.71}$$

The following three constraints must be also introduced in the MILP formulation:

$$\sum_{d=1}^{N_d} \delta_{i,d} = 1 \; \forall \; i \in \{1, \dots, N_d\} \tag{5.72}$$

$$\delta_{i,d} \leq y_i \; \forall \; i, d \; \in \{1, \dots, N_d\} \tag{5.73}$$

$$\sum_{i=1}^{N_d} y_i = N_k \tag{5.74}$$

where $\delta_{i,d}$ and y_i are binary variables. The variable $\delta_{i,d}$ is equal to 1 if period d is represented by period i and 0 otherwise. The variable y_i is equal to 1 if period i is chosen as representative for its cluster and 0 otherwise. The first constraint, i.e., Eq. (5.72), enforces that each period is associated to only another period, which has to be a reference period as stated by Eq. (5.73). Finally, Eq. (5.74) imposes that the number of reference periods must be equal to N_k. The most relevant advantage of the k-medoids algorithm is that a real period is taken as representative of the cluster. The typical profiles of the attributes are thus generally less smoothed than in the k-means case. However, unlike the k-means techniques, the total value of each attribute can differ from that of the original time series, especially when dealing with a small number of representative days [252].

Extreme period integration

Time series aggregation techniques can smooth the original input profiles and cut off peak periods. However, peak periods should be considered for a proper design of the energy system. Their influence is expected to be relevant especially when dealing with islanded systems or in contexts that require high reliability like power systems feeding hospitals [252]. Various techniques for the inclusion of extreme periods can be applied, as summarized by Kotzur *et al.* [233]:

1. Including the extreme period as an additional representative period (append technique).
2. Integration of the extreme period as an additional cluster centre.
3. The extreme period becomes the new cluster centre of the cluster it was originally assigned to.

An overestimation of the annual cost was observed when the cluster centre was replaced by the peak period (i.e., third variant) [233]. Clustering approaches to simultaneously select the most representative days of the year and the extreme days can also be found, as the k-MILP technique developed by Zatti *et al.* [252].

Because of its ability to preserve the total value of the original time series, the k-means clustering was adopted in the present analysis. The smoothness drawback was mitigated by integrating extreme periods according to the first and second variants above described. The day with peak electricity load and the day with the lowest availability of solar and wind energy were considered as extreme periods. Main features of the clustering procedure are summarized in Table 5.2.

Table 5.2 Main features of the clustering process.

Reference period	1 day
Length of the reference period, N_h	24 (hours in 1 day)
Number of periods, N_d	365 (days in 1 year)
Number of attributes*, N_a	Electrical load, ambient air temperature, solar irradiance and wind velocity
Number of reference period, N_k	Sensitivity analysis
Clustering technique	k-means
Extreme period integration	Append; Additional cluster centre
Extreme period type*	Peak electricity load and lowest PV and wind feed-in

*wind velocity was included when also considering wind turbines in the HRES

5.3.2 Integration of design days

In this section, the concept of design days is implemented in the MILP optimization framework. The approach developed in [226] is here adapted to a stand-alone micro-grid context and further investigated.

Operating variables were determined only for the selected reference periods, with consequent reduction in the computational burden (unlike the full-year optimization where the MILP problem must estimate the operating variables for each hour of the yearly time horizon). As an example, the energy balance of the hybrid renewable energy system was performed for each hour $h \in \{1, \ldots, N_h\}$ of each design day $k \in \{1, \ldots, N_k\}$ as follows:

$$\begin{aligned} P_{PV}(k,h) + P_{WT}(k,h) + P_{BT,dc}(k,h) + P_{FC}(k,h) + P_{DG}(k,h) + P_{NS}(k,h) \\ = P_{LD}(k,h) + P_{BT,ch}(k,h) + P_{EL}(k,h) + P_{CT}(k,h) \end{aligned} \tag{5.75}$$

The modelling of the energy storage systems was instead carried out hour by hour $t \in \{1, \ldots, 8760\}$ over the entire year, taking into account the chronological order of the representative days. This allows computing the energy stored at the beginning of a certain day d (i.e., $h = 1$) based on the energy in the storage system at the end of the previous day d-1 (i.e., $h = N_h$). However, each day is still described by its representative day, which means that the relative increase or decrease of the energy content will be the same for all the days of the year that are associated to the same design day. Eqs. (5.76) and (5.77) express the storage dynamics for the hydrogen device. The same considerations remain valid for the battery component.

Eq. (5.31) was applied to set the storage level at the beginning of the simulation (i.e., $t = t_{in}$). If the time step t corresponds to the first hour of a certain d-th day (i.e., $h = 1$), the energy content in the hydrogen storage becomes:

$$E_{H_2}(t) = E_{H_2}(t-1) + P_{EL,out}(\sigma_{d-1}, N_h)\,\Delta t - P_{FC,in}(\sigma_{d-1}, N_h)\,\Delta t \quad (5.76)$$

where σ stands for the yearly sequence of design days (i.e., σ_d corresponds to the design day related to day d). As shown by the above equation, the operating power of the electrolyzer and fuel cell systems is referred to the last hour of the design day that is used to describe day d-1. For any other hour of the d-th day, i.e., $h \in \{2, \ldots, N_h\}$, the hydrogen energy inside the storage was instead updated as follows:

$$E_{H_2}(t) = E_{H_2}(t-1) + P_{EL,out}(\sigma_d, h-1)\,\Delta t - P_{FC,in}(\sigma_d, h-1)\,\Delta t \quad (5.77)$$

where $P_{EL,out}$ and $P_{FC,in}$ are the operating powers at hour h-1 referred to the design day that is linked to the day d. Eq. (5.32) was finally added to have the periodicity constraint over the entire year.
The reliability constraint, necessary to make the energy system self-sufficient, was updated as follows:

$$\sum_{k=1}^{N_k}\left(D_k \sum_{h=1}^{N_h} \frac{P_{NS}(k,h)}{P_{LD}(k,h)}\right) = LPSP^* \quad (5.78)$$

where D_k represents the total number of design days of type k, which means that:

$$\sum_{k=1}^{N_k} D_k = N_d \quad (5.79)$$

The variable operating cost (in €/y) is now composed of the following two contributions (with i = BT_{ch}, BT_{dc}, EL, FC, DG):

$$C_{AC,op,var,1} = \sum_{k=1}^{N_k}\left(D_k \sum_{h=1}^{N_h} C_{op,var,i}(k,h)\right) \quad (5.80)$$

$$C_{AC,op,var,2} = \sum_{d=1}^{N_d}\left(C_{EL,start}(d,1) + C_{FC,start}(d,1) + C_{DG,fuel,start}(d,1)\right) \quad (5.81)$$

Eq. (5.81) is necessary when dealing with design days to take into account the start-up costs that potentially can occur at the first hour of a certain day, which depend on the operating mode of the device in the previous hour (belonging to the day before). However, this implies the introduction of N_d additional variables for each of the three start-up costs (related to EL, FC and DG). As an instance, the start-up cost associated to the electrolyzer and fuel cell at the beginning of each design day becomes (with j = EL, FC):

$$C_{j,start}(d,1) \geq 0 \tag{5.82}$$

$$C_{j,start}(d,1) \geq \frac{c_{j,stack}}{N_{start,tot,j}} \left(P_{j,rated,aux}(\sigma_d,1) - P_{j,rated,aux}(\sigma_{d-1},N_h)\right) \tag{5.83}$$

Start-up costs for $h \in \{2, \dots N_h\}$ are already described through Eq. (5.80). Start-up costs related to the diesel generator can be updated analogously.

It is important to note that the above described MILP formulation makes the two methodologies (with and without representative days) equivalent in case N_k is set to 365.

5.4 Results and discussion

The optimization problem was formulated in MATLAB environment employing IBM CPLEX as solver. Simulations were performed on a desktop computer with an Intel(R) Core(TM) i7-4770 CPU at 3.4 GHz and 32 GB RAM.

5.4.1 PWA approximation of performance and cost curves

Concerning the performance curve of both the PEM electrolyzer and PEM fuel cell systems, 4 line segments, corresponding to 5 breakpoints, were chosen since they were found to describe well the EL and FC performance as shown by the relative error graphs in Figure 5.2 and Figure 5.3. The main parameters of the PWA approximation are reported in Table 5.3 and Table 5.4, respectively.

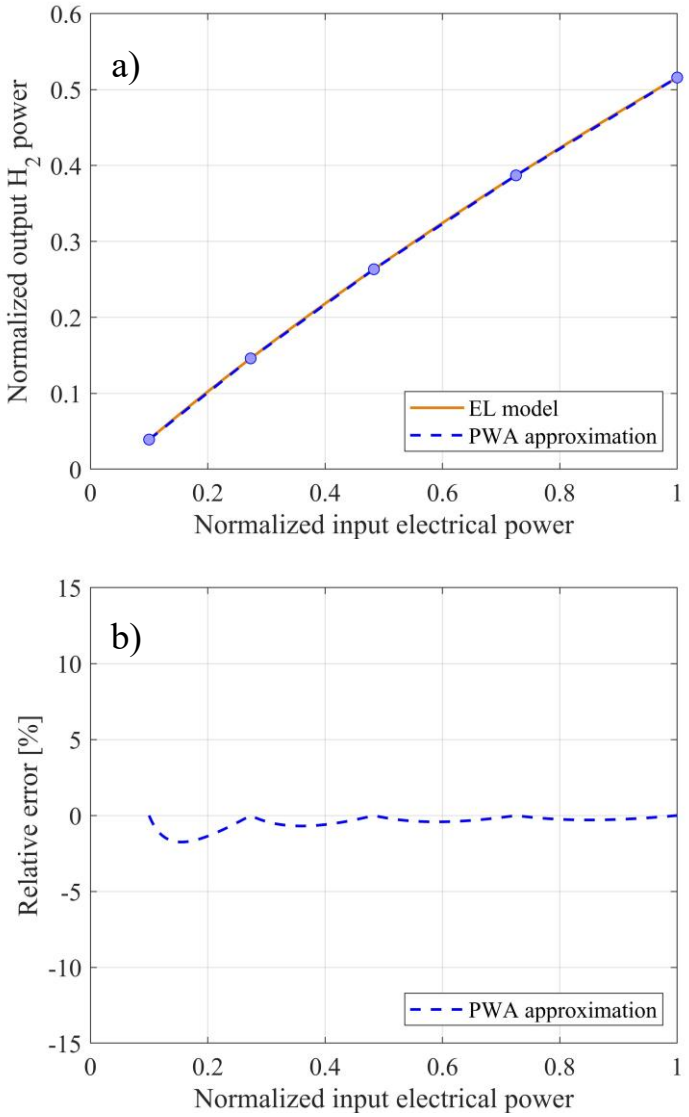

Figure 5.2 PWA approximation of the PEM electrolyzer performance curve: a) normalized output power as a function of the normalized input power, b) relative error as a function of the normalized input power.

Table 5.3 Parameters for the PWA approximation of the PEM electrolyzer performance curve

z_1	z_2	z_3	z_4	z_5
0.100	0.273	0.483	0.725	1.000
η_1	η_2	η_3	η_4	η_5
0.391	0.535	0.545	0.534	0.516

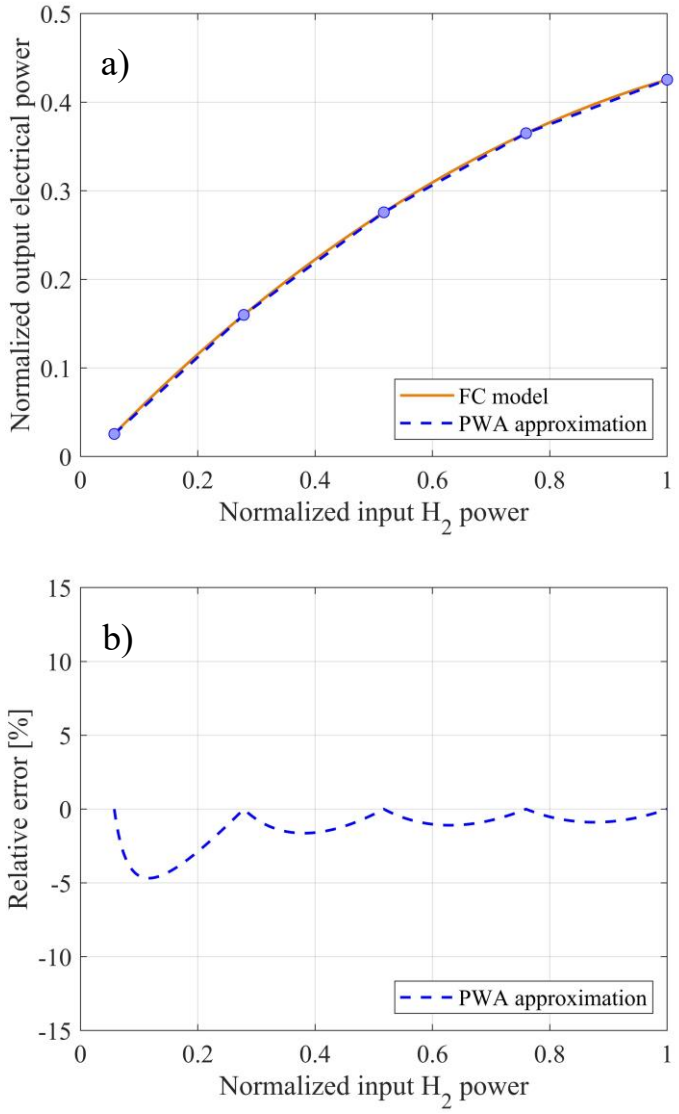

Figure 5.3 PWA approximation of the PEM fuel cell performance curve: a) normalized output power as a function of the normalized input power, b) relative error as a function of the normalized input power.

Table 5.4 Parameters for the PWA approximation of the PEM fuel cell performance curve.

z_1	z_2	z_3	z_4	z_5
0.058	0.278	0.517	0.759	1.000
η_1	η_2	η_3	η_4	η_5
0.442	0.574	0.533	0.481	0.425

In Table 5.3 and Table 5.4, the z_k term corresponds to the fraction of the rated inlet power in correspondence to the k-th breakpoint, whose efficiency (on LHV basis) is η_k. It can be noticed that z_1 is 0.1 for the PEM electrolyzer, which corresponds to the lower boundary of the EL modulation range (see Chapter 2, Table 2.6). The z_1 value reported in Table 5.4 for the PEM FC is instead slightly different from the minimum fuel cell power fraction (i.e., 6% of the rated net outlet power) since z_1 is referred to the rated inlet power, i.e., power in terms of hydrogen for the FC.

Parameters of the PWA approximation of the investment cost curve are shown in Table 5.5 for the electrolyzer and Table 5.6 for the fuel cell. The terms z_k and $c_{inv,k}$ represent the fraction of the maximum rated power (i.e., $P_{EL,rated,max}$ and $P_{FC,rated,max}$) and the specific investment cost (in €/kW) referred to the k-th breakpoint of the cost curve. Three line segments, i.e., four breakpoints, were considered in order to have an accurate representation, while limiting the number of binary variables (which would increase the computational burden).

Table 5.5 Parameters for the PWA approximation of the PEM electrolyzer cost function (c_{inv} is in €/kW). The maximum rated power is set to 200 kW.

z_1	z_2	z_3	z_4
0	0.105	0.430	1
$c_{inv,1}$	$c_{inv,2}$	$c_{inv,3}$	$c_{inv,4}$
0	$6.232 \cdot 10^3$	$3.805 \cdot 10^3$	$2.832 \cdot 10^3$

Table 5.6 Parameters for the PWA approximation of the PEM fuel cell cost function (c_{inv} is in €/kW). The maximum rated power is set to 100 kW.

z_1	z_2	z_3	z_4
0	0.120	0.450	1
$c_{inv,1}$	$c_{inv,2}$	$c_{inv,3}$	$c_{inv,4}$
0	$3.737 \cdot 10^3$	$2.514 \cdot 10^3$	$1.978 \cdot 10^3$

5.4.2 Reference configuration and comparison with metaheuristic approach

The MILP optimization problem was applied to the case study of Ginostra (see Section 3.2.1 and Section 4.3.1). The lithium-ion technology was considered

for the battery storage system. Electrolyzers of PEM type were chosen for the hydrogen production step. The reference configuration consists of a fully renewable energy system that rely on the local solar energy source.

A relative MIP gap tolerance of 0.1% was set in the MILP simulations, both for the first and for the second MILP run (see Figure 5.1). This means that the process stops when a feasible integer solution has been proved to be within 0.1% of optimality. As previously described, the second MILP optimization was performed to get a more accurate estimation of the system cost (with no PWA approximation of cost functions). The resulting cost is around 3.9% greater than that obtained from the first simulation.

Main results derived by applying the SL MILP-based method are shown in Table 5.7. For the sake of comparison, sizing results obtained through the TL metaheuristic approach presented in Chapter 4 (PSO algorithm for design phase with RBSs for the operation) are also reported. It can be noticed that the LCOE computed by means of the SL technique is around 11% lower than that derived when employing the TL methodology (0.455 €/kWh compared to 0.512 €/kWh). PV panels and hydrogen-based components are in fact smaller in size when applying the MILP-based technique. The battery capacity is instead slightly higher.

Table 5.7 Main sizing results of the renewable P2P system for the SL MILP-based and TL metaheuristic-based models.

Parameter		**SL model**	**TL model**
Photovoltaic modules	[kW]	185	211
Electrolyzer (PEM)	[kW]	3	7
Fuel cell (PEM)	[kW]	10	34
Hydrogen tank	[kWh]	3092	3505
Battery (Li-ion)	[kWh]	613	595
NPC	[€]	981,558	1,104,660
LCOE	[€/kWh]	0.455	0.512

The contribution of the various components to the levelized cost of energy is depicted in Figure 5.4 for the MILP approach. The battery storage system is the greatest contributor with around 50% of the total system cost, whereas the H_2 equipment (including EL, FC and HT) accounts for approximately 15%. Batteries in fact operate daily as shorter-term storage and their rated capacity should be sufficient to cover most of power shortages occurring throughout the year. Hydrogen instead intervenes less frequently. However, because of its longer-term

storage capability, hydrogen presence is essential to provide a cost-effective and reliable power supply service.

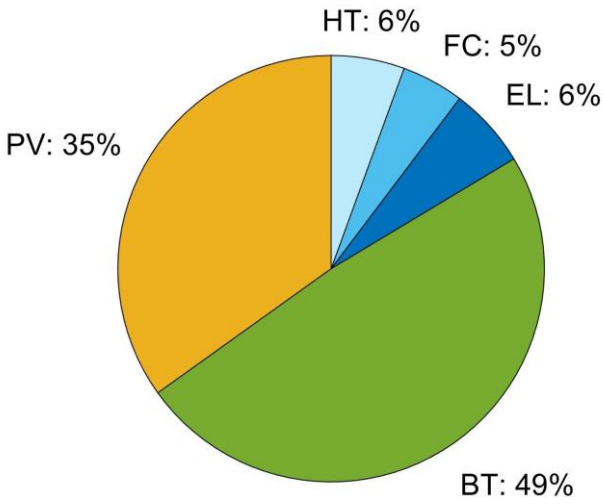

Figure 5.4 LCOE breakdown in Ginostra site (MILP-based approach).

The main technical KPIs are summarized in Table 5.8. A battery duration of approximately 13 years was derived, which is in line with the lifetime values employed in the literature for Li-ion batteries [32]. The lifetime of the PEM electrolyzer was found to be lower for the MILP-based method, due to the higher number of operating hours in the reference year (4739 hours for the SL technique compared to 1655 hours for the TL method). However, the electrolyzer size that was computed by the MILP-based approach is less than half that obtained when using the metaheuristic approach. This results in lower electrolyzer costs over the lifetime of the project for the SL model (despite the lower EL lifetime). No necessity of replacement of the fuel cell stack was observed for both the optimization methodologies. In fact, fuel cell operation is not required over the whole year, but its intervention is mainly focused on the summer period to cope with the increase in load.

The yearly profiles of the energy stored in the form of electrochemical (battery) and chemical (hydrogen) energy are shown in Figure 5.5 for the SL approach. It can be noticed that the battery component absorbs and desorbs energy on short term basis, thereby smoothing the RES fluctuating behaviour. The profile of the energy stored through hydrogen is instead less variable and shows a seasonal trend. The H_2 tank installed capacity is around 5 times higher than that of the battery (3092 kWh of HT compared to 613 kWh of BT). The small-size electrolyzer intervenes at full power almost every time there is a surplus of RES energy (4739 hours per year). Its size is sufficient to gradually produce hydrogen during the spring and fill the pressurized tank, which is then quickly emptied in

summer because of the increased energy consumption in Ginostra. The fuel cell operates mainly in summer (686 hours per year) and its size, which is around three times higher than that of the electrolyzer, is required to fully cover the peak demand.

Table 5.8 Main sizing results of the renewable P2P system for the SL MILP-based and TL metaheuristic-based models.

Parameter		**SL model**	**TL model**
EL operating hours per year	[h]	4739	1655
EL on-off per year	[-]	175	312
EL lifetime	[y]	7	10
FC operating hours per year	[h]	686	214
FC on-off per year	[-]	49	46
FC lifetime	[y]	NR*	NR*
BT lifetime	[y]	13	13

NR*: No replacement

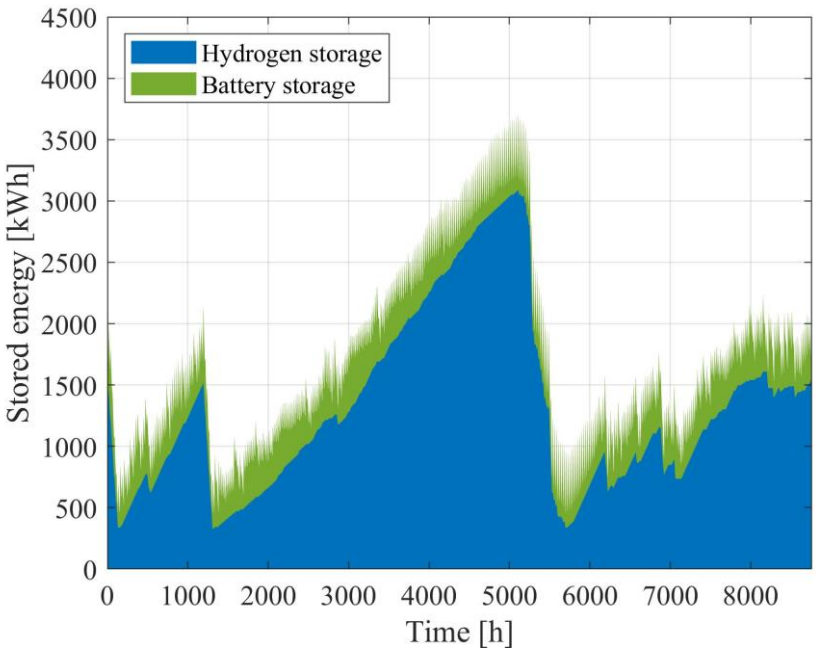

Figure 5.5 Hourly profile along the year of the energy stored through batteries and hydrogen (SL MILP-based model).

A stand-alone system with only batteries as storage medium was also analyzed to further highlight the role of hydrogen. The LCOE of this HRES configuration (of around 0.544 €/kWh) is higher than the LCOE of the hybrid storage case (i.e., 0.455 €/kW for the SL MILP). This is due to the higher PV rated power (291 kW) and BT capacity (941 kWh). Thus, hydrogen becomes crucial to avoid the over-dimensioning of the battery size and to better exploit the local solar source. It is also noteworthy that, concerning the battery-based system, the sizing outcomes derived by the MILP method are the same as those obtained through the metaheuristic approach with RBSs (Table 4.1). In fact, ruled-based EMSs are an effective way to address the operation of energy systems. However, the limits of RBSs start to be noticed when increasing the number of the HRES components, as the number of required rules (and hence alternatives to choose from) increases significantly. Instead, the MILP algorithm is able to perform an optimal distribution of power between the components, also taking advantage of its prediction capacity. This might explain the more performing results that have been achieved by the MILP technique when considering a hybrid battery-hydrogen configuration (Table 5.7).

Despite its advantages, the MILP-based approach presents some limitations that have to be pointed out. Unlike the TL method, the MILP formulation requires all non-linear equations to be linearized, which results in increased problem complexity. Moreover, the proposed SL method needs higher computational requirements to be solved: almost 4 hours are necessary to solve the MILP problem, whereas just a few minutes are sufficient for the other sizing technique. The inclusion of representative days will try to face and mitigate this last issue.

5.4.3 Effect of demand response program

It has been considered the possibility to change and shift the daily demand profile, planning some activities in other periods with the aim of decreasing the cost of the produced electricity. This could be performed, for example, by sending signals to consumers promoting behaviour changes as suggested in Ref. [251]. A demand-side management scheme was thus implemented in the MILP-based problem in order to assess its influence on the LCOE and sizing results. More specifically, the time of use (TOU) rate of DRP approach (described in Section 5.2.4) was considered in the present study. A sensitivity on the DRP_{MAX} parameter up to 30% was also carried out.

Table 5.9 reports the main sizing results for the various DRP scenarios. The total system cost is observed to decrease by implementing a demand response strategy. Moreover, the cost reduction becomes more relevant by increasing the amount of load that is allowed to participate in the DRP scheme (i.e., higher value of the DRP_{MAX} parameter). The LCOE drops from 0.455 €/kWh for the base case without DRP down to around 0.402 €/kWh when an DRP_{MAX} equal to 30% is applied. This cost reduction is mainly ascribed to the decrease in the Li-ion

battery capacity, which moves from 613 to 454 kWh when the DRP_{MAX} value changes from 0 to 30%. Almost no changes in size are noticed for the other system components (i.e., PV panels and H_2 equipment) when considering the demand response.

Table 5.9 Main sizing results of the renewable P2P system for different values of the DRP percentage.

Parameter		DRP 0%	DRP 10%	DRP 20%	DRP 30%
PV modules	[kW]	185	184	190	185
Electrolyzer	[kW]	3	3	3	4
Fuel cell	[kW]	10	9	8	9
Hydrogen tank	[kWh]	3092	3092	2946	3065
Battery	[kWh]	613	580	524	454
NPC	[€]	981,558	945,729	911,369	867,350
LCOE	[€/kWh]	0.455	0.439	0.423	0.402

The main contribution of the battery component to lowering the cost of energy in the presence of DRP can also be observed by looking at the LCOE breakdown for the various DRP cases shown in Figure 5.6. As previously reported, the battery device works as daily energy buffer to cope with renewable energy surplus and shortages. It is thus the HRES component that is most affected by the DRP. Instead, the hydrogen storage system, which acts mainly as a long-term storage device (to deal with the seasonal variations of the electrical demand), is almost not influenced by the adoption of DRP.

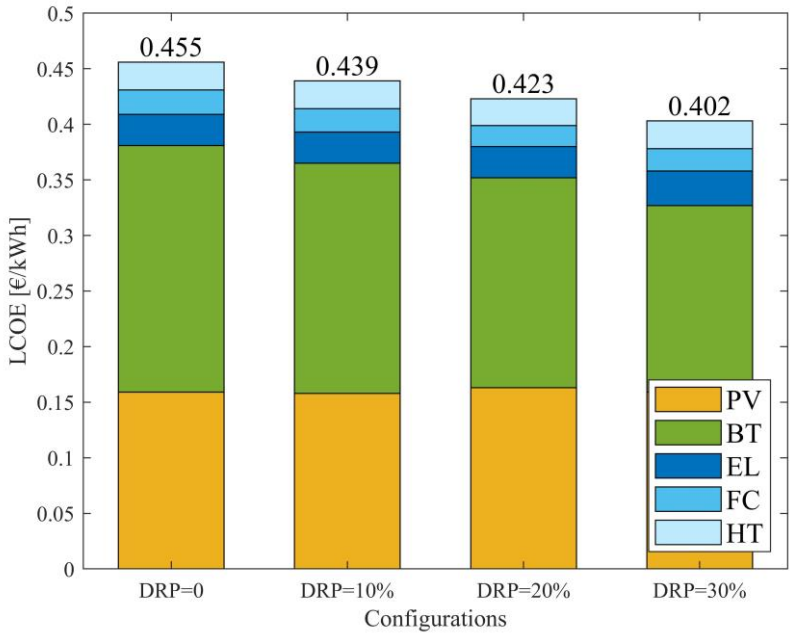

Figure 5.6 Breakdown of the system LCOE for the different DRP cases.

As an example, Figure 5.7 reports the scheduling results for a typical summer day. As depicted in Figure 5.7a, load is deferred from night hours to the period of the day during which there is excess renewable energy from the PV system. A smaller amount of energy therefore needs to be provided by the BSS, due to the increased direct consumption of solar energy, with a consequent decrease in the battery capacity that has to be installed. The profile of the operating power of the various components of the P2P system is shown in Figure 5.7b. It can be noticed that the battery is discharged during night and charged during the day storing the surplus PV energy. The electrolyzer also operates in the daytime producing hydrogen from the solar energy. As also highlighted previously, its rated power is small, but it is enough to generate the amount of hydrogen that is required by the fuel cell (the electrolyzer operates almost constantly during the day throughout the entire year to gradually fill the storage and deal with the increase in the summer load). Finally, the fuel cell intervenes (quite steadily and with no interruption) in the evening and at night to support the battery in covering the electrical load.

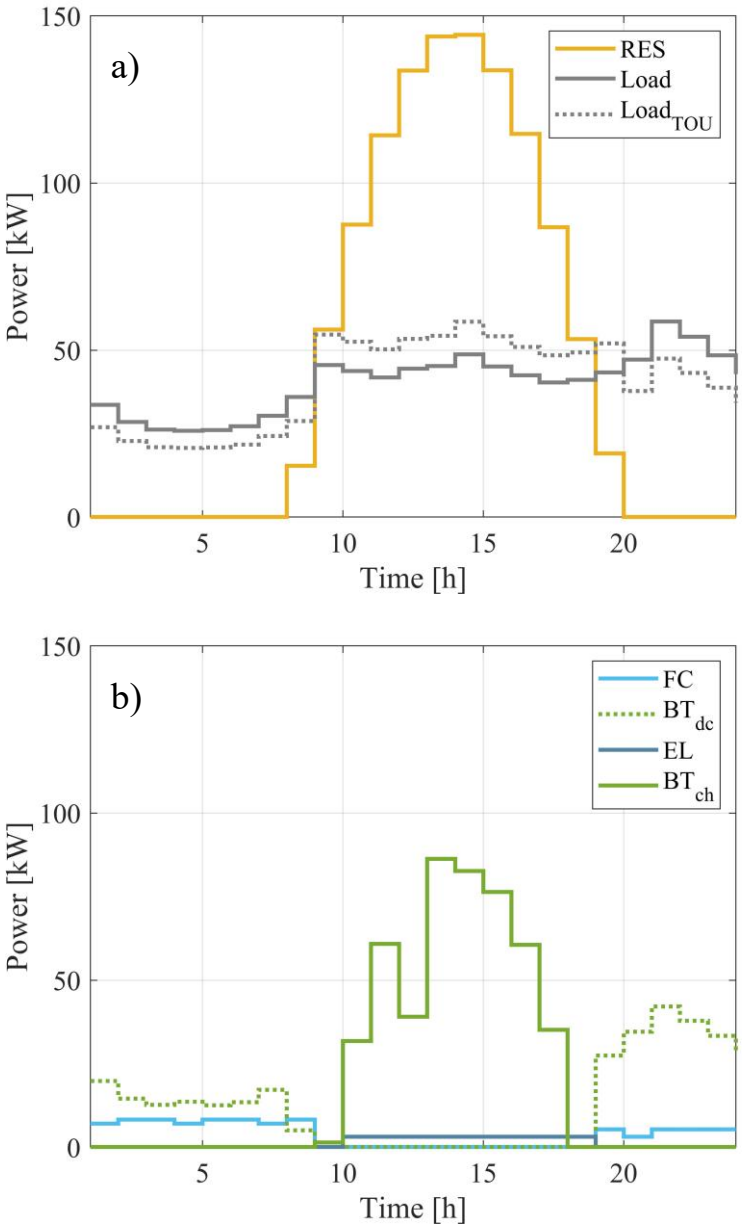

Figure 5.7 Scheduling results on a summer day considering DPR_{MAX} equal to 20%: a) hourly profile of RES, load and new load with DPR and b) hourly profiles of the operating power of the various devices of the P2P system.

It is thus shown the effectiveness of load deferral in reducing the LCOE, thanks to the reduction in the required energy storage capacity (of the battery in the case study under analysis). The adopted DRP formulation could be made more specific if more detailed information about the electrical load composition were available. In case the individual appliances that contribute to the electrical demand are known, it would be possible to choose those that are given the flexibility of load deferral and those that require immediate coverage.

The involvement of the end-user represents the greatest barrier to demand response deployment [242]. There is the need to make consumers more aware about how DRP works and to better underscore potential benefits derived from the DRP adoption [254]. In the present analysis, dispatchable loads were shown to reduce the mismatch between consumption and generation profiles, which resulted in a more affordable LCOE (thanks to the decreased capacity of the storage units). As previously stated, in the literature there are few studies about the optimal system sizing together with demand response. Research about this topic is thus highly relevant to better clarify the positive effects arising from DRP adoption and foster the end-users to engage in a demand response program. It should also be noted that, by increasing the extend of customer participation in the DPR (i.e., increasing the DRP_{MAX} parameter), the overall system costs progressively decrease. However, it will become increasingly difficult and unfeasible for the end-user to be involved in the DRP. As reported in Section 5.2.4, feasible values for DRP_{MAX} lie in the range of 0 to 20%. Finally, the adoption of DRP could also lead to environmental benefits, such as a reduction in the fossil-fuel consumption (and hence GHG emissions), which might further promote the social acceptance of demand response schemes.

5.4.4 Effect of further hybridization of the energy system

Additional HRES configurations have been analysed besides the reference one (composed of PV, battery and hydrogen). The aim was to evaluate the effect of the inclusion of the wind energy source and diesel generator on the optimal system design. Main sizing results are reported in Table 5.10. By adding the possibility to exploit local wind, the LCOE of the reference configuration is slightly reduced, from 0.455 €/kWh (C_1) to 0.448 €/kWh (C_2). Even though wind is scarce in the selected site, RES hybridization is therefore quite effective in achieving a cheaper solution. This is because the integration of wind leads to lower sizes of both the PV and the energy storage components (BT and HT). The diesel generator is added to the reference case in the third configuration (C_3). It can be observed that, when introducing diesel, the most cost-effective configuration does not include the hydrogen-based system, as also shown and discussed in Chapter 4. Hydrogen is necessary to make the system energy autonomous because it avoids the installation of too large batteries. However, if it is allowed the DG to operate without constraints, from an economic point of view it is generally more convenient to have a diesel genset rather than hydrogen in order to prevent the battery oversizing. Further reduction of the cost of energy was found when considering the possibility to install both the wind turbine and the diesel generator (C_4). Indeed, the hybridization of the power generation with wind and diesel allows the PV (151 kW) and battery (493 kWh) sizes to be further reduced.

Table 5.10 Main sizing results of the renewable P2P system with different configurations.

Parameter		**C_1**	**C_2**	**C_3**	**C_4**
		Ref.	**Ref. + WT**	**Ref. + DG**	**Ref. + WT + DG**
PV modules	[kW]	185	174	162	151
Wind turbine	[kW]	-	31	0	22
Electrolyzer	[kW]	3	3	0	0
Fuel cell	[kW]	10	9	0	0
Hydrogen tank	[kWh]	3092	2883	0	0
Battery	[kWh]	613	596	560	493
Diesel generator	[kW]	-	-	21	19
NPC	[€]	981,558	966,477	799,918	784,969
LCOE	[€/kWh]	0.455	0.448	0.371	0.364

5.4.5 Inclusion of design days

Design days were investigated with the aim of reducing the complexity of the MILP problem. The clustering process was performed through the k-means algorithm with the integration of extreme periods (i.e., days with the highest load demand and lowest RES production). Both the append and the additional-cluster-centre techniques (see Section 5.3.1) were considered for the inclusion of the extreme periods.

Figure 5.8 reports the original profile of the electrical load together with the aggregated profile with different number of design days (N_k). It can be observed that the approximation of the hourly-resolved demand improves by increasing the number of representative periods that are included in the MILP optimization problem.

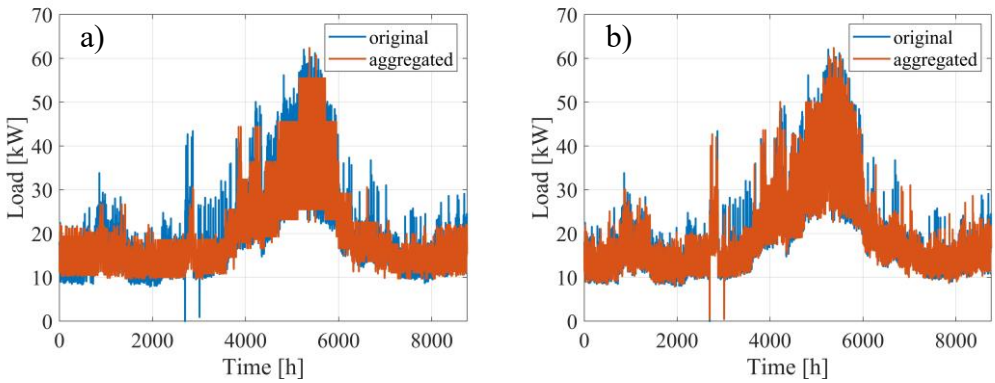

Figure 5.8 Original and aggregated load time series with 25 (a) and 150 (b) design days. Clustering is performed through k-means together with inclusion of extreme days (append technique in this case).

The MILP optimization was run several times performing a sensitivity analysis on the number of design days. The aim was to evaluate the number of representative periods that are required to achieve an accurate approximation of the sizing results based on the full-year time series.

The sizes of the HRES components as a function of the number of DDs are displayed in Figure 5.9, Figure 5.10 and Figure 5.11, where the dashed black lines refer to the full-year solution. The append technique was applied in the k-means clustering process to include the extreme periods. All the simulations were run imposing a relative MIP gap of 0.1%. Main results of the MILP simulations are summarized in Table 5.11.

Figure 5.9 shows that, except for the case with very few DDs, the PV size is a bit overestimated until around 100 DDs, where a value slightly higher than the exact one is reached (187 kW). As can be seen in Figure 5.10, the sizes of the electrolyzer and fuel cell start to oscillate around the full-year value from approximately 25 representative days. Figure 5.11 shows that the capacity of the battery component is well approximated even when considering very few DDs. On the contrary, the longer-term storage capacity of the hydrogen system requires a higher amount of design days to achieve an accurate approximation, at least roughly 100 DDs. This value is higher than that reported by Gabrielli *et al.* [226] (they found accurate sizing values with around 48 and 72 DDs, depending on the MILP methodology adopted). The higher value we found may be due to differences in the MILP formulation, but also to the different energy system under analysis. Dealing with stand-alone systems that rely on local RESs may require a greater level of detail, and hence higher number of DDs, to be able to catch the required storage capacity. Finally, the LPSP index of the second MILP run (defined by Eq. (5.59)) approaches the zero value from around 75-100 design days.

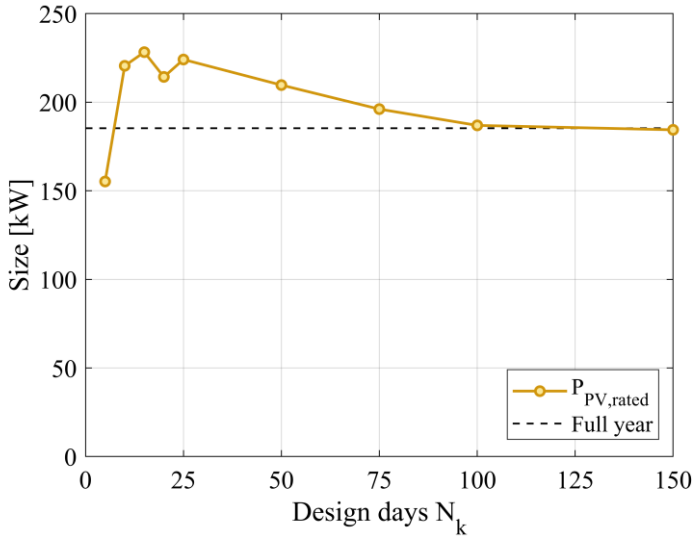

Figure 5.9 Size of the photovoltaic system as a function of the number of design days (N_k). The dashed line refers to the full-year solution.

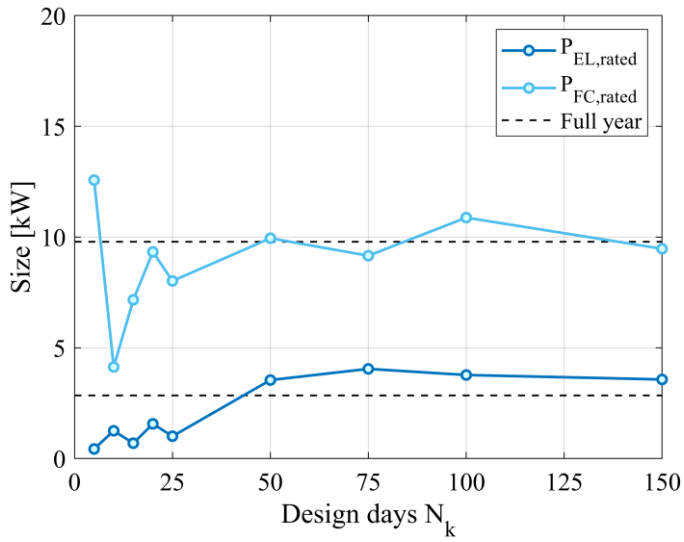

Figure 5.10 Size of the electrolyzer and fuel cell systems as a function of the number of design days (N_k). The dashed lines refer to the full-year solution.

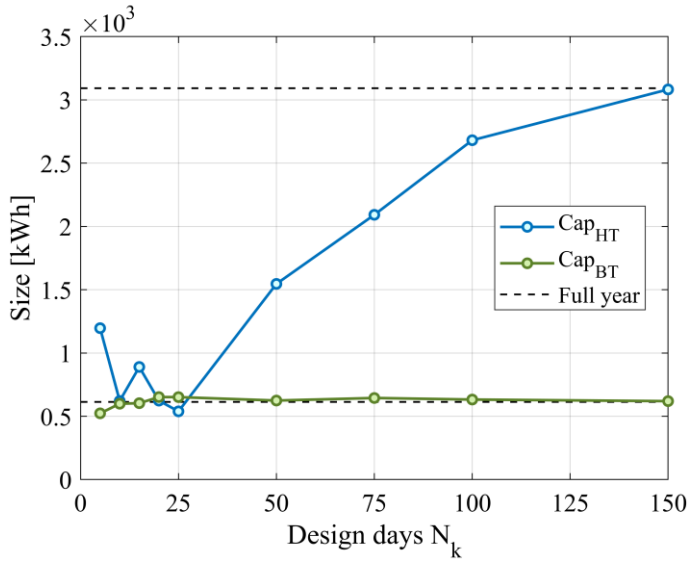

Figure 5.11 Size of the hydrogen and battery storage as a function of the number of design days (N_k). The dashed lines refer to the full-year solution.

Figure 5.12 shows the optimal sizes of the hydrogen devices when considering the append and the new-cluster-centre techniques (which are used for the integration of extreme periods). It can be noted that the second methodology leads to an overestimation of the EL, FC and HT sizes when around 5 design days are employed. This is because the use of very few DDs causes most of summer days to be associated to the extreme period with peak load demand. However, this overestimation disappears sharply by increasing the number of representative periods. It is noteworthy that the same sizing outcomes are achieved by the two techniques from around 25 design days.

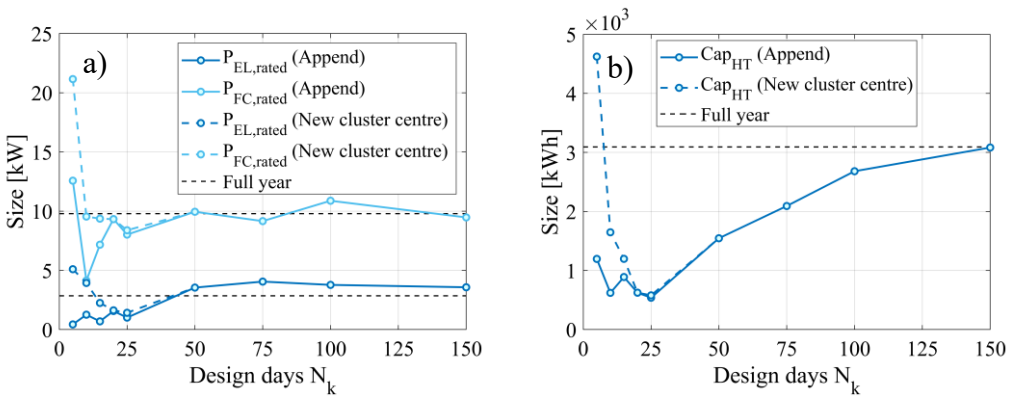

Figure 5.12 Size of electrolyzer and fuel cell (a), and size of the hydrogen storage (b) as a function of the number of design days. Append and new-cluster-centre techniques are applied for the inclusion of extreme days.

Table 5.11 Main outcomes from the MILP optimization as a function of the number of design days (Extreme periods are included by means of the append technique).

DD number	PV [kW]	EL [kW]	FC [kW]	HT [kWh]	BT [kWh]	LCOE [€/kWh]	Time [h]
5	155	0.4	12.6	1196	523	0.389	0.033
10	221	1.3	4.1	621	599	0.440	0.062
15	228	0.7	7.2	890	603	0.450	0.063
20	214	1.6	9.3	624	652	0.455	0.056
25	224	1.0	8.0	539	651	0.458	0.079
50	210	3.5	9.9	1546	624	0.462	0.114
75	196	4.0	9.2	2092	645	0.462	0.304
100	187	3.8	10.9	2681	632	0.459	0.377
150	184	3.6	9.5	3083	620	0.456	0.648
365	**185**	**2.8**	**9.8**	**3092**	**613**	**0.455**	**3.851**

The advantages deriving from the use of design days are clearly shown in Figure 5.13 in terms of computational time. It can be noted that DDs allow the CPU time to be decreased significantly compared to the full-year simulation. In fact, design days lead to a reduction in the number of binary variables, which are among the main causes of the computational complexity of MILP-based problems. A considerable reduction in the CPU time can be observed up to around 150 representative periods (where the optimization problem is already able to provide an accurate approximation of the hydrogen storage capacity). Compared to the full-year simulation, the speed-up is approximately 10 times at 100 DDs and 6 times at 150 DDs.

Thus, the implementation of representative periods was shown to be effective in dealing with the optimal design of off-grid HRESs, reducing the computational burden of the MILP problem. This may be useful (and, in some cases, unavoidable) especially when further increasing the number of variables and constraints in the MILP formulation, e.g., when energy systems with a different configuration and higher number of technologies have to be analysed.

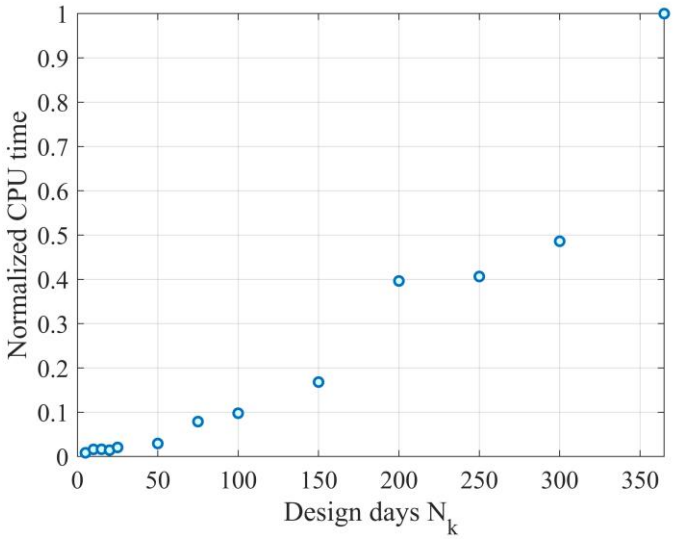

Figure 5.13 Normalized computational time as a function of the number of design days (N_k) for the reference HRES case.

Conclusions

The optimal design and yearly dispatch of a stand-alone renewable P2P system has been investigated. The entire year was considered in the simulation to take into account the seasonal variation of renewable energy production and site load. This is necessary to properly model the energy storage system, which is an essential component for off-grid areas that wish to achieve energy independence by relying on local renewable sources. Wear costs of batteries and H_2-based devices were included in the objective function of the optimization problem (i.e., the annual cost of the system). Demand-side management was implemented in the MILP formulation to assess its impact on the sizing results and LCOE. An optimization methodology with the integration of design days was finally developed to try decreasing the computational complexity of the problem, while maintaining accuracy in the sizing results.

The optimization framework was applied to the case study of Ginostra. Sizing outcomes revealed that the LCOE obtained by the MILP-based approach is around 11% cheaper than that derived by employing the metaheuristic method (which includes RBSs). In fact, a better power distribution between batteries, fuel cell and electrolyzer can be achieved by the MILP methodology thanks to its predictive capacity. However, greater computational resources were necessary to run the MILP problem. The hydrogen storage system is again confirmed to be useful in the optimal RES-based configuration to reach the energy self-sufficiency. This is because of its cost-effective long-term storage capability that allows the required battery capacity to be reduced. The implementation of a demand response program was also demonstrated to be effective in decreasing the

electricity generation cost. The LCOE moves from 0.455 €/kWh for the base case with no DRP to around 0.402 €/kWh when the DRP_{MAX} parameter is set equal to 30%. This cost reduction is mainly due to the decreased capacity of the battery storage system, which drops from 613 kWh to 454 kWh thanks to the improved balance of RES supply and demand. Almost no changes in size were instead observed for the other system components when considering DRP.

The optimization problem was finally performed with the inclusion of design days to investigate their influence on the sizing results. It was found that the hydrogen storage capacity starts to be accurately approximated from around 100 to 150 design days. At 100 DDs, the computational time is considerably lower compared to the full-year optimization, with a speed-up of approximately 10 times. The inclusion of design days seems therefore a promising technique to be applied especially when the complexity of the HRES configuration is further increased, for example for the analysis of poly-generation systems with greater number of technologies and different loads.

Chapter 6

Conclusions

Nowadays, electricity production in off-grid areas is mainly based on fossil fuels, despite the high fuel costs and the release of greenhouse gases. Grid extension is often unfeasible because of the expensive and invasive works in remote locations. Variable RESs, like solar and wind, have recently experienced relevant cost reduction and improvement in performance, which makes them ideal candidates to provide clean and low-cost energy to off-grid populations. However, because of their fluctuating nature, renewable generators need to be integrated with electrical energy storage devices to achieve high RES penetration levels. The optimal sizing of hybrid renewable energy systems is crucial to cope with RES variability and provide a stable and cost-competitive power supply service.

In this context, the present analysis investigates the techno-economic feasibility of different configurations of stand-alone HRESs to better highlight the role of hydrogen in achieving reliable and cost-effective energy systems. After describing the mathematical modelling of all the HRES components, four different case studies, defined in the framework of the REMOTE project, have been analysed: Ginostra and Ambornetti in Italy, Agkistro in Greece and Froan in Norway. For each site, the renewable H_2-based configuration was compared with an alternative option based on grid connection (when feasible) or diesel generators. The renewable solution was shown to be more profitable than the alternative one either in the short term or in the longer term for all the four sites. This is due to the high operating costs related to diesel consumption and to the capital-intensive initial cost to provide a connection to the main grid. The LCOE of the REMOTE systems ranges from around 0.4 to more than 1 €/kWh, with greater costs for the sites where the load factor is higher.

Off-grid energy systems need to be accurately designed to make the power supply reliable and economically feasible. The HRES sizing optimization was

hence addressed to ensure the total load coverage at the least cost of energy. Metaheuristic and MILP-based approaches have been considered to solve the optimization problem. The aim was to derive a general methodology that can be applied for the optimal design of any HRES.

Concerning the metaheuristic method, given its high robustness, the PSO algorithm was chosen to deal with the design problem. Rule-based control strategies were instead considered to manage the operation of the system. In fact, RBSs, which represent a practical and realistic way to simulate the micro-grid operation, are suitable to be implemented in the metaheuristic-based design methodology. Several energy storage architectures were investigated, including different types of batteries (Li-ion and lead-acid) and electrolyzers (alkaline and PEM), to analyse the role and potential of hydrogen in off-grid environments. The ε-constraint method was also employed to simultaneously cope with cost and environmental issues, and hence generate cost-emission Pareto fronts for different HRES configurations. The sizing methodology was applied to the insular locations of Ginostra and Froan, which are representative of many other isolated insular communities throughout the Mediterranean area and northern Europe, respectively. For both sites, it was proved that electrical energy storage systems are key elements to improve the exploitation of renewable energy sources and enhance the independence from imported fossil fuels. The hybridization of the energy storage, i.e., batteries together with hydrogen, is the most cost-effective choice when making the islands energy autonomous by relying entirely of local RESs. In Ginostra, the LCOE of the hybrid battery-hydrogen system is around 0.50 €/kWh compared to 0.54 €/kWh for a system with only batteries (considering the lithium-ion typology). This is because the hydrogen storage is useful to avoid the installation of batteries with too large capacity and to improve the exploitation of the solar energy source. Analogously, in Froan the presence of hydrogen is crucial to lower the cost of energy when progressively increasing the energy independence from fossil fuels. Concerning the case with no diesel, the LCOE of the energy system with hybrid storage is 0.41 €/kWh, which is approximately two-thirds of the LCOE of a system with only batteries. It should be noted that, when no constraints are imposed on the operation of the diesel generator, the cheapest configuration includes RESs together with battery and diesel genset. In fact, from an economic point of view, it is generally more convenient to have a diesel generator rather than hydrogen in order to prevent the oversizing of the battery component.

The optimal design of hybrid renewable energy systems was further investigated by means of a different approach based on the MILP technique. Piecewise-affine approximations of the performance curves of electrolyzer and fuel cell systems were employed to get reduced-order models for use in the MILP optimization framework. Wear costs of batteries and H_2-based devices were defined and included in the objective function as operating costs. Demand response program was also investigated with the purpose of lowering the cost of

energy. The involvement of the final consumers in demand response schemes is a fundamental step to make DRP successful. Thus, the benefits from DRP adoption should be analysed and better highlighted to encourage consumers to follow demand response, improving its social acceptance. The optimization framework was applied to the case study of Ginostra, reconfirming the key role of hydrogen in stand-alone RES-based energy systems. An LCOE of 0.46 €/kWh was found by employing the MILP methodology, which is around 11% lower than the cost of energy derived by the metaheuristic method. However, greater computational burden was required to run the MILP model because of the increased complexity and the larger number of decision variables. The DRP strategy was shown to be effective in reducing the cost of energy, mainly affecting the size of the short-term storage device, (i.e., the battery component). The optimal sizing was also formulated by including design days with the aim of decreasing the computational time required for the resolution of the problem. DDs were interconnected to preserve their chronological order throughout the year, which is needed for an adequate design of longer-term storage systems. The capacity of the hydrogen storage was found to be well approximated from around 100 to 150 design days. At 100 DDs, the CPU time is significantly lower compared to the full-scale optimization, with a speed-up of around 10 times.

To sum up, main achievements of this work are listed below.

- Derivation of an optimization framework for the optimal design of stand-alone hybrid renewable energy systems. A general methodology was formulated to be used for the optimal sizing of any off-grid HRES.
- Techno-economic analysis of H_2-based energy storage solutions in different remote areas (from alpine to insular) characterized by different typologies of RESs (solar, wind, biomass and hydro) and user loads (residential and industrial). A wider overview of these kinds of systems in off-grid environments was provided, also taking advantage of valuable data from the REMOTE project.
- Investigation of a rich portfolio of energy storage solutions. The analysis was applied to different HRES configurations (with and without RES and storage hybridization) including a wide range of technologies (e.g., Li-ion and lead acid batteries, alkaline and PEM electrolyzers) to gain insight into the role of hydrogen and batteries in providing a cost-effective and reliable power supply service.
- Inclusion of part-load performance curves of the hydrogen technologies in the HRES optimization framework and derivation of the lifetime of components based on their operating schedule. This was necessary to achieve a more accurate techno-economic evaluation. The usage of efficiency curves to model the behavior of the HRES components is particularly suited when dealing with systems that involve highly variable RESs.

- Formulation of an MILP-based methodology to deal with both the optimal design and scheduling of off-grid H_2-based storage systems. Degradation costs of components were included in the objective function to preserve as much as possible their state-of-health. The MILP method is able to handle a 1-year time horizon with hourly resolution, which is required to reliably design the off-grid HRES and cope with the seasonal variability of RES supply and load demand.
- Inclusion of design days within the proposed MILP-based approach. This made it possible to significantly decrease the computational time required for the resolution of the problem. Design days were fully coupled according to their chronological order along the year. Additional variables were also added for the start-up costs occurring at the beginning of each DD.

Worldwide there is plenty of areas where the electricity access is difficult, unreliable, or simply missing and unfeasible. Decentralized energy production by exploiting local RESs integrated with EES systems can represent a promising solution both from an economic and environmental point of view. Renewable battery-hydrogen systems were shown to be a reliable, cost-effective and eco-friendly option compared to more traditional alternatives based on diesel generators or grid connections. Energy storage systems are key components to improve the independence from fossil fuels, with hydrogen playing an essential role in reducing the cost of energy. Hydrogen, in fact, allows the battery and RES technologies not to be oversized, thanks to its cost-effective long-term storage capability.

Outlook

Based on the sizing approaches defined in this work, future steps could involve:

- The multi-objective optimization of off-grid HRESs based on a life cycle assessment (LCA) perspective. In this thesis, CO_2 emissions released by the HRES operation were considered in the sizing optimization by means of the ε-constraint method. The same approach could be applied to include various life-cycle impacts and derive cost-impacts Pareto fronts for different HRES configurations.
- The analysis of P2P storage systems acting as poly-generation plants: not only power storage and conversion, but also the use of hydrogen as transportation fuel or for the production of other energy outputs (e.g., heat) and chemicals. The MILP-based method is expected to be suitable to deal with energy systems characterized by several technologies and with different types of loads to satisfy. Moreover, the implementation of representative periods was proved to be effective to address the optimal sizing of off-grid H_2-based

HRESs since the computational burden was considerably decreased. Thus, design days could represent a promising technique to address the sizing of energy systems characterized by a greater level of complexity.

- The optimal design and operation of spatially-resolved energy systems. The system will consist of multiple interconnected nodes. In each node, energy can be converted, stored or used, following the sizing methodology presented here for off-grid HRESs. The interconnection between nodes could be modelled by the introduction of transmission technologies, e.g., gas pipelines, electricity transmission lines, and road/sea transport devices. This will allow RES- and hydrogen-based scenarios to be developed at larger spatial scales.
- The formulation of multi-year optimization approaches, which might be required for long-run energy planning (when, for example, it is expected a growth in the load demand over the lifetime of the project). Interconnected representative periods might be considered in the long-run optimization model to decrease the computation complexity, while maintaining the capability to model long-term storage devices (in this regard, we are currently dealing with the integration of typical periods and their chronological order in OSeMOSYS, an open source tool for the modelling of multi-scale energy systems [255]).

Supplementary material

Degradation insights on PEM electrolysis

Currently, the two principal technologies for a sustainable production of hydrogen are alkaline and proton exchange membrane (PEM) electrolyzers. Alkaline water electrolyzers (AWEs) represent a well-established, commercialized, and mature solution. PEM water electrolyzers (PEMWEs) can offer relevant advantages over AWEs: higher current densities, faster dynamic response time, higher operating modulation range, lower gas permeability, possibility to work with significant differential pressure, higher degree of gas purity and major system compactness. However, higher investment costs and lower durability than the alkaline alternative are the main problems to be solved to promote a widespread use of the PEM technology for hydrogen production [256].

For the sake of clarity, a schematic representation of an PEM cell cross section is displayed in Figure S.1. The main components and related materials of the cell are reported below:

- Anodic porous transport layer (PTL): Ti-based
- Anodic catalyst layer (CL): Ir, IrO_2 + PFSA
- Membrane: PFSA+PTFE
- Cathodic catalyst layer: Pt/C + PFSA
- Cathodic porous transport layer: C-based
- Bipolar plate (BP): Ti-based

In the following sections, a literature review about PEM water electrolysis has been performed to highlight the main cost and durability issues that currently affect this technology. An experimental analysis focusing on the monitoring of PFSA-based membrane degradation was then presented.

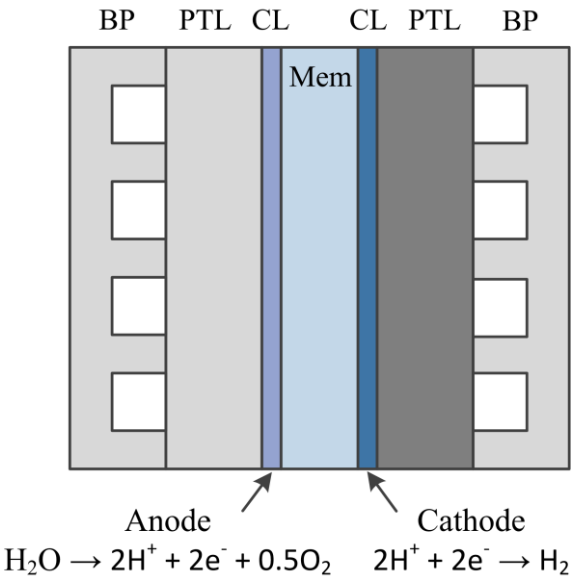

Figure S.1 Cross section of an PEM water electrolysis cell (the thicknesses are not in scale).

S.1 Cost issues of PEM water electrolysis

S.1.1 Bipolar plates

Titanium is required as bipolar plate material because of its high stability to corrosion in oxidative environments. However, the need for high purity Ti and the difficulty in the manufacturing process of Ti-based flow fields lead to high PB costs. Bertuccioli *et al.* [257] reported that Ti-based bipolar plates account for about half of the stack cost. Stainless steel (SS) has gained interest as an alternative since it is cheaper and easier to machine than titanium. However, because of SS corrosion issues at high potential in oxidative environments [258], a corrosion-resistant coating made of titanium should be adopted over SS as a protection. Proper modifications of the titanium surface are also required to mitigate the problem of Ti passivation, i.e., the formation of a semi-conductive oxide layer that would lead to an increase in the interfacial contact resistance (ICR) [259]. The coating over titanium should satisfy the following criteria [258]: good corrosion resistance, high electrical conductivity, low ICR, adherence to the substrate, low cost, ease to manufacture and resistance to H_2 embrittlement in the cathode compartment. The need for a protecting coating negatively impacts the PEMWE investment cost since precious and expensive materials are required. Platinum- and gold-based coatings are in fact generally used for bipolar plates [260]. Gago *et al.* [261] and Lettenmeier *et al.* [262] showed that platinum deposition can be an effective solution to avoid ICR increase. As an alternative to Pt, niobium was proved to be suitable for Ti-based coatings [263], especially for bipolar plates at the anode side [261]. The usage of Nb can represent a good

choice since it is more abundant and less expensive than Pt. Nitride protection layers were also reported as a possible solution by Bessarabov *et al.* [256].

S.1.2 Porous transport layer

Porous transport layers are usually made of carbon or metal materials. More specifically, carbon is used at the cathode side while titanium and stainless steel are generally preferred for the anode compartment because of its high potential and highly oxidative environment. High corrosion rates were observed when using SS as anodic PTL with subsequent cation release and membrane poisoning. Titanium is therefore preferred as PTL material because of its higher resistance to corrosion even if it is more expensive than SS. Similarly to BPs, the problem of Ti passivation can be addressed by applying protective coatings at the expense, however, of increased investment costs. The application of a coating is highly recommended especially when working at a high constant current density since it favors the formation of poorly conductive oxides on the PTL surface, with consequent increase in the ohmic resistance [260], [264], [265]. Uncoated Ti-based PTLs could be used in case the PEMWE is operated at low current densities (i.e., minor than around 1 A/cm^2) or in dynamic mode, thanks to the regenerative effect derived by dynamic operation [265]. Problems of coating detachment were reported by Rakousky *et al.* [266] at very high current density (i.e., 3 A/cm^2). Pt and Au are commonly employed to achieve high protection against Ti oxidation [256]. The sputtering of a very thin layer of iridium over the titanium PTL was also found to be effective in reducing the interface resistance between the PTL and the electrode [267]. Nitride coatings on PTLs through plasma nitridation are finally of great interest due to their low cost, high conductivity and good anticorrosion features [256].

S.1.3 Catalyst

Ir and IrO_2 are commonly employed as catalysts for the anodic catalyst layer [268], [269]. Oxides are generally preferred than metals at the anode side because of their greater stability at high potentials [270], [271]. RuO_2 would be an excellent and inexpensive material to catalyze the oxygen evolution reaction (OER) but it has lower stability than iridium-based catalysts. Platinum, finally, is not a good choice for the anode since it would be oxidized to a low-conducting oxide [271].

For the cathode catalyst layer, Pt supported over carbon is widely adopted to enhance the hydrogen evolution reaction (HER). The cathodic CL is thinner than the anodic one, as the HER is faster than the OER. A lower catalyst amount is therefore required for the cathode [78].

PEMWE stacks are currently based on high catalyst loadings [78], [272]: around 0.5 to 1 mg/cm^2 at the cathode and up to around 3 mg/cm^2 at the anode.

These values must be decreased to make the PEM-based technology less expensive and allow its commercialization (considering also that the availability of iridium is scarce). However, the catalyst lessening should be obtained without loss of performance and stability. Problems related to durability were in fact observed at low loadings [78]. As an example, Rozain *et al.* [273] showed that pure IrO_2 presented a threshold loading value of approximately 0.5 mg/cm^2 below which the electrochemical performance was degraded quickly. The reduction of the precious catalyst loading could be achieved by:

1. Adoption of a proper catalyst support. The catalyst loading could be reduced by dispersing the catalyst nanoparticles on the surface of a conductive support with large surface area. The support can also help to enhance the catalyst stability slowing down the catalyst dissolution thanks to the interaction catalyst-support. Concerning the HER, it is currently possible to reduce the use of Pt amount by its deposition on carbon-based supports, e.g., carbon nanotubes or carbon powders [274]. However, carbonaceous conductive supports cannot be used at the anode side because of the high anodic potential. The development of an appropriate oxide support with good conductivity, high surface area and able to withstand the harsh anodic environment (i.e., high potential, rich oxidation and low pH) still remains a challenge. Self-supported IrO_2 is therefore commonly used for the anodic compartment. Micro-sized titanium particles added to the anodic catalyst layer were proved to be effective in reducing the iridium amount (lower than 0.5 mg/cm^2), maintaining at the same time high performance and durability [272]. Within the NOVEL project [275], good results were also obtained by using TiO_2 as anodic support with Nb and Ta doping to improve the electrical conductivity.
2. Adoption of binary/ternary solid oxide solutions. Binary or ternary solid oxide solutions can be formed to reduce iridium content and thus lower PEMWE costs. Tunold *et al.* [276] reported that the addition of RuO_2 to iridium-based catalysts allowed high efficiency and stability to be achieved. Li *et al.* [277] found that a proper composition of $Ir_xSn_{1-x}O_2$ (e.g., x=0.67 and x=0.52) was effective in reducing the iridium content to less than 0.8 mg/cm^2, while maintaining good levels of performance and stability.

S.1.4 Operating conditions

Operating at high current densities can help to reduce the PEMWE investment cost thanks to the increased rate of hydrogen production per unit cell area of the electrolyzer. However, this would lead to higher operational costs because of the greater voltage losses [278]. Solutions to minimize the cell overpotential rise are therefore necessary to improve the electrolyzer efficiency when working at

elevated current densities. Lettenmeier *et al.* [279] reported that the adoption of a titanium macro-porous layer (MPL) over the PTL allowed them to significantly increase the efficiency of the device in the high current density region. In fact, thanks to its morphological properties, the MPL was able to reduce both the ICR (by around 20 m$\Omega \cdot cm^2$) and mass transport losses. Some studies have also focused on the usage of thinner membranes with the aim of decreasing the ohmic resistance, thus achieving higher current densities with good conversion efficiency [280]. Problems associated to thin membranes such as higher gas crossover and greater susceptibility to mechanical failure could be addressed by incorporating recombination catalysts and using reinforced membranes, respectively [280], [281]. Current densities up to approximately 20 A/cm^2 were reported by Lewinski *et al.* [282] when employing nano-structured thin film (NSTF) supports.

An in-depth understanding of the long-term stability of PEM water electrolyzers working at high currents is necessary before employing such conditions on a large scale. Increasing attention is therefore being addressed to the investigation of how high current density profiles can affect the PEMWE degradation. Gago *et al.* [264] reported that operating at high current densities negatively impacted on the cell performance due to irreversible degradation phenomena. The resulting high cell voltages in fact caused an increase in the ohmic resistance due to the formation of poorly conductive oxides at the interface between the anodic PTL and catalyst layer. This made necessary the application of protective coatings to cope with titanium passivation. Rakousky *et al.* [266] also found that anti-corrosion coatings were required under operation at high currents to improve the electrolyzer durability. Siracusano *et al.* [283] investigated novel side-chain PFSA membranes in terms of performance and durability and observed great stability when working at 3 A/cm^2.

S.2 Stability issues of PEM water electrolysis

S.2.1 Effect of impurities

Metallic cation impurities have a strong negative impact on the performance of the electrolyzer [284]. They are mainly originated from feed water, corrosion of pipes and stack components and fabrication processes of the membrane electrode assembly (MEA) [256]. The most important effects due to cationic species can be summarized as follows:

1. <u>Reduction of the ionic conductivity of the membrane</u>. The ionic conductivity of the Nafion membrane is negatively influenced by the presence of metallic ions since they occupy the ion exchange sites of the membrane, resulting in increased ohmic resistivity. In fact, the membrane presents a higher affinity to metal ions than protons [285]–[287]. Agglomerations of contaminants are mainly located in the near-cathode

membrane region. Grigoriev *et al.* [288], [289] reported that the dimensions of clusters formed by impurities and their distribution density decreased by moving away from the cathode towards the anode. In fact, the ion impurities are forced to move towards the cathode because of the water flow crossing the membrane (in the anode to cathode direction). As the impurities get close to the cathode, they tend to be reduced with subsequent deposition [289].

2. Catalyst poisoning. Metallic cations tend to migrate towards the catalyst layer occupying the ion exchange sites of the ionomer and covering the surface of the catalyst particles. Pt-based catalysts are especially subject to the blockage by external cations [274], [286], [287]. This causes an increase in the charge transfer resistance and a decrease in the double-layer capacitance at the electrode-electrolyte interface (i.e., decrease of the roughness factor).
3. Damage of the membrane by chemical degradation. Metallic cations favor the formation of radicals, which attack the PFSA of the membrane with subsequent release of fluoride ions in the water flow [111], [290].

The first two effects are generally reversible by performing a regeneration process, which consists in soaking the MEA into an acidic aqueous solution [256]. Because of the above cited negative effects, it is strongly recommended the use of highly purified feed water and the employment of pipelines made of corrosion-resistant materials.

S.2.2 BP and PTL degradation

As described in Section S.1, titanium is usually employed for BPs and PTLs because of its resistance to corrosion. However, during the electrolyzer operation, titanium tends to passivate, thus causing an increase in the ICR and a reduction in the energetic efficiency. The process of Ti passivation is enhanced at high temperatures and high current densities. The adoption of costly surface modifications are therefore usually required.

S.2.3 Catalyst degradation

1. Catalyst dissolution. Iridium dissolution is favored at a high potential and elevated current densities. The dissolution process also depends on the oxidation state of the catalyst due to its interaction with the support. The presence of a support can in fact lower the catalyst oxidation state and, consequently, slow down the degradation process [256]. Pt catalyst may degrade during shut down because of current reversal leading to catalyst migration from the catalyst layer with consequent decrease of activity. During shutdown, in fact, the system could work in fuel cell mode because of the presence of residual hydrogen and oxygen in the electrode

compartments. The well-known mechanism of Pt dissolution affecting PEM fuel cells could thus lead to loss of Pt from the cathodic CL as reported by Grigoriev *et al.* [288]. Mechanical stress, bubble formation, high gas generation rates, membrane thinning with lower adhesion of the catalyst layer may finally cause particle loss and layer detachment [256].

2. Metallic cation poisoning. Sources of impurities are materials constituting the MEA, the electrolysis stack and external piping. The presence of impurities can result in increased overvoltage losses as described in Section S.2.1.
3. Catalyst agglomeration. During electrolysis operation, catalyst particles may sinter leading to crystal size growth and loss of electrochemical surface area (ECSA). Pt nanoparticles agglomeration was observed after duration tests with rise in the mean particle size [78]. Millet *et al.* [274] reported that the coalescence of Pt particles was directly proportional to the temperature and to the duration of electrolysis operation. Rakousky *et al.* [265] also found the growth of Pt particles to be enhanced when operating with frequent current interruptions. Similarly, Brightman *et al.* [291] observed that power cycling negatively impacted on the electrochemical surface area of the platinum cathode. However, the Pt particle size increase was shown not to make a significant contribution to the overall cell voltage increment [260]. Although less often, catalyst agglomeration was also reported for the anode regarding catalysts based on iridium [78].
4. Support passivation. The oxidation of the metal support contributes to the increase in the ohmic resistance. Concerning IrO_2 supported by titanium, the support passivation was observed to become more relevant when rising the current density [256].

S.2.4 Membrane degradation

In PEM water electrolysis, membrane is necessary to separate the produced gases (i.e., hydrogen and oxygen), to transport protons from the anode to the cathode compartment, to block conduction of electrons and to support the catalyst layer. Therefore, it needs to possess good proton conductivity, low electronic conductivity, high resistance to crossover of both H_2 and O_2 gases and also excellent chemical, mechanical and thermal stability [78]. PFSA-based membranes are usually employed because of their great durability and better proton conductivity compared to alternatives. Nevertheless, the PFSA membrane is reported to be among the weakest components in an PEMWE for long term performance [256].

Unlike PEMFC systems (which are subject to relevant dimensional changes due to repeated hydration and dehydration cycles), in PEM electrolyzers dimensional changes are more limited since the device is constantly kept hydrated

by liquid water. However, membrane degradation can be caused by pinholes and foreign materials that are introduced during the MEA manufacturing process, inhomogeneous compression, uneven feed water distribution, excessive water flow rate values and non-uniform current distribution [78]. The operation at high current densities may result in uneven distribution of current lines, with consequent generation of hot spot and unequal membrane swelling [274].

Among the different causes affecting the membrane stability, chemical degradation is considered as one of the most severe degradation mechanisms. Stucki *et al.* [292] showed that the electrolyzer failure was mainly due to the degradation process of the Nafion-based membrane. Their system had to be shut down for safety reasons after detecting excessive levels of hydrogen in oxygen. The reason was a substantial thinning of the cell membranes in the stack, which caused an increase in the gas cross-permeation effects. Grigoriev *et al.* [287] also reported that chemical degradation was an important contributor to PEM cell failure because of the membrane thinning process.

The various steps that lead to the chemical attack of the polymer membrane are summarized in Figure S.2. Main reactions that are supposed to be involved in the degradation process are shown in Table S.1: reaction 1 describes the generation of hydrogen peroxide (H_2O_2), reactions 2 to 4 correspond to the formation of radicals from H_2O_2 decomposition, reactions 5 to 13 refer to parasite consumption of radicals and finally reaction 14 is about the membrane attack mechanism due to radicals [290], [293]. The above reactions involving free radicals were taken from studies about ionomer degradation in polymer electrolyte fuel cells [294], [295].

During the electrolysis process, oxygen crossover occurs from the anode to the cathode side due to diffusive and convective phenomena [91], [296]. In the presence of platinum, as in the case of PEMWE cathode catalyst layers, hydrogen peroxide can be generated according to reaction 1. Other oxygen reduction reactions (ORRs), such as water recombination, can be neglected being the cathodic potential lower than 0.4 V [297]. Although working conditions in the electrolysis mode are different from those in fuel cell operation, degradation mechanisms during electrolysis can be deduced from PEMFC research since the adopted membrane materials are the same. In the presence of metal ions, hydrogen peroxide can lead to the formation of radicals, which are responsible for the chemical attack to the membrane. Certain transition metal ions, such as iron and copper, were found to be the most dangerous regarding the acceleration of the degradation process [298]. In particular, ferrous ions (Fe^{2+}) were revealed to have the highest impact on the chemical degradation rate [299], [300]. Indeed, the presence of ferrous ions allows hydrogen peroxide to be decomposed into highly reactive hydroxyl radicals (OH*) through the Fenton's reaction mechanism (reaction 3). The impact of secondary radicals, i.e., hydroperoxyl (OOH^*) and hydrogen (H^*) radicals, is often neglected since they are much less reactive compared to the hydroxyl radical [300]. Radicals may also be generated without

the involvement of metallic ions, as shown by reaction 2. However, Ghelichi *et al.* [294] reported that R2 did not have any significant impact on radical formation. The so formed radicals are then responsible for attacking the membrane (reaction 14), with consequent membrane thinning and release of fluoride ions. Chandesris *et al.* [290] and Fouda-Onana *et al.* [111] observed that the fluoride release rate (FRR), which is related to the membrane chemical attack, is enhanced at high temperatures and has a peak in the low current density region.

As the membrane becomes thinner, the oxygen crossover increases and the membrane degradation accelerates (due to the increased cathodic oxygen concentration, which enhances H_2O_2 formation through reaction 1), thus speeding up the membrane thinning. This results in serious problems from a safety point of view since the enhanced gas crossover increases the molar percentage of H_2 in O_2 in the anodic compartment. Chandesris *et al.* [290] reported that the time evolution of the H_2 in O_2 percentage has an exponential increase. A significant increase in gas crossover was also observed by Inaba *et al.* [301], who performed durability tests in PEMFCs to investigate the membrane degradation. Therefore, the H_2 in O_2 concentration (which is strictly related to the chemical degradation of the membrane) represents a serious limit for the lifetime of PEM electrolyzers considering that the gas mixture becomes explosive at an H_2 content volume of around 4 vol.%.

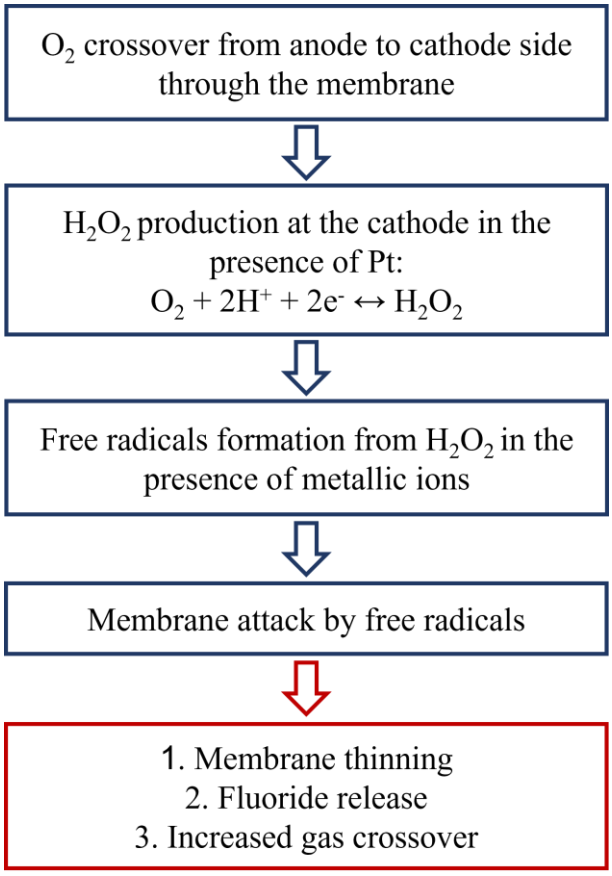

Figure S.2 Steps leading to membrane chemical degradation via radical attack.

Table S.1 Main reactions involved in the membrane chemical degradation.

H_2O_2 formation	
R1	$O_2 + 2H^+ + 2e^- \rightarrow H_2O_2$
Radical formation	
R2	$H_2O_2 \rightarrow 2OH^*$
R3	$H_2O_2 + Fe^{2+} \rightarrow Fe^{3+} + OH^* + OH^-$
R4	$H_2O_2 + Fe^{3+} \rightarrow Fe^{2+} + OOH^* + H^+$
Radical consumption	
R5	$OH^* + Fe^{2+} \rightarrow Fe^{3+} + OH^-$
R6	$OH^* + H_2O_2 \rightarrow OOH^* + H_2O$
R7	$OH^* + O_2 \rightarrow OOH^* + H_2O$
R8	$OOH^* + Fe^{3+} \rightarrow Fe^{2+} + O_2 + H^+$
R9	$OOH^* + Fe^{2+} + H^+ \rightarrow Fe^{3+} + H_2O_2$
R10	$OOH^* + H_2O_2 \rightarrow OH^* + H_2O + O_2$
R11	$2OOH^* \rightarrow H_2O_2 + O_2$
R12	$OH^* + OH^* \rightarrow H_2O_2$
R13	$OOH^* + OH^* \rightarrow H_2O + O_2$
Membrane attack	
R14	$R_f\text{-}CF_2COOH + OH^* \rightarrow products$

Going deeper into detail of membrane chemical attack, in the PEM fuel cell field it is generally accepted that the degradation process occurs via an unzipping mechanism involving carboxylic acid end groups (-COOH) [302]. The various steps of the unzipping process that lead to membrane fragmentation because of hydroxyl radical attack are presented below:

$$R_f\text{-}CF_2COOH + OH^* \rightarrow R_f\text{-}CF_2CO_2^* + H_2O \qquad \text{(S.1)}$$

$$R_f\text{-}CF_2CO_2^* \rightarrow R_F\text{-}CF_2^* + CO_2 \quad \text{(S.2)}$$

$$R_f\text{-}CF_2^* + OH^* \rightarrow R_f\text{-}CF_2OH \quad \text{(S.3)}$$

$$R_f\text{-}CF_2OH \rightarrow R_f\text{-}COF + HF \quad \text{(S.4)}$$

$$R_f\text{-}COF + H_2O \rightarrow R_f\text{-}COOH + HF \quad \text{(S.5)}$$

Overall, each carboxylic acid end group reacts with two hydroxyl radicals, leading to the release of one CF_2 unit in the form of one CO_2 molecule and two HF molecules:

$$\text{-}(CF_2)_j\text{-}COOH + 2OH^* \rightarrow \text{-}(CF_2)_{j-1}\text{-}COOH + CO_2 + 2HF \quad \text{(S.6)}$$

Carboxylic acid end group units are usually located at the end of the main chain of the fresh Nafion-based structure. However, more chemically-stabilized membrane typologies have recently been developed, reducing the terminal -COOH groups to negligible levels [303]. Carboxylic acid end groups can also be generated within the membrane through different pathways occurring during the operation of the electrolyzer. One option is that -COOH originates from the weak non-perfluorinated polymer end groups after reacting with hydroxyl radicals. Another mechanism suggests the Nafion side chain to be the -COOH source [304], [305]. The latter mechanism is much more impactful compared to the first option [304]. Nevertheless, once the –COOH unit is formed, the degradation process propagates according to the unzipping reaction, i.e., Equations (S.1)-(S.5), with subsequent release of HF molecules [306].

Recent experimental results suggest that the membrane degradation initiates by the side chain degradation with subsequent -COOH formation. The ether groups (αOCF_2 and βOCF_2) and the C-S bond located at the side chain terminal are generally supposed as the main targets of the radical attack. They are graphically displayed in Figure S.3, where the general structure of the Nafion-based membrane is shown. By applying the density functional theory (DFT) method, Ishimoto *et al.* [307] observed that the C-O bond in the ether group closed to the sulfo group (αOCF_2) was the main initiator of the side chain degradation due to the attack of OH^* species. They found that the αOCF_2 group was more vulnerable than βOCF2 (the other ether group that connects the side chain to the main chain). Similar considerations were reported by Ghassemzadeh *et al.* [303], who showed αOCF_2 to be likely the first point of radical attack. The ether groups of the side chain were also considered as the main points of hydroxyl radical attack by Dreizler *et al.* [308], who suggested to minimize the number of ether groups as much as possible during the manufacturing process in order to increase the durability of the membrane. Results from Kumar *et al.* [309] showed

instead that the degradation of the side chain by OH^* species can begin with the cleavage of the C-S bond located at the side chain end. Zhao *et al.* [310] also reported that the C-S bond was the weakest site against radical attack.

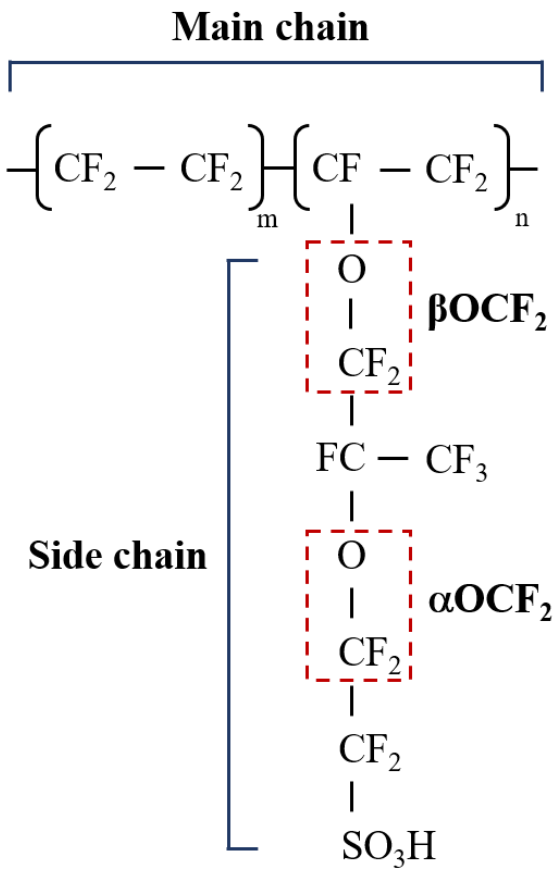

Figure S.3 Structure from Nafion (adapted from [311]*).*

S.2.5 Ageing tests

Ageing tests must be carried out to investigate the degradation of the PEM electrolyzer over time. They can be performed by applying a wide variety of operating conditions over different time horizons. Table S.2 and Table S.3 report a list of stability tests under steady-state and dynamic power conditions, respectively. The development of accelerated stress tests (ASTs) is necessary to understand the degradation mechanisms that affect PEM water electrolysis, while reducing testing time and efforts. An increasing number of projects are thus addressing the problem of PEMWE durability by developing specific AST protocols. In the framework of the NOVEL project [312], accelerated stress tests were defined at the single-cell level for lifetime evaluation and durability investigation of novel components. These tests were designed with the attempt to

magnify the membrane thinning and the increase in the electrical resistance. Similarly, AST protocols for single cells were developed by the ELECTRE project [313] in order to derive a cost effective way to predict the component lifetime. Testing protocols for PEMWE stacks were proposed by the NEPTUNE project [314] to investigate performance, efficiency and durability issues under high current density (up to 8 A/cm^2), high temperature (up to 140 °C) and high pressure (up to 100 bar). However, there remains the need for commonly agreed harmonized testing protocols to facilitate the comparison of experimental results within the scientific community [280].

Table S.2 List of steady-state ageing tests from the literature.

Duration [h]	**Current density [A/cm^2]**	**Temperature [°C]**	**Pressure [bar]**	**Configuration**	**Ref.**
120	1	80	Ambient	Single cell	[315]
200	1.2	70	Ambient	Single cell	[258]
500	0.5	80	-	Single cell	[277]
1000	0.2; 0.4; 1	60; 80	Ambient	Single cell	[111][a]
1000	1	-	-	Stack	[261]
1000	1	38	6.5	Stack	[262]
1000	1	38	6.5	Stack	[263]
1000	2	80	Ambient	Single cell	[260]
1000	1; 2	80	Ambient	Single cell	[265][b]
1000	1; 3	80	-	Single cell	[283][b]
1940	2; 2.5; 3	80	Ambient	Single cell	[266][a]
2000	1.1	Ambient	-	Single cell	[271]
5000	2	80	Ambient	Single cell	[282]
5700	1	55	-	Single cell	[284]
7800	0.5	60	Ambient	Stack	[286]

[a] Single long-term test
[b] Different long-term tests

Table S.3 List of dynamic ageing tests from the literature.

Duration [h]	Current density [A/cm^2]	Temperature [°C]	Pressure [bar]	Configuration	Ref.
300	Solar profile	80	Ambient	Single cell	[270]
450	3-0.1-0	80	10	Single cell	[316]
500	1-2	60	-	Single cell	[317]
1000	0-2; 1-2	80	Ambient	Single cell	[265][b]
1940	1-2; 1-2.5; 1-3	80	Ambient	Single cell	[266][a]
2000	0.08-up to 5	50	8	Stack	[318][a]
5500	0-1	90	-	Single cell	[287]
1500; 6500	0-up to 2; solar profile	80; 60	Ambient	Single cell	[272][b]

[a] Single long term test
[b] Different long term tests

The schematic representation of how a stability test can be designed is shown in Figure S.4. The loss of performance during the course of the ageing test can be monitored by means of in-situ characterization techniques such as: polarization curves (I-V curve) to evaluate the overall electrochemical performance [319]; electrochemical impedance spectroscopy (EIS) to distinguish between ohmic, activation and concentration losses [320]; cyclic voltammetry (CV) to measure reaction kinetics and estimate the electrochemical active surface area [321] and FRR measurements to detect the amount of fluoride ions released by the polymer electrolyte membrane. Fluoride detection is generally performed by means of ion selective electrodes (ISEs). As shown in Figure S.4, the electrochemical characterization (EC) by means of polarization curves, EIS and CV should be performed periodically during the course of electrolyzer ageing test.

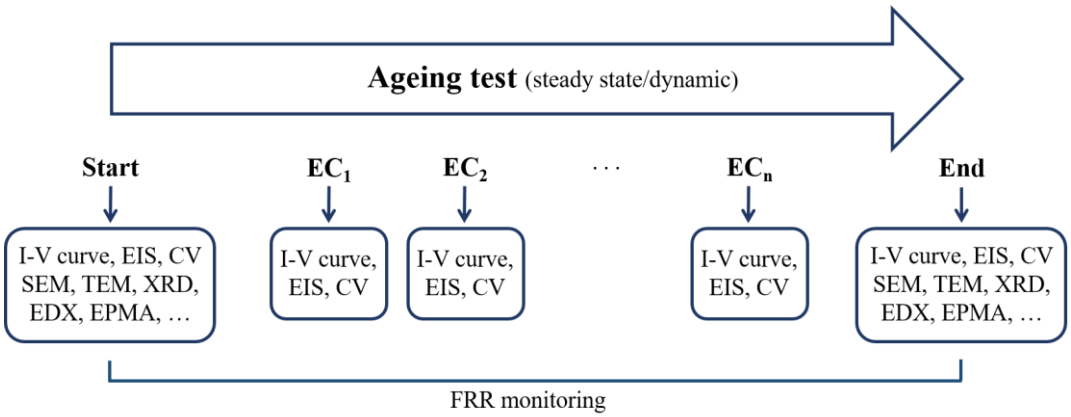

Figure S.4 Ageing test layout.

Along with in-situ monitoring, ex-situ tests can also provide important information on degradation mechanisms. Main ex-situ techniques commonly applied before and after a durability/stress test are reported below: scanning electron microscopy (SEM) to investigate membrane and catalyst layer thinning [111] and coating detachment [258]; transmission electron microscopy (TEM) to evaluate changes in the mean particle size and particle size distribution [260]; X-Ray powder diffraction (XRD) to determine structural and crystallite size changes [260]; electron probe microanalysis (EPMA) and Energy-dispersive X-ray spectroscopy (EDX) to determine the distribution of cation impurities along the cross section of the catalyst coated membrane (CCM) [260], [286], [287].

S.3 Online monitoring of membrane chemical degradation through Ion Chromatography

As highlighted in the previous sections, cost and stability issues must be tackled to further promote the spread and commercialization of the PEM electrolysis technology. Strategies commonly adopted to lower the electrolyzer costs deal with the reduction of precious metal catalysts and the replacement of titanium with stainless steel. However, it is widely recognized that increasing the operating current density, while keeping the efficiency at suitable levels, can represent the most relevant contribution in reducing costs of PEM electrolyzers [322]. As thick membranes in the range of 180 μm are commonly used in PEMWEs, thinner PFSA membranes can be a promising way to decrease both energy use and investment costs since reduced voltage losses and thus higher current densities can be achieved. Concerning the electrolyzer stability, the PFSA membrane is considered to be among the components that are most susceptible to degradation and failure [256]. Chemical degradation caused by radical attack and subsequent membrane thinning and loss of functional groups is indeed one of the main degradation mechanisms (see Section S.2.4). It is therefore extremely important to identify the operating conditions that can cause an enhancement of the chemical attack of the membrane and to define proper techniques to monitor its degradation over time.

Given that the unzipping process (globally described by Eq. (S.6)) causes the release of HF molecules, the rate of chemical degradation could be determined by measuring the fluoride ion content in the PEM electrolyzer exhaust. Baldwin *et al.* [323] reported a correlation between the emission of fluoride ions and the PEM cell lifetime. Since then, the monitoring of the fluoride release rate has become a reliable diagnostic tool to assess the chemical durability in the PEMFC field [324]. However, studies dealing with FRR measurements during electrolysis operation are few [111], [290], [293], [299], [312]. The fluoride ion selective electrode is usually employed for fluoride monitoring because of its simplicity and accuracy. Ion chromatography (IC) is another effective, but less straightforward, method for F^- ion detection [325]. Fouda-Onana *et al.* [111]

investigated the membrane degradation using two different ageing protocols at 60°C and 80°C, respectively. They analyzed the chemical degradation by regularly collecting exhaust water at the anode and cathode side and subsequently measuring the FRR by means of an ISE. Fluoride was mainly found on the cathode side, which is in accordance with the mechanism of membrane degradation caused by radical attack. With a similar set-up, Chandesris *et al.* [290] confirmed that most of the chemical degradation occurs at the cathode side and showed that temperature has a strong influence on the degradation rate, with a peak of FRR at a current density of around 0.2-0.4 A/cm^2. A 1D PEMWE model was also developed to analyze the influence of both temperature and current density and to study the time evolution of the membrane thickness. The model developed by Chandesris *et al.* [290] was later improved by Frensch *et al.* [293], who investigated the influence of iron and hydrogen peroxide. Their results showed that H_2O_2 acts as required precursor, while iron impurities catalyze the reaction considerably. In the framework of the FCH-JU project NOVEL [312], accelerated stress tests were carried out and their impact on the membrane chemical durability was also monitored by means of FRR measurements using the ISE technique. Low current values and high temperatures were found to speed up the membrane chemical attack. Within NOVEL, a long-term durability test at stack level was also performed showing that the degradation rate of H_2 in O_2 gas purity was about 0.45 ppm/h.

As above reported, studies dealing with PEMWE fluoride monitoring usually employ an ISE device to perform fluoride measurements in water samples that are periodically collected at the electrolyzer exhaust [111], [290]. The main aim of the study presented in this section is to develop a methodology to effectively monitor F^- ions by means of ion chromatography in an automated and online way. Ion chromatography is a highly interesting technique since, unlike ISE, it has the advantage of being able to simultaneously measure fluoride and other degradation products. Moreover, IC allows eliminating most of the interferences that potentially exist with ISE [325]. Another objective of this analysis is to give an insight into membrane chemical degradation referring also to thinner membranes. Thinner membranes allow the operation at high current densities with reduced voltage losses, which is necessary to decrease the investment cost of PEM water electrolyzers [23]. However, the increased crossover of gases due to the reduced membrane thickness may not only become potentially dangerous if the hydrogen concentration reaches the lower explosion limit (LEL), but it may negatively affect CCM degradation rates. Fluoride measurements under different operating conditions were carried out both at single-cell and stack level.

S.3.1 Experimental set-up

Electrolyzer cell and stack

Two different CCMs based on Nafion 117 and Nafion 212 with membrane thickness of 183 and 50.8 micrometers, respectively, have been investigated. The geometric area of the CCMs is 25 cm^2 using an Ir-based anode CL and Pt-based cathode CL, with loadings of approximately 2 mg/cm^2 Ir and 1 mg/cm^2 Pt. More detailed specifications about the catalyst layers are proprietary information and cannot be disclosed. More importantly for this study, both the Nafion 117 and Nafion 212 CCMs have the same catalyst type, catalyst loading, ionomer type and ionomer loading, and therefore can be directly compared. Flow fields at the anode and cathode side are both made of titanium. Platinum-coated titanium is used for the anode and cathode porous transport layers. Titanium is required because of its high stability to corrosion. As described in Section S.1, a platinum-based protective coating over titanium is also needed to avoid Ti passivation that could result in high interfacial contact resistance [256].

Pressure paper tests were performed to have a good homogeneous pressure distribution across the CCM area. A clamping torque of 15 Nm/bolt was found to be optimal for the electrolyzer cell assembly. The single-cell PEM electrolyzer was subject to a hydration and a break-in procedure. The hydration procedure included circulating 0.2 LPM of DI-water at both anode and cathode overnight at 40 °C and half of the final clamping torque (7.5 Nm/bolt). The cell was afterwards clamped to 15 Nm/bolt before starting the break-in procedure. This procedure involved polarising the electrolyzer in steps of 0.1 A/cm^2 for 5 min until reaching 2 V for 60 °C, 70 °C and 80 °C. The electrolyzer was then left at open circuit voltage (OCV) overnight at 40 °C with recirculation of 0.2 LPM of DI-water at both anode and cathode. After the initial membrane hydration and break-in procedure, the various CCMs were characterized in terms of polarization curves under various operating conditions, i.e., temperature (60-80 °C range) and cathode side pressure (0-4 barg range). Polarization curves measurements were carried out following the testing procedure reported by Malkow *et al.* [326]. Tests were performed under galvanostatic control and aborted when reaching a cut-off voltage of 2 V or a current density upper limit of 4 A/cm^2.

Fluoride monitoring was also performed at stack level to validate the IC measurement methodology for larger cells. The PEM water electrolysis short stack was purchased from Proton Onsite, and all the electrolyzer components (i.e., CCM, PTLs and BPs) are proprietary information and were not disclosed. The stack is composed of 10 cells and is designed to operate in the temperature range of 35 to 60 °C (with 50 °C as nominal temperature) and with a maximum current density of 1.86 A/cm^2. The single cell and stack under analysis are displayed in Figure S.5.

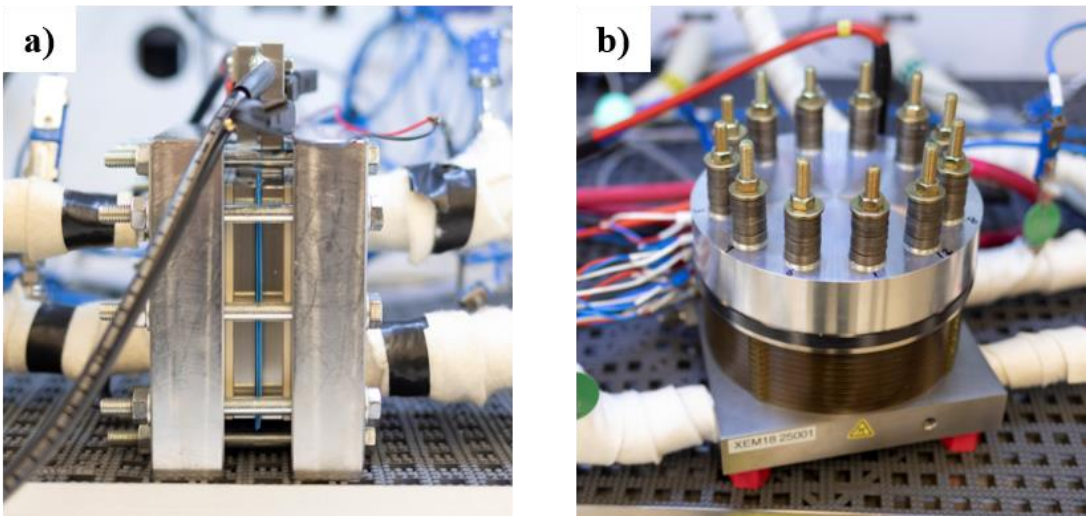

Figure S.5 Single-cell (a) and stack (b) PEM electrolyzers.

Test station

Commercial PEMWE test stations from Greenlight Innovation installed at the Norwegian Fuel Cell and Hydrogen Center were used in all the measurements [327]. A Greenlight E40 test station with maximum power supply of 100 A was used for the testing of the single cell. A Greenlight E100 test station with 500 A maximum power supply was instead employed for the stack testing. Both test stations have anode and cathode water circuits, where both the anode and cathode circuits are designed to work with water recirculation.

The schematic of the cathode-side circuit is shown in Figure S.6 (the anode one is analogous). The water flow exiting the cathode outlet is sent to the H_2 separator and then recirculated by a pump. The pump controls the liquid flow rate using signals from the mass flow meter located at the electrolyzer inlet. As displayed in Figure S.6, a portion of the recirculated water enters a mixed bed filled polisher containing a ion exchange resin (Aldex MB-1 (SC)). The water ratio at the polisher inlet is controlled by a needle valve. The functionality of the resin is very important in commercial PEMWEs, as highly purified water is required to minimize metallic cation impurities. As reported in Section S.2.1, cationic species can in fact lead to a reduction in the ionic conductivity of the membrane [285], [286], [289], contribute to catalyst poisoning [286] and enhance the chemical degradation process of the membrane [111]. A heat exchanger for cooling purposes and an electric heater are also present for thermal management by acting on the temperature of the recirculated water flow. Water conductivity was measured by means of ConduMax W CLS 13 conductivity sensors. The percentage level of hydrogen in oxygen was monitored with an K1550 series H_2 analyser. An anodic hydrogen content of 2 vol.%, which corresponds to around

50% of the lower explosion limit, was set as upper limit, above which the machine is automatically stopped for safety precautions.

All IC measurements of fluoride ion concentration were carried out on the cathode side of the PEM electrolyzers. This is because fluoride release has been shown to be far larger at the cathode than at the anode [111], [290], [312], which is in accordance with the hypothesis of membrane degradation occurring mainly in the cathode-side region. In fact, platinum, which catalyses the H_2O_2 formation reaction (i.e., reaction 1 of Table S.1), is mainly found in the cathode CL of the PEM cell. The low cathodic potential also favours reaction 1, whose equilibrium potential is 0.695 V vs. SHE [297], [328]. As shown in Figure S.6, a fraction of the water flow exiting the cathode channel was periodically delivered to the IC for fluoride evaluation in automated way. For a correct quantification of the FRR, the fluoride ions concentration at the cathode inlet was also measured. This is because water is recirculated and fractioned between the electrolyzer and the resin. Fluoride ions can thus be present in the portion of the recirculated water stream entering the cathode channel.

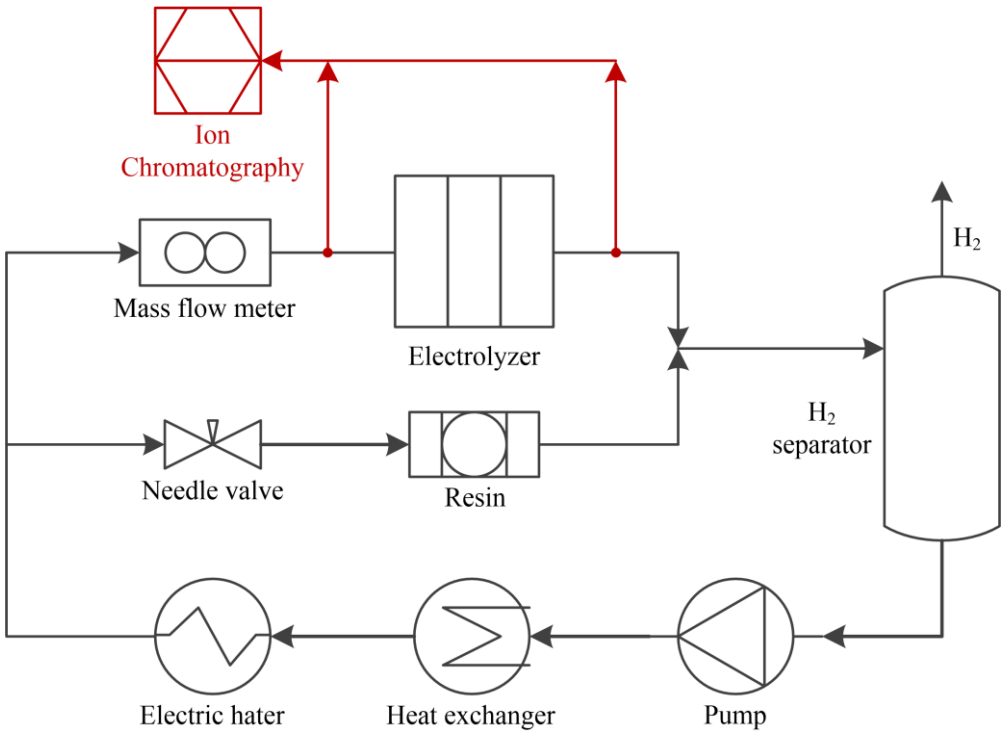

Figure S.6 Schematic of the cathode-side circuit (for both the single-cell and stack test station) including the electrolyzer cell/stack, hydrogen separator, circulating pump, heat exchanger and electric heater. The anode-side circuit is analogous to the cathodic one.

Measurements of fluoride ions

Ion chromatography was employed for the monitoring of fluoride ion concentration in the water flow of the electrolysis circuit. More specifically, an 850 Professional IC – Anion – MCS - Prep 2 device [329] was used to carry out automated online measurements of the fluoride concentration at the cathode outlet and inlet (Figure S.6).

The overall flow diagram of the IC measuring process is displayed in Figure S.7. The eluent, i.e., the fluid carrier, is first pumped alone through the system making it circulate through the column, until reaching equilibrium. During this initial step, anions (X^-) bonded to the resin are replaced by eluent anions (E^-) up to saturate the resin surface as follows:

$$Res^+\text{-}X^- + E^- \leftrightarrow Res^+\text{-}E^- + X^- \tag{S.7}$$

When a stable baseline is reached, a sample of the mixture to be analysed, i.e., the analyte, is added to the eluent by means of an injection valve. The stream with the eluent together with analyte is then supplied to the chromatographic column where the analyte separation process occurs after interacting with the resin according to the following reaction:

$$Res^+\text{-}E^- + A^- \leftrightarrow Res^+\text{-}A^- + E^- \tag{S.8}$$

where A^- is a generic anion contained in the analyte sample. After the analyte injection step, the continued addition of the eluent causes the sample ions (A^-) to be gradually displaced by E^- ions and to be pushed down the column. After leaving the column, the sample ions pass through a detector cell for the measurement of the various analyte peaks. The above main steps were repeated along the entire test to obtain a profile of the fluoride concentration during the electrolyzer operation. An ad-hoc script was written in the IC software to automatize the whole measuring procedure.

All the steps involved in the IC measuring process are detailed below. Referring to the eluent, a mixture of Na_2CO_3 and $NaHCO_3$ dissolved in deionized (DI) water with flow rate of 0.7 mL/min was adopted. Its pathway from the storage container to the injector consists of the following components [329]:

- Eluent bottle. The eluent is stored in a bottle connected to the degasser through an aspiration tube. The bottle is equipped with an aspiration filter (filter 0.45 μm) to protect the high pressure pump from foreign particles.
- Eluent degasser. Its presence is necessary to remove gas bubbles and dissolved gases from the eluent since they could cause unstable measurements when flowing through the high pressure pump. The degasser consists of a vacuum chamber with a fluoropolymer capillary.

- High pressure pump. It is required to overcome the circuit pressure drops, allowing the eluent to flow through the system.
- Purge valve. It is used for deaerating the high pressure pump, which requires air bubbles to be removed to work properly. Deaeration is performed by connecting the purge valve to a syringe for aspirating the eluent until bubble-free eluent is found. This process must be done whenever the device is switched on and after every change of eluent.
- Inline filter. It serves as a protection of the separation column against particles that may be present in the eluent.
- Pulsation dampener. It is needed to protect the separation column against pressure oscillations that could be generated by the injection valve switching.

As shown in Figure S.7, the analyte sample pathway to reach the injection valve is composed of a peristaltic pump followed by a degasser unit:

- Peristaltic pump. It works according to the principle of displacement and is used for pumping the sample towards the degasser and the injection valve.
- Sample degasser. This unit was added to remove gas bubbles and dissolved gases from the sample before being analysed. The presence of H_2 gases in the analyte could in fact cause poor reproducibility since the quantity of sample in the sample loop would not always be the same. For degassing, the sample is run though a fluoropolymer capillary in a vacuum chamber.

A certain amount of analyte is continuously taken from the electrolyzer cathode circuit and circulated throw the analyte circuit by means of the peristaltic pump (see Figure S.7). The analyte stream normally flows through the injection valve without mixing with the eluent and then is directed to a waste container. The eluent and analyte paths are connected only during the sample injection step through a rapid and precise switchover of the valve. Once the eluent is mixed with the sample through the injector, the liquid is sent to the chromatographic column (Molsieve 15 cm) where the separation of the analyte components occurs. After separation, a two-step suppression is performed to decrease the eluent background conductivity and enhance the conductivity of the sample ions. Finally, the analyte quantification process is performed by using a conductivity detector. The various steps incurred from injection up to the final detection are listed below:

- Injection valve. It enables the mixing of the eluent with a precise amount of sample solution, which depends on the size of the sample loop (set to 20 μL). This sample quantity is then dragged by the eluent flow to the separation column.
- Separation column. It separates the various ions based on their interaction with the column. Ions will then move through the IC column at a speed

that depends on their affinity with the resin contained in the column. As the eluent flows through the column, ions with lower affinity with the resin will move faster reaching the column outlet in less time. Vice versa, the elution time will increase in case of greater ion-resin affinity.

- Chemical suppression. The Metrohm suppressor module (MSM), composed of three different units, is employed to perform the chemical suppression during anion measurements. These units must be continuously regenerated with H_2SO_4 and rinsed with pure deionized water. Both the regeneration and rinsing solutions are fed to the MSM by means of a peristaltic pump.
- CO_2 suppression. The Methrom CO_2 suppressor (MCS) is used for the suppression of CO_2 from the liquid flow, thus lowering the background conductivity before detection. Possible CO_2 sources are the eluent itself or the MSM, where CO_2 might originate from suppression reactions. The MCS consists of a degassing cell equipped with a fluoropolymer membrane through which CO_2 can diffuse leaving the eluent stream.
- Conductivity detector. It is needed for the measurement of the conductivity of the liquid coming from the suppression steps. The resulting signals are displayed as peaks on the chromatogram. The flow at the detector outlet is then sent to a waste container.

The above described IC set-up allows obtaining an automated online IC measurement every approximately 24 minutes: around 5 minutes for the sample rinsing time plus 19 minutes of recording time (to allow all the analyte to cross the column). The sample rinsing time was chosen to prevent contamination of samples by the previous sample. During fluoride monitoring tests, the containers with the eluent, regenerative and rinsing solutions for MSM must be periodically refilled.

Main settings for the IC measurements are summarized in Table S.4. The values of these parameters were accurately chosen to be able to detect fluoride concentration, which was very low in all the performed tests (always in the range of ppb level).

Table S.4 IC main settings.

Parameter	Value
Eluent	Na_2CO_3 (0.339 g/L) + $NaHCO_3$ (0.084 g/L) + H_2O[a]
Eluent flow rate	0.7 mL/min
Regenerator for MSM	H_2SO_4 + H_2O[a]
Rinsing solution for MSM	H_2O[a]
Amount of sample loop	20 µL
Sample rinsing time	5 min

[a] highly purified DI water (18 Mohm)

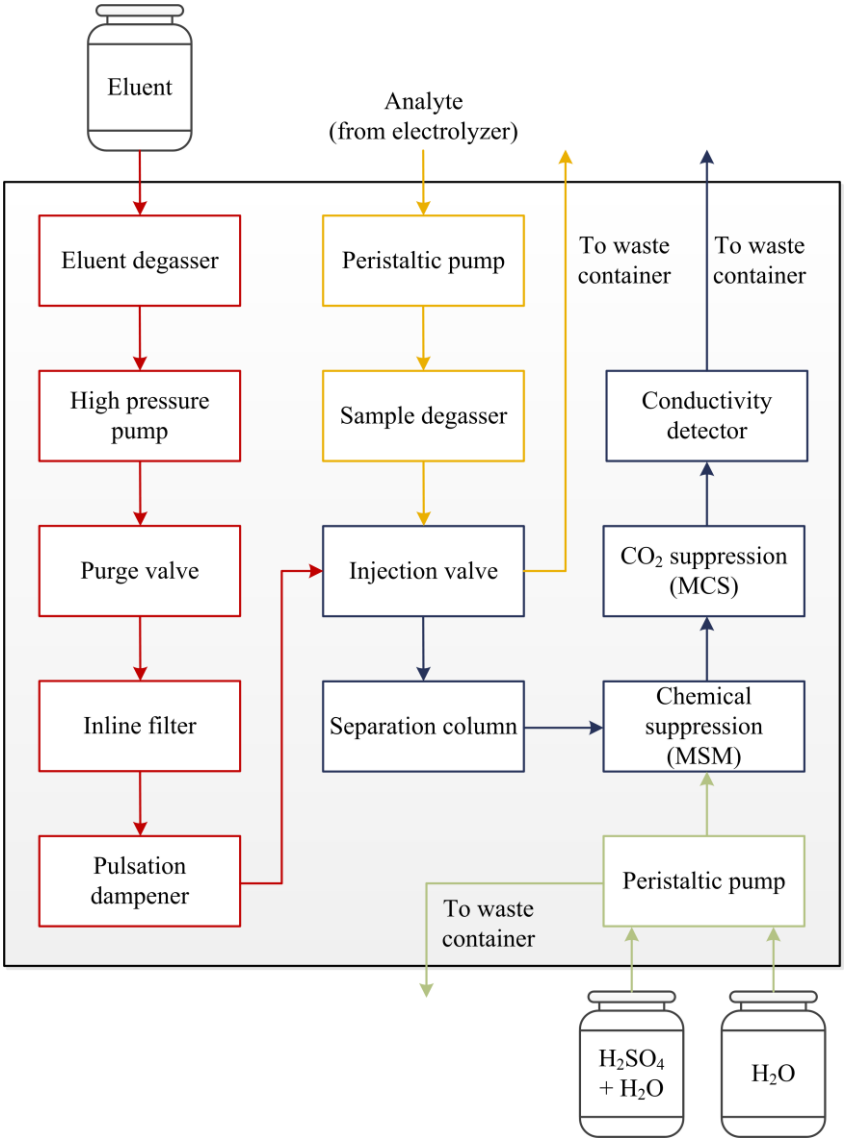

Figure S.7 Flow diagram of the fluoride measuring process by means of ion chromatography.

IC calibration is required to convert peak areas from the measured samples into concentrations. By diluting a multi-element IC anion standard solution (Multi Anion Standard 1 for IC from Sigma-Aldrich), standard samples with different known fluoride ion concentration were made and used for the calibration of the ion chromatography instrument. The different values of peak area were then plotted versus the fluoride ion concentration and a calibration curve, as the one shown in Figure S.8, was obtained by linear fitting. The calibration process was performed periodically to guarantee accuracy of results.

Current sensitivity tests were carried out to investigate the effect of current density on the concentration of F^- ions. The influence of temperature was also analysed. Each operating condition was maintained for a certain time interval to reach stabilization in IC fluoride measurements. Besides the continuous acquisition of fluoride concentration values over the test period, other PEMWE parameters were monitored and logged, e.g., voltage, current, temperature and pressure (at the inlet and outlet of both the anode and cathode), conductivity of the stream in the anode and cathode circuit, mass flow rate of H_2 production and H_2 in O_2 signal at the anode.

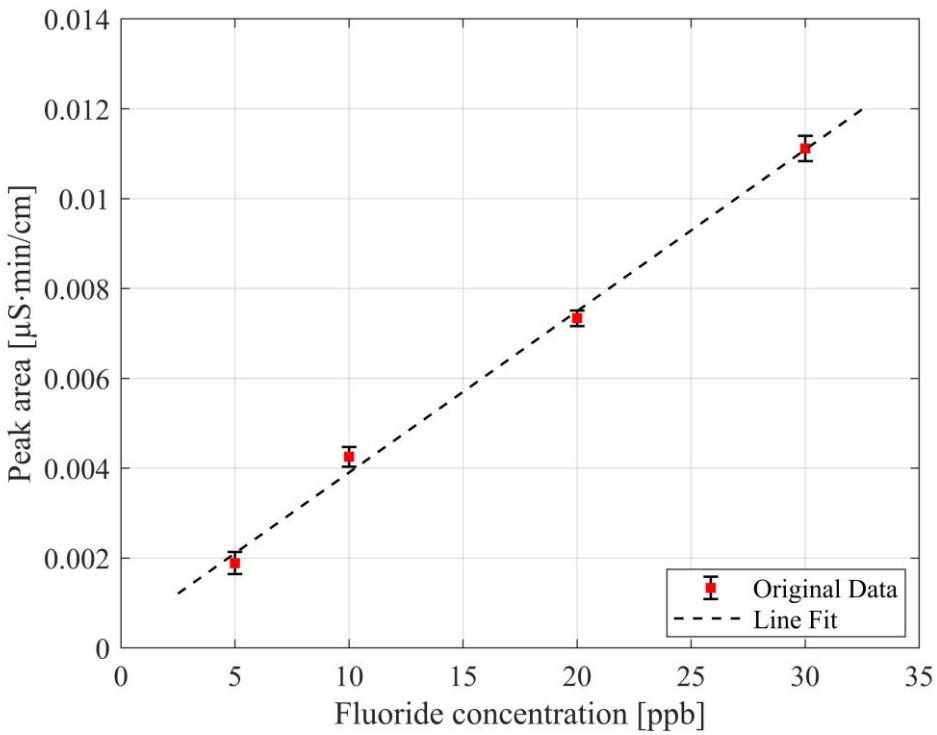

Figure S.8 Example of IC calibration curve that relates fluoride peak areas with fluoride concentration values.

S.3.2 Single cell: results and discussion

The performance of the three tested CCMs at single-cell level was investigated by recording a set of polarization curves. For the sake of comparison, Figure S.9 shows the polarization curve measurements at 60 °C (a) and at 80 °C (b) and ambient pressure at the beginning of life (BOL), just after the break-in procedure of the CCMs.

As can be observed in Figure S.9a, when working at 60 °C, the performance of the two Nafion 117-based membranes are quite similar, with a current density of around 1.5 A/cm^2 at the cut-off voltage of 2 V. Due to the lower slope of the curve (i.e., reduced ohmic resistance), the performance of the Nafion 212-based CCM is drastically improved: at 2 V, the corresponding current density is around 3.7 A/cm^2, which is more than double the one of Nafion 117 CCMs.

Polarization curves at 80 °C are displayed in Figure S.9b, showing an enhancement of the cell performance compared to 60 °C. This is because of improved OER and HER kinetics, as well as lower ohmic resistance at higher temperatures, as water uptake and proton conductivity is increased. Current density for the Nafion 117 membranes increases from 1.5 A/cm^2 at 60°C to approximately 2 A/cm^2 at 80°C at the cut-off voltage of 2 V. Moreover, the thinner membrane is able to reach current densities as high as 4 A/cm^2 at around 1.9 V. Only slightly higher voltages in the activation region were observed when changing the cathode pressure from 0 to 4 barg.

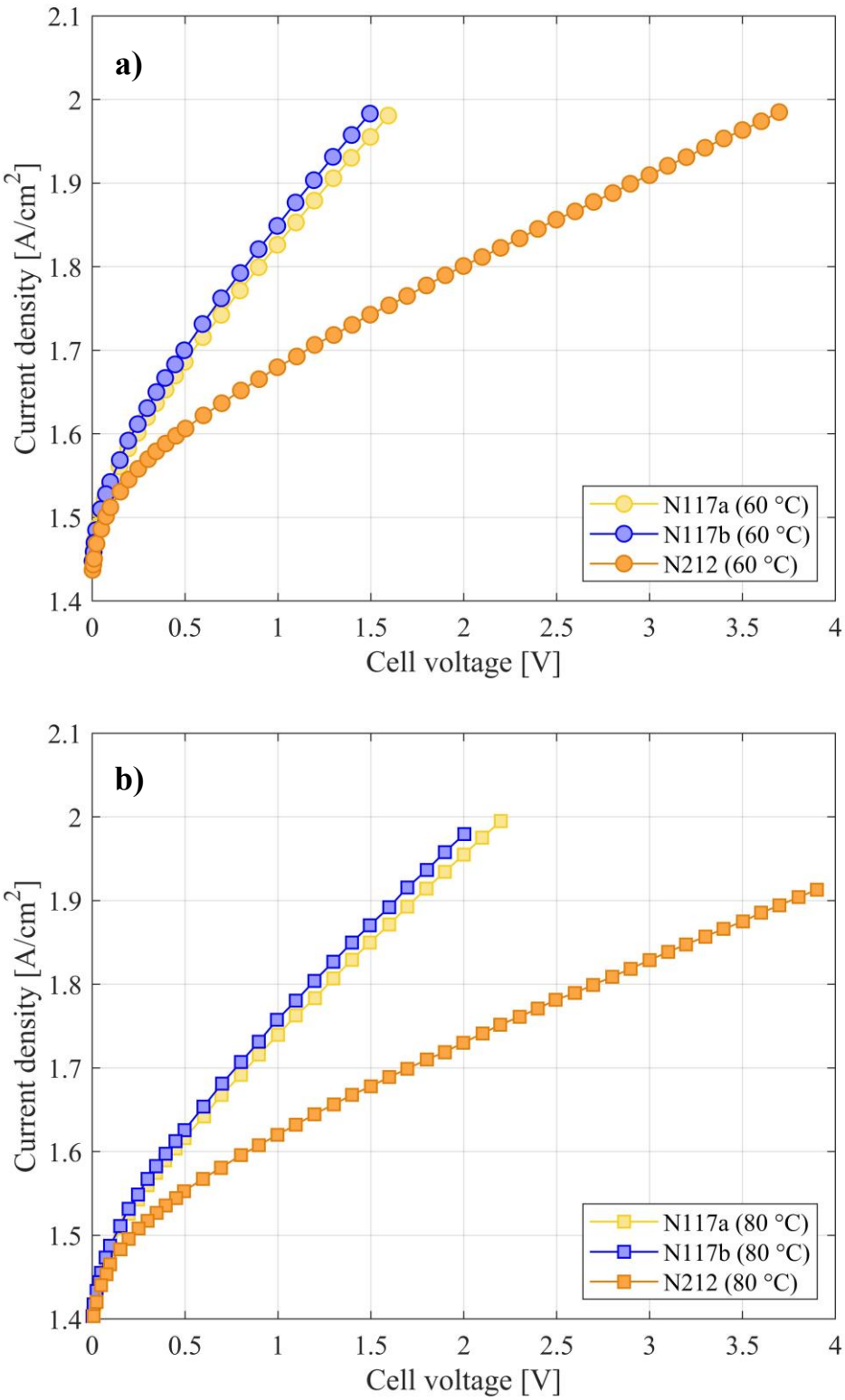

Figure S.9 BOL polarization curves of CCMs at ambient pressure, 0.2 LPM of water flow rate (both at the anode and cathode inlet) and temperature of 60 °C (a) and 80 °C (b).

Figure S.10 shows the effect of the operating current density on the fluoride concentration at the cathode outlet stream for the first tested Nafion 117-based CCM (i.e. Nafion 117a). The behaviour of the water conductivity at the cathode is also shown in the same figure. Due to the continuous online fluoride monitoring, it was possible to detect transients in fluoride emission. The current range between 0.2 to 2 A/cm^2 was swept with steps of 0.2 A/cm^2. Each current density was set constant for around 6 hours, before moving to the subsequent value. The entire test was carried out at a constant temperature of 60 °C and with a cathode recirculated water flow rate of 0.15 LPM. A maximum in the fluoride ion concentration can be observed at a current density of 0.4 A/cm^2 with a gradual reduction by increasing the operating current. It is also evident that there is a similar trend for the fluoride concentration and cathode conductivity profiles.

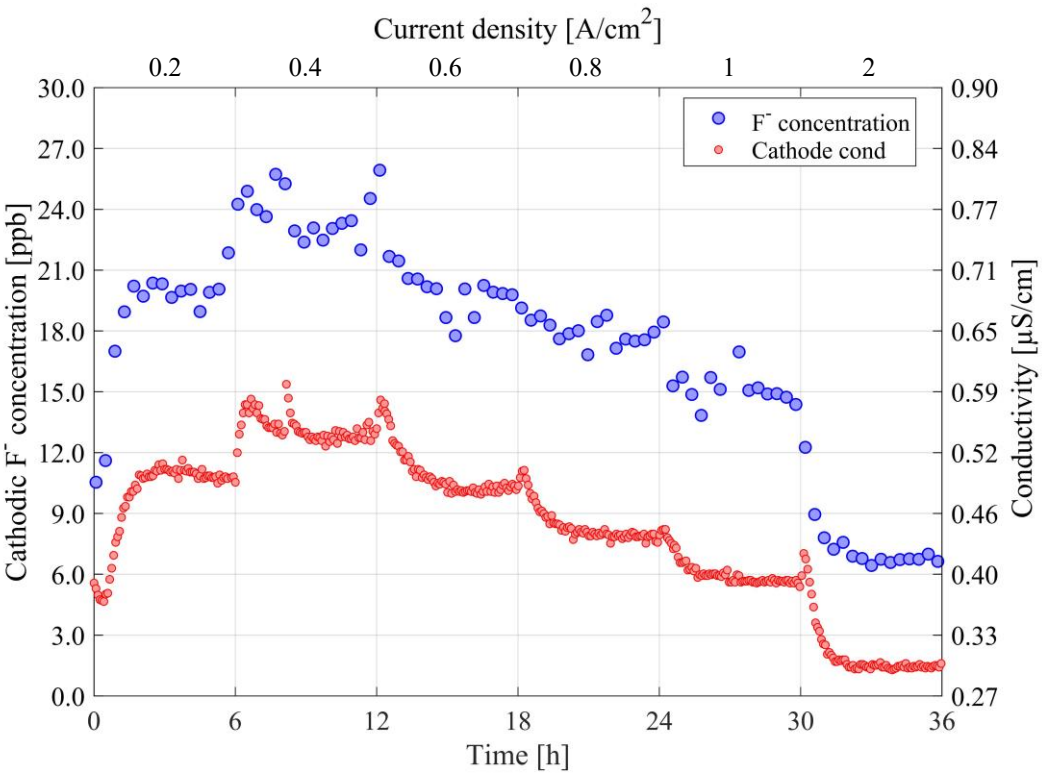

Figure S.10 Current sensitivity at 60 °C for the Nafion 117a CCM with 0.15 LPM recirculated water at the cathode side: effect of current density on the fluoride concentration at the cathode outlet and on the cathode water conductivity.

Similarly, the current density influence was analyzed for the other Nafion 117 CCM, i.e., Nafion 117b (Figure S.11) and the thinner Nafion 212 CCM (Figure S.12). The effect of temperature was also investigated by performing current sensitivity tests at two different temperatures, 60 and 80 °C. As it can be seen from Figure S.11, a fluoride peak at quite low current densities, at around 0.4 to 0.6 A/cm^2, is evident for both the tests at 60 and 80 °C. During the operation at 80 °C (i.e., Figure S.11b), the test was stopped after around 12 hours because of an

unexpected external event and started again from the 0.6 A/cm^2 case. Higher values of fluoride ions are observed when the temperature is changed from 60 to 80 °C. The measured fluoride concentration at 80 °C was found to be around five to six times higher than that at 60 °C for all the considered values of current density. Figure S.11 also shows both the anodic and cathodic water conductivity values along the test. The change in the value of the conductivity at the anode side by varying the current density is very low, even when operating at high temperatures as clearly displayed in Figure S.11b.

Figure S.12 shows the fluoride concentration and water conductivity for the Nafion 212 CCM. An additional 6-hour test was also performed at 3 A/cm^2 to investigate the fluoride release at even higher current densities. The Nafion 212 shows a much lower fluoride concentration compared to the two Nafion 117 CCMs, with a fluoride peak at 60 °C of around 6.3 ppb (for the Nafion 117 was around 24 ppb). The fluoride peak for the thinner CCM is shifted to slightly higher currents densities compared to the thicker CCMs. Referring to the 60 °C case, the fluoride concentration reaches its maximum when operating at 0.6 A/cm^2 (Figure S.12a). The fluoride peak also shifts with increasing temperature to a value of around 0.8 A/cm^2 when working at 80 °C (Figure S.12b). A two to three-fold increase in fluoride concentration was detected for the Nafion 212 membrane in the range of 0.2 to 3 A/cm^2 when moving from 60 to 80 °C. Likewise to the other tested CCMs, the cathodic fluoride concentration and water conductivity present a similar behavior along the test. A very low variation of the anodic water conductivity value by changing current can be seen as well.

The experimentally observed trends as a function of current and temperature are in accordance with what reported by Fouda-Onana *et al.* [111] and Chandesris *et al.* [290], who focused on Nafion 117-based membranes. In fact, they showed that the fluoride release (and hence the membrane degradation) had a maximum at low current densities, around 0.4 A/cm^2. Chandesris *et al.* [290] developed a cell model that incorporates the chemical degradation of the membrane to try to justify their experimental results. They explained the decrease in fluoride release at higher current densities by the reduced molar percentage of oxygen at the cathode side (oxygen becomes more diluted by increasing current because of the enhanced H_2 production). In fact, by decreasing the oxygen concentration, the peroxide formation (reaction 1 from Table S.1) is slowed down with consequent reduction in the formation of free radicals. The observed fluoride peak at low current was instead explained by the competition that occurs between the reaction involving H_2O_2 and OH* (reaction 6) and the reaction leading to membrane attack (reaction 14). Reaction 6 and 14 are reported to be the main consumption reactions of hydroxyl radicals. Specifically, in the low current density range, the high cathodic oxygen molar fraction favors the formation of hydrogen peroxide through reaction 1. Due to the high H_2O_2 concentration, reaction 6 is enhanced and, below a certain current, becomes predominant over the membrane attack reaction (reaction 14), leading to a decrease in the degradation rate, i.e., lower fluoride emission.

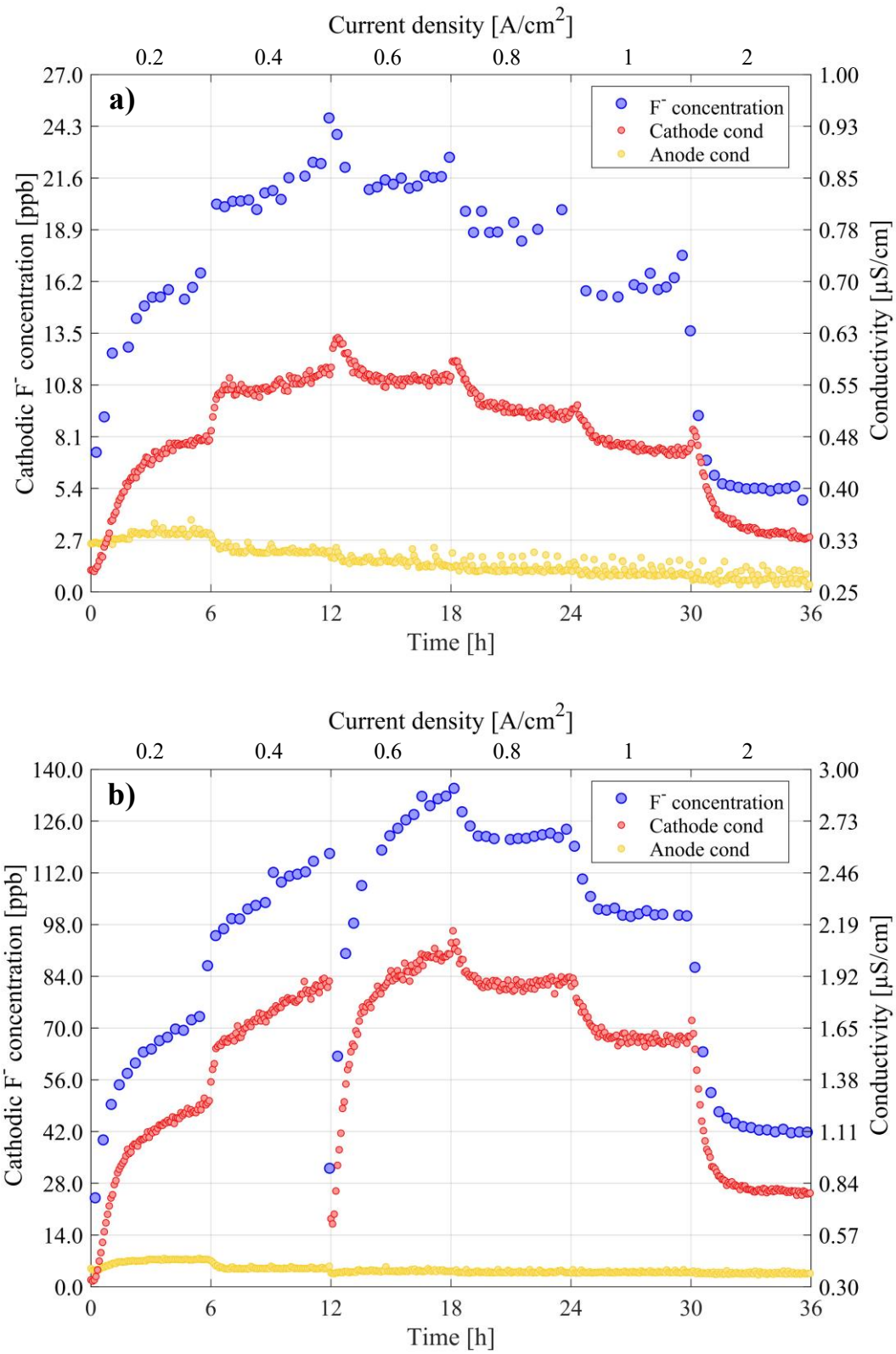

Figure S.11 Current sensitivity at 60 °C (a) and 80 °C (b) for the Nafion 117b CCM with 0.15 LPM recirculated water at the cathode side: effect of current density on the fluoride concentration at the cathode outlet and on the cathode/anode water conductivity.

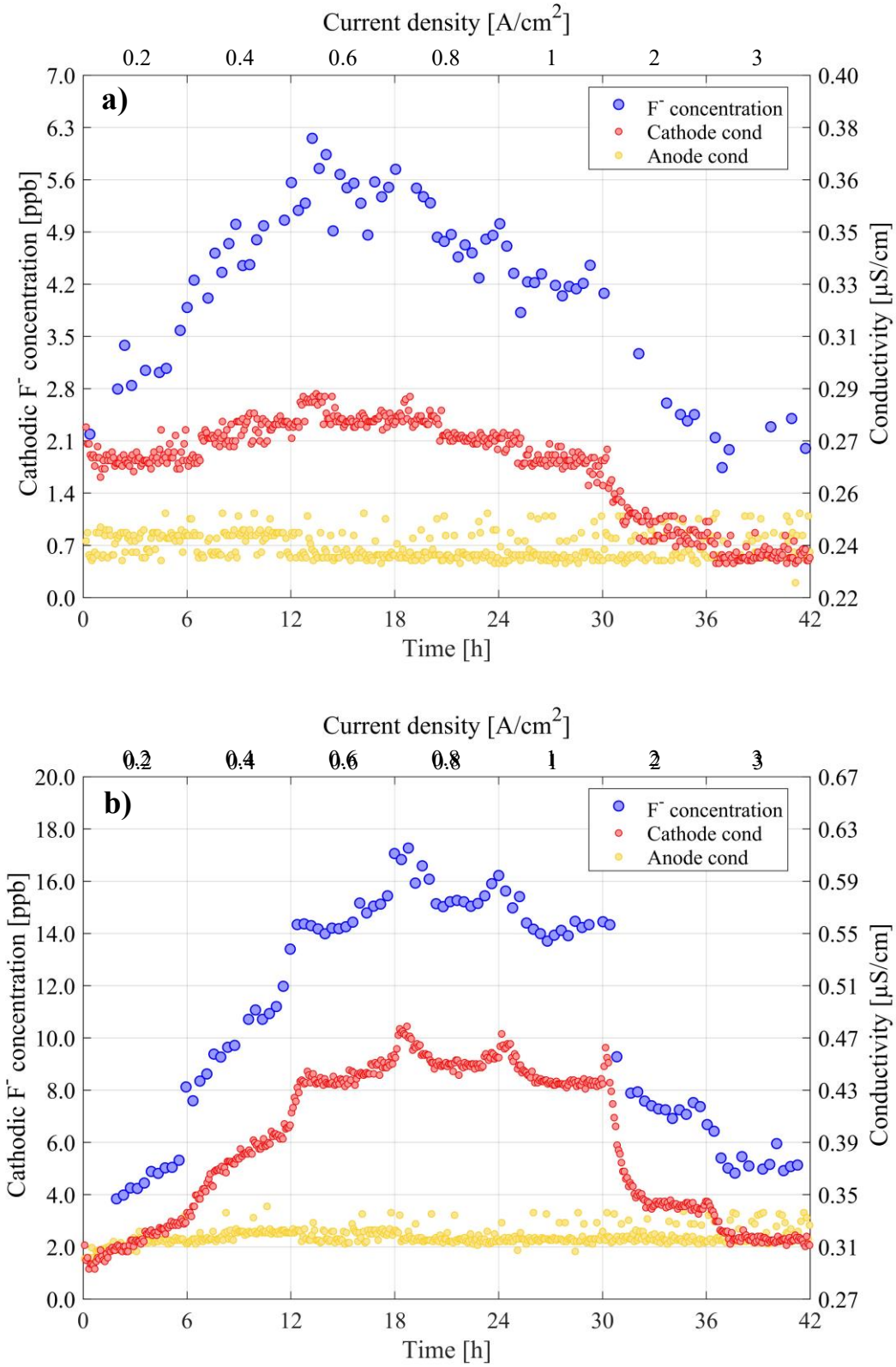

Figure S.12 Current sensitivity at 60 °C (a) and 80 °C (b) for the Nafion 212 CCM with 0.15 LPM recirculated water at the cathode side: effect of current density on the fluoride concentration at the cathode outlet and on the cathode/anode water conductivity.

In Figure S.13 fluoride IC measurements are plotted against measured conductivity to investigate possible correlations between the two variables. All IC measurements of the various tests at 60 and 80 °C referred to the three tested CCMs have been taken into account. A good linear correlation can be seen with a coefficient of determination (R^2) of approximately 0.949 at 60 °C (Figure S.13a) and 0.998 at 80 °C (Figure S.13b).

A linear correlation between water conductivity and F^- ions concentration has been reported earlier by Pozio *et al.* [330], but referring to the PEM fuel cell field. Water conductivity depends mainly on H^+ ions, whose release can be justified in the presence of anions to guarantee water charge neutrality [330]. It can be deduced the concomitant occurrence of F^- and H^+ ions in the water flow as also showed by Healy *et al*. [331], where a relationship between fluoride concentration in fuel cell exhaust water (in terms of pF, i.e., $-\log_{10}[F^-]$) and pH was demonstrated. The measured fluoride is thus released primarily in the form of HF, which is a weak acid (pK_a equal to 3.2) and will dissociate into H^+ and F^- ions. This is in accordance with a degradation process that involves radical attack on fluorinated backbones with consequent HF production, as reported by the unzipping mechanism described by Equation (S.6). The measured conductivity values are also in line with HF conductivity data estimated from the theory of ionic solutions [332], thus confirming that HF is the main product released by the membrane and affecting the water conductivity.

Very low variations of water conductivity in the anode circuit were observed when changing the working current and temperature of the PEM electrolyzer (see Figure S.11 and Figure S.12). By reasonably supposing the existence of a correlation between fluoride concentration and conductivity also on the anode side, it can be deduced that the FRR occurs mainly at the cathode side, which is in line with other experimental observations [111], [290] and the commonly accepted CCM chemical degradation mechanism.

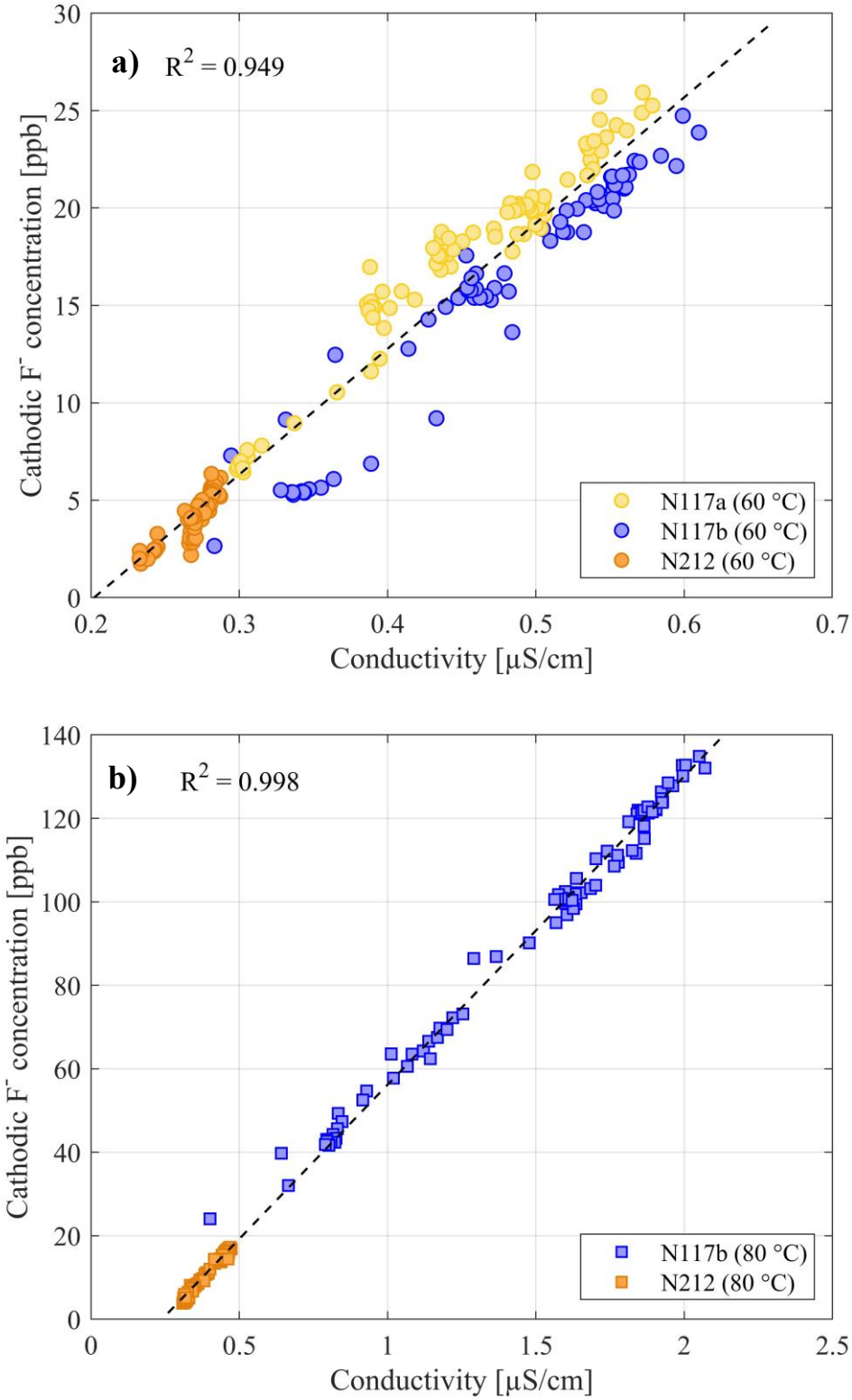

Figure S.13 Fluoride concentration at the cathode outlet vs. water conductivity in the cathode circuit for all the three CCMs at 60 °C (a) and 80 °C (b).

The cathodic area specific fluoride release rate (FRR_A) was computed to quantify the fluoride amount coming from the PEM membrane. FRR_A represents the amount of fluoride that is released in the cathode channel per unit of CCM area and per unit of time. It was derived according to the following relationship:

$$FRR_A = \frac{\left(ppb_{F,cat,out}\,\dot{V}_{H_2O,cat,out} - ppb_{F,cat,in}\,\dot{V}_{H_2O,cat,in}\right)60}{A_{cell}} \tag{S.9}$$

where FRR_A (in μg/h/cm^2) is the area specific FRR, $ppb_{F,cat,out/in}$ (in parts per billion) corresponds to the cathodic fluoride concentration at the cathode outlet/inlet, $\dot{V}_{H_2O,cat,out/in}$ (in LPM) represents the volume flow rate of water at the cathode outlet/inlet and A_{cell} (in cm^2) is the CCM geometric area.

As reported in the above FRR formula, the amount of F^- ions at the inlet of the cathode needs to be measured as well for a proper quantification of the FRR. In fact, fluoride ions are also found at the cell inlet since, as previously reported, the cathode circuit is designed to operate with water recirculation and with the cell and the resin unit arranged in parallel, as commonly done for commercial electrolyzer systems. It was found that the inlet fluoride concentration (i.e., $ppb_{F,cat,in}$) was at all times 83% of the cathode outlet when working with a recirculated water feed flow rate of 0.15 LPM. This value was then used to compute the net fluoride released by the CCM.

The volume flow rate of water exiting the cathode channel is:

$$\dot{V}_{H_2O,cat,outlet} = \dot{V}_{H_2O,cat,in} + \dot{V}_{H_2O,cross} \tag{S.10}$$

where $\dot{V}_{H_2O,cross}$ (in LPM) stands for the amount of water flowing through the PEM membrane. It is mainly due to the electro-osmotic drag process and the pressure gradient across the polymeric membrane as follows:

$$\dot{V}_{H_2O,cross} = \dot{V}_{H_2O,eod} - \dot{V}_{H_2O,dp} \tag{S.11}$$

In molar terms (mol/s), the electro-osmotic transport can be defined by the following expression:

$$\dot{n}_{H_2O,eod} = n_{eod}\,A_{cell}\,\frac{i}{F} \tag{S.12}$$

where n_{eod} is the electro-osmotic drag coefficient, i (in A/cm^2) is the current density and F (equal to 96,485 C/mol) corresponds to the Faraday constant. The n_{eod} coefficient represents the number of water molecules dragged for each proton when crossing the membrane from anode to cathode. It is usually assumed in the range of 2.16 to 4.03 [98], [103]. Marangio *et al.* [83] supposed this

coefficient to be equal to 7 based on the measured large amount of water flowing through the membrane. A temperature-dependent linear expression was presented by Onda *et al.* [100] when referring to a fully hydrated membrane. An experimental relationship depending on temperature was also adopted by Yigit *et al.* [82].

The Darcy's law can be applied to mathematically describe the water transport mechanism due to the presence of a pressure gradient:

$$\dot{n}_{H_2O,dp} = \frac{\rho_{H_2O}}{M_{H_2O}} A_{cell} \frac{K_{mem}}{\mu_{H_2O}} \frac{\Delta p}{t_{mem}} \tag{S.13}$$

where $\dot{n}_{H_2O,dp}$ (in mol/s) is the water crossover flow driven by differential pressure, ρ_{H_2O} (in g/cm^3) is the water density, M_{H_2O} (in g/mol) is the water molecular weight, K_{mem} (in cm^2) is the hydraulic permeability of the membrane, μ_{H_2O} (in Pa·s) is the water dynamic viscosity, Δp (in Pa) is the absolute pressure difference between the cathodic and anodic compartment and t_{mem} (in cm) is the membrane thickness. The membrane permeability was assumed to be $5 \cdot 10^{-16}$ cm^2 by Trinke *et al.* [92]. A value of $1.58 \cdot 10^{-14}$ cm^2 is also widely adopted [79], [83], [89]. A temperature-dependent correlation for the dynamic viscosity of water can be found in the publication by Birgersson *et al.* [99].

By applying the above formula to estimate the water flow rate crossing the CCM, it was found that the term $\dot{V}_{H_2O,cross}$ is negligible compared to the chosen value of water entering the cathode (which is 0.15 LPM) for all the analyzed electrolyzer operating conditions. The outlet flow of water can be thus approximated considering it equal to the inlet without losing accuracy in the computation of the FRR.

Figure S.14 shows the averaged outlet F^- ions concentration and the related derived area specific FRR for the various CCMs at 60°C (Figure S.14a) and 80°C (Figure S.14b) with values computed as an average of the last three IC measurements. As shown in Figure S.14a, a clear difference in FRR between the two Nafion 117 CCMs and the thinner Nafion 212 exists. The Nafion 117-based CCMs are characterized by quite similar values of FRR_A in the investigated current density range except for the values at 0.2 A/cm^2 where a more relevant difference is observed. The thinner CCM presents instead much lower FRR_A values with respect to the thicker membranes. Concerning for example the 60°C case, the Nafion 212- and 117-based cells have an area specific FRR peak of approximately 0.3 and 1.3-1.4 µg/h/cm^2, respectively. The FRR_A values computed by Fouda-Onana *et al.* [111] and Chandesris *et al.* [290] are of the same order of magnitude as those presented in this study.

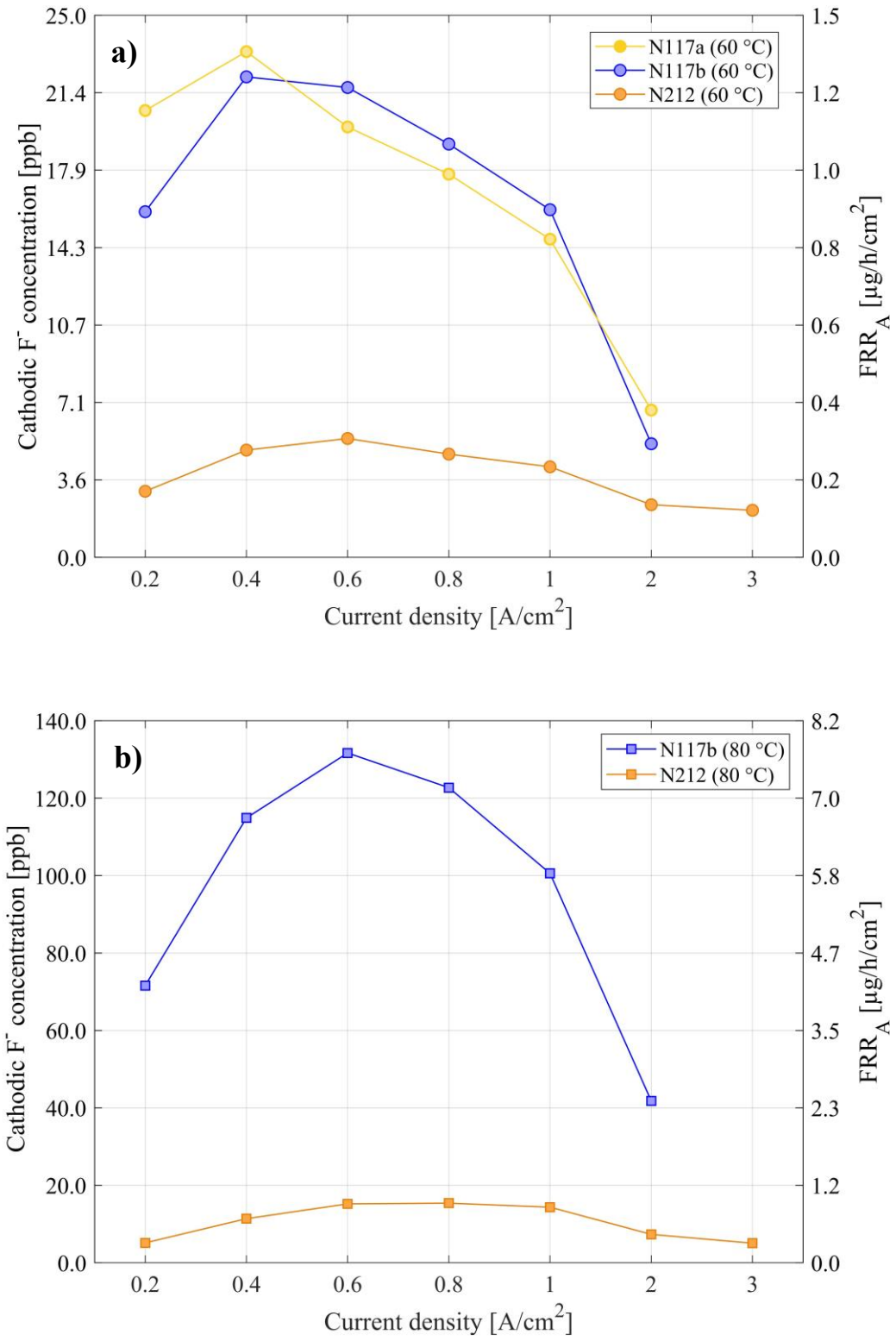

Figure S.14 Cathode outlet concentration and area specific FRR at different current densities at 60 °C (a) and 80 °C (b)

It should be pointed out that the thin membrane has an equivalent weight (EW) of around 2100 g/mol, which is higher than that of Nafion 117 CCMs (about 1100 g/mol). Lower EW increases the water uptake of the membrane and improves the proton conductivity. However, it may also result in reduced mechanical integrity because of swelling-related issues [333]. Higher EW is therefore beneficial for thinner membranes, which are more susceptible to mechanical failure. The EW parameter may also affect the rate of fluoride emission. Rodgers *et al.* [334] observed that the EW of PFSA membranes had a relevant effect on their properties with consequent impact on fuel cell performance and durability, showing that the FRR was approximately 50% lower for a 1100 EW-based cell compared to the 950 EW. The increased chemical stability with higher EW was ascribed to the lower concentration of sulfonic acid side chains. The side chain attack by radicals is in fact considered as a possible initiation of membrane degradation, resulting in -COOH formation and subsequent unzipping mechanism [311]. In particular, the C-S bond located at the side chain end (see Figure S.3) was shown to be one of the main targets and the weakest site against hydroxyl radical attack [303], [309].

On the other hand, the measured FRR in PEMWEs cannot exclusively be attributed to side chain degradation. Hence, the FRR cannot be expected to be proportional to the EW.

S.3.3 Stack: results and discussion

The aim of the stack measurements is to show that the online IC monitoring methodology is also applicable and feasible for larger commercially available PEM electrolyzers. IC measurement tests were carried out on an PEMWE short stack composed of 10 cells.

The stack performance was analysed by performing polarization curves at different operating conditions. Figure S.15 shows the polarization curves at ambient pressure and at three different temperatures (35, 50 and 60 °C, respectively). The water flow rate at the anode inlet was set to 3 LPM.

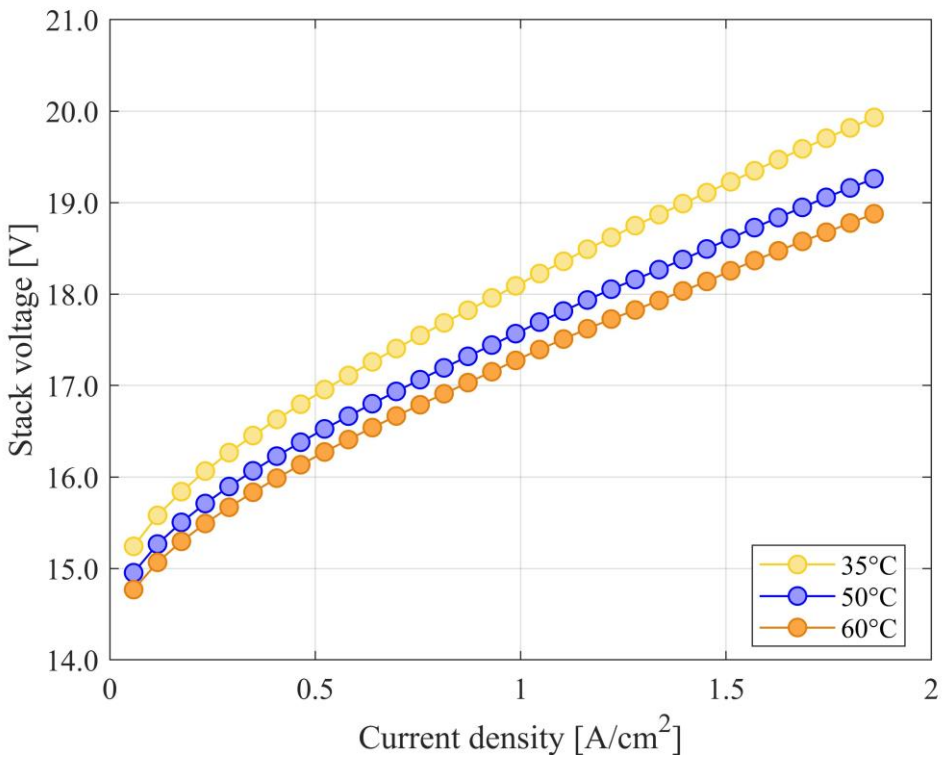

Figure S.15 Polarization curve at ambient pressure, 3 LPM water flow rate at the anode inlet and at 35, 50 and 60 °C.

The ion chromatography system (850 Professional IC – Anion – MCS - Prep 2) was connected to the cathode outlet. For all the IC measurements, a small water flow rate of 0.2 LPM was set to recirculate through the cathode circuit. As shown in Figure S.16, the effect of current on the release of fluoride ions was investigated by performing current sensitivity tests in the range 0.2 to 1.9 A/cm^2, keeping constant each operating condition for 3 hours. 60 °C was set as working temperature for the test. It can be noticed a peak in fluoride concentration of 9.5 ppb at around 0.2 A/cm^2. Similarly to the single-cell tests, a cathode conductivity peak is also observed.

In order to have a quantitative estimation of the FRR, additional IC measurements were performed at the cathode inlet. However, no fluoride concentration was detected in the recirculated water flow, even at low current densities. Additionally, an experiment with no cathodic water recirculation (dead-end operation) at 0.2 A/cm^2 was carried out, resulting in a fluoride concentration of around 23 ppb. This value is higher than that of Figure S.16, which is approximately 9.5 ppb, since the water stream is less diluted (no water is recirculated through the cathode). This last test was necessary to quantify the FRR considering the effect of water crossing the membrane. Indeed, assuming the same FRR for the tests with and without water recirculation and applying Eq. (S.9) and

Eq. (S.10) to both cases, the following formula was derived to express the area specific FRR per cell:

$$FRR_A = \dot{V}_{H_2O,cat,in,1} \frac{ppb_{F,cat,out,2}\left(ppb_{F,cat,out,1} - ppb_{F,cat,in,1}\right)}{\left(ppb_{F,cat,out,2} - ppb_{F,cat,out,1}\right)} \frac{60}{A_{cell}\, n_{cell}} \quad \text{(S.14)}$$

where the subscripts 1 and 2 refer to the test with and without water recirculation, respectively, and n_{cell} is the number of cells composing the stack. Considering the 0.2 A/cm^2 case ($ppb_{F,cat,in,1}$ = 0, $ppb_{F,cat,out,1}$ = 9.5 ppb and $ppb_{F,cat,out,2}$ = 23 ppb), by applying Eq. (S.14), it was found that the area specific FRR is around 0.22 µg/h/cm^2/cell. This value is lower compared to what computed for the N117 single cells at the same temperature of 60°C (whose FRR in that current density region was around 0.8 to 1.2 µg/h/cm^2), but still in the same order of magnitude.

As shown in Eq. (S.14), an average FRR per cell was defined dividing the total amount of released fluoride by the number of cells in the stack. However, it cannot be discarded that some cells may deviate from the average FRR value. Analyzing the long term behavior of PEM stacks, Stucki *et al.* [292] found the membrane degradation process (in terms of membrane thinning) to depend on the position of the cell in the stack. Inhomogeneities in current distributions could for example lead to an uneven temperature distribution inside the electrolyzer. Temperature, as shown in the present study from single-cells results, has a strong influence on the membrane loss of fluoride. Moreover, it should be noted that the stack under analysis was operated for at least 500 hours before performing the FRR tests, unlike the single cells where the measurements were taken directly after the break-in. This could further contribute in the discrepancy between the obtained stack and single-cells results. As an example, in the framework of the NOVEL project [312], a long term durability test was carried out showing a progressive reduction in the detected fluoride release with increasing operating time. Finally, a difference in concentration of metallic ions in the water flow of the single-cell and stack system could have a relevant impact on the fluoride release. Chandesris *et al.* [290] for example showed that the degradation rate of the membrane is almost directly proportional to the Fe^{2+} source term.

Nevertheless, analogously to the single-cell tests, when performing the current sensitivity experiment, fluoride concentration and cathodic conductivity profiles were found to have a similar trend. An acceptable linear correlation between these two quantities was observed, with an R-squared value of around 0.77. The water conductivity at the anode side was also shown to have low variation when changing operating condition and to be lower than that at the cathode in the whole tested operating range. The usage of the online IC monitoring technique was demonstrated to be able to capture the dynamic of change in fluoride release for both single cells and stacks.

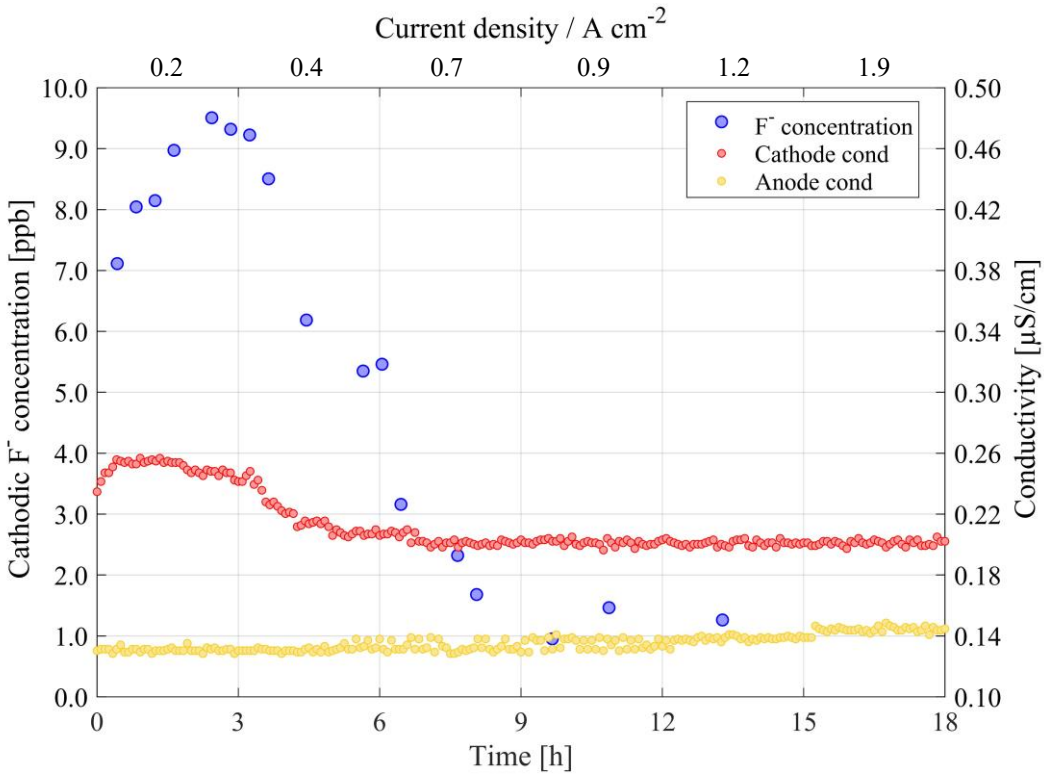

Figure S.16 Current sensitivity at 60 °C, ambient pressure and water recirculation at the cathode side (0.2 LPM): effect of current density on the fluoride concentration at the cathode outlet and on the cathode water conductivity

Conclusions

A literature review about PEM electrolysis has been performed to highlight the main aspects on which research should focus to improve the competitiveness of this technology.

Cost issues can be addressed by considering different types of solutions ranging from materials to operating conditions. The amount of precious catalysts could be decreased by applying catalyst supports or by adopting specific solid oxide solutions. The use of titanium, which is currently the main choice due to its high resistance to corrosion, could be reduced by employing stainless steel with protective coatings. New techniques to allow the operation at higher current densities (while limiting the overvoltage losses) should be also developed so as to increase the rate of hydrogen production per unit cell area of the electrolyzer, and hence lower the PEMWE investment cost.

The electrolyzer stability is another important issue to be faced and that requires further improvements. The increase in electrical resistance and the membrane chemical degradation are the two main degradation processes that affect PEM electrolyzers. The resistance increase is mainly caused by titanium passivation, which could be mitigated by adopting appropriate surface

modifications, e.g., Pt, Au and nitride coatings. The ultimate life of PEMWEs is generally considered to be primarily related to the chemical stability of the membrane. Membrane degradation is in fact a major problem for PEMWEs since it leads to progressive membrane thinning, with consequent increase in gas crossover, resulting in serious safety issues. The chemical attack mechanisms consist in oxygen cross-over from anode to cathode, H_2O_2 formation at the cathode side, H_2O_2 reaction with cation impurities to generate free radicals and finally membrane attack by radicals. High temperatures and quite low current densities are reported to foster the degradation of the PFSA-based membrane. When investigating degradation in PEM electrolysis, it still remains the need to define proper harmonized ageing tests and stressors to trigger the degradation of specific components.

It was then presented an experimental study with the purpose of addressing two relevant issues in the field of PEM electrolysis: membrane chemical degradation and high current density operation. Being the membrane one of the weakest components for long term performance, it is necessary to define techniques that are able to effectively monitor its degradation over time. From previous works, it was found that the measurement of F^- ions in the exhaust water of PEMWEs represents a reliable indicator for the membrane stability. However, studies that deal with fluoride measurements in PEM electrolysis are few. They usually employ the ISE technique to measure the fluoride amount in water samples periodically collected from the electrolyzer circuit. In the present study, the fluoride ions measurements were instead performed by means of ion chromatography through an automatized process. FRR was also investigated when operating with CCMs characterized by reduced thickness. Thinner membranes represent a promising way to enable the operation at higher current and therefore their behaviour towards membrane degradation deserves to be investigated.

The online IC measurement methodology developed in this study was shown to be an effective and accurate way to continuously monitor fluoride ion release, allowing us to observe transients in fluoride production when changing the electrolyzer operating conditions both at single-cell and stack level. Current density and temperature were found to have a considerable effect on FRR regardless of the membrane thickness. It was confirmed that low current densities (i.e., 0.4 to 0.6 A/cm^2) and increased operating temperature lead to an enhancement in the release of fluoride ions, thus inducing an acceleration of the membrane chemical attack. These operating conditions can therefore represent ideal stressors for testing protocols to trigger the degradation of the membrane component. The thinner Nafion 212 CCM was observed to have lower area specific FRR values compared to the thicker Nafion 117-based membranes. This lower release of fluoride ions may be ascribed to the higher equivalent weight (solution which is generally preferred for thinner CCMs to improve their mechanical integrity). Thin CCMs seem therefore to have sufficient membrane chemical stability, with reduced F^- ion emission, to be considered as a potentially

viable way to reduce today's PEMWE capital expenditures as long as high hydrogen crossover and safety issues can be avoided.

Finally, a linear correlation between fluoride concentration at the electrolyzer outlet and water conductivity at the cathode was found. At single-cell level, R^2 was approximately 0.95 and 0.99 for 60 °C and 80 °C tests, respectively. These two quantities were acceptably correlated at the stack level as well, with an R-squared value of 0.77. This is in accordance with a membrane degradation mechanism that involves radical attack and subsequent release of HF molecules, as described by the unzipping reaction. Conductivity was also shown to be much lower in the anode water circuit, in line with CCM chemical attack occurring mainly at the cathode side. Because of this strict correlation between conductivity and fluoride concentration, the measurement of conductivity, which can be performed through low-cost sensors (generally found in all PEM electrolysis test systems), could represent a practical and low-cost indicator for the monitoring of the membrane chemical stability over time.

References

[1] IPCC - The Intergovernmental Panel on Climate Change, "Climate Change 2014. Synthesis report.," 2014. [Online]. Available: https://www.ipcc.ch/report/ar5/syr/.

[2] V. Masson-Delmotte *et al.*, "Summary for Policymakers. Global Warming of 1.5 °C," 2018. [Online]. Available: https://www.ipcc.ch/sr15/chapter/spm/.

[3] M. Almuni, T. Dauwe, I. Moorkens, R. J. Saarikivi, and M. Tomescu, "Renewable energy in Europe - 2020. Recent growth and knock-on effects," 2020. [Online]. Available: https://www.eionet.europa.eu/etcs/etc-cme/products/etc-cme-reports/renewable-energy-in-europe-2019-recent-growth-and-knock-on-effects.

[4] IRENA, "Renewable power generation costs in 2019," 2020. [Online]. Available: https://www.irena.org/publications/2020/Jun/Renewable-Power-Costs-in-2019.

[5] Wind Europe, "Wind energy in Europe: Scenarios for 2030," 2017. [Online]. Available: https://windeurope.org/about-wind/reports/wind-energy-in-europe-scenarios-for-2030/.

[6] IRENA and EC, "Renewable energy prospects for the European Union," 2018. [Online]. Available: https://www.irena.org/publications/2018/Feb/Renewable-energy-prospects-for-the-EU.

[7] International Electrochemical Commission, "Electrical Energy Storage - white paper," 2019. [Online]. Available: https://www.iec.ch/basecamp/electrical-energy-storage.

[8] X. Luo, J. Wang, M. Dooner, and J. Clarke, "Overview of current development in electrical energy storage technologies and the application potential in power system operation," *Appl. Energy*, vol. 137, pp. 511–536, 2015, doi: 10.1016/j.apenergy.2014.09.081.

[9] T. M. Gür, "Review of electrical energy storage technologies, materials and systems: challenges and prospects for large-scale grid storage," *Energy Environ. Sci.*, vol. 11, no. 10, pp. 2696–2767, 2018, doi: 10.1039/C8EE01419A.

[10] A. G. Olabi, C. Onumaegbu, T. Wilberforce, M. Ramadan, M. A. Abdelkareem, and A. H. Al – Alami, "Critical review of energy storage systems," *Energy*, vol. 214, p. 118987, 2021, doi: 10.1016/j.energy.2020.118987.

[11] M. Lehner, R. Tichler, S. Horst, and M. Koppe, *Power-to-Gas : Technology and Business Models*. Springer, 2014.

[12] G. Buffo, P. Marocco, D. Ferrero, A. Lanzini, and M. Santarelli, "Power-to-X and power-to-power routes," *Sol. Hydrog. Prod.*, pp. 529–557, 2019, doi: 10.1016/B978-0-12-814853-2.00015-1.

[13] A. Buttler and H. Spliethoff, "Current status of water electrolysis for energy storage, grid balancing and sector coupling via power-to-gas and power-to-liquids: A review," *Renew. Sustain. Energy Rev.*, vol. 82, pp. 2440–2454, 2018, doi: https://doi.org/10.1016/j.rser.2017.09.003.

[14] O. Schmidt, A. Gambhir, I. Staffell, A. Hawkes, J. Nelson, and S. Few, "Future cost and performance of water electrolysis: An expert elicitation study," *Int. J. Hydrogen Energy*, vol. 42, no. 52, pp. 30470–30492, 2017, doi: 10.1016/j.ijhydene.2017.10.045.

[15] J. Proost, "State-of-the art CAPEX data for water electrolysers, and their impact on renewable hydrogen price settings," *Int. J. Hydrogen Energy*, vol. 44, no. 9, pp. 4406–4413, 2019, doi: 10.1016/j.ijhydene.2018.07.164.

[16] M. Götz *et al.*, "Renewable Power-to-Gas: A technological and economic review," *Renew. Energy*, vol. 85, pp. 1371–1390, 2016, doi: 10.1016/j.renene.2015.07.066.

[17] Tractebel and Hinicio, "Study on early business cases for H2 in energy storage and more broadly power to H2 applications," 2017. [Online]. Available: https://www.fch.europa.eu/sites/default/files/P2H_Full_Study_FCHJU.pdf.

[18] D. Parra and M. K. Patel, "Techno-economic implications of the electrolyser technology and size for power-to-gas systems," *Int. J. Hydrogen Energy*, vol. 41, no. 6, pp. 3748–3761, 2016, doi: 10.1016/j.ijhydene.2015.12.160.

[19] P. Marocco, D. Ferrero, A. Lanzini, and M. Santarelli, "Optimal design of stand-alone solutions based on RES + hydrogen storage feeding off-grid communities," *Energy Convers. Manag.*, vol. 238, p. 114147, Jun. 2021, doi: 10.1016/j.enconman.2021.114147.

[20] A. Hauch *et al.*, "A Decade of Solid Oxide Electrolysis Improvements at DTU Energy," *ECS Trans.*, vol. 75, no. 42, pp. 3–14, 2017, doi: 10.1149/07542.0003ecst.

[21] K. Schwarze, O. Posdziech, S. Kroop, N. Lapeña-Rey, and J. Mermelstein, "Green Industrial Hydrogen via Reversible High-Temperature Electrolysis," *ECS Trans.*, vol. 78, no. 1, pp. 2943–2952, 2017, doi: 10.1149/07801.2943ecst.

[22] Y. Zheng *et al.*, "A review of high temperature co-electrolysis of H2O and CO2 to produce sustainable fuels using solid oxide electrolysis cells (SOECs): advanced materials and technology," *Chem. Soc. Rev.*, vol. 46, no. 5, pp. 1427–1463, 2017, doi: 10.1039/C6CS00403B.

[23] N. Kochetova, I. Animitsa, D. Medvedev, A. Demin, and P. Tsiakaras, "Recent activity in the development of proton-conducting oxides for high-temperature applications," *RSC Adv.*, vol. 6, no. 77, pp. 73222–73268, 2016, doi: 10.1039/C6RA13347A.

[24] S. Hossain, A. M. Abdalla, S. N. B. Jamain, J. H. Zaini, and A. K. Azad, "A review on proton conducting electrolytes for clean energy and intermediate temperature-solid oxide fuel cells," *Renew. Sustain. Energy Rev.*, vol. 79, no. May, pp. 750–764, 2017, doi: 10.1016/j.rser.2017.05.147.

[25] I. Vincent and D. Bessarabov, "Low cost hydrogen production by anion

exchange membrane electrolysis: A review," *Renew. Sustain. Energy Rev.*, vol. 81, no. February, pp. 1690–1704, 2018, doi: 10.1016/j.rser.2017.05.258.

[26] E. Giglio, A. Lanzini, M. Santarelli, and P. Leone, "Synthetic natural gas via integrated high-temperature electrolysis and methanation: Part I—Energy performance," *J. Energy Storage*, vol. 1, pp. 22–37, Jun. 2015, doi: http://dx.doi.org/10.1016/j.est.2015.04.002.

[27] M. Bailera, P. Lisbona, L. M. Romeo, and S. Espatolero, "Power to Gas projects review: Lab, pilot and demo plants for storing renewable energy and CO2," *Renew. Sustain. Energy Rev.*, vol. 69, pp. 292–312, 2017, doi: 10.1016/j.rser.2016.11.130.

[28] IRENA, "Off-grid renewable energy systems: status and methodological issues," 2015. [Online]. Available: https://www.irena.org/-/media/Files/IRENA/Agency/Publication/2015/IRENA_Off-grid_Renewable_Systems_WP_2015.pdf.

[29] D. Groppi, D. Astiaso Garcia, G. Lo Basso, F. Cumo, and L. De Santoli, "Analysing economic and environmental sustainability related to the use of battery and hydrogen energy storages for increasing the energy independence of small islands," *Energy Convers. Manag.*, vol. 177, no. September, pp. 64–76, 2018, doi: 10.1016/j.enconman.2018.09.063.

[30] P. Blechinger, C. Cader, P. Bertheau, H. Huyskens, R. Seguin, and C. Breyer, "Global analysis of the techno-economic potential of renewable energy hybrid systems on small islands," *Energy Policy*, pp. 1–14, 2016, doi: 10.1016/j.enpol.2016.03.043.

[31] Federal Ministry for Economic Affairs and Energy, "Markets for Battery Storage. Sub-sector analysis on the market potential for battery storage in Tanzania," 2015. [Online]. Available: https://reiner-lemoine-institut.de/wp-content/publications/Battery_TZA/2015-en-battery-storage-tanzania.pdf.

[32] P. Marocco *et al.*, "A study of the techno-economic feasibility of H2-based energy storage systems in remote areas," *Energy Convers. Manag.*, vol. 211, p. 112768, 2020, doi: 10.1016/j.enconman.2020.112768.

[33] IEA, "World Energy Outlook 2019." https://www.iea.org/reports/world-energy-outlook-2019 (accessed Jun. 30, 2020).

[34] "ELY4OFF project official website," 2016. http://ely4off.eu/ (accessed May 30, 2021).

[35] "HAEOLUS project official website," 2018. http://www.haeolus.eu/ (accessed May 30, 2021).

[36] "REMOTE project official website," 2018. https://www.remote-euproject.eu/ (accessed May 30, 2021).

[37] "GREEN HYSLAND project," 2021. https://cordis.europa.eu/project/id/101007201 (accessed May 09, 2021).

[38] W. Zhang, A. Maleki, M. A. Rosen, and J. Liu, "Optimization with a simulated annealing algorithm of a hybrid system for renewable energy including battery and hydrogen storage," *Energy*, vol. 163, pp. 191–207, 2018, doi: 10.1016/j.energy.2018.08.112.

[39] N. D. Nordin and H. A. Rahman, "Sizing and economic analysis of stand alone photovoltaic system with hydrogen storage," *IOP Conf. Ser. Earth Environ. Sci.*, vol. 93, no. 1, 2017, doi: 10.1088/1755-1315/93/1/012068.

[40] R. Hosseinalizadeh, H. Shakouri G, M. S. Amalnick, and P. Taghipour,

"Economic sizing of a hybrid (PV-WT-FC) renewable energy system (HRES) for stand-alone usages by an optimization-simulation model: Case study of Iran," *Renew. Sustain. Energy Rev.*, vol. 54, pp. 139–150, 2016, doi: 10.1016/j.rser.2015.09.046.

[41] P. Puranen, A. Kosonen, and J. Ahola, "Technical feasibility evaluation of a solar PV based off-grid domestic energy system with battery and hydrogen energy storage in northern climates," *Sol. Energy*, vol. 213, pp. 246–259, 2021, doi: 10.1016/j.solener.2020.10.089.

[42] W. Dong, Y. Li, and J. Xiang, "Optimal sizing of a stand-alone hybrid power system based on battery/hydrogen with an improved ant colony optimization," *Energies*, vol. 9, no. 10, 2016, doi: 10.3390/en9100785.

[43] F. Dawood, G. M. Shafiullah, and M. Anda, "Stand-alone microgrid with 100% renewable energy: A case study with hybrid solar pv-battery-hydrogen," *Sustain.*, vol. 12, no. 5, 2020, doi: 10.3390/su12052047.

[44] C. H. Li, X. J. Zhu, G. Y. Cao, S. Sui, and M. R. Hu, "Dynamic modeling and sizing optimization of stand-alone photovoltaic power systems using hybrid energy storage technology," *Renew. Energy*, vol. 34, no. 3, pp. 815–826, 2009, doi: 10.1016/j.renene.2008.04.018.

[45] B. S. Richards and G. J. Conibeer, "A comparison of hydrogen storage technologies for solar-powered stand-alone power supplies: A photovoltaic system sizing approach," *Int. J. Hydrogen Energy*, vol. 32, no. 14, pp. 2712–2718, 2007, doi: 10.1016/j.ijhydene.2006.09.013.

[46] N. D. Nordin and H. A. Rahman, "Comparison of optimum design, sizing, and economic analysis of standalone photovoltaic/battery without and with hydrogen production systems," *Renew. Energy*, vol. 141, pp. 107–123, 2019, doi: 10.1016/j.renene.2019.03.090.

[47] L. Gracia, P. Casero, C. Bourasseau, and A. Chabert, "Use of Hydrogen in Off-Grid Locations, a Techno-Economic Assessment," *Energies*, vol. 11, no. 11, p. 3141, 2018, doi: 10.3390/en11113141.

[48] A. Perrigot, M. Perier-Muzet, P. Ortega, and D. Stitou, "Technical economic analysis of PV-driven electricity and cold cogeneration systems using particle swarm optimization algorithm," *Energy*, vol. 211, p. 119009, 2020, doi: 10.1016/j.energy.2020.119009.

[49] M. Jamshidi and A. Askarzadeh, "Techno-economic analysis and size optimization of an off-grid hybrid photovoltaic, fuel cell and diesel generator system," *Sustain. Cities Soc.*, vol. 44, pp. 310–320, 2019, doi: 10.1016/j.scs.2018.10.021.

[50] W. Cai *et al.*, "Optimal sizing and location based on economic parameters for an off-grid application of a hybrid system with photovoltaic, battery and diesel technology," *Energy*, vol. 201, p. 117480, 2020, doi: 10.1016/j.energy.2020.117480.

[51] H. Lund, P. Sorknæs, B. V. Mathiesen, and K. Hansen, "Beyond sensitivity analysis: A methodology to handle fuel and electricity prices when designing energy scenarios," *Energy Res. Soc. Sci.*, vol. 39, pp. 108–116, 2018, doi: 10.1016/j.erss.2017.11.013.

[52] O. D. T. Odou, R. Bhandari, and R. Adamou, "Hybrid off-grid renewable power system for sustainable rural electrification in Benin," *Renew. Energy*, vol. 145, pp. 1266–1279, 2020, doi: 10.1016/j.renene.2019.06.032.

[53] E. Ozden and I. Tari, "PEM fuel cell degradation effects on the

performance of a stand-alone solar energy system," *Int. J. Hydrogen Energy*, vol. 42, no. 18, pp. 13217–13225, 2017, doi: 10.1016/j.ijhydene.2017.04.017.

[54] W. Margaret Amutha and V. Rajini, "Techno-economic evaluation of various hybrid power systems for rural telecom," *Renew. Sustain. Energy Rev.*, vol. 43, pp. 553–561, 2015, doi: 10.1016/j.rser.2014.10.103.

[55] A. Kafetzis, C. Ziogou, K. D. Panopoulos, S. Papadopoulou, P. Seferlis, and S. Voutetakis, "Energy management strategies based on hybrid automata for islanded microgrids with renewable sources, batteries and hydrogen," *Renew. Sustain. Energy Rev.*, vol. 134, no. April, p. 110118, 2020, doi: 10.1016/j.rser.2020.110118.

[56] F. J. Vivas, A. De las Heras, F. Segura, and J. M. Andújar, "A review of energy management strategies for renewable hybrid energy systems with hydrogen backup," *Renew. Sustain. Energy Rev.*, vol. 82, no. Part 1, pp. 126–155, 2018, doi: https://doi.org/10.1016/j.rser.2017.09.014.

[57] T. Khatib, I. A. Ibrahim, and A. Mohamed, "A review on sizing methodologies of photovoltaic array and storage battery in a standalone photovoltaic system," *Energy Convers. Manag.*, vol. 120, pp. 430–448, 2016, doi: 10.1016/j.enconman.2016.05.011.

[58] P. Marocco, D. Ferrero, M. Gandiglio, and M. Santarelli, "Deliverable number 2.2 Technical specification of the technological demonstrators," 2018. [Online]. Available: https://www.remote-euproject.eu/remote18/rem18-cont/uploads/2019/03/REMOTE-D2.2.pdf.

[59] P. Vermeiren, R. Leysen, H. Beckers, J. P. Moreels, and A. Claes, "The influence of manufacturing parameters on the properties of macroporous Zirfon® separators," *J. Porous Mater.*, vol. 15, no. 3, pp. 259–264, 2008, doi: 10.1007/s10934-006-9084-0.

[60] A. Ursúa and P. Sanchis, "Static-dynamic modelling of the electrical behaviour of a commercial advanced alkaline water electrolyser," *Int. J. Hydrogen Energy*, vol. 37, no. 24, pp. 18598–18614, 2012, doi: 10.1016/j.ijhydene.2012.09.125.

[61] J. Balej, "Water vapour partial pressures and water activities in potassium and sodium hydroxide solutions over wide concentration and temperature ranges," *Int. J. Hydrogen Energy*, vol. 10, no. 4, pp. 233–243, 1985, doi: 10.1016/0360-3199(85)90093-X.

[62] M. Hammoudi, C. Henao, K. Agbossou, Y. Dubé, and M. L. Doumbia, "New multi-physics approach for modelling and design of alkaline electrolyzers," *Int. J. Hydrogen Energy*, vol. 37, no. 19, pp. 13895–13913, 2012, doi: 10.1016/j.ijhydene.2012.07.015.

[63] H. Vogt and R. J. Balzer, "The bubble coverage of gas-evolving electrodes in stagnant electrolytes," *Electrochim. Acta*, vol. 50, no. 10, pp. 2073–2079, 2005, doi: 10.1016/j.electacta.2004.09.025.

[64] Z. Abdin, C. J. Webb, and E. M. A. Gray, "Modelling and simulation of an alkaline electrolyser cell," *Energy*, vol. 138, pp. 316–331, 2017, doi: 10.1016/j.energy.2017.07.053.

[65] M. Carmo, D. L. Fritz, J. Mergel, and D. Stolten, "A comprehensive review on PEM water electrolysis," *Int. J. Hydrogen Energy*, vol. 38, no. 12, pp. 4901–4934, 2013, doi: 10.1016/j.ijhydene.2013.01.151.

[66] C. Henao, K. Agbossou, M. Hammoudi, Y. Dubé, and A. Cardenas,

"Simulation tool based on a physics model and an electrical analogy for an alkaline electrolyser," *J. Power Sources*, vol. 250, pp. 58–67, 2014, doi: 10.1016/j.jpowsour.2013.10.086.

[67] A. Bhanu and Y. V Ramana, "Mathematical Modelling and Simulation Analysis of Alkaline Water Electrolyser for Stationary Electrolyte in Atmospheric Pressure," vol. 3, no. 5, pp. 171–177, 2015.

[68] R. J. Gilliam, J. W. Graydon, D. W. Kirk, and S. J. Thorpe, "A review of specific conductivities of potassium hydroxide solutions for various concentrations and temperatures," *Int. J. Hydrogen Energy*, vol. 32, no. 3, pp. 359–364, 2007, doi: 10.1016/j.ijhydene.2006.10.062.

[69] J. Milewski, G. Guandalini, and S. Campanari, "Modeling an alkaline electrolysis cell through reduced-order and loss-estimate approaches," *J. Power Sources*, vol. 269, pp. 203–211, 2014, doi: 10.1016/j.jpowsour.2014.06.138.

[70] H. Vogt, "The incremental ohmic resistance caused by bubbles adhering to an electrode," *J. Appl. Electrochem.*, vol. 13, no. 1, pp. 87–88, 1983, doi: 10.1007/BF00615891.

[71] J. Stojadinovic *et al.*, "Electrochemical Characterization of Porous Diaphragms in Development for Gas Separation," *ECS Electrochem. Lett.*, vol. 1, no. 4, pp. F25–F28, 2012, doi: 10.1149/2.002204eel.

[72] Ø. Ulleberg, "Modeling of advanced alkaline electrolyzers:a system simulation approach," *Int. J. Hydrogen Energy*, vol. 28, pp. 21–33, 2003, doi: 10.1016/S0360-3199(02)00033-2.

[73] W. Hug, H. Bussmann, and A. Brinner, "Intermittent operation and operation modeling of an alkaline electrolyzer," *Int. J. Hydrogen Energy*, vol. 18, no. 12, pp. 973–977, 1993, doi: 10.1016/0360-3199(93)90078-O.

[74] H. Wendt and V. Plzak, "Electrocatalytic and thermal activation of anodic oxygen and cathodic hydrogen-evolution in alkaline water electrolysis," *Electrochim. Acta*, vol. 28, no. 1, pp. 27–34, 1983.

[75] A. Godula-Jopek and D. Stolten, *Hydrogen production by electrolysis*. Wiley-VCH, 2015.

[76] A. Mayyas, M. Ruth, B. Pivovar, G. Bender, and K. Wipke, "Manufacturing Cost Analysis for Proton Exchange Membrane Water Electrolyzers," 2019. doi: 10.2172/1557965.

[77] J. Brauns and T. Turek, "Alkaline water electrolysis powered by renewable energy: A review," *Processes*, vol. 8, no. 2, 2020, doi: 10.3390/pr8020248.

[78] D. Bessarabov, H. wang, H. Li, and N. Zhao, *PEM Electrolysis for Hydrogen Production: Principles and Applications*. 2015.

[79] V. Liso, G. Savoia, S. S. Araya, G. Cinti, and S. K. Kær, "Modelling and Experimental Analysis of a Polymer Electrolyte Membrane Water Electrolysis Cell at Different Operating Temperatures," *Energies*, vol. 11, no. 12, 2018, doi: 10.3390/en11123273.

[80] J. Kai, R. Saito, K. Terabaru, H. Li, H. Nakajima, and K. Ito, "Effect of Temperature on the Performance of Polymer Electrolyte Membrane Water Electrolysis: Numerical Analysis of Electrolysis Voltage Considering Gas/Liquid Two-Phase Flow," *J. Electrochem. Soc.*, vol. 166, no. 4, pp. F246–F254, 2019, doi: 10.1149/2.0521904jes.

[81] P. Marocco, D. Ferrero, A. Lanzini, and M. Santarelli, "Benefits from heat pipe integration in H 2 /H 2 O fed SOFC systems," *Appl. Energy*, vol. 241,

no. January, pp. 472–482, 2019, doi: 10.1016/j.apenergy.2019.03.037.

[82] T. Yigit and O. F. Selamet, "Mathematical modeling and dynamic Simulink simulation of high-pressure PEM electrolyzer system," *Int. J. Hydrogen Energy*, vol. 41, no. 32, pp. 13901–13914, 2016, doi: 10.1016/j.ijhydene.2016.06.022.

[83] F. Marangio, M. Santarelli, and M. Calì, "Theoretical model and experimental analysis of a high pressure PEM water electrolyser for hydrogen production," *Int. J. Hydrogen Energy*, vol. 34, no. 3, pp. 1143–1158, 2009, doi: 10.1016/j.ijhydene.2008.11.083.

[84] Z. Abdin, C. J. Webb, and E. M. A. Gray, "PEM fuel cell model and simulation in Matlab–Simulink based on physical parameters," *Energy*, vol. 116, pp. 1131–1144, 2016, doi: 10.1016/j.energy.2016.10.033.

[85] M. Espinosa-López *et al.*, "Modelling and experimental validation of a 46 kW PEM high pressure water electrolyzer," *Renew. Energy*, vol. 119, pp. 160–173, 2018, doi: 10.1016/j.renene.2017.11.081.

[86] R. O'Hayre, S.-W. Cha, W. G. Colella, and F. B. Prinz, *Fuel cell fundamentals*, Third Edit. Wiley, 2016.

[87] R. García-Valverde, N. Espinosa, and A. Urbina, "Simple PEM water electrolyser model and experimental validation," *Int. J. Hydrogen Energy*, vol. 37, no. 2, pp. 1927–1938, 2012, doi: 10.1016/j.ijhydene.2011.09.027.

[88] T. E. Springer, T. a. Zawodzinski, and S. Gottesfeld, "Polymer electrolyte fuel cell model," *J. Electrochem. Soc.*, vol. 138, no. 8, pp. 2334–2342, 1991, doi: 10.1149/1.2085971.

[89] M. W. Bernardi, Dawn M., Verbrugge, "Mathematical model of a gas diffusion electrode bonded to a polymer electrolyte," *AIChE J.*, vol. 37, no. 8, pp. 1151–1163, 1990, doi: 10.1002/aic.690370805.

[90] G. Tsotridis and A. Pilenga, "EU harmonized terminology for low-temperature water electrolysis for energy-storage applications," 2018. doi: 10.2760/138987.

[91] M. Schalenbach, M. Carmo, D. L. Fritz, J. Mergel, and D. Stolten, "Pressurized PEM water electrolysis: Efficiency and gas crossover," *Int. J. Hydrogen Energy*, vol. 38, no. 35, pp. 14921–14933, 2013, doi: 10.1016/j.ijhydene.2013.09.013.

[92] P. Trinke, P. Haug, J. Brauns, B. Bensmann, R. Hanke-Rauschenbach, and T. Turek, "Hydrogen Crossover in PEM and Alkaline Water Electrolysis: Mechanisms, Direct Comparison and Mitigation Strategies," *J. Electrochem. Soc.*, vol. 165, no. 7, pp. F502–F513, 2018, doi: 10.1149/2.0541807jes.

[93] M. Schalenbach, T. Hoefner, P. Paciok, M. Carmo, W. Lueke, and D. Stolten, "Gas Permeation through Nafion. Part 1: Measurements," *J. Phys. Chem. C*, vol. 119, no. 45, pp. 25145–25155, Nov. 2015, doi: 10.1021/acs.jpcc.5b04155.

[94] S. A. Grigoriev, V. I. Porembskiy, S. V. Korobtsev, V. N. Fateev, F. Auprêtre, and P. Millet, "High-pressure PEM water electrolysis and corresponding safety issues," *Int. J. Hydrogen Energy*, vol. 36, no. 3, pp. 2721–2728, 2011, doi: 10.1016/j.ijhydene.2010.03.058.

[95] H. Ito, T. Maeda, A. Nakano, and H. Takenaka, "Properties of Nafion membranes under PEM water electrolysis conditions," *Int. J. Hydrogen Energy*, vol. 36, no. 17, pp. 10527–10540, 2011, doi:

10.1016/j.ijhydene.2011.05.127.

[96] R. F. Mann, J. C. Amphlett, B. A. Peppley, and C. P. Thurgood, "Henry's Law and the solubilities of reactant gases in the modelling of PEM fuel cells," *J. Power Sources*, vol. 161, no. 2, pp. 768–774, 2006, doi: 10.1016/j.jpowsour.2006.05.054.

[97] D. L. Wise and G. Houghton, "The diffusion coefficients of ten slightly soluble gases in water at 10-60°C," *Chem. Eng. Sci.*, vol. 21, no. 11, pp. 999–1010, 1966, doi: 10.1016/0009-2509(66)85096-0.

[98] P. Medina and M. Santarelli, "Analysis of water transport in a high pressure PEM electrolyzer," *Int. J. Hydrogen Energy*, vol. 35, no. 11, pp. 5173–5186, 2010, doi: 10.1016/j.ijhydene.2010.02.130.

[99] E. Birgersson, M. Noponen, and M. Vynnycky, "Analysis of a Two-Phase Non-Isothermal Model for a PEFC," *J. Electrochem. Soc.*, vol. 152, no. 5, p. A1021, 2005, doi: 10.1149/1.1877992.

[100] K. Onda, T. Murakami, T. Hikosaka, M. Kobayashi, R. Notu, and K. Ito, "Performance Analysis of Polymer-Electrolyte Water Electrolysis Cell at a Small-Unit Test Cell and Performance Prediction of Large Stacked Cell," *J. Electrochem. Soc.*, vol. 149, no. 8, pp. A1069–A1078, 2002, doi: 10.1149/1.1492287.

[101] P. Marocco *et al.*, "Online measurements of fluoride ions in proton exchange membrane water electrolysis through ion chromatography," *J. Power Sources*, vol. 483, p. 229179, 2021, doi: https://doi.org/10.1016/j.jpowsour.2020.229179.

[102] B. Han, S. M. Steen, J. Mo, and F. Y. Zhang, "Electrochemical performance modeling of a proton exchange membrane electrolyzer cell for hydrogen energy," *Int. J. Hydrogen Energy*, vol. 40, no. 22, pp. 7006–7016, 2015, doi: 10.1016/j.ijhydene.2015.03.164.

[103] D. Ferrero and M. Santarelli, "Investigation of a novel concept for hydrogen production by PEM water electrolysis integrated with multi-junction solar cells," *Energy Convers. Manag.*, vol. 148, pp. 16–29, 2017, doi: 10.1016/j.enconman.2017.05.059.

[104] Z. Abdin, C. J. Webb, and E. M. Gray, "Modelling and simulation of a proton exchange membrane (PEM) electrolyser cell," *Int. J. Hydrogen Energy*, vol. 40, no. 39, pp. 13243–13257, 2015, doi: 10.1016/j.ijhydene.2015.07.129.

[105] P. Choi, D. G. Bessarabov, and R. Datta, "A simple model for solid polymer electrolyte (SPE) water electrolysis," *Solid State Ionics*, vol. 175, no. 1–4, pp. 535–539, 2004, doi: 10.1016/j.ssi.2004.01.076.

[106] A. Awasthi, K. Scott, and S. Basu, "Dynamic modeling and simulation of a proton exchange membrane electrolyzer for hydrogen production," *Int. J. Hydrogen Energy*, vol. 36, no. 22, pp. 14779–14786, 2011, doi: 10.1016/j.ijhydene.2011.03.045.

[107] A. H. A. Rahim and A. S. Tijani, "Modeling and Analysis the Effects of Temperature and Pressure on the Gas-Crossover in Polymer Electrolyte Membrane Electrolyzer," *World Acad. Sci. Eng. Technol. Int. J. Electr. Comput. Energ. Electron. Commun. Eng.*, vol. 10, no. 1, pp. 1–7, 2015.

[108] P. Colbertaldo, S. L. Gómez Aláez, and S. Campanari, "Zero-dimensional dynamic modeling of PEM electrolyzers," *Energy Procedia*, vol. 142, pp. 1468–1473, 2017, doi: 10.1016/j.egypro.2017.12.594.

[109] P. Trinke, G. P. Keeley, M. Carmo, B. Bensmann, and R. Hanke-Rauschenbach, "Elucidating the Effect of Mass Transport Resistances on Hydrogen Crossover and Cell Performance in PEM Water Electrolyzers by Varying the Cathode Ionomer Content," *J. Electrochem. Soc.*, vol. 166, no. 8, pp. F465–F471, 2019, doi: 10.1149/2.0171908jes.

[110] P. Trinke, B. Bensmann, S. Reichstein, R. Hanke-Rauschenbach, and K. Sundmacher, "Hydrogen Permeation in PEM Electrolyzer Cells Operated at Asymmetric Pressure Conditions," *J. Electrochem. Soc.*, vol. 163, no. 11, pp. F3164–F3170, 2016, doi: 10.1149/2.0221611jes.

[111] F. Fouda-Onana, M. Chandesris, V. Médeau, S. Chelghoum, D. Thoby, and N. Guillet, "Investigation on the degradation of MEAs for PEM water electrolysers part I: Effects of testing conditions on MEA performances and membrane properties," *Int. J. Hydrogen Energy*, vol. 41, no. 38, pp. 16627–16636, 2016, doi: 10.1016/j.ijhydene.2016.07.125.

[112] D. Ferrero *et al.*, "REMOTE deliverable 1.4. First annual data reporting," 2019.

[113] A. Mayyas and M. Mann, "Manufacturing competitiveness analysis for hydrogen refueling stations and electrolyzers," 2018. https://www.hydrogen.energy.gov/pdfs/review18/mn017_mann_2018_p.pdf (accessed Oct. 31, 2020).

[114] Y. Wang, D. F. Ruiz Diaz, K. S. Chen, Z. Wang, and X. C. Adroher, "Materials, technological status, and fundamentals of PEM fuel cells – A review," *Mater. Today*, vol. 32, pp. 178–203, 2020, doi: https://doi.org/10.1016/j.mattod.2019.06.005.

[115] Y. Wang, K. S. Chen, J. Mishler, S. C. Cho, and X. C. Adroher, "A review of polymer electrolyte membrane fuel cells: Technology, applications, and needs on fundamental research," *Appl. Energy*, vol. 88, no. 4, pp. 981–1007, 2011, doi: https://doi.org/10.1016/j.apenergy.2010.09.030.

[116] I. M. M. SALEH, R. ALI, and H. ZHANG, "Simplified mathematical model of proton exchange membrane fuel cell based on horizon fuel cell stack," *J. Mod. Power Syst. Clean Energy*, vol. 4, no. 4, pp. 668–679, 2016, doi: 10.1007/s40565-016-0196-5.

[117] S. K. Park and S. Y. Choe, "Dynamic modeling and analysis of a 20-cell PEM fuel cell stack considering temperature and two-phase effects," *J. Power Sources*, vol. 179, no. 2, pp. 660–672, 2008, doi: 10.1016/j.jpowsour.2008.01.029.

[118] J. C. Amphlett, R. M. Baumert, R. F. Mann, B. A. Peppley, P. R. Roberge, and T. J. Harris, "Performance modeling of the Ballard Mark IV solid polymer electrolyte fuel cell: I. mechanistic model development," *J. Electrochem. Soc.*, vol. 142, pp. 1–8, 1995.

[119] J. M. Corrêa, F. A. Farret, L. N. Canha, and M. G. Simoes, "An electrochemical-based fuel-cell model suitable for electrical engineering automation approach," *IEEE Trans. Ind. Electron.*, vol. 51, no. 5, pp. 1103–1112, 2004, doi: 10.1109/TIE.2004.834972.

[120] R. B. Bird, W. E. Stewart, and E. N. Lightfoot, *Transport phenomena*. 2002.

[121] S. T. Revankar and P. Majumdar, "Fuel cells: Principles, design, and analysis," *Fuel Cells Princ. Des. Anal.*, pp. 1–748, 2016.

[122] M. M. Tomadakis and S. V. Sotirchos, "Ordinary, transition, and Knudsen

regime diffusion in random capillary structures," *Chem. Eng. Sci.*, vol. 48, no. 19, pp. 3323–3333, 1993, doi: 10.1016/0009-2509(93)80149-K.

[123] J. H. Nam and M. Kaviany, "Effective diffusivity and water-saturation distribution in single- and two-layer PEMFC diffusion medium," *Int. J. Heat Mass Transf.*, vol. 46, no. 24, pp. 4595–4611, 2003, doi: 10.1016/S0017-9310(03)00305-3.

[124] F. N. Büchi *et al.*, "Towards re-electrification of hydrogen obtained from the power-to-gas process by highly efficient H2/O2 polymer electrolyte fuel cells," *RSC Adv.*, vol. 4, no. 99, pp. 56139–56146, 2014, doi: 10.1039/c4ra11868e.

[125] W. Caisheng, M. H. Nehrir, and S. R. Shaw, "Dynamic models and model validation for PEM fuel cells using electrical circuits," *IEEE Trans. Energy Convers.*, vol. 20, no. 2, pp. 442–451, 2005, doi: 10.1109/tec.2004.842357.

[126] L. Xing, Q. Cai, C. Xu, C. Liu, K. Scott, and Y. Yan, "Numerical study of the effect of relative humidity and stoichiometric fl ow ratio on PEM (proton exchange membrane) fuel cell performance with various channel lengths : An anode partial flooding modelling," *Energy*, vol. 106, pp. 631–645, 2016, doi: 10.1016/j.energy.2016.03.105.

[127] Jay Tawee Pukrushpan and J. T. Pukrushpan, "Modeling and control of fuel cell systems and fuel processors," *Mech. Eng.*, p. 133, 2003, doi: 10.1016/S0096-3003(03)00207-8.

[128] M. G. Santarelli, M. F. Torchio, and P. Cochis, "Parameters estimation of a PEM fuel cell polarization curve and analysis of their behavior with temperature," *J. Power Sources*, vol. 159, no. 2, pp. 824–835, 2006, doi: 10.1016/j.jpowsour.2005.11.099.

[129] A. Singh, P. Baredar, and B. Gupta, "Techno-economic feasibility analysis of hydrogen fuel cell and solar photovoltaic hybrid renewable energy system for academic research building," *Energy Convers. Manag.*, vol. 145, pp. 398–414, 2017, doi: 10.1016/j.enconman.2017.05.014.

[130] B. Li, R. Roche, and A. Miraoui, "Microgrid sizing with combined evolutionary algorithm and MILP unit commitment," *Appl. Energy*, vol. 188, pp. 547–562, 2017, doi: 10.1016/j.apenergy.2016.12.038.

[131] A. Bouakkaz, S. Haddad, J. A. M.- García, A. J. Gil-mena, and R. J.-Castañeda, "Optimal Scheduling of Household Appliances in Off-Grid Hybrid Energy System using PSO Algorithm for Energy Saving," *Int. J. Renew. Energy Res.*, vol. 9, no. 1, 2019.

[132] J. J. Hwang, L. K. Lai, W. Wu, and W. R. Chang, "Dynamic modeling of a photovoltaic hydrogen fuel cell hybrid system," *Int. J. Hydrogen Energy*, vol. 34, no. 23, pp. 9531–9542, 2009, doi: 10.1016/j.ijhydene.2009.09.100.

[133] B. Laoun, A. Khellaf, M. W. Naceur, and A. M. Kannan, "Modeling of solar photovoltaic-polymer electrolyte membrane electrolyzer direct coupling for hydrogen generation," *Int. J. Hydrogen Energy*, vol. 41, no. 24, pp. 10120–10135, 2016, doi: 10.1016/j.ijhydene.2016.05.041.

[134] K. Bakirci, "Estimation of Solar Radiation by Using ASHRAE Clear-Sky Model in Erzurum, Turkey," *Energy Sources, Part A Recover. Util. Environ. Eff.*, vol. 31, no. 3, pp. 208–216, 2009, doi: 10.1080/15567030701522534.

[135] "Photovoltaic Geographical Information System (PVGIS)." https://ec.europa.eu/jrc/en/pvgis (accessed Mar. 11, 2021).

[136] LG, "LG NeON® R solar module." https://www.lg.com/us/business/solar-panels/lg-LG365Q1C-A5 (accessed Mar. 11, 2021).
[137] G. J. May, A. Davidson, and B. Monahov, "Lead batteries for utility energy storage: A review," *J. Energy Storage*, vol. 15, pp. 145–157, 2018, doi: 10.1016/j.est.2017.11.008.
[138] M. K. Deshmukh and S. S. Deshmukh, "Modeling of hybrid renewable energy systems," *Renew. Sustain. Energy Rev.*, vol. 12, no. 1, pp. 235–249, 2008, doi: 10.1016/j.rser.2006.07.011.
[139] "Wind Energy Solutions WES." https://windenergysolutions.nl/.
[140] P. Rullo, L. Braccia, P. Luppi, D. Zumoffen, and D. Feroldi, "Integration of sizing and energy management based on economic predictive control for standalone hybrid renewable energy systems," *Renew. Energy*, vol. 140, pp. 436–451, 2019, doi: 10.1016/j.renene.2019.03.074.
[141] L. Moretti, M. Astolfi, C. Vergara, E. Macchi, J. I. Pérez-Arriaga, and G. Manzolini, "A design and dispatch optimization algorithm based on mixed integer linear programming for rural electrification," *Appl. Energy*, vol. 233–234, pp. 1104–1121, 2019, doi: 10.1016/j.apenergy.2018.09.194.
[142] E. Lockhart *et al.*, "Comparative Study of Techno-Economics of Lithium-Ion and Lead-Acid Batteries in Micro-Grids in Sub-Saharan Africa," *Natl. Renew. Energy Lab.*, no. NREL/TP-7A40-73238, p. 36, 2019, doi: 10.2172/1526204.
[143] A. Maleki and A. Askarzadeh, "Optimal sizing of a PV/wind/diesel system with battery storage for electrification to an off-grid remote region: A case study of Rafsanjan, Iran," *Sustain. Energy Technol. Assessments*, vol. 7, pp. 147–153, 2014, doi: 10.1016/j.seta.2014.04.005.
[144] H. Borhanazad, S. Mekhilef, V. Gounder Ganapathy, M. Modiri-Delshad, and A. Mirtaheri, "Optimization of micro-grid system using MOPSO," *Renew. Energy*, vol. 71, pp. 295–306, 2014, doi: 10.1016/j.renene.2014.05.006.
[145] R. Dufo-López, L. A. Fernández-Jiménez, I. J. Ramírez-Rosado, J. S. Artal-Sevil, J. A. Domínguez-Navarro, and J. L. Bernal-Agustín, "Daily operation optimisation of hybrid stand-alone system by model predictive control considering ageing model," *Energy Convers. Manag.*, vol. 134, pp. 167–177, 2017, doi: 10.1016/j.enconman.2016.12.036.
[146] R. Dufo-López, I. R. Cristóbal-Monreal, and J. M. Yusta, "Stochastic-heuristic methodology for the optimisation of components and control variables of PV-wind-diesel-battery stand-alone systems," *Renew. Energy*, vol. 99, pp. 919–935, 2016, doi: 10.1016/j.renene.2016.07.069.
[147] C. D. Barley and C. B. Winn, "Optimal dispatch strategy in remote hybrid power systems," *Sol. Energy*, vol. 58, no. 4–6, pp. 165–179, 1996, doi: 10.1016/S0038-092X(96)00087-4.
[148] A. Malheiro, P. M. Castro, R. M. Lima, and A. Estanqueiro, "Integrated sizing and scheduling of wind/PV/diesel/battery isolated systems," *Renew. Energy*, vol. 83, pp. 646–657, 2015, doi: 10.1016/j.renene.2015.04.066.
[149] R. Dufo-López and J. L. Bernal-Agustín, "Multi-objective design of PV-wind-diesel-hydrogen-battery systems," *Renew. Energy*, vol. 33, no. 12, pp. 2559–2572, 2008, doi: 10.1016/j.renene.2008.02.027.
[150] R. Dufo-López *et al.*, "Multi-objective optimization minimizing cost and life cycle emissions of stand-alone PV-wind-diesel systems with batteries

storage," *Appl. Energy*, vol. 88, no. 11, pp. 4033–4041, 2011, doi: 10.1016/j.apenergy.2011.04.019.

[151] B. Fleck and M. Huot, "Comparative life-cycle assessment of a small wind turbine for residential off-grid use," *Renew. Energy*, vol. 34, no. 12, pp. 2688–2696, 2009, doi: 10.1016/j.renene.2009.06.016.

[152] A. Q. Jakhrani, A. R. H. Rigit, A. K. Othman, S. R. Samo, and S. A. Kamboh, "Estimation of carbon footprints from diesel generator emissions," in *Proceedings of the 2012 International Conference in Green and Ubiquitous Technology, GUT 2012*, 2012, pp. 78–81, doi: 10.1109/GUT.2012.6344193.

[153] A. H. Hermelink and D. de Jager, "Evaluating our future: the crucial role of discount rates in European Commission energy system modelling," 2015.

[154] D. Thomas, D. Mertens, M. Meeus, W. Van der Laak, and I. Francois, "Power-to-gas Roadmap for Flanders," Brussels, 2016. [Online]. Available: https://www.waterstofnet.eu/_asset/_public/powertogas/P2G-Roadmap-for-Flanders.pdf.

[155] Battelle Memorial Institute, "Manufacturing Cost Analysis of PEM Fuel Cell Systems for 5- and 10-kW Backup Power Applications," 2016. [Online]. Available: https://energy.gov/sites/prod/files/2016/12/f34/fcto_cost_analysis_pem_fc_5-10kw_backup_power_0.pdf.

[156] Battelle Memorial Institute, "Manufacturing Cost Analysis: 1, 5, 10 and 25 kW Fuel Cell Systems for Primary Power and Combined Heat and Power Applications," 2017. [Online]. Available: https://www.energy.gov/sites/prod/files/2018/02/f49/fcto_battelle_mfg_cost_analysis_1 _to_25kw_pp_chp_fc_systems_jan2017_0.pdf.

[157] J. C. Alberizzi, J. M. Frigola, M. Rossi, and M. Renzi, "Optimal sizing of a Hybrid Renewable Energy System: Importance of data selection with highly variable renewable energy sources," *Energy Convers. Manag.*, vol. 223, p. 113303, 2020, doi: 10.1016/j.enconman.2020.113303.

[158] C. Bordin, H. O. Anuta, A. Crossland, I. L. Gutierrez, C. J. Dent, and D. Vigo, "A linear programming approach for battery degradation analysis and optimization in offgrid power systems with solar energy integration," *Renew. Energy*, vol. 101, pp. 417–430, 2017, doi: 10.1016/j.renene.2016.08.066.

[159] M. F. Zia, E. Elbouchikhi, and M. Benbouzid, "Optimal operational planning of scalable DC microgrid with demand response, islanding, and battery degradation cost considerations," *Appl. Energy*, vol. 237, pp. 695–707, 2019, doi: https://doi.org/10.1016/j.apenergy.2019.01.040.

[160] S. Few, O. Schmidt, A. Gambhir, E. Stephenson, and A. DelCore, "Energy storage trends for off-grid services in emerging markets. Insight from social enterprises," 2018. [Online]. Available: https://shellfoundation.org/app/uploads/2018/10/Shell-Foundation_Energy-Storage-Report.pdf.

[161] P. Gabrielli, M. Gazzani, and M. Mazzotti, "Electrochemical conversion technologies for optimal design of decentralized multi-energy systems: Modeling framework and technology assessment," *Appl. Energy*, vol. 221, pp. 557–575, 2018, doi: 10.1016/j.apenergy.2018.03.149.

[162] A. El-Kharouf, A. Chandan, M. Hattenberger, and B. G. Pollet, "Proton

exchange membrane fuel cell degradation and testing: Review," *J. Energy Inst.*, vol. 85, no. 4, pp. 188–200, 2012, doi: 10.1179/1743967112Z.00000000036.

[163] M. Santos and I. Marino, "Energy analysis of the Raggovidda integrated system," 2019. [Online]. Available: https://www.haeolus.eu/wp-content/uploads/2019/01/D5.1.pdf.

[164] J. P. Torreglosa, P. García-Triviño, L. M. Fernández-Ramirez, and F. Jurado, "Control based on techno-economic optimization of renewable hybrid energy system for stand-alone applications," *Expert Syst. Appl.*, vol. 51, pp. 59–75, 2016, doi: 10.1016/j.eswa.2015.12.038.

[165] M. Boussetta, R. El Bachtiri, M. Khanfara, and K. El Hammoumi, "Assessing the potential of hybrid PV–Wind systems to cover public facilities loads under different Moroccan climate conditions," *Sustain. Energy Technol. Assessments*, vol. 22, no. 2017, pp. 74–82, 2017, doi: 10.1016/j.seta.2017.07.005.

[166] M. F. Shehzad, M. B. Abdelghany, D. Liuzza, V. Mariani, and L. Glielmo, "Mixed logic dynamic models for MPC control of wind farm hydrogen-based storage systems," *Inventions*, vol. 4, no. 4, pp. 1–17, 2019, doi: 10.3390/inventions4040057.

[167] I. Tsiropoulos, D. Tarvydas, and N. Lebedeva, "Li-ion batteries for mobility and stationary storage applications," 2018. doi: 10.2760/87175.

[168] S. Schopfer, V. Tiefenbeck, and T. Staake, "Economic assessment of photovoltaic battery systems based on household load profiles," *Appl. Energy*, vol. 223, pp. 229–248, 2018, doi: https://doi.org/10.1016/j.apenergy.2018.03.185.

[169] A. Ahadi and X. Liang, "A stand-alone hybrid renewable energy system assessment using cost optimization method," in *Proceedings of the IEEE International Conference on Industrial Technology*, 2017, pp. 376–381, doi: 10.1109/ICIT.2017.7913260.

[170] A. Maleki and A. Askarzadeh, "Comparative study of artificial intelligence techniques for sizing of a hydrogen-based stand-alone photovoltaic/wind hybrid system," *Int. J. Hydrogen Energy*, vol. 39, no. 19, pp. 9973–9984, 2014, doi: 10.1016/j.ijhydene.2014.04.147.

[171] W. Zhang, A. Maleki, M. A. Rosen, and J. Liu, "Sizing a stand-alone solar-wind-hydrogen energy system using weather forecasting and a hybrid search optimization algorithm," *Energy Convers. Manag.*, vol. 180, pp. 609–621, 2019, doi: https://doi.org/10.1016/j.enconman.2018.08.102.

[172] J. Lian, Y. Zhang, C. Ma, Y. Yang, and E. Chaima, "A review on recent sizing methodologies of hybrid renewable energy systems," *Energy Convers. Manag.*, vol. 199, p. 112027, 2019, doi: 10.1016/j.enconman.2019.112027.

[173] A. Brka, Y. M. Al-Abdeli, and G. Kothapalli, "The interplay between renewables penetration, costing and emissions in the sizing of stand-alone hydrogen systems," *Int. J. Hydrogen Energy*, vol. 40, no. 1, pp. 125–135, 2015, doi: 10.1016/j.ijhydene.2014.10.132.

[174] Y. A. Katsigiannis, P. S. Georgilakis, and E. S. Karapidakis, "Multiobjective genetic algorithm solution to the optimum economic and environmental performance problem of small autonomous hybrid power systems with renewables," *IET Renew. Power Gener.*, vol. 4, no. 5, p. 404,

2010, doi: 10.1049/iet-rpg.2009.0076.
[175] Ø. Ulleberg, "The importance of control strategies in PV-hydrogen systems," *Sol. Energy*, vol. 76, no. 1–3, pp. 323–329, 2004, doi: 10.1016/j.solener.2003.09.013.
[176] L. Olatomiwa, S. Mekhilef, M. S. Ismail, and M. Moghavvemi, "Energy management strategies in hybrid renewable energy systems: A review," *Renew. Sustain. Energy Rev.*, vol. 62, no. Supplement C, pp. 821–835, 2016, doi: https://doi.org/10.1016/j.rser.2016.05.040.
[177] K. Zhou, J. A. Ferreira, and S. W. H. de Haan, "Optimal energy management strategy and system sizing method for stand-alone photovoltaic-hydrogen systems," *Int. J. Hydrogen Energy*, vol. 33, no. 2, pp. 477–489, 2008, doi: 10.1016/j.ijhydene.2007.09.027.
[178] D. Ipsakis, S. Voutetakis, P. Seferlis, F. Stergiopoulos, and C. Elmasides, "Power management strategies for a stand-alone power system using renewable energy sources and hydrogen storage," *Int. J. Hydrogen Energy*, vol. 34, no. 16, pp. 7081–7095, 2009, doi: 10.1016/j.ijhydene.2008.06.051.
[179] H. He, S. Quan, F. Sun, Y. X. Wang, and Y. X. Wang, "Model predictive control with lifetime constraints based energy management strategy for proton exchange membrane fuel cell hybrid power systems," *IEEE Trans. Ind. Electron.*, vol. 67, no. 10, pp. 9012–9023, 2020, doi: 10.1109/TIE.2020.2977574.
[180] F. Garcia-Torres, C. Bordons, and M. A. Ridao, "Optimal economic schedule for a network of microgrids with hybrid energy storage system using distributed model predictive control," *IEEE Trans. Ind. Electron.*, vol. 66, no. 3, pp. 1919–1929, 2019, doi: 10.1109/TIE.2018.2826476.
[181] F. Garcia-Torres, L. Valverde, and C. Bordons, "Optimal Load Sharing of Hydrogen-Based Microgrids with Hybrid Storage Using Model-Predictive Control," *IEEE Trans. Ind. Electron.*, vol. 63, no. 8, pp. 4919–4928, 2016, doi: 10.1109/TIE.2016.2547870.
[182] R. Jallouli and L. Krichen, "Sizing, techno-economic and generation management analysis of a stand alone photovoltaic power unit including storage devices," *Energy*, vol. 40, no. 1, pp. 196–209, 2012, doi: 10.1016/j.energy.2012.02.004.
[183] G. Bruni *et al.*, "Fuel cell based power systems to supply power to Telecom Stations," *Int. J. Hydrogen Energy*, vol. 39, no. 36, pp. 21767–21777, 2014, doi: 10.1016/j.ijhydene.2014.07.078.
[184] M. Castañeda, A. Cano, F. Jurado, H. Sánchez, and L. M. Fernández, "Sizing optimization, dynamic modeling and energy management strategies of a stand-alone PV/hydrogen/battery-based hybrid system," *Int. J. Hydrogen Energy*, vol. 38, no. 10, pp. 3830–3845, 2013, doi: 10.1016/j.ijhydene.2013.01.080.
[185] C. Ziogou *et al.*, "Automation infrastructure and operation control strategy in a stand-alone power system based on renewable energy sources," *J. Power Sources*, vol. 196, no. 22, pp. 9488–9499, 2011, doi: 10.1016/j.jpowsour.2011.07.029.
[186] Enel Green Power, "Enel Green Power web site." https://www.enelgreenpower.com/ (accessed May 11, 2019).
[187] ENGIE-Eps, "ENGIE-Eps web site." https://engie-eps.com/ (accessed May 11, 2019).

[188] Horizon SA, "Horizon SA web site." http://orizon-ate.eu/ (accessed May 11, 2019).
[189] IRIS, "IRIS web page." http://www.irissrl.org/ (accessed May 11, 2019).
[190] Spanner Re^2 GmbH, "Biomass CHP HKA 49." www.holz-kraft.com (accessed Nov. 15, 2019).
[191] D. Clark, "Information paper - 4 CO2e emissions from biomass and biofuels," 2013.
[192] T. Gebreegziabher, A. O. Oyedun, and C. W. Hui, "Optimum biomass drying for combustion - A modeling approach," *Energy*, vol. 53, pp. 67–73, 2013, doi: 10.1016/j.energy.2013.03.004.
[193] H. M. Ridha, C. Gomes, H. Hizam, M. Ahmadipour, A. A. Heidari, and H. Chen, "Multi-objective optimization and multi-criteria decision-making methods for optimal design of standalone photovoltaic system: A comprehensive review," *Renew. Sustain. Energy Rev.*, vol. 135, no. April 2020, p. 110202, 2021, doi: 10.1016/j.rser.2020.110202.
[194] C. Mokhtara, B. Negrou, A. Bouferrouk, Y. Yao, N. Settou, and M. Ramadan, "Integrated supply–demand energy management for optimal design of off-grid hybrid renewable energy systems for residential electrification in arid climates," *Energy Convers. Manag.*, vol. 221, p. 113192, 2020, doi: 10.1016/j.enconman.2020.113192.
[195] S. Sinha and S. S. Chandel, "Review of software tools for hybrid renewable energy systems," *Renew. Sustain. Energy Rev.*, vol. 32, pp. 192–205, 2014, doi: 10.1016/j.rser.2014.01.035.
[196] A. C. Duman and Ö. Güler, "Techno-economic analysis of off-grid PV/wind/fuel cell hybrid system combinations with a comparison of regularly and seasonally occupied households," *Sustain. Cities Soc.*, vol. 42, pp. 107–126, 2018, doi: 10.1016/j.scs.2018.06.029.
[197] Y. Kalinci, I. Dincer, and A. Hepbasli, "Energy and exergy analyses of a hybrid hydrogen energy system: A case study for Bozcaada," *Int. J. Hydrogen Energy*, vol. 42, no. 4, pp. 2492–2503, 2017, doi: 10.1016/j.ijhydene.2016.02.048.
[198] S. A. Amirkhalili and A. R. Zahedi, "Techno-economic Analysis of a Stand-alone Hybrid Wind/Fuel Cell Microgrid System: A Case Study in Kouhin Region in Qazvin," *Fuel Cells*, vol. 18, no. 4, pp. 551–560, 2018, doi: 10.1002/fuce.201700149.
[199] D. N. Luta and A. K. Raji, "Optimal sizing of hybrid fuel cell-supercapacitor storage system for off-grid renewable applications," *Energy*, vol. 166, pp. 530–540, 2019, doi: 10.1016/j.energy.2018.10.070.
[200] V. Suresh, M. Muralidhar, and R. Kiranmayi, "Modelling and optimization of an off-grid hybrid renewable energy system for electrification in a rural areas," *Energy Reports*, vol. 6, pp. 594–604, 2020, doi: 10.1016/j.egyr.2020.01.013.
[201] V. Suresh, M. Muralidhar, and R. Kiranmayi, "Techno-economic analysis of off-grid solar/wind/biogas/biomass/fuel cell/battery system for electrification in a cluster of villages by HOMER software," *Environ. Dev. Sustain.*, 2020, doi: 10.1007/s10668-019-00583-2.
[202] L. Tribioli, R. Cozzolino, L. Evangelisti, and G. Bella, "Energy management of an off-grid hybrid power plant with multiple energy storage systems," *Energies*, vol. 9, no. 8, 2016, doi: 10.3390/en9080661.

[203] A. Kashefi Kaviani, G. H. Riahy, and S. M. Kouhsari, "Optimal design of a reliable hydrogen-based stand-alone wind/PV generating system, considering component outages," *Renew. Energy*, vol. 34, no. 11, pp. 2380–2390, 2009, doi: 10.1016/j.renene.2009.03.020.

[204] D. P. Clarke, Y. M. Al-Abdeli, and G. Kothapalli, "The impact of using Particle Swarm Optimisation on the operational characteristics of a stand-alone hydrogen system with on-site water production," *Int. J. Hydrogen Energy*, vol. 39, no. 28, pp. 15307–15319, 2014, doi: 10.1016/j.ijhydene.2014.07.116.

[205] H. R. Baghaee, M. Mirsalim, and G. B. Gharehpetian, "Multi-objective optimal power management and sizing of a reliable wind/PV microgrid with hydrogen energy storage using MOPSO," *J. Intell. Fuzzy Syst.*, vol. 32, no. 3, pp. 1753–1773, 2017, doi: 10.3233/JIFS-152372.

[206] D. Feroldi and D. Zumoffen, "Sizing methodology for hybrid systems based on multiple renewable power sources integrated to the energy management strategy," *Int. J. Hydrogen Energy*, vol. 39, no. 16, pp. 8609–8620, 2014, doi: 10.1016/j.ijhydene.2014.01.003.

[207] N. S. Attemene, K. S. Agbli, S. Fofana, and D. Hissel, "Optimal sizing of a wind, fuel cell, electrolyzer, battery and supercapacitor system for off-grid applications," *Int. J. Hydrogen Energy*, vol. 45, no. 8, pp. 5512–5525, 2020, doi: 10.1016/j.ijhydene.2019.05.212.

[208] A. Maleki and A. Askarzadeh, "Artificial bee swarm optimization for optimum sizing of a stand-alone PV/WT/FC hybrid system considering LPSP concept," *Sol. Energy*, vol. 107, pp. 227–235, 2014, doi: 10.1016/j.solener.2014.05.016.

[209] M. M. Samy, S. Barakat, and H. S. Ramadan, "A flower pollination optimization algorithm for an off-grid PV-Fuel cell hybrid renewable system," *Int. J. Hydrogen Energy*, vol. 44, no. 4, pp. 2141–2152, 2019, doi: 10.1016/j.ijhydene.2018.05.127.

[210] M. J. Hadidian Moghaddam, A. Kalam, S. A. Nowdeh, A. Ahmadi, M. Babanezhad, and S. Saha, "Optimal sizing and energy management of stand-alone hybrid photovoltaic/wind system based on hydrogen storage considering LOEE and LOLE reliability indices using flower pollination algorithm," *Renew. Energy*, vol. 135, pp. 1412–1434, 2019, doi: 10.1016/j.renene.2018.09.078.

[211] A. Fathy, "A reliable methodology based on mine blast optimization algorithm for optimal sizing of hybrid PV-wind-FC system for remote area in Egypt," *Renew. Energy*, vol. 95, pp. 367–380, 2016, doi: 10.1016/j.renene.2016.04.030.

[212] S. Dehghan, H. Saboori, A. Parizad, and B. Kiani, "Optimal sizing of a hydrogen-based wind/PV plant considering reliability indices," *Electr. Power Energy Convers. Syst. 2009. EPECS'09. Int. Conf.*, pp. 1–9, 2009.

[213] M. Sharafi and T. Y. ELMekkawy, "Multi-objective optimal design of hybrid renewable energy systems using PSO-simulation based approach," *Renew. Energy*, vol. 68, pp. 67–79, 2014, doi: 10.1016/j.renene.2014.01.011.

[214] T. Kerdphol, K. Fuji, Y. Mitani, M. Watanabe, and Y. Qudaih, "Optimization of a battery energy storage system using particle swarm optimization for stand-alone microgrids," *Int. J. Electr. Power Energy*

Syst., vol. 81, pp. 32–39, 2016, doi: 10.1016/j.ijepes.2016.02.006.

[215] M. Nunes Fonseca, E. de Oliveira Pamplona, A. R. de Queiroz, V. E. de Mello Valerio, G. Aquila, and S. Ribeiro Silva, "Multi-objective optimization applied for designing hybrid power generation systems in isolated networks," *Sol. Energy*, vol. 161, pp. 207–219, 2018, doi: 10.1016/j.solener.2017.12.046.

[216] R. J. Rathish, K. Mahadevan, S. K. Selvaraj, and J. Booma, "Multi-objective evolutionary optimization with genetic algorithm for the design of off-grid PV-wind-battery-diesel system," *Soft Comput.*, vol. 0123456789, 2020, doi: 10.1007/s00500-020-05372-y.

[217] A. L. Bukar, C. W. Tan, L. K. Yiew, R. Ayop, and W. S. Tan, "A rule-based energy management scheme for long-term optimal capacity planning of grid-independent microgrid optimized by multi-objective grasshopper optimization algorithm," *Energy Convers. Manag.*, vol. 221, no. June, p. 113161, 2020, doi: 10.1016/j.enconman.2020.113161.

[218] C. D. Rodríguez-Gallegos, D. Yang, O. Gandhi, M. Bieri, T. Reindl, and S. K. Panda, "A multi-objective and robust optimization approach for sizing and placement of PV and batteries in off-grid systems fully operated by diesel generators: An Indonesian case study," *Energy*, vol. 160, pp. 410–429, 2018, doi: 10.1016/j.energy.2018.06.185.

[219] M. J. Mayer, A. Szilágyi, and G. Gróf, "Environmental and economic multi-objective optimization of a household level hybrid renewable energy system by genetic algorithm," *Appl. Energy*, vol. 269, p. 115058, 2020, doi: 10.1016/j.apenergy.2020.115058.

[220] R. Wang, G. Li, M. Ming, G. Wu, and L. Wang, "An efficient multi-objective model and algorithm for sizing a stand-alone hybrid renewable energy system," *Energy*, vol. 141, pp. 2288–2299, 2017, doi: 10.1016/j.energy.2017.11.085.

[221] M. R. Quitoras, P. E. Campana, and C. Crawford, "Exploring electricity generation alternatives for Canadian Arctic communities using a multi-objective genetic algorithm approach," *Energy Convers. Manag.*, vol. 210, p. 112471, 2020, doi: 10.1016/j.enconman.2020.112471.

[222] F. Fodhil, A. Hamidat, and O. Nadjemi, "Potential, optimization and sensitivity analysis of photovoltaic-diesel-battery hybrid energy system for rural electrification in Algeria," *Energy*, vol. 169, pp. 613–624, 2019, doi: 10.1016/j.energy.2018.12.049.

[223] S. Mazzola, M. Astolfi, and E. Macchi, "The potential role of solid biomass for rural electrification: A techno economic analysis for a hybrid microgrid in India," *Appl. Energy*, vol. 169, pp. 370–383, 2016, doi: 10.1016/j.apenergy.2016.02.051.

[224] S. Mazzola, C. Vergara, M. Astolfi, V. Li, I. Perez-Arriaga, and E. Macchi, "Assessing the value of forecast-based dispatch in the operation of off-grid rural microgrids," *Renew. Energy*, vol. 108, pp. 116–125, 2017, doi: 10.1016/j.renene.2017.02.040.

[225] J. Kennedy and R. Eberhart, "Particle swarm optimization," *Proc. IEEE Int. Conf. Neural Networks*, pp. 1942–1948, 1995.

[226] P. Gabrielli, M. Gazzani, E. Martelli, and M. Mazzotti, "Optimal design of multi-energy systems with seasonal storage," *Appl. Energy*, vol. 219, pp. 408–424, 2018, doi: 10.1016/j.apenergy.2017.07.142.

[227] C. Yang and J. Ogden, “Determining the lowest-cost hydrogen delivery mode,” *Int. J. Hydrogen Energy*, vol. 32, no. 2, pp. 268–286, 2007, doi: 10.1016/j.ijhydene.2006.05.009.

[228] Ø. Ulleberg and R. Hancke, “Techno-economic calculations of small-scale hydrogen supply systems for zero emission transport in Norway,” *Int. J. Hydrogen Energy*, vol. 45, no. 2, pp. 1201–1211, 2020, doi: 10.1016/j.ijhydene.2019.05.170.

[229] B. Li, R. Roche, D. Paire, and A. Miraoui, “Sizing of a stand-alone microgrid considering electric power, cooling/heating, hydrogen loads and hydrogen storage degradation,” *Appl. Energy*, vol. 205, pp. 1244–1259, 2017, doi: 10.1016/j.apenergy.2017.08.142.

[230] D. Fioriti, D. Poli, P. Cherubini, G. Lutzemberger, A. Micangeli, and P. Duenas-Martinez, “Comparison among deterministic methods to design rural mini-grids: Effect of operating strategies,” *2019 IEEE Milan PowerTech, PowerTech 2019*, pp. 1–6, 2019, doi: 10.1109/PTC.2019.8810717.

[231] A. Bischi *et al.*, “A detailed MILP optimization model for combined cooling, heat and power system operation planning,” *Energy*, vol. 74, no. C, pp. 12–26, 2014, doi: 10.1016/j.energy.2014.02.042.

[232] J. C. Alberizzi, M. Rossi, and M. Renzi, “A MILP algorithm for the optimal sizing of an off-grid hybrid renewable energy system in South Tyrol,” *Energy Reports*, vol. 6, pp. 21–26, 2020, doi: 10.1016/j.egyr.2019.08.012.

[233] L. Kotzur, P. Markewitz, M. Robinius, and D. Stolten, “Impact of different time series aggregation methods on optimal energy system design,” *Renew. Energy*, vol. 117, pp. 474–487, 2018, doi: 10.1016/j.renene.2017.10.017.

[234] F. Domínguez-Muñoz, J. M. Cejudo-López, A. Carrillo-Andrés, and M. Gallardo-Salazar, “Selection of typical demand days for CHP optimization,” *Energy Build.*, vol. 43, no. 11, pp. 3036–3043, 2011, doi: 10.1016/j.enbuild.2011.07.024.

[235] P. Stadler, A. Ashouri, and F. Maréchal, “Model-based optimization of distributed and renewable energy systems in buildings,” *Energy Build.*, vol. 120, pp. 103–113, 2016, doi: 10.1016/j.enbuild.2016.03.051.

[236] P. Nahmmacher, E. Schmid, L. Hirth, and B. Knopf, “Carpe diem: A novel approach to select representative days for long-term power system modeling,” *Energy*, vol. 112, pp. 430–442, 2016, doi: 10.1016/j.energy.2016.06.081.

[237] H. Teichgraeber and A. R. Brandt, “Clustering methods to find representative periods for the optimization of energy systems: An initial framework and comparison,” *Appl. Energy*, vol. 239, pp. 1283–1293, 2019, doi: 10.1016/j.apenergy.2019.02.012.

[238] K. Poncelet, H. Hoschle, E. Delarue, A. Virag, and W. Drhaeseleer, “Selecting representative days for capturing the implications of integrating intermittent renewables in generation expansion planning problems,” *IEEE Trans. Power Syst.*, vol. 32, no. 3, pp. 1936–1948, 2017, doi: 10.1109/TPWRS.2016.2596803.

[239] B. van der Heijde, A. Vandermeulen, R. Salenbien, and L. Helsen, “Representative days selection for district energy system optimisation: a solar district heating system with seasonal storage,” *Appl. Energy*, vol. 248,

pp. 79–94, 2019, doi: 10.1016/j.apenergy.2019.04.030.

[240] T. Schütz, M. H. Schraven, M. Fuchs, P. Remmen, and D. Müller, "Comparison of clustering algorithms for the selection of typical demand days for energy system synthesis," *Renew. Energy*, vol. 129, pp. 570–582, 2018, doi: 10.1016/j.renene.2018.06.028.

[241] L. Kotzur, P. Markewitz, M. Robinius, and D. Stolten, "Time series aggregation for energy system design: Modeling seasonal storage," *Appl. Energy*, vol. 213, pp. 123–135, 2018, doi: 10.1016/j.apenergy.2018.01.023.

[242] S. Nolan and M. O'Malley, "Challenges and barriers to demand response deployment and evaluation," *Appl. Energy*, vol. 152, pp. 1–10, 2015, doi: 10.1016/j.apenergy.2015.04.083.

[243] S. Nojavan, M. Majidi, A. Najafi-Ghalelou, M. Ghahramani, and K. Zare, "A cost-emission model for fuel cell/PV/battery hybrid energy system in the presence of demand response program: ε-constraint method and fuzzy satisfying approach," *Energy Convers. Manag.*, vol. 138, pp. 383–392, 2017, doi: 10.1016/j.enconman.2017.02.003.

[244] M. Majidi, S. Nojavan, and K. Zare, "Optimal stochastic short-term thermal and electrical operation of fuel cell/photovoltaic/battery/grid hybrid energy system in the presence of demand response program," *Energy Convers. Manag.*, vol. 144, pp. 132–142, 2017, doi: 10.1016/j.enconman.2017.04.051.

[245] R. Palma-Behnke *et al.*, "A microgrid energy management system based on the rolling horizon strategy," *IEEE Trans. Smart Grid*, vol. 4, no. 2, pp. 996–1006, 2013, doi: 10.1109/TSG.2012.2231440.

[246] R. Palma-Behnke, C. Benavides, E. Aranda, J. Llanos, and D. Sáez, "Energy management system for a renewable based microgrid with a demand side management mechanism," *IEEE SSCI 2011 - Symp. Ser. Comput. Intell. - CIASG 2011 2011 IEEE Symp. Comput. Intell. Appl. Smart Grid*, pp. 131–138, 2011, doi: 10.1109/CIASG.2011.5953338.

[247] T. Tu, G. P. Rajarathnam, and A. M. Vassallo, "Optimization of a stand-alone photovoltaic–wind–diesel–battery system with multi-layered demand scheduling," *Renew. Energy*, vol. 131, pp. 333–347, 2019, doi: 10.1016/j.renene.2018.07.029.

[248] M. H. Amrollahi and S. M. T. Bathaee, "Techno-economic optimization of hybrid photovoltaic/wind generation together with energy storage system in a stand-alone micro-grid subjected to demand response," *Appl. Energy*, vol. 202, pp. 66–77, 2017, doi: 10.1016/j.apenergy.2017.05.116.

[249] P. Gabrielli, B. Flamm, A. Eichler, M. Gazzani, J. Lygeros, and M. Mazzotti, "Modeling for optimal operation of PEM fuel cells and electrolyzers," *EEEIC 2016 - Int. Conf. Environ. Electr. Eng.*, pp. 1–7, 2016, doi: 10.1109/EEEIC.2016.7555707.

[250] S. Seyyedeh-Barhagh, M. Majidi, S. Nojavan, and K. Zare, "Optimal Scheduling of Hydrogen Storage under Economic and Environmental Priorities in the Presence of Renewable Units and Demand Response," *Sustain. Cities Soc.*, vol. 46, p. 101406, 2019, doi: 10.1016/j.scs.2018.12.034.

[251] R. Palma-Behnke, D. Ortiz, L. Reyes, G. Jiménez-Estévez, and N. Garrido, "A social SCADA approach for a renewable based microgrid - The Huatacondo project," *IEEE Power Energy Soc. Gen. Meet.*, 2011, doi:

10.1109/PES.2011.6039749.
[252] M. Zatti *et al.*, “k-MILP: A novel clustering approach to select typical and extreme days for multi-energy systems design optimization,” *Energy*, vol. 181, pp. 1051–1063, 2019, doi: 10.1016/j.energy.2019.05.044.
[253] D. Pinel, “Clustering Methods Assessment for Investment in Zero Emission Neighborhoods Energy System,” pp. 1–12, 2020, [Online]. Available: http://arxiv.org/abs/2001.08936.
[254] A. Nilsson, C. J. Bergstad, L. Thuvander, D. Andersson, K. Andersson, and P. Meiling, “Effects of continuous feedback on households’ electricity consumption: Potentials and barriers,” *Appl. Energy*, vol. 122, pp. 17–23, 2014, doi: 10.1016/j.apenergy.2014.01.060.
[255] M. Howells *et al.*, “OSeMOSYS: The Open Source Energy Modeling System. An introduction to its ethos, structure and development.,” *Energy Policy*, vol. 39, no. 10, pp. 5850–5870, 2011, doi: 10.1016/j.enpol.2011.06.033.
[256] Q. Feng *et al.*, “A review of proton exchange membrane water electrolysis on degradation mechanisms and mitigation strategies,” *J. Power Sources*, vol. 366, pp. 33–55, 2017, doi: 10.1016/j.jpowsour.2017.09.006.
[257] L. Bertuccioli, A. Chan, D. Hart, F. Lehner, B. Madden, and Eleanor Standen, “Fuel cells and hydrogen Joint undertaking Development of Water Electrolysis in the European Union,” 2014. [Online]. Available: https://www.fch.europa.eu/node/783.
[258] A. S. Gago *et al.*, “Protective coatings on stainless steel bipolar plates for proton exchange membrane (PEM) electrolysers,” *J. Power Sources*, vol. 307, pp. 815–825, 2016, doi: 10.1016/j.jpowsour.2015.12.071.
[259] S. Lædre, O. E. Kongstein, A. Oedegaard, H. Karoliussen, and F. Seland, “Materials for Proton Exchange Membrane water electrolyzer bipolar plates,” *Int. J. Hydrogen Energy*, vol. 42, no. 5, pp. 2713–2723, 2017, doi: 10.1016/j.ijhydene.2016.11.106.
[260] C. Rakousky, U. Reimer, K. Wippermann, M. Carmo, W. Lueke, and D. Stolten, “An analysis of degradation phenomena in polymer electrolyte membrane water electrolysis,” *J. Power Sources*, vol. 326, pp. 120–128, 2016, doi: 10.1016/j.jpowsour.2016.06.082.
[261] A. S. Gago, P. Lettenmeier, S. Stiber, A. S. Ansar, L. Wang, and K. A. Friedrich, “Cost-Effective PEM Electrolysis: The Quest to Achieve Superior Efficiencies with Reduced Investment,” vol. 85, no. 13, pp. 3–13, 2018, doi: 10.1149/08513.0003ecst.
[262] P. Lettenmeier, R. Wang, R. Abouatallah, F. Burggraf, A. S. Gago, and K. A. Friedrich, “Coated Stainless Steel Bipolar Plates for Proton Exchange Membrane Electrolyzers,” *J. Electrochem. Soc.*, vol. 163, no. 11, pp. F3119–F3124, 2016, doi: 10.1149/2.0141611jes.
[263] P. Lettenmeier *et al.*, “Low-cost and durable bipolar plates for proton exchange membrane electrolyzers,” *Sci. Rep.*, vol. 7, no. September 2016, pp. 1–12, 2017, doi: 10.1038/srep44035.
[264] A. S. Gago *et al.*, “Degradation of Proton Exchange Membrane (PEM) Electrolysis: The Influence of Current Density,” *ECS Trans.*, vol. 86, no. 13, pp. 695–700, 2018, doi: 10.1149/08613.0695ecst.
[265] C. Rakousky *et al.*, “Polymer electrolyte membrane water electrolysis: Restraining degradation in the presence of fluctuating power,” *J. Power

Sources, vol. 342, pp. 38–47, 2017, doi: 10.1016/j.jpowsour.2016.11.118.

[266] C. Rakousky, G. P. Keeley, K. Wippermann, M. Carmo, and D. Stolten, "The stability challenge on the pathway to high-current-density polymer electrolyte membrane water electrolyzers," *Electrochim. Acta*, vol. 278, pp. 324–331, 2018, doi: 10.1016/j.electacta.2018.04.154.

[267] C. Liu *et al.*, "Performance enhancement of PEM electrolyzers through iridium-coated titanium porous transport layers," *Electrochem. commun.*, vol. 97, no. September, pp. 96–99, 2018, doi: 10.1016/j.elecom.2018.10.021.

[268] F. Andolfatto, R. Durand, A. Michas, P. Millet, and P. Stevens, "Solid polymer electrolyte water electrolysis: electrocatalysis and long-term stability," *Int. J. Hydrogen Energy*, vol. 19, no. 5, pp. 421–427, 1994, doi: 10.1016/0360-3199(94)90018-3.

[269] A. Savan, B. Ratna, S. Merzlikin, B. Breitbach, A. Ludwig, and K. J. J. Mayrhofer, "Oxygen and hydrogen evolution reactions on Ru, RuO2, Ir, and IrO2 thin film electrodes in acidic and alkaline electrolytes: A comparative study on activity and stability," *Catal. Today*, vol. 262, pp. 170–180, 201AD, doi: 10.1016/j.cattod.2015.08.014.

[270] T. Audichon, E. Mayousse, T. W. Napporn, C. Morais, C. Comminges, and K. B. Kokoh, "Elaboration and characterization of ruthenium nano-oxides for the oxygen evolution reaction in a Proton Exchange Membrane Water Electrolyzer supplied by a solar profile," *Electrochim. Acta*, vol. 132, pp. 284–291, 2014, doi: 10.1016/j.electacta.2014.03.141.

[271] H. Ma, C. Liu, J. Liao, Y. Su, X. Xue, and W. Xing, "Study of ruthenium oxide catalyst for electrocatalytic performance in oxygen evolution," *J. Mol. Catal. A Chem.*, vol. 247, no. 1–2, pp. 7–13, 2006, doi: 10.1016/j.molcata.2005.11.013.

[272] C. Rozain, E. Mayousse, N. Guillet, and P. Millet, "Influence of iridium oxide loadings on the performance of PEM water electrolysis cells: Part II - Advanced oxygen electrodes," *Appl. Catal. B Environ.*, vol. 182, pp. 123–131, 2016, doi: 10.1016/j.apcatb.2015.09.011.

[273] C. Rozain, E. Mayousse, N. Guillet, and P. Millet, "Applied Catalysis B : Environmental Influence of iridium oxide loadings on the performance of PEM water electrolysis cells : Part I – Pure IrO 2 -based anodes," *"Applied Catal. B, Environ.*, vol. 182, pp. 153–160, 2016, doi: 10.1016/j.apcatb.2015.09.013.

[274] P. Millet *et al.*, "PEM water electrolyzers: From electrocatalysis to stack development," *Int. J. Hydrogen Energy*, vol. 35, no. 10, pp. 5043–5052, 2010, doi: 10.1016/j.ijhydene.2009.09.015.

[275] "NOVEL project." https://www.sintef.no/projectweb/novel/.

[276] R. Tunold, A. Marshall, E. Rasten, M. Tsypkin, L.-E. Owe, and S. Sunde, "Materials for Electrocatalysis of Oxygen Evolution in PEM Water Electrolysis," *ECS Trans.*, vol. 25, no. 23, 2010, doi: 10.1149/1.3328515.

[277] G. Li *et al.*, "Highly effective IrxSn1-xO2electrocatalysts for oxygen evolution reaction in the solid polymer electrolyte water electrolyser," *Phys. Chem. Chem. Phys.*, vol. 15, no. 8, pp. 2858–2866, 2013, doi: 10.1039/c2cp44496h.

[278] M. Suermann, T. J. Schmidt, and F. N. Büchi, "Investigation of mass transport losses in polymer electrolyte electrolysis cells," *ECS Trans.*, vol.

69, no. 17, pp. 1141–1148, 2015, doi: 10.1149/06917.1141ecst.
[279] P. Lettenmeier, S. Kolb, F. Burggraf, A. S. Gago, and K. A. Friedrich, "Towards developing a backing layer for proton exchange membrane electrolyzers," *J. Power Sources*, vol. 311, pp. 153–158, 2016, doi: 10.1016/j.jpowsour.2016.01.100.
[280] U. Babic, M. Suermann, F. N. Büchi, L. Gubler, and T. J. Schmidt, "Review - Identifying critical gaps for polymer electrolyte water electrolysis development," *J. Electrochem. Soc.*, vol. 164, no. 4, pp. F387–F399, 2017, doi: 10.1149/2.1441704jes.
[281] K. E. Ayers *et al.*, "Research Advances Towards Low Cost, High Efficiency PEM Electrolysis," *ECS Trans.*, vol. 33, no. 1, pp. 3–15, 2010.
[282] K. A. Lewinski, D. Van Der Vliet, and S. M. Luopa, "NSTF advances for PEM electrolysis - The effect of alloying on activity of NSTF electrolyzer catalysts and performance of NSTF based PEM electrolyzers," *ECS Trans.*, vol. 69, no. 17, pp. 893–917, 2015, doi: 10.1149/06917.0893ecst.
[283] S. Siracusano, V. Baglio, N. Van Dijk, L. Merlo, and A. S. Aricò, "Enhanced performance and durability of low catalyst loading PEM water electrolyser based on a short-side chain perfluorosulfonic ionomer," *Appl. Energy*, vol. 192, pp. 477–489, 2017, doi: 10.1016/j.apenergy.2016.09.011.
[284] S. Siracusano, N. Van Dijk, R. Backhouse, L. Merlo, and V. Baglio, "Degradation issues of PEM electrolysis MEAs," *Renew. Energy*, vol. 123, pp. 52–57, 2018, doi: 10.1016/j.renene.2018.02.024.
[285] M. J. Kelly, G. Fafilek, J. O. Besenhard, H. Kronberger, and G. E. Nauer, "Contaminant absorption and conductivity in polymer electrolyte membranes," *J. Power Sources*, vol. 145, pp. 249–252, 2005, doi: 10.1016/j.jpowsour.2005.01.064.
[286] S. Sun, Z. Shao, H. Yu, G. Li, and B. Yi, "Investigations on degradation of the long-term proton exchange membrane water electrolysis stack," *J. Power Sources*, vol. 267, pp. 515–520, 2014, doi: 10.1016/j.jpowsour.2014.05.117.
[287] S. A. Grigoriev, K. A. Dzhus, D. G. Bessarabov, P. Millet, and O. Cedex, "Failure of PEM water electrolysis cells : Case study involving anode dissolution and membrane thinning," *Int. J. Hydrogen Energy*, vol. 39, no. 35, pp. 20440–20446, 2014, doi: 10.1016/j.ijhydene.2014.05.043.
[288] S. A. Grigoriev, D. G. Bessarabov, and V. N. Fateev, "Degradation Mechanisms of MEA Characteristics during Water Electrolysis in Solid Polymer Electrolyte Cells," vol. 53, no. 3, pp. 318–323, 2017, doi: 10.1134/S1023193517030065.
[289] S. A. Grigoriev, D. G. Bessarabov, A. S. Grigoriev, N. V Kuleshov, and V. N. Fateev, "On the contamination of membrane-electrode assemblies of water electrolysers based on proton exchange membrane in the course of operation," *Bulg. Chem. Commun.*, vol. 50, no. Special Issue A, pp. 102–107, 2018.
[290] M. Chandesris, V. Medeau, N. Guillet, S. Chelghoum, D. Thoby, and F. Fouda-Onana, "Membrane degradation in PEM water electrolyzer : Numerical modeling and experimental evidence of the influence of temperature and current density," *Int. J. Hydrogen Energy*, vol. 40, no. 3, pp. 1353–1366, 2015, doi: 10.1016/j.ijhydene.2014.11.111.
[291] E. Brightman, J. Dodwell, N. Van Dijk, and G. Hinds, "In situ

characterisation of PEM water electrolysers using a novel reference electrode," *Electrochem. commun.*, vol. 52, pp. 1–4, 2015, doi: 10.1016/j.elecom.2015.01.005.

[292] S. Stucki, G. G. Scherer, S. Schlagowski, and E. Fischer, "PEM water electrolysers: Evidence for membrane failure in 100 kW demonstration plants," *J. Appl. Electrochem.*, vol. 28, no. 10, pp. 1041–1049, 1998, doi: 10.1023/A:1003477305336.

[293] S. H. Frensch *et al.*, "Impact of iron and hydrogen peroxide on membrane degradation for polymer electrolyte membrane water electrolysis : Computational and experimental investigation on fluoride emission," *J. Power Sources*, vol. 420, pp. 54–62, 2019, doi: 10.1016/j.jpowsour.2019.02.076.

[294] M. Ghelichi, P. É. A. Melchy, and M. H. Eikerling, "Radically coarse-grained approach to the modeling of chemical degradation in fuel cell ionomers," *J. Phys. Chem. B*, vol. 118, no. 38, pp. 11375–11386, 2014, doi: 10.1021/jp506333p.

[295] L. Gubler, S. M. Dockheer, and W. H. Koppenol, "Radical (HO●, H● and HOO●) Formation and Ionomer Degradation in Polymer Electrolyte Fuel Cells," *J. Electrochem. Soc.*, vol. 158, no. 7, p. B755, 2011, doi: 10.1149/1.3581040.

[296] P. Trinke, B. Bensmann, and R. Hanke-Rauschenbach, "Experimental evidence of increasing oxygen crossover with increasing current density during PEM water electrolysis," *Electrochem. commun.*, vol. 82, pp. 98–102, 2017, doi: 10.1016/j.elecom.2017.07.018.

[297] V. A. Sethuraman, J. W. Weidner, A. T. Haug, S. Motupally, and L. V. Protsailo, "Hydrogen Peroxide Formation Rates in a PEMFC Anode and Cathode," *J. Electrochem. Soc.*, vol. 155, no. 1, p. B50, 2008, doi: 10.1149/1.2801980.

[298] H. Liu, F. D. Coms, J. Zhang, H. A. Gasteiger, and A. B. LaConti, *Chemical Degradation: Correlations Between Electrolyzer and Fuel Cell Findings*. 2009.

[299] A. B. LaConti, H. Liu, C. Mittelsteadt, and R. C. McDonald, "Polymer electrolyte membrane degradation mechanisms in fuel cells- findings over the past 30 years and comparison with electrolyzers," *ECS Trans.*, vol. 1, no. 8, pp. 199–219, 2006.

[300] K. H. Wong and E. Kjeang, "Mitigation of Chemical Membrane Degradation in Fuel Cells : Understanding the Effect of Cell Voltage and Iron Ion Redox Cycle," *ChemSusChem*, vol. 8, pp. 1072–1082, 2015, doi: 10.1002/cssc.201402957.

[301] M. Inaba, T. Kinumoto, M. Kiriake, R. Umebayashi, A. Tasaka, and Z. Ogumi, "Gas crossover and membrane degradation in polymer electrolyte fuel cells," *Electrochim. Acta*, vol. 51, pp. 5746–5753, 2006, doi: 10.1016/j.electacta.2006.03.008.

[302] M. Danilczuk, S. Schlick, and F. D. Coms, "Degradation Mechanism of Perfluorinated Membranes," in *The Chemistry of Membranes Used in Fuel Cells*, 2018, pp. 19–53.

[303] L. Ghassemzadeh and S. Holdcroft, "Quantifying the Structural Changes of Perfluorosulfonated Acid Ionomer upon Reaction with Hydroxyl Radicals," *J. Am. Chem. Soc.*, vol. 135, no. 22, pp. 8181–8184, 2013.

[304] T. Xie and C. A. Hayden, "A kinetic model for the chemical degradation of perfluorinated sulfonic acid ionomers : Weak end groups versus side chain cleavage," *Polymer (Guildf).*, vol. 48, no. 19, pp. 5497–5506, 2007, doi: 10.1016/j.polymer.2007.07.043.

[305] M. Pianca, E. Barchiesi, G. Esposto, and S. Radice, "End groups in fluoropolymers," *J. Fluor. Chem.*, vol. 95, no. 1–2, pp. 71–84, 1999, doi: 10.1016/S0022-1139(98)00304-2.

[306] H. Monjid, "PEM Electrolyzer Incorporating an Advanced Low Cost Membrane," 2013.

[307] E. C. S. Transactions and T. E. Society, "Theoretical Study on Chemical Degradation Mechanism of Nafion Side Chain by the Attack of OH Radical in Polymer Electrolyte Fuel Cell T. Ishimoto," vol. 35, no. 27, pp. 1–6, 2011.

[308] A. M. Dreizler and E. Roduner, "Reaction Kinetics of Hydroxyl Radicals with Model Compounds of Fuel Cell Polymer Membranes," no. 1, pp. 132–140, 2012, doi: 10.1002/fuce.201100157.

[309] M. Kumar and S. J. Paddison, "Side-chain degradation of perfluorosulfonic acid membranes : An ab initio study," *J. Mater. Res.*, vol. 27, no. 15, pp. 1982–1991, 2012, doi: 10.1557/jmr.2012.191.

[310] Y. Zhao, M. Yamaguchi, E. Tsuchida, Y. Choe, and T. Ikeshoji, "DFT Studies of Perfluorosulfonic Acid Ionomer Degradation in Fuel Cells," *J. Phys. Chem. C*, vol. 122, pp. 20135–20143, 2018, doi: 10.1021/acs.jpcc.8b05908.

[311] K. H. Wong and E. Kjeang, "Macroscopic In-Situ Modeling of Chemical Membrane Degradation in Polymer Electrolyte Fuel Cells," *J. Electrochem. Soc.*, vol. 161, no. 9, pp. 823–832, 2014, doi: 10.1149/2.0031409jes.

[312] NOVEL project, "NOVEL project website." https://www.sintef.no/projectweb/novel/ (accessed Mar. 15, 2021).

[313] F. P. F. van Berkel and S. ten Hoopen, "Evaluating lifetime of electrolyzers managing fluctuating supply of renewable energy," 2018. [Online]. Available: https://publicaties.ecn.nl/PdfFetch.aspx?nr=ECN-E--18-022.

[314] N. Project, "NEPTUNE project." http://www.neptune-pem.eu/en/ (accessed Mar. 26, 2021).

[315] H. Su, V. Linkov, and B. J. Bladergroen, "Membrane electrode assemblies with low noble metal loadings for hydrogen production from solid polymer electrolyte water electrolysis," *Int. J. Hydrogen Energy*, vol. 38, no. 23, pp. 9601–9608, 2013, doi: 10.1016/j.ijhydene.2013.05.099.

[316] A. Weiß, A. Siebel, M. Bernt, T. H. Shen, V. Tileli, and H. A. Gasteiger, "Impact of intermittent operation on lifetime and performance of a PEM water electrolyzer," *J. Electrochem. Soc.*, vol. 166, no. 8, pp. F487–F497, 2019, doi: 10.1149/2.0421908jes.

[317] S. H. Frensch, A. C. Olesen, S. S. Araya, and S. K. Kaer, "Model-supported Analysis of Degradation Phenomena of a PEM Water Electrolysis Cell under dynamic Operation," *ECS Trans.*, vol. 85, no. 11, pp. 37–45, 2018.

[318] K. A. Friedrich, P. Lettenmeier, R. Wang, F. Burggraf, R. Abouatallah, and A. S. Gago, "Proton Exchange Membrane Electrolyzer Systems Operating Dynamically at High Current Densities," *ECS Trans.*, vol. 72, no. 23, pp. 11–21, 2016, doi: 10.1149/07223.0011ecst.

[319] T. Malkow, A. Pilenga, G. Tsotridis, and G. De Marco, "EU harmonised polarisation curve test method for low-temperature water electrolysis," 2018. doi: 10.2760/324006.
[320] T. Malkow, A. Pilenga, and G. Tsotridis, "EU harmonised test procedure: electrochemical impedance spectroscopy for water electrolysis cells," 2018. doi: 10.2760/8984.
[321] T. Malkow, G. De Marco, and G. Tsotridis, "EU harmonised cyclic voltammetry test method for low-temperature water electrolysis single cells," 2018. doi: 10.2760/140687.
[322] S. Siracusano *et al.*, "Chemically stabilised extruded and recast short side chain Aquivion® proton exchange membranes for high current density operation in water electrolysis," *J. Memb. Sci.*, vol. 578, pp. 136–148, 2019, doi: https://doi.org/10.1016/j.memsci.2019.02.021.
[323] R. Baldwin, M. Pham, A. Leonida, J. Mcelroy, and T. Nalette, "Hydrogen-oxygen proton-exchange membrane fuel cells and electrolyzers," *J. Power Sources*, vol. 29, pp. 399–412, 1990.
[324] T. A. Aarhaug, "Assessment of PEMFC Durability by Effluent Analysis," Norwegian University of Science and Technology, Trondheim, 2011.
[325] H. Wang, Y. Xiao-Zi, and H. Li, *PEM fuel cell diagnostic tools*. CRC Press, Taylor & Francis Group, Boca Raton, Florida, 2012.
[326] T. Malkow, A. Pilenga, and G. Tsotridis, "EU harmonised polarisation curve test method for low temperature water electrolysis," 2018. doi: 10.2760/179509.
[327] "Norwegian Fuel Cell and Hydrogen Centre." https://www.sintef.no/projectweb/nfch/ (accessed Jun. 29, 2020).
[328] V. A. Sethuraman, J. W. Weidner, A. T. Haug, M. Pemberton, and L. V. Protsailo, "Importance of catalyst stability vis-à-vis hydrogen peroxide formation rates in PEM fuel cell electrodes," *Electrochim. Acta*, vol. 54, no. 23, pp. 5571–5582, 2009, doi: 10.1016/j.electacta.2009.04.062.
[329] Metrohm, "Manual for 850 Professional IC, 2.850.2150 - Anion MCS Prep 2." https://www.metrohm.com/en/documents/88508048 (accessed Mar. 17, 2021).
[330] A. Pozio, R. F. Sil, M. De Francesco, and L. Giorgi, "Nafion degradation in PEFCs from end plate iron contamination," *Electrochim. Act*, vol. 48, no. 11, pp. 1543–1549, 2003, doi: 10.1016/S0013-4686(03)00026-4.
[331] J. Healy *et al.*, "Aspects of the Chemical Degradation of PFSA Ionomers used in PEM Fuel Cells," *Fuel Cells*, vol. 5, no. 2, pp. 302–308, 2005, doi: 10.1002/fuce.200400050.
[332] W. J. Hamer and H. J. DeWane, "Electrolytic Conductance and the Conductances of the Halogen Acids in Water," 1970, p. 37.
[333] F. Barbir, *PEM Fuel Cells. Theory and practice*, 2nd Editio. 2013.
[334] M. P. Rodgers, B. P. Pearman, N. Mohajeri, L. J. Bonville, and D. K. Slattery, "Effect of perfluorosulfonic acid membrane equivalent weight on degradation under accelerated stress conditions," *Electrochim. Acta*, vol. 100, pp. 180–187, 2013, doi: 10.1016/j.electacta.2013.03.112.